Evaluation of environmental impacts of buildings in China

Long Pei

HAL Id: tel-03282128
https://pastel.hal.science/tel-03282128

Submitted on 8 Jul 2021

PSL★
UNIVERSITÉ PARIS

THÈSE DE DOCTORAT
DE L'UNIVERSITÉ PSL

Préparée à MINES ParisTech

Évaluation des impacts environnementaux des bâtiments en Chine
Evaluation of environmental impacts of buildings in China

Soutenue par
Long PEI
Le 29 Septembre 2020

École doctorale n° 621
Ingénierie des Systèmes, Matériaux, Mécanique, Énergétique

Spécialité
Energétique et Génie des Procédés

MINES ParisTech | PSL★

Composition du jury :

Vincent, LEMORT
Professeur, Université de Liège   *Rapporteur*

Monica SIROUX
Professeur, Institut National des
Sciences Appliquées de Strasbourg   *Rapporteuse*

Assaad, ZOUGHAIB
Professeur, PSL-Mines ParisTech   *Président du jury*

Youcef, BOUZIDI
Professeur, Université de technologie de Troyes   *Examinateur*

Christophe, GOBIN
Docteur, VINCI Construction France   *Examinateur*

Lu, XING
Docteur, Huazhong University of Science and
Technology   *Examinatrice*

Bruno, PEUPORTIER
Directeur de recherche, PSL-Mines ParisTech   *Directeur de thèse*

Patrick, SCHALBART
Docteur, PSL-Mines ParisTech   *Maître de thèse*

Acknowledgment

When I firstly stepped into the university, I never imagined that I would sit in the office in Paris to write down the acknowledgement of a PhD thesis twelve years later. Finishing the thesis is an essential an unforgettable period in my lifetime, and I am sure I can not arrive here without the help of many people. This one-page acknowledgment is not possible to cover all of them, but still many thanks to them from my heart, no matter where they are right now.

First of all, I would like to express my sincere thanks to my supervisors. Thank you to Bruno. This "thank you" can go back to the year 2014, when my research career in the building and environment field started, by doing a 6 months internship with Bruno in his group ETB. Three years later, I started my thesis in the same group, and had the chance to investigate more in this interesting field. I really appreciate the two opportunities that Bruno gave to me. His support for my French courses is important to my life in France. Besides, his scientific knowledge, rigorous attitude and enthusiasm towards research have been motivating me to explore more during the thesis. This will encourage me to overcome the difficulties in the future career. Similarly, thank you to Patrick. His solid academic background and innovate ideas always inspired me. I learned a lot during every conversation we had, about the geothermal model, heat exchanger, LCA method, etc. He not only helped me in the research but also many aspects in the daily life. I really appreciate his patience when I speak French, which can be painful to understand. He showed me the charm of science, as well as the French culture (including but not limited to the Blood Bowl).

I want to thank the China Scholarship Council for providing me the financial support during the thesis. Thanks to the thesis reporters and the jury members. The interesting questions proposed made me investigate more deeply in this field and improve the quality of my thesis.

Also, I am grateful to all my colleagues in ETB. Thanks to Simon for his aids in the geothermal model. Thanks to Mija for his help in the LCI database development. Thanks to Aurore and Lucas for the discussions in the research and also the preparation of my defense pot. Thanks to Charbel, Fatima, Marie, Michaël, Rachna, Samih and Stéphane for all your kind help. Thanks to my Chinese friends Boyang and Rupu for the happy time we spent together during the three years. Thanks to the administration and IT staffs of the center CES for all the administrative and PC problems.

Especially, I would like to thank my family for their unconditional support and love. They always encourage me during the difficult time and share the happiness of every success with me, no matter big or small. Their optimism helps me go through the hard time. It is their education during my whole life brings me here.

Last but not least, this thesis is accomplished in the year 2020, which is a special year that COVID-19 spreads all over the world. The pandemic was firstly breakout in my hometown, Wuhan, China. I witnessed the great and unselfish sacrifice from the medical staffs, not only in China, but also all over the world. I would like to express all my respect and acknowledgement to them.

Content

NOMENCLATURE

List of symbols

$a_1 - a_8$	Location factor parameter, –
α_m	Fractional change in monthly mean climatic variable for month m, –
A_{cd}	Surface area that heat transfer take place for condenser, m^2
A_{ev}	Surface area that heat transfer take place for evaporator, m^2
A_{soil_surf}	Amplitude of oscillation of soil surface temperature, °C
b	Dimensionless position parameter, –
B	Borehole spacing, m
C_f	Characterisation factor matrix, –
C_l	Compressor loss rate, m^3.Pa/s
$c_{p,fl}$	Fluid heat capacity, J/kg.K
$c_{p,w}$	Heat capacity of water, J/kg.K
$c_{p,wg}$	Heat capacity of water-glycol solution, J/kg.K
COP_{DWH}	Annual average COP for DWH, –
COP_{DHW}^{Carnot}	Annual average COP at Carnot efficiency for DWH, –
COP_{fl}	COP at full load, –
$COP_{heating}$	Annual average COP for heating, –
$COP_{heating}^{Carnot}$	Annual average COP at Carnot efficiency for heating, –
COP_{pl}	COP at partial load, –
erfc	Complementary error function, –
E	Amount of electricity used in material fabrication, kWh
$E_{i,j}^k$	Electricity production of technology i in province k in year j, MWh
$E_{i,j}^{nation}$	Electricity production of technology i in the whole nation in year j, MWh
$EER_{cooling}$	Annual EER for "normal" cooling (cooling in summer) , –
$EER_{cooling}^{Carnot}$	Annual average EER at Carnot efficiency for "normal" cooling, –
$EER_{heating}$	Annual EER for "virtual" cooling (in "virtual" reverse cycle under the same condition as heating) , –
$EER_{heating}^{Carnot}$	Annual average EER at Carnot efficiency for "virtual" cooling under the heating mode condition, –
g	g-function, –
G	Thermal response factor, –
G_{2i}	Thermal response factor for borehole wall temperature using integral mean temperature, –
$G_{2i,borehole}$	Thermal response factor for a certain borehole wall temperature under all boreholes' effect using integral mean temperature, –

$G_{2i,GHE}$	Thermal response factor for GHE using integral mean temperature, –
G_{3p}	Thermal response factor for borehole wall temperature using three points method, –
$G_{3p,borehole}$	Thermal response factor for a certain borehole wall temperature under all boreholes' effect using three points method, –
$G_{3p,GHE}$	Thermal response factor for GHE using three points method, –
G_m	Thermal response factor for borehole wall temperature using middle point temperature, –
$G_{m,borehole}$	Thermal response factor for a certain borehole wall temperature under all boreholes' effect using middle point temperature, –
$G_{m,GHE}$	Thermal response factor for GHE using middle point temperature, –
h	Integral variable along borehole depth, –
h_f	Convective heat transfer coefficient, W/m^2.K
H	Borehole length, m
H_{bottom}	Borehole depth of botome point in three points method, m
H_{top}	Borehole depth of top point in three points method, m
i	i^{th} boreheole in chapter 2 and 3, –
	i^{th} hour in chapter 4, –
	Energy technology i (thermal, hydro, nuclear, wind, solar, or total) in chapter 5, –
I	Number of cells on x-axis in ENVI-met model, –
I_{FR}	Environmental impacts of one kWh electricity in France, –
$I_{FR}^{material}$	Environmental impacts of a material under French context, –
I_i	Environmental impacts related to electricity production using technology i and network infrastructure, –
$I_{loc,year}$	Environmental impacts of 1 kWh supplied by grid in a certain location in a certain year, –
$I_{loc,year}^{material}$	Environmental impacts of one material in a certain location in China and in a certain year, –
j	j^{th} boreheole in chapter 2 and 3, –
	j^{th} day in representative week in chapter 4, –
	Year (2019, and every 5 years from 2020 to 2050) in chapter 5, –
j_{re1}	Day number of the 1st representative day, –
j_{re2}	Day number of the 2nd representative day, –
J	Number of cells on y-axis in ENVI-met model, –
k	k^{th} timestep in chapter 2 and 3, –
	Province (HU, BJ, GD, NM,YN) in chapter 5, –
K	Number of cells on z-axis in ENVI-met model, –
l	Electricity lost during transmission in transport network, –
l_p	Averaging range for averaging period p, –
LCI_i	Life cycle inventory of one kWh produced by technology "i" , –

$LCI_{\text{network},i}$	Life cycle inventory of electricity network infrastructure per kWh for technology "i" , –
m	Timestep in chapter 2, –
	Month in chapter 1, –
m_{IES}	Initial effect simplification timestep, –
m_{TAS}	Averaging simplification timestep, –
$\dot{m}_{\text{b}}$	Fluid mass flow rate of borehole, kg/s
$\dot{m}_{\text{cd}}$	Fluid mass flow rate of condenser, kg/s
$\dot{m}_{\text{ev}}$	Fluid mass flow rate of evaporator, kg/s
$\dot{m}_{\text{GHE}}$	Fluid mass flow rate of GHE, kg/s
$\dot{m}_{\text{leak}}$	Leakage in refrigerant flow rate of compressor, kg/s
n	Distance category, in chapter 2, –
	Level of the cell, in chapter 4, –
	Total number of electricity production technologies, in chapter 5, –
N_{b}	Number of boreholes in GHE , –
$N_{\text{b,sym}}$	Number of boreholes after symmetry, –
N_{d}	Number of total distance categories, –
N_{h}	Number of different heights, –
N_{l}	Number of U-pipe legs, –
N_r	Number of radius distance r occurs, –
NTU_{cd}	Number of transfer units of condenser, –
NTU_{ev}	Number of transfer units of evaporator, –
Nu	Nusselt number, –
p	Averaging range, –
P	Atmosphere pressure, Pa
P_0	Reference pressure, Pa
P_{bottom}	Bottom point in three-points method, –
P_{cd}	Condensing pressure, Pa
P_{dis}	Internal discharge pressure, Pa
P_{ev}	Evaporating pressure, Pa
P_{middle}	Middle point in three-points method, –
P_{suc}	Internal suction pressure, Pa
P_{top}	Top point in three-points method, –
Pr	Prandtl number, –
q	Heat load per meter, W/m
q_1	Heat load per meter along pipe 1, W/m

q_2	Heat load per meter along pipe 2, W/m
$q_{i,m}$	Heat load per meter of ith boreheole at timestep m, W/m
q_k	Heat load per meter of each boreheole at timestep k, W/m
Q_b	Heat load of building, W
Q_{cd}	Heat flux of condenser, W
Q_{dis}	Heat flux of distribution unit, W
Q_{ev}	Heat flux of condenser, W
Q_{ev}^{annual}	Annual total heat flux in evaporator, W
Q_{GHE}	Heat load of GHE, W
r	Radial distance to borehole centre line, m
r_b	Radius of borehole, m
r_i	Inside radius of the pipe, m
$r_{i,j}$	Distance between i^{th} boreheole and j^{th} boreheole, m
r_n	Distance of nth distance category, m
r_o	Outside radius of the pipe, m
R	Thermal resistance of wall, m^2.K/W
R_1'	Thermal resistance between the circulating fluid in pipe 1 and borehole wall, m.K/W
R_2'	Thermal resistance between the circulating fluid in pipe 2 and borehole wall, m.K/W
R_{12}'	Thermal resistance between pipe 1 and pipe 2, m.K/W
R_1^{Δ}	Thermal resistance parameter, m.K/W
R_{12}^{Δ}	Thermal resistance parameter, m.K/W
R_2^{Δ}	Thermal resistance parameter, m.K/W
R_b	Linear borehole thermal resistance, m.K/W
R_{bp}	Linear borehole-to-pipe thermal resistance, m.K/W
Re	Reynolds number, –
$R_{i,j}^k$	Ratio of the electricity production of technology i of province k to nation in year j, –
$R_{loc,year}^i$	Share of technology i in a certain location and in a certain year, –
R_p	Linear pipe thermal resistance, m.K/W
$R_{p,cond}$	Linear pipe conductive thermal resistance, m.K/W
$R_{p,conv}$	Linear pipe convective thermal resistance, m.K/W
t	Time, s
t_m	Time at timestep m, s
t_s	Steady time, s
T	Ground temperature, °C
T_0	Undisturbed ground temperature, °C

$T_{\text{air,ENVImet}}$	Air temperature converted from potential air temperature of ENVI-met simulation, °C
$T_{\text{air,EPW}}$	Air temperature in EPW file, °C
$T_{\text{air,EPW}}^{\text{abs}}$	Absolute air temperature in EPW file, K
$T_{\text{av},i}$	Average air temperature of ith hour of representative week, °C
T_{b}	Borehole wall temperature, °C
$T_{\text{b,j}}$	Borehole wall temperature of jth boreheole, °C
T_{bedrock}	Soil temperatures of bedrock layer, °C
T_{deep}	Soil temperatures of deep layer, °C
T_{ext}	External air temperature, °C
T_{f1}	Average fluid temperature of pipe 1, °C
T_{f2}	Average fluid temperature of pipe 2, °C
$T_{\text{f,in}}$	Inlet fluid temperature of borehole, °C
$T_{\text{f,out}}$	Outlet fluid temperature of borehole, °C
$T_{\text{fl},j}$	Mean fluid temperature of jth borehole, °C
T_i^j	Air temperature of the ith hour of the jth day in representative week, °C
$T_{\text{in,dis}}$	Inlet temperatures of distribution unit, °C
$T_{\text{in,cd}}$	Inlet temperatures of condenser, °C
$T_{\text{in,ev}}$	Inlet temperatures of evaporator, °C
$T_{\text{in,GHE}}$	Inlet temperatures of GHE, °C
T_{middle}	Soil temperatures of middle layer, °C
$T_{\text{out,dis}}$	Outlet temperatures of distribution unit, °C
$T_{\text{out,cd}}$	Outlet temperatures of condenser, °C
$T_{\text{out,cd}}^{\text{DWH}}$	Annual average outlet water temperature of condenser for DWH, K
$T_{\text{out,cd}}^{\text{heating}}$	Annual average outlet water temperature of condenser for heating, K
$T_{\text{out,cd}}^{\text{cooling}}$	Nominal outlet water temperature of condenser for cooling, K
$T_{\text{out,ev}}$	Outlet temperatures of evaporator, °C
$T_{\text{out,ev}}^{\text{cooling}}$	Nominal outlet water temperature of evaporator for cooling, K
$T_{\text{out,ev}}^{\text{DWH}}$	Annual average outlet water temperature of evaporator for DWH, K
$T_{\text{out,ev}}^{\text{heating}}$	Annual average outlet water temperature of evaporator for heating, K
$T_{\text{out,GHE}}$	Outlet fluid temperature of GHE, °C
$T_{\text{out},j}$	Outlet fluid temperature of jth borehole, °C
T_{soil}	Temperature of soil in chapter 4, °C
$\overline{T_{\text{soil\_surf}}}$	Average temperature of soil surface, °C
T_{upper}	Soil temperatures of upper layer, °C
u	Integration variable, –

U	Uppermost part of borehole, m
U_{cd}	Heat transfer coefficient for condenser, W/(m^2.K)
U_{ev}	Heat transfer coefficient for evaporator, W/(m^2.K)
U_{w}	Window heat transfer coefficient, W/(m^2.K)
v_{i}	Built-in volume ratio, –
v_{suc}	Specific volume at suction state, kg/m^3
$\dot{V}_{r}$	Volume flow rate of refrigerant, m^3/s
W	Total power consumption of compressor, W
W^{annual}	Annual total energy consumption by compressor, W
$\dot{W}_{is}$	Power consumption of compressor under isentropic process, W
$\dot{W}_{loss}$	Electromechanical power losses of compressor, W
$\dot{W}_{t}$	Power consumption of compressor without losses, W
x	X-axis coordinate of, m
	Time parameter in equation (1-3), –
x_0	Existing hourly climatic variable, –
$\langle x_0 \rangle_m$	Climatic variable x_o average over month m, –
x_1	Location of pipe 1 on x-axis, m
x_1'	Dimensionless position parameter, –
x_c	Half spacing between legs of U-tube, m
x_{dis}	Location factor of top point, –
x_{n}	Hourly climatic variable after morphing, –
x_{p}	Polytropic coefficient, –
y	Y-axis coordinate of, m;
	Distance parameter in equation (1-3), –
y_1	Location of pipe 1 on y-axis, m
y_1'	Dimensionless position parameter, –
z	Vertical coordinate of borehole, m

List of Greek letters

α	Coefficient to determine PLF, –
α_s	Thermal diffusivity of ground, m^2/s
β	Coefficient to determine PLF, –
γ	Isentropic coefficient, –
ΔP	Difference of condensing pressure and evaporating pressure, W
ΔT_{sh}	Overheat temperature at the outlet of evaporator, °C
Δx	Resolution of cell on x-axis in ENVI-met model, m
Δx_m	Absolute change in monthly mean climatic variable for month m, –
Δy	Resolution of cell on y-axis in ENVI-met model, m
Δz	Resolution of cell on z-axis in ENVI-met model, m
ε_{cd}	Effectiveness of condenser, –
ε_{ev}	Effectiveness of evaporator, –
ε_{IES}	Accuracy of initial effect simplification , –
ε_{TAS}	Accuracy of time averaging simplification, –
ψ	Thermal bridge, W/K.m
λ_b	Thermal conductivity of grout, W/m.K
λ_f	Thermal conductivity of fluid, W/m.K
λ_p	Thermal conductivity of pipe, W/m.K
λ_s	Thermal conductivity of ground, W/m.K
η	Electromechanical efficiency of compressor, –
θ_{he}	Temperature variation in 2D heat equation, K
π	External pressure ratio in chapter 3, –
π_i	Built-in pressure ratio in chapter 3, –
$\rho_{cd,sat}$	Density of fluid at the beginning of condensation, kg/m^3
σ	Dimensionless conduction parameter, –
φ_{soil_surf}	Phase shift of soil surface temperature, rad
ω	Pulsation of oscillation of soil surface temperature, rad/s,

Abbreviation

1D, One-dimensional

2D, Two-dimensional

3D, Three-dimensional

ach, air change per hour

ADP, Abiotic resources Depletion Potential

AP, Acidification Potential

BEP, Building Effect Parameterization

Biodiv, Damage to Biodiversity

BJ, Beijing

C, Cold climate zone

CAT, Canyon Air Temperature

CDD, Cooling Degree Day

CED, Cumulative Energy Demand

CFD, Computational Fluid Dynamics

CIM, Canopy Interface Model

CLCD, Chinese Reference Life Cycle Database

COP, Coefficient Of Performance

CPLCID, Process-based Life Cycle Inventory Database

CTRF, Calculation Time Reduction Factor

DAE, Dynamic Assessment Eelements

DALY, Disability Adjusted Life Years

DBES, Dynamic Building Energy Simulation

DHW: Domestic Hot Water

DLCA, Dynamic Life Cycle Assessment

DST, Duct ground STorage

E, East

EER, Energy Efficiency Rratio

ELC, Enhanced Low Carbon

EP, Eutrophication Potential

EPW, EnergyPlus Weather

ERI, Energy Research Institute

ES, Energy Saving

ETB, Eco-conception et Thermique des Bâtiments

FFT, Fast Fourier Transform

FLS, Finite Line Source

GCHP, Ground-Coupled Heat Pump

GD, Guangdong

GFA, Gross Floor Area

GHE, Ground Heat Exchanger

GHG, Greenhouse Gases

GSHP, Ground Source Heat Pump

Gtce, Gigatons of standard coal equivalent

GWHP, Ground Water Heat Pump

GWP, Global Warming Potential

HDPE, High-Density PolyEthylene

HP, Heat Pump

HRE, High Renewable Energy

HSCW, Hot Summer and Cold Winter climate zone

HSJG, HaiShan JinGu block

HSWW, Hot Summer and Warm Winter climate zone

HU, Hubei

Hum, Damage to human health

HVAC, Heating, Ventilating, and Air Conditioning

IES, Initial Effect Simplification

ILS, Infinite Line Source

IPAC, Integrated Policy Assessment model of China

ISO, International Organization for Standardization

Land, Land use

LC, Low Carbon

LCA, Life Cycle Assessment

LCI, Life Cycle Inventory

LCIA, Life Cycle Inventory Assessment

LPG, Liquefied Petroleum Gas

M, Mild climate zone

MAE, Mean Absolute Error

MOHURD, Ministry Of Housing and Urban-Rural Development

Mtce, Million tons of standard coal equivalent

N, North

NDRCC, National Development and the Reform Commission of China

NFFs, Non-Fossil Fuels

NM, Inner Mongolia

NZEB, Net-Zero Energy Building

PDF, Potentially Disappeared Fraction

PE, PolyEthylene

PLF, Partial Load Factor

PLR, Partial Load Ratio

POP, Photochemical Ozone Production

PVC, PolyVinyl Chloride

Rad.W, Radioactive Waste

RMSE, Root Mean Square Error

S, South

SC, Severe Cold climate zone

SWHP, Surface Water Heat Pump

TAS, Time Averaging Simplification

TEB, Town Energy Balance

TMM, Typical Meteorological Month

TMY, Typical Meteorological Year

TPE, Total Primary Energy Consumption

UCI, Urban Cool Island

UCIdh, Urban Cool Island degree-hours

UCII, Urban Cool Island Intensity

UCM , Urban Climate Modelling

UHI, Urban Heat Island

UHIdh, Urban Heat Island degree-hours

UHII, Urban Heat Island Intensity

UWG, Urban Weather Generator

VOC, Volatile Organic Compounds

W, West

Water, Water used

WRF, Weather Research and Forecast

XPS, eXtruded PolyStyrene foam

YN, Yunnan

Chapter 1.   Introduction

Urbanisation process in China makes the Chinese building construction sector very active. This leads to a high pressure on resources, as well as environmental impacts such as energy consumption and GHG emissions during a building's long lifespan. It is beneficial to reduce the environmental impacts during a building's design phase, with the aid of the computer tools. The environmental impacts evaluation of a building depends on various aspects. The thesis aims at improving the quantitative evaluation methodology of a building's environmental impacts based upon dynamic building energy simulation and life cycle assessment, by refining three boundary conditions: the ground, the microclimate, and the background systems in LCA.

Résumé du chapitre

La Chine a connu un processus d'urbanisation rapide au cours des dernières décennies et il se poursuivra à l'avenir. Cela rend le secteur chinois de la construction de bâtiments très actif, ce qui entraîne une forte pression sur les ressources, ainsi que des impacts environnementaux tels que la consommation d'énergie et les émissions de gaz à effet de serre pendant la longue durée de vie des bâtiments. Le plus grand potentiel de réduction de ces impacts correspond aux décisions prises lors de la phase de conception des bâtiments. Ce processus peut être mené à l'aide d'outils informatiques de simulation / évaluation. Les impacts environnementaux d'un bâtiment dépendent de nombreux aspects en interaction, de sorte qu'un outil d'évaluation systémique comme l'analyse du cycle de vie (ACV) est approprié. Mais cela nécessite de définir des conditions aux limites pertinentes.

Dans cette thèse, trois conditions aux limites liées à l'évaluation de la performance énergétique et environnementale sont discutées : le sol, le microclimat et les systèmes d'arrière-plan en ACV. Le sol est une condition aux limites directement reliée à un bâtiment et également pour le système de pompe à chaleur verticale (GCHP), qui est de plus en plus largement utilisé dans les zones urbaines en Chine. Les conditions climatiques sont une autre condition limite pour l'évaluation de la consommation d'énergie d'un bâtiment ; des microclimats urbains locaux sont générés pendant l'urbanisation. Les systèmes d'arrière plan tels que le mix de production électrique ont une forte influence sur les résultats de l'ACV. La Chine est un grand pays, ce qui induit une variété de mix régionaux de production d'électricité en fonction des conditions régionales. L'évolution du système électrique est également importante. Une revue détaillée de la littérature concernant chaque condition aux limites a été réalisée.

La thèse vise à améliorer la méthodologie d'évaluation quantitative des impacts environnementaux des bâtiments basée sur la simulation énergétique dynamique du bâtiment (DBES) et l'ACV, en affinant ces trois conditions aux limites. Le premier objectif est de proposer un modèle GCHP équipé d'un champ de sondes à grande échelle, représentant un bon compromis entre temps de calcul et précision, et de l'implémenter dans un outil DBES. Le deuxième objectif est de développer une méthodologie d'évaluation quantitative des effets du microclimat sur la performance énergétique des bâtiments. Les effets des îlots de chaleur urbains sur la performance énergétique des bâtiments à Wuhan (Chine) ont alors été étudiés. Le troisième objectif est de réaliser l'évaluation des impacts environnementaux par la méthodologie ACV, en tenant compte de systèmes d'arrière-plan locaux (par exemple, le mix de production d'électricité) en Chine et dans différentes provinces avec des caractéristiques de mix énergétique local. L'évolution temporelle de ces systèmes d'arrière-plan est également prise en compte. Le modèle amélioré a été appliqué à un immeuble résidentiel chinois de grande hauteur à Wuhan.

Les méthodes proposées dans la thèse ont été intégrées dans les outils informatiques qui sont utiles aux concepteurs pour améliorer les performances environnementales des bâtiments. Ce travail de thèse devrait fournir des résultats d'évaluation plus fiables des impacts environnementaux des bâtiments en Chine.

Abstract

China has been under a rapid urbanisation process during the past decades and it will continue in the future. This makes the Chinese building construction sector very active, which leads to a high pressure on resources, as well as the environmental impacts such as energy consumption and greenhouse gas emissions during a building's long lifespan. The highest potential reduction of these impacts corresponds to decisions made during the building's design phase. This process can be accomplished with the aid of computer simulation/evaluation tools. The environmental impacts of a building depend on many interacting aspects, so that a systemic evaluation tool like life cycle assessment (LCA) is appropriate. But this requires to define relevant boundary conditions.

In this thesis, three boundary conditions related to the energy and environmental performance evaluation are discussed: the ground, the microclimate, and the background systems in LCA. The ground is a boundary condition directly connected to a building and also for the vertical ground coupled heat pump (GCHP) system, which is more and more widely used in urban areas. Climate condition is another boundary condition for a building's energy consumption evaluation and local urban microclimates are generated during urbanisation. Thirdly, background systems such as the electricity production and distribution system have a strong influence on the LCA results. China is a large country, leading to a regional electricity production mix based on regional conditions. The evolution of the electric system is also important. A detailed literature review regarding each boundary condition was conducted.

The thesis aims at improving the quantitative evaluation methodology of buildings' environmental impacts based upon dynamic building energy simulation (DBES) and LCA, by refining these three boundary conditions. The first objective is to propose a GCHP model equipped with a large-scale boreholes field, representing a good compromise between calculation time and accuracy and implement it in a DBES tool. The second objective is to develop a methodology for quantitative evaluation of the microclimate's effects on the building's energy performance. Afterwards, the urban heat island effects on the building energy performance in Wuhan (China) were investigated. The third objective is to perform the environmental impacts evaluation by LCA methodology, accounting for local background systems (e.g. the electricity production mix) in China and different provinces with local energy mix features. The temporal evolution of the background systems is taken into consideration as well. The improved model was applied to a high-rise Chinese residential building in Wuhan.

The methods proposed in the thesis were integrated in the computer tools which are beneficial to building designers to improve a building's environmental performance. The accomplishments of the thesis are expected to provide more reliable evaluation results of the environmental impacts of Chinese buildings.

1.1. Background

1.1.1. *Urbanisation in China*

Urbanisation has been a defining global phenomenon and a key driving force for social and economic development during the past century (Liu et al., 2014). Urbanisation is the process of transferring people and their ability to work from rural areas to urban areas, accompanied by a national transition from an economy dominated by agriculture to one dominated by secondary and tertiary industries (Deng and Jiang, 2018). The level of urbanisation is usually described by the urbanisation rate, denoted by the percentage of the urban population to the total. Since the 1987 institutional reforms, demographic shifted to smaller families. Increased receipts of foreign direct investment have stimulated rural to urban migration in China (Fan et al., 2017). In consequence, China has experienced a rapid urbanisation process during the past four decades. According to Figure 1.1, China's urban population increased by a factor 4 from 1980 to 2015, from 191 million to 771 million urban residents, with the urbanisation rate going from 19.4 % to 56.1 %. Moreover, the urbanisation accelerated after 1996, with annual increase of 1.4 % between 1996 and 2014 compared to that of 0.6 % between 1980 and 1995. If the current trend continues, China's urbanisation rate will reach 70 % by 2030, and more than 1 billion Chinese will live in urban areas (Wei et al., 2016).
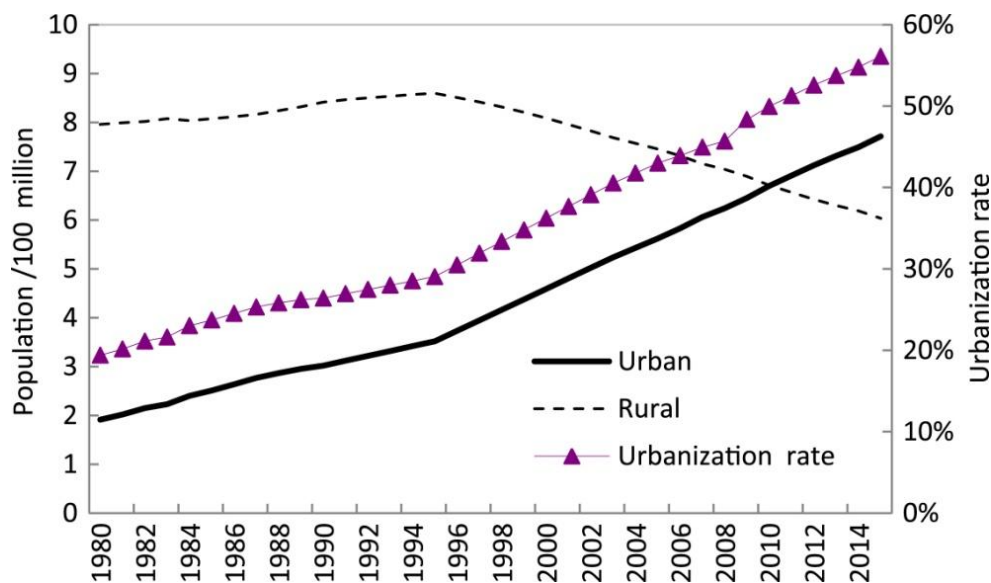
Figure 1.1: Changes of urban and rural populations in China during 1980–2015 (Fan et al., 2017)

On the one hand, urbanisation concentrates industries and population in and around cities, facilitating the development of economies of scale (Li, 2017), and brings benefits such as improved employment opportunities, sanitation, income, and access to infrastructure services (Liang and Yang, 2019). On the other hand, it causes various problems regarding the society, the economy, the energy and the environment (Zhou et al., 2015). One of the most related areas is the building sector. Numerous buildings with various functions (e.g. residential buildings, commercial buildings, schools,

etc.) have been built and will be built because of urbanisation. This leads to a high pressure on resources, as well as future environmental impacts related to energy and water consumed in buildings during their operation stage, and waste generation at their end of life and renovation.

1.1.2. *Building and environmental impacts*

The environmental impacts exist throughout a building's lifespan, from the fabrication of the building materials to the disposal of the building at the end of life. One of the most important causes of environmental impacts is energy consumption. As urbanisation processed, the gross floor area (GFA) of urban residential building increased from 10 800 millions of m^2 to 24 800 millions of m^2 in 2001-2015. Meanwhile, the total primary energy consumption (TPE) of the building sector increased steadily from 309 millions of tons to 857 millions of tons of standard coal equivalent (Mtce), with an average annual growth rate of 11.8 %, as illustrated in Figure 1.2. According to *China Building Energy Use 2018* (Jiang et al., 2018), building energy consumption is one of the three main energy consumption domains including industry and transportation, accounting for approximately 20 % of TPE in China in 2016.
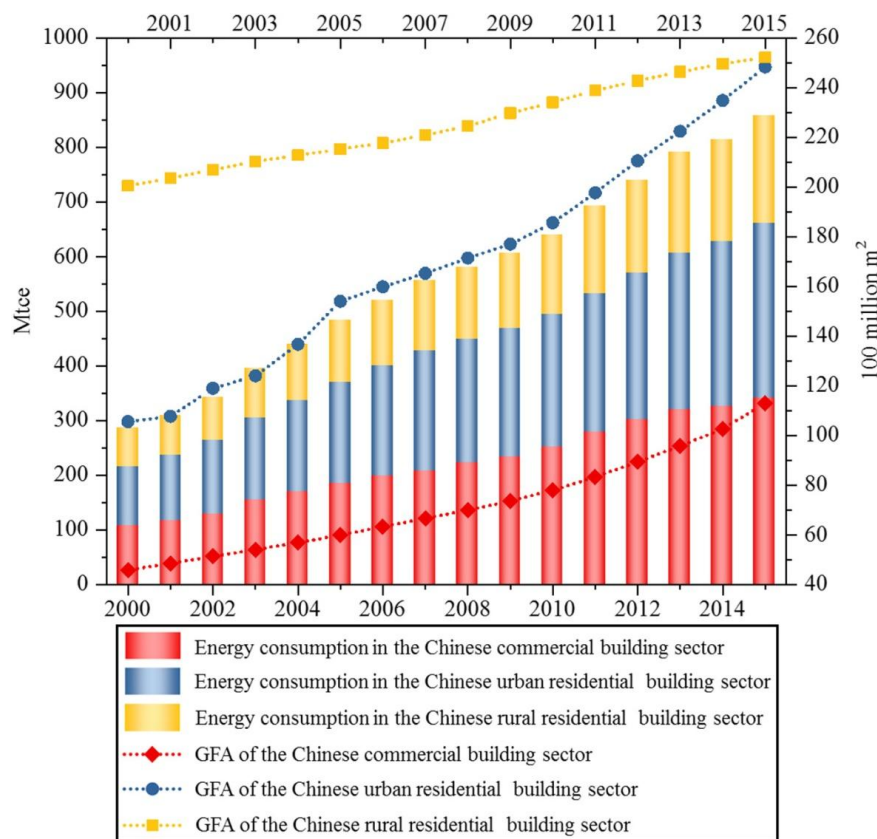
Figure 1.2: Trends of energy consumption and GFA values for the Chinese civil building sector during 2000 – 2015 (Ma et al., 2018)

Another environmental impact is the greenhouse gases (GHG) emissions. The building sector is one of the main sources for GHG emissions with the consequence of global warming (Li et al., 2014c).

As a quickly developing country relying on coal fire plants to produce electricity, China overtook the United States to become the world's largest contributor to CO_2 emissions in 2007 (International Energy Agency, 2010). As shown in Figure 1.3, CO_2 emissions of the building sector in China increased from around 0.9 Gt in 2001 to around 2 Gt in 2016. 60 % of CO_2 emissions were direct emissions and 40 % were indirect emissions from electricity production. CO_2 emissions of the building sector occupies approximately 19 % of the total emissions (Jiang et al., 2018).
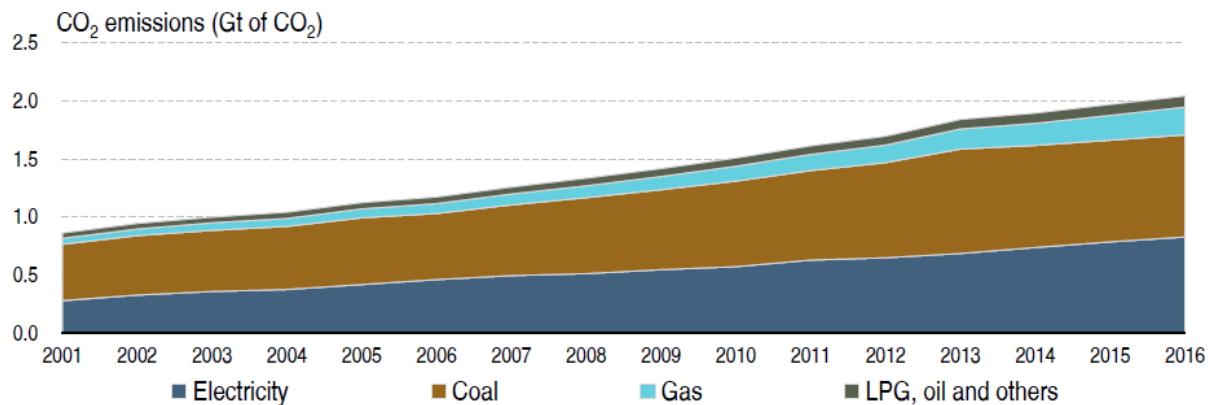
Figure 1.3: CO_2 emission of the building sector in China from 2001 to 2016 (Jiang et al., 2018)

More impacts are observed related to buildings. Buildings occupy large land areas. During the use stage, a large amount of water is consumed. Impacts related to acidification occur as well due to the emission of gases like SO_2 e.g. in thermal electricity plants and factories. In addition, a high level of waste is generated in the construction, retrofit and demolition stages as well as household waste during its lifespan (Villoria Sáez et al., 2014). The emissions (e.g. from waste water) could pollute water through eutrophication. Wastes and pollutants can be transported into different ecological compartments for instance air, surface water, soil, etc. and degrade over time, transfer into food and become a threat to human health and biodiversity (Gens et al., 2014). In China, most regulations regarding buildings only concern about energy, ignoring other environmental impacts (Li and Shui, 2015). To achieve the goal of transforming to a sustainable development and environment-friendly society, it is essential to have a comprehensive evaluation of building environmental impacts instead of considering only energy issues.

With the energy crisis and the global warming drawing the global attention, Chinese government launched several policies concerning energy conservation and GHG emissions reduction (Zhang and Wang, 2013). In 2017, the National Development and Reform Commission of China (NDRCC) released *Energy Production and Consumption Revolution Strategy (2016–2030)*[1], which included several targets. By 2020, TPE is expected to be less than 5 gigatons of standard coal equivalent (Gtce), whereas the proportion of non-fossil fuels (NFFs) will reach more than 15 %; CO_2 emissions will drop by 18 % compared to 2015. By 2030, TPE will measure less than 6 Gtce, the proportion of NFFs will

---

[1] https://www.ndrc.gov.cn/xxgk/zcfb/tz/201704/t20170425_962953.html

approximate 20 %, the share of natural gas will reach 15 %, and CO_2 emissions will peak to have a reduction of 60 – 65 % compared to 2005. By 2050, TPE will stabilise, and the proportion of NFFs will reach higher than 50 %.

1.1.3. *Main context of thesis*

To achieve the abovementioned goals, the building sector is considered as one of the most promising areas. On the one hand, it is one of the main causes of energy consumption and GHG emissions; on the other hand, it has a large potential for energy conservation and GHG emissions reduction. Therefore, improving the building's energy efficiency is an essential topic in both academic and regulation aspects (Lin and Liu, 2015). Renewable resources such as geothermal heat pump systems (Lucia et al., 2017), PV panels (Kosorić et al., 2018), and small-scale wind turbines (Elbakheit, 2018) can be used in high-performance buildings which are feasible to improve building energy efficiency and electricity production mix. Besides, the building's environmental impacts other than energy are also drawing more attention (Maslesa et al., 2018), which is important for ecological development.

The highest potential to reduce these impacts corresponds to decisions made during the design phase. Evaluating environmental impacts can help designers progress towards sustainable construction by comparing alternatives and optimising architectural and urban projects. With the development of computer science, traditional building design based on experience to control energy consumption in buildings is not appropriate and convenient. A fast and accurate building simulation tool is more efficient to evaluate the environmental impacts e.g. energy loads and GHG emissions. Various simulation models have been developed for dynamic building energy simulation (DBES) such as EnergyPlus (Crawley et al., 2001), COMFIE (Peuportier and Blanc-Sommereux, 1990), DeST (Yan et al., 2004), eQUEST (Van Ooteghem and Xu, 2012), TRNSYS (Beckman et al., 1994) and ECOTECH (Utama and Gheewala, 2008). Some of these models can be linked with life cycle inventory (LCI) database to perform life cycle assessment (LCA), aiming at quantitatively evaluating a building's environmental impacts through its lifespan.

COMFIE is a multizone model based on the finite volume method and modal analysis, which was developed by our research group (ETB, Eco-conception et thermique des bâtiments, MINES ParisTech). A multizone approach is used in COMFIE to model the building consisting of different elements (zones, walls, material layers, etc.). In this approach, the building is decomposed into small volumes called nodes, assumed to be at a uniform temperature. A heat balance is expressed for each node: the energy stored (temperature change multiplied by heat capacity) equals the heat gains minus energy losses. Each zone model is reduced by modal analysis. It has been validated in several projects (Brasselet et al., 1993 ; Peuportier, 1993 ; Peuportier, 2005 ; Brun et al., 2009 ; Spitz, 2012 ; Recht et al., 2014), including under Wuhan (China) context (Pei, 2015). It is coupled to the building LCA tool

EQUER. These two tools are integrated in the commercial software Pleiades[2], which is used in this thesis to evaluate the environmental impacts of a Chinese building.

The environmental impacts evaluation of a building depends on various aspects, such as ambient temperature (Li et al., 2019), building characteristics (Zhao and Magoulès, 2012), the performance and schedule of electrical appliances (e.g., lighting, refrigerators, washing machines, etc.) and heating, ventilating, and air conditioning (HVAC) systems (Yang et al., 2016), occupant activities (Kavousian et al., 2013), electricity production mix in LCA (Roux et al., 2016a), etc. Some limits of simulation tools were identified, e.g. regarding some aspects that are not included, causing less precise simulation results. A building simulation tool integrating a wide range of renewable energy systems (including e.g. geothermal heat pumps) can be beneficial to the building designers or researchers to optimise the building design or the system performance, especially if it requires low computation time. The urban climate usually shows different characteristics compared to the rural climate, requiring local climatic data which are rarely available. As a widely used methodology for environmental impacts evaluation, LCA is strongly connected with its background systems such as the local electricity production system.

In this thesis, three boundary conditions related to the energy and environmental performance evaluation are discussed: the ground, the microclimate, and the background systems in LCA. This thesis aims at improving the environmental impacts evaluation based on these three boundary conditions, using the DBES model COMFIE and the LCA tool EQUER integrated in Pleiades. The improved model will be applied to a high-rise Chinese residential building in Wuhan (China). The accomplishments of the thesis are expected to help decision making to reduce the environmental impacts of Chinese buildings in the design phase.

1.2. Three boundary conditions regarding building environmental impacts evaluation

1.2.1. *First boundary condition: ground*

The ground stores solar energy. At a certain depth, the ground has a relatively constant temperature, warmer than the air in winter and cooler than the air in summer (Mustafa Omer, 2008). It can serve as a heat source or a heat sink to supply heating or cooling, respectively in winter and summer, as well as domestic hot water (DHW) (Sarbu and Sebarchievici, 2014). Based on this fact, geothermal heat pump systems have been developed exchanging heat with the ground. This type of system is also called ground source heat pump (GSHP). The ground is a boundary condition directly connected to a building and also a boundary condition for the GSHP system, which is related to the energy performance evaluation of a building.

The GSHPs have been studied and commercially used for more than 100 years. The earliest concept of using the ground as a heat source was found in a Swiss patent issued in 1912 (Ball et al.,

---

[2] https://www.izuba.fr

1983). After that, the research concerning the GSHPs stopped until Ingersoll and Plass (1948) proposed the basic analytical theory of the ground pipe for the heat pump in 1948.

The GSHP systems are classified into three categories: (1) ground water heat pump (GWHP), (2) surface water heat pumps (SWHP) and (3) ground-coupled heat pumps (GCHP), as shown in Figure 1.4.
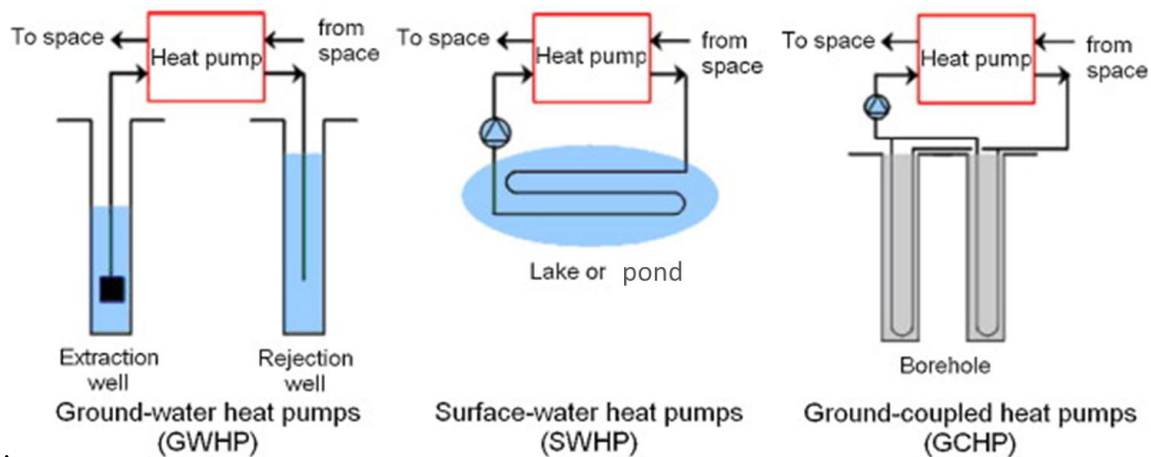
Figure 1.4: Schematics of different ground-source heat pumps (Sarbu and Sebarchievici, 2014)

The GWHP systems, also known as the open-loop systems, are the original type of the GSHP systems, first installed in the late 1940s. They involve vertical wells and well pumps to extract ground water to a heat pump or directly to the applications. The used ground water is discharged to a suitable receptor. These systems require the ground-water availability and its chemical quality (Lucia et al., 2017). They have some advantages such as low cost, simplicity in realisation and small need of ground area. Disadvantages and problems are related to the possible limited availability, poor chemical quality, ground water withdrawal and re-injection (Lucia et al., 2017) and the high maintenance cost due to fouling and corrosion in pipes and equipment (Sarbu and Sebarchievici, 2014).

In a SWHP system, the circulating working fluid injects or extracts heat with the surface water through high-density polyethylene (HDPE) pipes positioned at an adequate depth within a lake, pond, reservoir, or the suitable open channels. The major disadvantage of the system is that the surface water temperature is more affected by the weather condition, especially in winter (Sarbu and Sebarchievici, 2014).

The GCHP system uses a closed loop, mainly classified as the horizontal and vertical ground heat exchangers (GHEs), to exchange heat with the ground through the working fluid e.g. (pure water or antifreeze fluid). The horizontal GHE consists of a series of parallel pipe arrangements laid out in dug trenches approximately 1 – 2 m below the ground surface (Yang et al., 2010a). The initial fee of this type is lower compared to the vertical GHE, but the main disadvantage is that the performance of the horizontal GHE is easily affected by the ambient temperature and the other weather parameters such as rain fall. The needed construction area is also much larger than the vertical GHE.

Due to the advantages of less land area requirement and wide range of applicability, the vertical GCHP system has been studied and used more and more by researchers and engineers. During the past few decades, a considerable number of studies have been carried out to investigate the development and applications of the GCHP systems with various types of GHEs and addressed their individual advantages and disadvantages in detail (Yang et al., 2010a). Recently, various hybrid GCHP systems coupled with different supplemental heat rejection/generation device have been developed to make the systems more efficient and economic (Man et al., 2010a ; Gong et al., 2018 ; Liu et al., 2019 ; Zurmuhl et al., 2019 ; Hou et al., 2020). The vertical GHE system usually consists of various boreholes from one to hundreds. The main flaw of this system is the initial construction fee which can be high. In some projects, the construction fee of GHEs can be near the total price of traditional air conditioning equipments.

A GCHP system basically includes three general subsystems: (1) a ground connection system, (2) a heat pump system (HP) and (3) a heat distribution system, as shown in Figure 1.5. The ground heat exchanger is the major difference from other types of GSHP and conventional air conditioners. The construction cost and the size of a GHE may have a huge impact on the economic and performance of a GCHP system (Healy and Ugursal, 1997). It is important to study the thermal behaviour of the GHE to optimise both the economical and technical aspects.
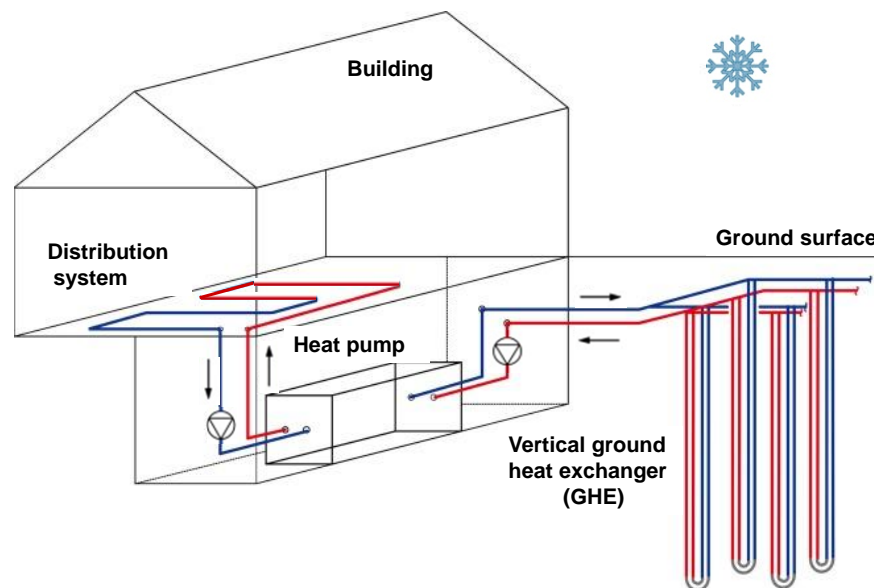
Figure 1.5: Schematic of a typical vertical GCHP system for heating (Li et al., 2018b)

This thesis focuses on the vertical GCHP system, because of various advantages. It utilises geothermal power, one type of renewable energies, which is beneficial to the environment (e.g. lower GHG emissions). Due to the stability of ground temperature under a certain depth, it could achieve higher energy efficiency compared to traditional air conditioners. The much smaller ground area required by the vertical GCHP is another advantage compared to the ground heat pumps with horizontal tubes, which is important to the buildings in the urban areas with limited available land.

The optimisation of the design and control of the GCHP systems can yield more energy efficient buildings (Zanchini and Jahanbin, 2018). A DBES tool integrated with a vertical GCHP model can be beneficial for building designers' decisions making, and interesting for researchers to study the overall performance of a GCHP system. Residential buildings in China are usually high-rise and population intensive, leading to larger boreholes fields which may contain hundreds of boreholes due to their high energy loads (Gultekin et al., 2019). However, the calculation load is massive when a large-scale boreholes field operates over a long time (e. g. a 26×26 boreholes field during 20 years) under dynamic loads. Long time scales (larger amount of data), varying loads (thermal history) and multiple boreholes (thermal interactions) are the three major challenges to obtain the optimal design of GHEs based on the operating performance simulation of GCHPs (Zhang et al., 2018a). The intensive computation brings difficulty to integrate the models into the DBES tools.

Although several studies have been carried out on the modelling of GHE, HP and buildings (Shonder and Hughes, 1998 ; Shonder et al., 2000 ; Yavuzturk and Spitler, 2000 ; Zhang et al., 2015 ; Zogou and Stamatelos, 2007), few focused on coupling the large-scale boreholes field with a DBES tool. Some DBES tools such as TRNSYS (Magnier and Haghighat, 2010) and EnergyPlus (Padhmanabhan, 2005) have implemented simplified ground exchanger models. But a more user friendly way to model such systems as a whole and a better accuracy and lower computation time would be useful to study the overall performance of GCHP systems in China. Therefore, one of the objectives of this thesis is to develop an integrated vertical GCHP model with a large-scale boreholes field in China, with a good balance between calculation speed and accuracy. Afterwards, this integrated model can be used to improve the building efficiency.

1.2.2.   *Second boundary condition: microclimate*

The second boundary condition is the microclimate around a building. A building's energy consumption is closely related to the climate (Chua et al., 2013), and the accuracy of the weather file comprising 8 760 hours of various climatic parameters such as air temperature and solar radiation, strongly influences the simulation results (Tsoka et al., 2018). During the urbanisation process, urban settlements are formed by replacing natural surroundings by urban environments and the latter create their own, unique microclimates (Toparlar et al., 2017). For example, the ground surface is altered to more hard materials such as concrete and asphalt and the area of vegetation is sharply reduced (Maheshwari et al., 2020). Urban microclimate can be defined as the local climate observed in urban areas, which can be significantly different from the climate of surrounding rural areas (Toparlar et al., 2018). Urban microclimate involves the local climate characteristics between the near-ground atmosphere and the topsoil in a relatively small space, including temperature, humidity, etc. (Li et al., 2014a). The interactions of microclimate among city block, building surroundings and building are shown in Figure 1.6.
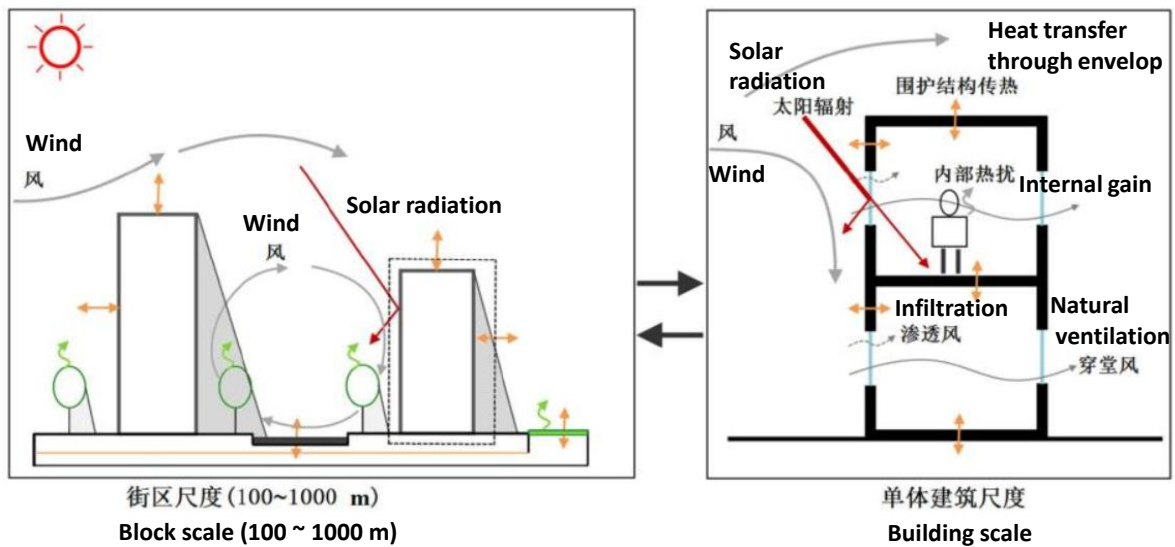
Figure 1.6: Interactions of microclimate among city block, surroundings and building (Yang, 2012)

Some climate parameters could be changed due to the urban environment. The solar radiation received by the urban building could be affected by the surroundings, e.g. the trees, the buildings and the reflections from other surfaces. The surrounding surfaces' temperatures and emissivities can influence the longwave radiation and further affect the heat transfer process of the building's envelope. The wind speed and direction can be different from the measurements in the rural meteorological station due to the layout of building blocks (Jin et al., 2017a) and the shapes of buildings. The air humidity also has a strong relationship with the plants (Zhang et al., 2018b), the water body (Jin et al., 2017b) and the ground layers, by exchanging water with each other.

Another well-known microclimate characteristic is the urban heat island (UHI) effect. It describes the phenomenon that air temperature in urban areas is higher than the surrounding rural areas. It is observed in many urban areas regardless the size and location (Imhoff et al., 2010 ; Li et al., 2018a ; Li et al., 2017 ; Oke, 1982 ; Santamouris, 2015 ; Yang et al., 2020 ; Zhou et al., 2017). It can be quantitatively described by the urban heat island intensity (UHII) (Yang et al., 2020), which is urban air temperature minus rural air temperature. Air temperature is one of the most important factors as it directly drives the operation of cooling/heating system and influences the corresponding building cooling and heating energy consumption (Li et al., 2019). Many studies reported that the UHI effect increases the cooling energy consumption and decreases the heating energy consumption (Li et al., 2019 ; Lowe, 2016 ; Skelhorn et al., 2016 ; Sun and Augenbroe, 2014).

DBES tools are widely used by building designers and engineers to investigate the energy saving potential through applying different design plans, involved building equipments and operating scenarios. Although some DBES tools have been improved to be able to accurately simulate the building envelopes and systems, the surroundings are usually not taken into consideration, or only assumed as shadows. In present DBES tools, the mostly used weather file format is the Typical Meteorological Year (TMY) format, which consists of 12 Typical Meteorological Months (TMM) in

the past decades (Tsoka et al., 2018). These data usually come from meteorological stations located in the peripheral zones (e.g. the airport), which have a significant different morphological form with the urban areas composed of dense buildings. They generally cannot represent the specific site interacting with the studied building affected by both the natural and the built environment. The energy performance evaluation of the buildings in urban area might bring non-negligible errors if TMY weather file is directly used in a DBES tool.

A weather input file considering the local microclimate of the building can yield a more accurate result, especially in the urban areas where the UHI effects are observed. A coupling method of a microclimate evaluation and DBES tools for predicting the building's thermal behaviour is necessary. This method can provide a quantitative evaluation of the building's energy consumption under the microclimate's effects. It can also help the building designers and engineers achieve better building energy performance and less environmental impacts.

1.2.3. *Third boundary condition: background system in LCA*

As an indispensable tool for quantifying the environmental performance of products or services, LCA is widely used in the building sector to support the improvement of construction materials, eco-design, and green certification, among others (Ortiz-Rodríguez et al., 2009 ; Su et al., 2016 ; Su et al., 2017). LCA addresses the environmental aspects and potential environmental impacts (e.g. use of resources and the environmental consequences of emissions) throughout a product's life cycle from raw material extraction through production, use, end-of-life treatment, recycling and final disposal (i.e. cradle-to-grave) (ISO 14040:2006, 2006).

An LCI database is often used to evaluate the environmental impacts. These databases usually include background systems which are sensitive to the region and other local elements (e.g. local electricity production mix). Therefore, an LCI database with local background is beneficial for the accuracy of the environmental impacts evaluation.

Presenting an essential background system in LCA, the energy mix or electricity production mix strongly influences the LCA results (Roux et al., 2016a), especially for the buildings (Blom et al., 2011 ; Shah and Ries, 2009). Different energy mixes cause different impacts of building materials during fabrication. Compared to the fabrication stage, even though construction materials gain importance in contribution analyses due to the development of low-energy buildings, the energy consumption during the operation stage remains an important contributor (Blengini and Di Carlo, 2010). Buildings are expected to have a lifespan of $15 - 50$ years for commercial buildings, and of $50 - 100$ years for residential buildings (Aktas and Bilec, 2012). During this long period, the energy mix will evolve towards more renewable electricity production in many countries, e.g. China (Liu et al., 2018). Current practice in LCA is to use an annual average electricity supply mix based on a documented reference year. This method cannot represent the evolution of energy mix during the building's lifespan.

China is a large country, leading to a regional electricity production mix based on the regional conditions, as shown in Figure 1.7. For example, the locations of the nuclear power plants are

normally near to the seas or rivers, thus larger share of nuclear is observed in the coastal provinces, such as Guangdong and Fujian. Inner Mongolia has a larger potential for wind energy, leading to larger wind power share. Hubei is a province next to Yangtze river, where the largest hydroelectric power plant, the *Three Gorges Dam*, is located. As a result, hydroelectric power occupies an important part of the electricity production. Due to the electricity's regional characteristics, it is not appropriate to directly use China's average electricity production mix. A more regional electricity production mix should be applied in the LCA of a building.
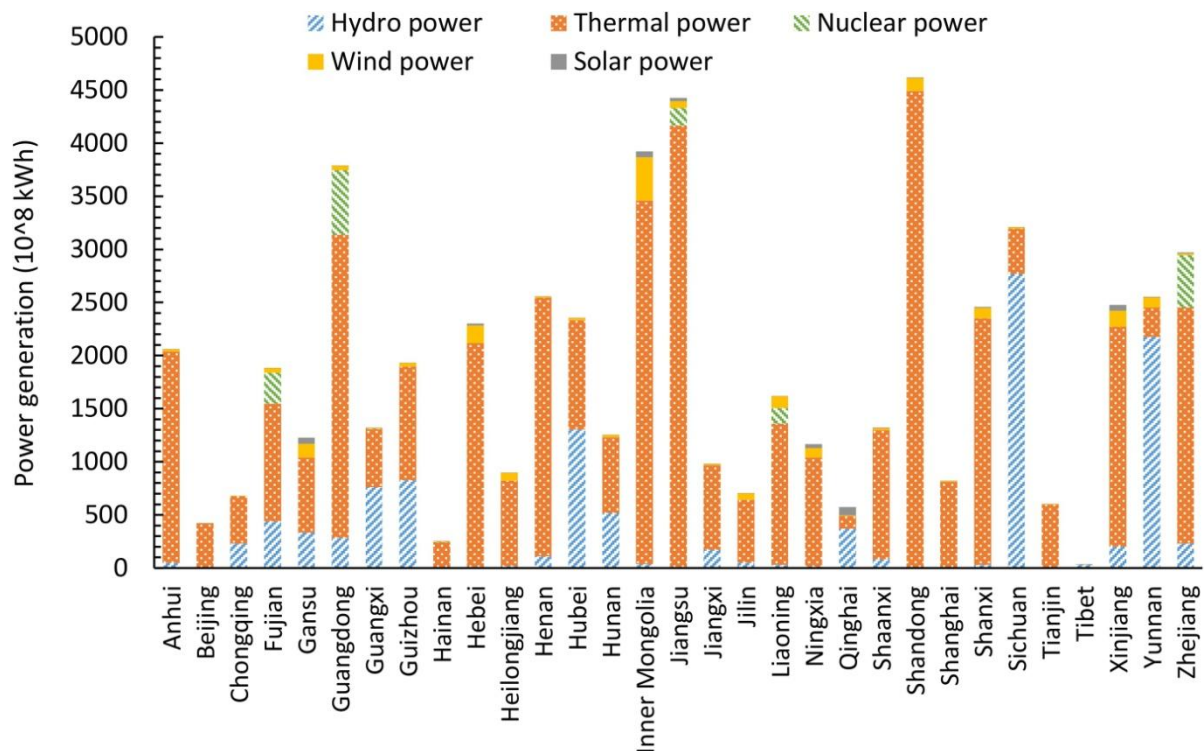
Figure 1.7: Amount and structure of electricity generation per province in China in 2015 (Xie et al., 2020b)

Therefore, this thesis considers the local background systems of LCA, particularly the local electricity production mix, aiming at providing a more reasonable evaluation of environmental impacts under Chinese context (especially the regional context). Contextualised LCI databases concerning China and Hubei Province can be beneficial for researchers or decision makers to apply LCA in Chinese building sector. The impact of the electricity production mix evolution on the building environmental performance is also studied in this thesis.

1.3.   Review of GCHP

One aim of this thesis is to develop a GCHP model with a large-scale vertical GHE and link it to COMFIE, thus in this review we focus on the vertical GHE model. As a key component in the GCHP system, the GHE plays an important role in the system performance. A GHE usually consists of one or numerous boreholes, depending on the building loads. The thermal analysis of a GHE is essential for

the design of a GCHP system and its performance simulation. The most utilised method to analyse a large-scale boreholes field is to firstly use the heat transfer model of a single borehole and secondly employ Duhamel's superposition principle (Eskilson, 1987) to obtain the ground temperature responses caused by all the boreholes in the field. As abovementioned, it is a challenge to model a large-scale boreholes field which can be solved in a reasonable time.

Therefore, this review contains three parts:

- the model of one borehole,

- the fast calculation method for a large-scale boreholes field,

- the integration of a GCHP model with a DBES tool.

1.3.1. *Analytical models of a borehole*

The simulation of a GHE mainly aims at predicting its returning fluid temperature (which is an essential input for the HP system) and the ground temperature in the borehole field (Yang et al., 2010a). Fast and accurate calculation of these temperatures is essential for the long-term evaluation of the GCHP performance and the proper design of the system (Chen et al., 2019 ; Cimmino, 2018). In the past decades studies, the energy analysis models for one borehole can be divided into the analytical models and the numerical models. Although the numerical models (Yang and Li, 2014 ; Ozudogru et al., 2014 ; Biglarian et al., 2017 ; Naldi and Zanchini, 2019 ; Chen et al., 2020 ; Yu et al., 2020 ; Kerme and Fung, 2020) can take into account all the elements (including U-pipe, grout and ground) and offer more accurate results compared to the analytical models using simplifying assumptions (Zarrella et al., 2011), they are very complex. Moreover, the numerical models usually require pre-computed data that must be stored in a massive database, thus they are not convenient to be integrated into a building design and simulation tool. Since this thesis tries to develop a GHE model and link it to a building model (to further integrate it into the DBES tool Pleiades), only the analytical models are focused.

A typical vertical grouted borehole usually consists of single or double U-tubes, in which the circulating fluid exchanges heat with the ground. The borehole is filled with grout to prevent contamination of ground water. Typical U-tubes have a nominal diameter in the range of 20 – 40 mm and each borehole is normally 20 – 200 m deep with a diameter ranging from 100 mm to 200 mm (Sarbu and Sebarchievici, 2014). The scheme of a borehole with a single-U tube borehole is illustrated in Figure 1.8.

The heat transfer process of a GHE is rather complex due to the various uncertainties such as ground water flow, soil thermal properties and building loads. Thus, it is often considered as two separated regions: (1) the soil outside the borehole where the heat transfer process must be treated as a transient process; and (2) the region inside the borehole including the grout, the U-tube pipes and the circulating fluid inside the pipes, which are sometimes analysed as steady-state process and sometimes as transient process. These two regions are linked through the temperature of the borehole wall.
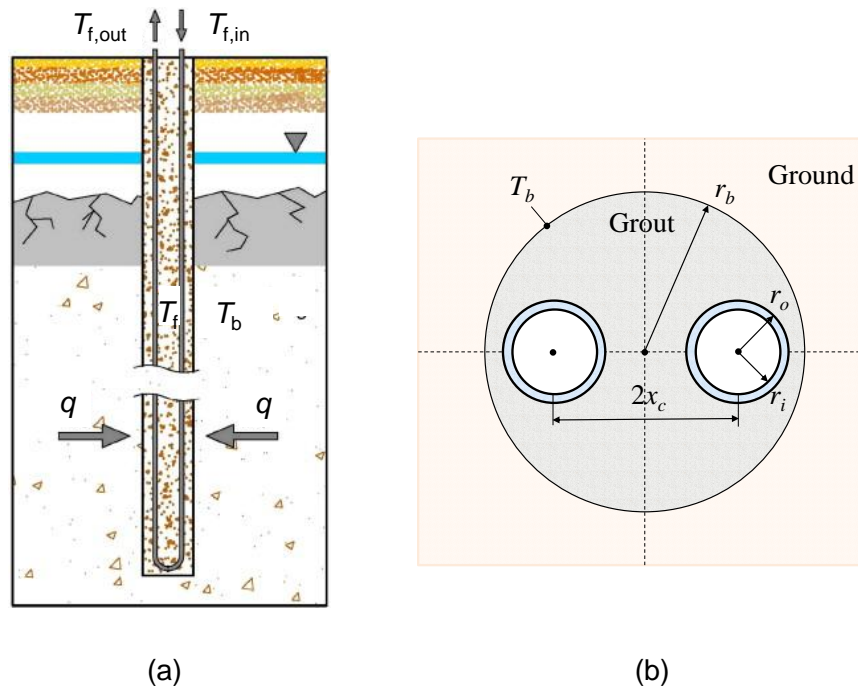
Figure 1.8: Schematic of (a) a borehole with a single-U tube (Sarbu and Sebarchievici, 2014) and (b) its cross-section

1.3.1.1.   Heat conduction outside borehole

(1) Kelvin's line source (infinite line source) model

One of the earliest theories to calculate the thermal behaviour of a borehole is Kelvin's line-source theory (Ingersoll and Plass, 1948). This theory applies Lord Kelvin's heat source to GHEs. Some assumptions are made in this theory: the borehole is an infinite line source, the initial ground temperature is uniform, the heat transfer in the direction of the borehole axis is neglected, and the heat transfer is applied at the centre of the borehole instead of the contact boundary with the ground. Thus the heat conduction process in the ground is simplified as a one-dimensional one. This method is also called the infinite line source (ILS) model. The temperature response of the ground due to a constant heat rate is given by:

$$T(r,t) - T_0 = \frac{-q}{2\pi\lambda_s} \int_{r/2\sqrt{\alpha_s t}}^{\infty} \frac{\exp(-u^2)}{u} du \tag{1-1}$$

where r is the distance from the line-source and t is the time since the start of operation; T is the temperature of the ground at distance r and time t; T_0 is the undisturbed temperature of the ground; q is the heating rate per length of the line source (positive values when a borehole extracts heat from the ground); and λ_s and α_s are the thermal conductivity and diffusivity of the ground and u is integration variable.

The solutions to the integral term have been achieved in several studies and a number of improvements have been proposed to gain the accuracy (Hart and Couvillion, 1986).

The advantages of the infinite line source model are its simplicity and short calculation time. However due to the assumptions of this model, it can only be applied to intermediate time from a few hours to months in small (≤50 mm diameter) pipes. Otherwise this model can bring non-negligible errors in the calculation (Ingersoll, 1954). The pipe has to be long enough so that the heat flow is only perpendicular to the pipe.

(2) Infinite cylindrical source model

This approach was first developed by Carslaw and Jaeger (1946). Ingersoll et al. (1954) improved this theory. In this model, some assumptions are made: the borehole is an infinite cylinder, the heat transfer in the direction of the borehole axis is neglected, the ground has constant properties and a constant transfer rate per unit length q is fixed at the contact of the borehole and the soil at $r = r_b$, and r_b is the borehole radius. The temperature distribution of ground is given in the following governing equations and boundary and initial conditions:

$$\begin{cases} \alpha_s \left(\dfrac{\partial^2 T}{\partial r^2} + \dfrac{1}{r} \dfrac{\partial T}{\partial r} \right) = \dfrac{\partial T}{\partial t} & r_b < r < \infty \\ 2\pi r_b \lambda_s \dfrac{\partial T}{\partial r} = q & r = r_b, t > 0 \\ T - T_0 = 0 & t = 0, r > r_b \end{cases} \tag{1-2}$$

The solution is given below:

$$T(r,t) - T_0 = \frac{-q}{\lambda_s} G(x,y) \tag{1-3}$$

where $x = \dfrac{\alpha_s t}{r_b}$ and $y = \dfrac{r}{r_b}$.

In fact, the $G(x,y)$ function is complex and involves the integration of some complicated functions including Bessel functions, thus it is difficult to evaluate. Some studies carried out some tabulated values. Ingersoll et al. (1954) provided tabulated values of the integral for different values of x and four values of y (=1, 2, 5 and 10). Bernier (2001) presented curve-fitted correlations for the same values of y. With these correlations it is possible to quickly calculate $G(x,y)$. An approximate method for G was proposed by Hellstrom (1991) and presented by Liu and Shi (2001).

Man et al. (2010b) developed a new finite and infinite solid cylindrical source model for borehole and pile ground heat exchangers based on infinite cylindrical source model. The radial dimension and the heat capacity of the borehole or pile are taken into account, and a more adequate formulation of actual heat conduction in the borehole and the pile GHEs is presented. Expressions of the analytical solution are derived for 1D and 2D new models by means of Green's function method. The author indicated that the analytical solutions have simple expression forms and the model can deal with short-term temperature response in the boreholes.

(3) Eskilson's model

In order to take the axial heat flow into consideration, Eskilson (1987) proposed his approach. In the assumptions of this model, the ground has constant initial and boundary temperatures, and the thermal capacitance of the borehole elements are not considered. The model is described as the following heat conduction equations in cylindrical coordinates:

$$\begin{cases} \dfrac{\partial^2 T}{\partial r^2} + \dfrac{1}{r} \cdot \dfrac{\partial T}{\partial r} + \dfrac{\partial^2 T}{\partial z^2} = \dfrac{1}{\alpha_s} \cdot \dfrac{\partial T}{\partial t} \\ T(r,0,t) = T_0 \\ T(r,z,0) = T_0 \\ q(t) = \dfrac{1}{H} \displaystyle\int_U^{U+H} 2\pi r \lambda_s \dfrac{\partial T}{\partial r}\Big|_{r=r_b} dz \end{cases} \tag{1-4}$$

where H is the borehole length; U means the uppermost part of the borehole, which can be thermally neglected in engineering practice.

In this model, the numerical finite-difference method was used to obtain the temperature response. The temperature of the borehole wall T_b was derived:

$$T_b - T_0 = -\frac{q}{2\pi\lambda_s} g\left(\frac{t}{t_s}, \frac{r_b}{H}\right) \tag{1-5}$$

where $t_s = {H^2}/{9\alpha_s}$ is the characteristic time. The *g*-function is essentially the dimensionless temperature response at the borehole wall, which was computed numerically.

Eskilson's model is a combination of analytical solution and numerical solution. This model takes the axial heat flow into consideration. Moreover, the overall temperature response of the GHE to any heat rejection/extraction at any time can be determined by the spatial and temporal superpositions. However, since this model uses numerical solutions and the *g*-functions of the GHEs with different configurations have to be pre-computed and stored in the program as a massive database, the calculation is time-consuming, and it is difficult to integrate it into a design and energy analysis program for practical applications. The interpolation function when using the database may also lead to some computing errors.

(4) Finite line source model

Zeng et al. (2002) developed an analytical solution to Eskilson's model which includes the initial and boundary temperatures' influence, which is called the finite line source (FLS) model. Several assumptions are made:

- The ground is regarded as a homogeneous semi-infinite medium with constant thermophysical properties.

- The boundary of the medium, i. e. the ground surface, keeps a constant temperature (T_0), equal to its initial value.

- The radial dimension of the borehole is neglected so that it may be approximated as a line-source stretching from the boundary to a certain depth, H.

- As a basic case study, the heating rate per length of the source, q, does not vary since the initial time, $t = 0$.

The solution is given below:

$$T(r, z, t) - T_0 = \frac{-q}{2\pi\lambda_s}$$

$$\cdot \frac{1}{2} \int_0^H \left\{ \frac{\text{erfc}\left(\frac{\sqrt{(r)^2 + (z-h)^2}}{2\sqrt{\alpha_s t}} \right)}{\sqrt{(r)^2 + (z-h)^2}} - \frac{\text{erfc}\left(\frac{\sqrt{(r)^2 + (z+h)^2}}{2\sqrt{\alpha_s t}} \right)}{\sqrt{(r)^2 + (z+h)^2}} \right\} dh \qquad \textbf{(1-6)}$$

where erfc denotes the complementary error function.

The authors compared the computation results with the numerical results in the references and it showed a good match when $\alpha_s t / r_b^2 \geq 5$, because this model takes the boundary effects into consideration. This model indicates that the middle point ($z = 0.5\,H$) temperature and the integral mean temperature could be two representative steady-state borehole wall temperatures, and the middle point is more often chosen for its convenience. The computation speed is rather faster than Eskilson's model, thus it can be applied to design and simulation tools.

1.3.1.2. Heat conduction inside borehole

The heat transfer process in the region inside the borehole has a significant influence on the performance of the whole GHE, mainly due to the thermal resistance inside the borehole. The main goal is to calculate the entering/exiting temperatures of the circulating fluid to/from the heat pump according to the borehole wall temperature, thermal resistance and its heat flow (Yang et al., 2010a). Some models have been proposed to describe this process.

(1) One-dimensional (1D) model

In this approach the U-tube is treated as a single "equivalent" pipe. The ground is regarded as infinite around the borehole, so the thermal capacity is negligible. The axial heat flows in the grout and pipe walls are also not considered. Thus the heat transfer in this region is regarded as a steady-state process (Gu and O'Neal, 1998).

The borehole thermal resistance R_b is defined by the sum of the pipe thermal resistance R_p (composed by the heat conducion resistance $R_{p,cond}$ and heat convection resistance $R_{p,conv}$) and the borehole-to-pipe thermal resistance R_{bp}:

$$R_b = R_p + R_{bp} = R_{p,conv} + R_{p,cond} + R_{bp}$$

$$= \frac{1}{2\pi r_i h_f} + \frac{1}{2\pi \lambda_p} \ln\left(\frac{\sqrt{2}r_o}{\sqrt{2}r_o - (r_o - r_i)}\right) + \frac{1}{2\pi \lambda_b} \ln\left(\frac{r_b}{\sqrt{2}r_o}\right) \tag{1-7}$$

where λ_p is the thermal conductivity of the pipe; λ_b is the thermal conductivity of the grout; r_o and r_i are the outside and inside radius of the pipe; h_f is the convective heat transfer coefficient.

The author suggested that the errors were larger during the start-up of a transient process, so it is more appropriate for longer duration process and engineering design. However in reality, the interactions between U-tube legs (called "short circuiting") may have an influence on the performance of GHEs, which is neglected; several assumptions may reduce the accuracy of this approach.

Javed and Claesson (2011) developed an analytical short-term response borehole model, which accounts for thermal capacitances of borehole grout and circulating fluid, suitable for calculating average borehole fluid temperature for timesteps smaller than an hour. Pipe legs of a single U-tube are modelled as a single equivalent-diameter pipe, in which the fluid temperature is equal to the average of supply and return pipe leg temperatures. Heat transfer is modelled as radial and solved with the help of Laplace transforms. Javed and Claesson validated their analytical model against measurement data and against their own developed numerical solution and showed a good agreement.

(2) Two-dimensional (2D)model

This approach was modified by Hellström (1991) from the cross-section perpendicular to the borehole axis, as shown in Figure 1.9. In his assumption, the borehole wall temperature T_b along the depth is constant. The heat transmission on the axial flow is not taken into consideration, because the depth is much larger than the radius and the average temperature of the fluid changes. Thus it becomes a two-dimensional problem. The average fluid temperatures of the two pipes T_{f1} and T_{f2} under corresponding heat flux q_1 and q_2 are expressed in the following equations:

$$\begin{cases} T_b - T_{f1} = R_1' q_1 + R_{12}' q_2 \\ T_b - T_{f2} = R_{12}' q_1 + R_2' q_2 \end{cases} \tag{1-8}$$

where R_1' and R_2' are the thermal resistances between the circulating fluid in each pipe and the borehole wall, and R_{12}' is the resistance between the two pipes.

The heat transfer from the fluid to the borehole wall can be simplified by a line source of heat flux q located at the tube centre (x_1, y_1). The temperature response is given by using the virtual line sink method for $r \leq r_b$:

$$T(x, y) = \frac{-q}{2\pi \lambda_b} \left\{ \ln \frac{r_b}{\sqrt{(x - x_1)^2 + (y - y_1)^2}} + \sigma \ln \frac{r_b/b}{\sqrt{(x - x_1')^2 + (y - y_1')^2}} \right\} \tag{1-9}$$

where $\sigma = \frac{\lambda_b - \lambda_s}{\lambda_b + \lambda_s}$, $b = \frac{\sqrt{x_1^2 + y_1^2}}{r_b}$, $x_1' = \frac{x_1}{b^2}$, and $y_1' = \frac{y_1}{b^2}$.
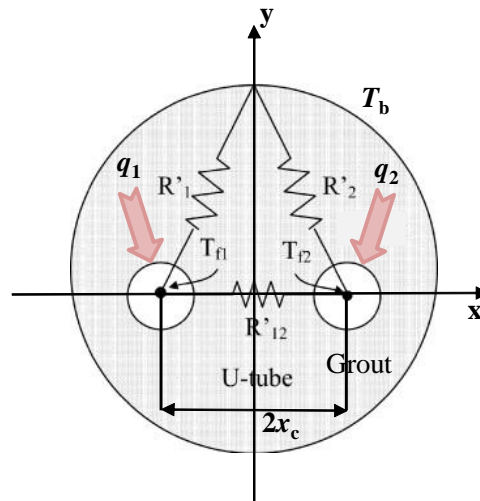
Figure 1.9: Configuration of a single U-tube in a borehole and the corresponding thermal Δ-circuit in two-dimensional model (Lamarche et al., 2010)

Considering the geometric parameters in Figure 1.9, R_1', R_2' and R_{12}' are given by:

$$R_1' = R_2' = \frac{1}{2\pi\lambda_b}\left[\ln\left(\frac{r_b}{r_o}\right) + \sigma\ln\left(\frac{r_b^2}{r_b^2 - x_c^2}\right)\right] + R_p \tag{1-10}$$

$$R_{12}' = \frac{1}{2\pi\lambda_b}\left[\ln\left(\frac{r_b}{2x_c}\right) + \sigma\ln\left(\frac{r_b^2}{r_b^2 - x_c^2}\right)\right] \tag{1-11}$$

where $R_p = R_{p,cond} + R_{p,conv} = \frac{1}{2\pi\lambda_p}\ln\left(\frac{r_o}{r_i}\right) + \frac{1}{2\pi r_i h_f}$.

The total borehole thermal resistance R_b is given by (Hellström, 1991):

$$R_b = \frac{R_1' + R_{12}'}{2} = \frac{1}{4\pi\lambda_b}\left[\ln\left(\frac{r_b}{r_o}\right) + \ln\left(\frac{r_b}{2x_c}\right) + \sigma\ln\left(\frac{r_b^4}{r_b^4 - x_c^4}\right)\right] + \frac{R_p}{2} \tag{1-12}$$

R_b for a double U-tube borehole is given by (Conti et al., 2016):

$$R_b = \frac{1}{8\pi\lambda_b}\left[\ln\left(\frac{r_b}{r_o}\right) + 2\ln\left(\frac{r_b}{\sqrt{2}x_c}\right) + \ln\left(\frac{r_b}{2x_c}\right) - \sigma\ln\left(\frac{r_b^8 - x_c^8}{r_b^8}\right)\right] + \frac{R_p}{4} \tag{1-13}$$

This model can provide a more precise result compared to the empirical expressions and the 1D model. However the thermal "short-circuit" effect between the legs and the fluid temperature variation along the borehole depth are still not considered, which may cause an error compared to the real mechanism.

(3) Quasi-three-dimensional (quasi-3D) model

Zeng et al. (2003) proposed the quasi-three-dimensional model aiming at considering the fluid temperature variation along the borehole depth, based on the two-dimensional model. This model still

neglects the conductive heat flows in the grout, pipe wall and soil in axial direction to keep the model concise and analytically manageable. Equation (1-8) is converted to:

$$\begin{cases} q_1 = \dfrac{T_{\mathrm{b}} - T_{\mathrm{f1}}}{R_1^\Delta} + \dfrac{(T_{\mathrm{f2}} - T_{\mathrm{f1}})}{R_{12}^\Delta} \\[2mm] q_2 = \dfrac{T_{\mathrm{b}} - T_{\mathrm{f2}}}{R_2^\Delta} + \dfrac{(T_{\mathrm{f1}} - T_{\mathrm{f2}})}{R_{12}^\Delta} \end{cases} \tag{1-14}$$

where $R_1^\Delta = \dfrac{R_1' R_2' - {R_{12}'}^2}{R_2' - R_{12}'}$, $R_2^\Delta = \dfrac{R_1' R_2' - {R_{12}'}^2}{R_1' - R_{12}'}$ and $R_{12}^\Delta = \dfrac{R_1' R_2' - {R_{12}'}^2}{R_{12}'}$

The heat transfer inside the borehole is treated as steady-state. q_1 and q_2 varies along the borehole depth. The energy equilibrium equations can be written for down-flow and up-flow of the circulating fluid:

$$\left. \begin{aligned} -\dot{m}_{\mathrm{b}} c_{\mathrm{p,fl}} \frac{dT_{\mathrm{f1}}(z)}{dz} &= \frac{(T_{\mathrm{f1}}(z) - T_b)}{R_1^\Delta} + \frac{(T_{\mathrm{f1}}(z) - T_{\mathrm{f2}}(z))}{R_{12}^\Delta} \\ \dot{m}_{\mathrm{b}} c_{\mathrm{p,fl}} \frac{dT_{\mathrm{f2}}(z)}{dz} &= \frac{(T_{\mathrm{f2}}(z) - T_b)}{R_2^\Delta} + \frac{(T_{\mathrm{f2}}(z) - T_{\mathrm{f1}}(z))}{R_{12}^\Delta} \end{aligned} \right\} \quad (0 \le z \le H) \tag{1-15}$$

where $\dot{m}_{\mathrm{b}}$ is the fluid mass flow rate per borehole, and $c_{\mathrm{p,fl}}$ is the heat capacity of the fluid.

There are two boundary conditions:

$$\left. \begin{aligned} z = 0, &\qquad T_{\mathrm{f1}} = T_{\mathrm{f,in}} \\ z = H, &\qquad T_{\mathrm{f1}} = T_{\mathrm{f2}} \end{aligned} \right\} \tag{1-16}$$

where $T_{\mathrm{f,in}}$ is the inlet temperature of the fluid.

Zeng et al. derived the solution by Laplace transformation; it has a high complexity (Zeng and Fang, 2002). The borehole thermal resistance of a symmetric single U-tube borehole is expressed as:

$$R_{\mathrm{b}} = \frac{H \sqrt{\dfrac{R_1' + R_{12}'}{R_1' - R_{12}'}}}{2 \dot{m}_{\mathrm{b}} c_{\mathrm{p,fl}} \tanh \dfrac{H}{\dot{m}_{\mathrm{b}} c_{\mathrm{p,fl}} \sqrt{(R_1' + R_{12}')(R_1' - R_{12}')}}} \tag{1-17}$$

This method considers the thermal "short-circuit" effect between the legs and the fluid temperature variation along the borehole depth. The authors also validated that the quasi-3D model has a higher accuracy than other models and can serve as a useful tool in design and simulation of the GHEs. Due to the reason that the effects of conduction in the vertical direction are indeed negligible for the duration of in-situ tests (Diao et al., 2004), Beier (2011) adopted this model and transformed the equations into dimensionless variables to identify the least number of dimensionless parameters for a subsequent parameter sensitivity study and obtained the vertical temperature profile model during in-situ tests. This analytical model was compared to the numerical solution from the study of Marcotte and Pasquier (2008a) and the results showed a good match. Conti et al. (2016) presented the explicit analytic expressions of this method for double U-tube boreholes depending on flow arrangement within borehole tubes.

1.3.1.3. Newly developed models

(1) Infinite composite-medium line source model

The 1D model, the 2D model and the quasi-3D model all consider the heat transfer inside the borehole as a steady-state process, due to the much smaller dimensions and heat capacity. This means they may cause errors when simulating the short time response of the GHEs.

Li and Lai (2012) developed the infinite composite-medium line source model to solve this problem. This approach enables the removal of the equivalent diameter assumption and can tackle the difficulties associated both with the composite medium and the geometric installations of U-shaped pipes. New solutions for continuous line and cylindrical surface sources were derived based on Jaeger's instantaneous line-source solution. The new response functions for a single U-tube, a double U-tube and energy piles with spiral tubes were presented. This model can deal with short-time simulation and takes the medium inside the borehole into consideration compared to 1D model, the 2D model and the quasi-3D model. However, due to the complicated mathematical equations and long computation time, it is difficult to be integrated in the simulation tools. Besides, it cannot predict the long-term thermal process.

(2) Full-scale model

Li et al. (2014b) proposed a full-scale model which aims at covering the entire simulation period from minutes to decades. Before this model, Javed (2011) attempted to propose an analytical method to calculate the borehole fluid temperatures for time scales ranging from minutes to decades. But in their approach, the equilibrium-diameter assumption is used which causes a temperature difference between the short and long-term solutions and an arbitrary temperature shift called breaking time. The breaking time is empirically determined and not based on any established theory, which may cause errors in the model.

The full-scale model is a composite solution combining the composite-medium line-source solution (inner solution) for short time, the conventional infinite line-source model for intermediate time, and the conventional finite line-source solution (outer solution) for long time. Based on the three sub-models, the full-scale G-function for a single U-tube GHE is given in (Li et al., 2014b).

This model's main advantage is the wide application time range: from minutes to decades. Besides the analytical model has a solid mathematical base and consists of no empirical simplification. So this model can provide relatively accurate solutions. However, several points are not considered. Firstly, the heat flux along the U-pipe which varies with length in reality, is considered as a constant in the full-scale model. Secondly, the thermal interaction between two legs of the U-shaped pipe is not considered and the heat flux for the inlet and outlet pipes is assumed to be the same in the model which is not the reality. Thirdly, it can only work effectively under a strict borehole geometric configuration.

Ma et al. (2015) proposed a new quasi-3D model for the circulating fluid in U-shaped GHEs to tackle the variation of the fluid temperature along the U-shaped channels based on the full-scale temperature response function. In this approach, the fluid temperatures in the descending and ascending legs are derived as functions of time and borehole depth. Further several new expressions for effective overall thermal resistances were developed. However this approach cannot tackle the thermal interaction between adjacent boreholes. Some other influencing factors such as groundwater flows and moisture migration are also ignored.

(3) Transient quasi-3D entire time scale line source model

Zhang et al. (2016) proposed a transient model named "transient quasi-3D entire time scale line source model". This model introduces the concept of transient borehole thermal resistance and considers the heat flux profile along the U-pipe as a variable. The proposed model is also compared with several existing models, including several traditional line source models and a full scale response model, using the data collected from a reported Sandbox experiment (Beier et al., 2011). The results showed that the transient quasi-3D entire time scale line source model is a more effective method for the fluid and ground temperature prediction and may offer the theoretical basis for the system control and the borehole distance determination. The impact of the heat flux profile along the U-pipe on the ground temperature profile prediction was also investigated, which showed that when the heat flux profile along the U-pipe was considered as a variable, the determination of borehole distance would be much more accurate.

1.3.2.   *Fast calculation method for a large-scale boreholes field*

A few studies have been conducted to simplify the calculation for a large-scale boreholes GHE operating for a long period. Yavuzturk and Spitler (1999) proposed the load-aggregation algorithm to lump the hourly loads on GHEs into larger blocks of time. Cullin and Spitler (2011) proposed a computationally efficient hybrid time-step methodology for simulation of GHEs by setting a reasonable peak load and peak load duration according to the daily load profiles. Bernier et al. (2004) presented a multiple load aggregation algorithm to perform annual hourly energy simulations, by subdividing the past thermal history into four time intervals. Claesson and Javed (2012) proposed a new load-aggregation scheme to perform multi-year simulations of GHEs using a step-response function. Mitchell and Spitler (2019) investigated the different parameters in the developed load aggregation methods and claimed a 73-fold reduction in simulation time when compared to non-aggregated simulations. However, the computed hourly temperature is not exactly that corresponding to the heat-load history obtained by the load-aggregation algorithm (Zhang et al., 2018a). Lamarche and Beauchamp (2007) presented a history-independent mathematical algorithm to calculate ground dynamic thermal response by applying Green function to solve heat conduction problem of the infinite cylinder source model. It can be applied in GHEs under any kind of step response (Lamarche, 2009).

Zhang et al. (2018c) used the fast Fourier transform (FFT) method to reduce computational complexity but did not provide a detailed description. Marcotte and Pasquier (2008b) proposed a method to reduce the computing time by sub-sampling the analytical function at a few selected times

with a geometric sequence using the cubic spline interpolant, and based on FFT. Xu (2010) proposed the finite cylinder-source model consisting of a certain area of boreholes as the inner heat source to study the long-time operation of a GHE. This method cannot be easily applied in simulation tools due to its mathematical complexity and long computing time. Katsura et al. (2008) presented a high-speed algorithm to calculate the ground temperature of multiple GHEs, reducing the computation time by about a factor 135. Zhang (2010) indicated that a representative boreholes matrix of 3×3 can be employed to substitute the large-scale boreholes GHEs based on his study for a GHE operating for dozens of days. However, this representative boreholes matrix is not appropriate for longer operation time. Chen et al. (2019) combined a δ-function (a thermal response factor to unit rectangular heat pulse) with FFT; it took only less than 1.5 minutes for a 30-years hourly simulation of 5×8 boreholes. Some researchers (Kurevija et al., 2012 ; Teza et al., 2012) used monthly loads to simulate long-term operation to avoid long calculation time. Beck et al. (2013) divided a rectangle borehole field into four mirror symmetric quadrants so the calculation time can be reduced to one fourth, but even a single month by month load for a period of 30 years still required a calculation time of several minutes.

Yu et al. (2016) indicated that a representative boreholes matrix can replace the original large-scale GHE for heat transfer analysis and proposed the method to determine the number of the representative boreholes matrix from the thermal influence radius of a single borehole. This method indeed reduces calculation complexity by using geometric simplification but still cannot solve the difficulty of the large computing resources needed when the operation time is long. Cimmino and Bernier (2014) introduced a new methodology for the generation of thermal response factors of geothermal borehole fields. They proposed to divide boreholes into segments to consider the variation of the heat extraction rates along the length of the boreholes. However, this method will increase the calculation time. Then, Cimmino (2018) introduced a similarity identification method and a load history reconstruction method for fast calculation. The similarity identification method identifies the pairs of boreholes that have the same FLS calculation value, and the load history reconstruction method evaluates the thermal response factors at non-uniform timesteps. The thermal response factor of a field of 7×7 boreholes over 2 000 years was calculated in 98 seconds using a geometric timestep expansion scheme, however the accuracy was not well validated.

1.3.3.   *Integration of a GCHP model in a DBES tool*

The EnergyPlus program[3], one of the most popular DBES tools in the worldwide, was extended to perform GCHP system simulations (Fisher et al., 2006) by the integration of a water-source heat pump and a vertical GHE. The GHE model uses Eskilson's "*g*-functions" to model the response to time-varying heat fluxes and has been extended to include a computationally efficient variable time-step load aggregation scheme. The GCHP model was compared to an experiment. The results showed an average error in the predicted ground heat transfer rate of less than 6 % and average errors in the

---

[3] https://energyplus.net

predicted heat pump power and the predicted source-side heat transfer rate of less than 3 % and 4 %, respectively.

Another building energy analysis program eQUEST and its simulation engine DOE-2.2[4] were enhanced to facilitate the design and energy analysis of the GCHP systems (Liu and Hellstrom, 2014). The vertical GHE model also used the *g*-function algorithm, and implemented in the Building Creation Wizard of eQUEST with a water-to-air heat pump. The author claimed from the validation results that the enhanced eQUEST/DOE-2.2 is a very useful tool for GCHP system design and energy analysis.

The GHE model which is also based on the *g*-function was integrated in the HVACSIM+ modelling environment which is capable of modelling HVAC systems, HVAC controls, building energy management systems and other thermal systems (Khan et al., 2003). It was extended by the addition of ground loop heat exchanger models, water-to-water and water-to-air heat pump models, pavement heating system models, and heat rejection pond models. This model also allows the simulation of a hybrid GCHP incorporating with both ground loop heat exchangers and supplemental heat rejecters, such as cooling towers, cooling ponds, or pavement heating systems.

To calculate the heat transfer process inside the borehole, an effective steady-state borehole thermal resistance was used to in all these three DBES tools. In general, the three similar models of GHEs, which take advantage of the wide functionality of the DBES tools, can conveniently calculate the building heating and cooling loads and facilitate the design and energy analysis of the GCHP systems. They also have the flexibility to compare the energy consumption between the GCHP system and a conventional HVAC system (Yang et al., 2010a).

Different from the tools using analytical models, TRNSYS[5] integrated a DST-module developed by Pahud and Hellstrom (1996), using numerical simulation based on the finite-difference method. TRNSYS is a modular system simulation package where users can describe the components that compose the system and the manner in which these components are interconnected. Thus, the duct ground storage model (DST) for the vertical GHEs is easily added to the existing component libraries.

1.3.4. *Conclusions*

This section reviewed some classical and recently developed borehole analytical models, including inside and outside the borehole; the methods to reduce the computation load of a multi-boreholes heat exchanger and some examples of the integration of the GCHP models with the DBES tools. Through the review, it can be inferred that although some efforts have been made on reducing the computation load, there is still a lack of a global, convenient and fast model to simulate the large-scale boreholes GHE, especially one which can be easily linked to the GCHP models and integrated into a DBES model. Thus, a new global model of the large-scale boreholes GHE which can overcome this issue will be presented in chapter 2 and the integration of this model with COMFIE will be illustrated in chapter 3.

---

[4] http://www.doe2.com/equest

[5] http://www.trnsys.com/

1.4.   Review of microclimate models

In order to quantitatively evaluate the building's environmental impacts under the microclimate's effects (particularly the UHI effect), the microclimate conditions should be assessed, which is mainly accomplished by in-situ measurements or microclimate simulation. This thesis focuses on the microclimate simulation instead of measurements. The coupling of microclimate simulation tool and the DBES tool is a further step. Thus, the review is presented according to the following three parts:

- microclimate simulation tools,

- quantitative evaluation of the UHI effect on the building's energy consumption,

- coupling of a microclimate simulation tool with a DBES tool.

1.4.1.   *Microclimate simulation tools*

Urban climate modelling (UCM) is usually performed at different scales related to the land surface represented and the resolution at which balance equations are written (Oke, 2002). The urban climates models were developed from the mesoscale (several kilometers) down to the microscale (several meters to one hundred meter). At the mesoscale, the whole city and its surroundings (suburban and rural regions) can be examined. At the local scale, only a part of the city (e.g. a district) is considered, whose dimensions range from hundreds of meters to a few kilometers. This scale allows for the representation of the meteorological phenomena in the urban canopy layer. Building forms, materials, natural surfaces, etc. can be considered explicitly or through mean parameters (rugosity, albedo, etc.) (Lauzet et al., 2019). At the microscale, a smaller zone of a few meters or a hundred meters is considered, in which the physical processes are computed in more detail (1 m). According to the review (Lauzet et al., 2019), some common used UCMs are classified in Figure 1.10, based on the spatial scale of the represented areas (in terms of urban scale) and the horizontal resolution (the horizontal size of the mesh elements used in the model). In this thesis, the microclimate refers to the local scale or smaller.

On the city scale, several UCMs were developed. The MESO-NH model (Lac et al., 2018) is a non-hydrostatic mesoscale model that has been applied in many studies of climate change impacts at the city scale (Broadbent et al., 2018 ; Pigeon et al., 2014). The Town Energy Balance (TEB) model (Masson, 2000) is a single layer urban canopy model that incorporates multiple urban parameterisations. The Weather Research and Forecast (WRF) model is a numerical weather prediction system designed to serve both atmospheric research and operational forecasting needs. Building Effect Parameterization (BEP) is a multi-layered canopy model that provides direct interactions with the planetary boundary layer, which is integrated into WRF. On the street scale, some models have been developed, e.g. the zonal model (Liang et al., 2018) and TEB canyon model (Redon et al., 2017).

On the district scale, two categories of models are distinguished (Lauzet et al., 2019). The first category brings together models that do not represent the urban shapes explicitly but use parameters

that translate their impact, e.g. Urban Weather Generator (UWG) (Bueno et al., 2013), Canyon Air Temperature (CAT) models (Erell and Williamson, 2006) and Canopy Interface Model (CIM) (Mauree et al., 2017). They produce homogeneous data for the district examined. The second includes models that use the geometrical representation of the district and mesh it so that they explicitly resolve the governing equation for the inter-exchanges. SOLENE-Microclimat mainly consists of a computational fluid dynamics (CFD) open source code Code-Saturne[6] and SOLENE, which is a radiative tool (Miguet and Groleau, 2002). Different modules have been added to represent conventional built elements (conduction in paved soil, building thermal models) as well as natural elements and climate adaptation solutions (trees, natural soil, green roofs and walls, water ponds, pavement watering) (Azam et al., 2018 ; Musy et al., 2015). Another widely used model is ENVI-met[7], which is a prognostic, three-dimensional, grid based microclimate model, designed to simulate complex surface-vegetation-air interactions in the urban environment. Based on the fundamental laws of fluid dynamics and thermodynamics, ENVI-met can simulate the diurnal cycle of major climatic variables involving air and soil temperature and humidity, wind speed and direction, radiative fluxes, etc. with a typical horizontal resolution from 0.5 to 5 m and a timestep of 1 to 5 s (Bruse and Fleer, 1998 ; Huttner, 2012). It has been validated (Sharmin and Steemers, 2017 ; López-Cabeza et al., 2018 ; Elwy et al., 2018 ; Ayyad and Sharples, 2019) and utilised for several studies (Elnabawi et al., 2013 ; Salata et al., 2016 ; Deng et al., 2016 ; Tsoka et al., 2017 ; Acero and Arrizabalaga, 2018 ; Lobaccaro et al., 2018 ; Cardinali et al., 2020). ENVI-met just released its latest version 4.4.4, which is used as the microclimate simulation tool in this thesis. More detail description about this tool is presented in chapter 4.
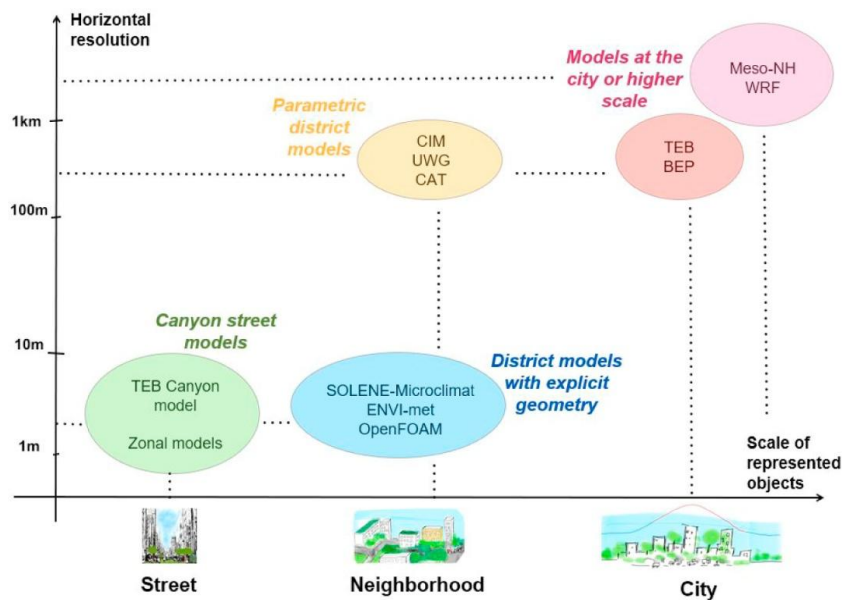
Figure 1.10: Classification of UCMs in terms of their spatial study scales and resolution (Lauzet et al., 2019)

---

[6] https://www.code-saturne.org/cms/documentation

[7] https://www.envi-met.com

1.4.2. *Quantitative evaluation of UHI effect on building's energy consumption*

As mentioned in section 1.2.2, it is a fact that the UHI effect might increase the air temperature in urban areas. As an important input of DBES, the weather files of the DBES models are mostly measured in the rural areas. The effects of UHI on building energy consumption were understudied due to challenges associated with quantifying UHI-induced temperature change and evaluating building energy consumption (Li et al., 2019). A more accurate evaluation can be obtained if the UHI effect is considered in DBES tools.

A review article by Li et al. (2019) summarised the procedure in evaluating UHI impacts on building energy consumption, which includes three steps: (1) preparing two temperature datasets with and without UHI effect; (2) simulating/estimating building energy consumption respectively using two temperature datasets; and (3) evaluating the impacts of UHI on building energy consumption by comparing two results, as shown in Figure 1.11. The urban temperatures are mainly obtained by measurements or simulation.
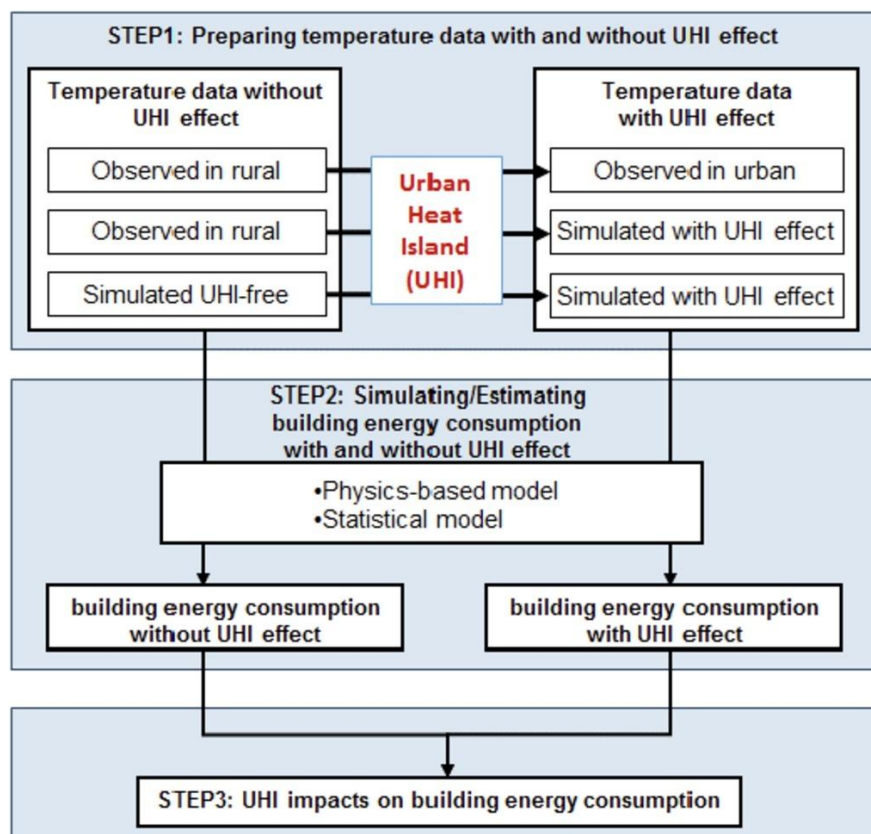
Figure 1.11: Flowchart of modelling the UHI impacts on building energy consumption (Li et al., 2019)

Hassid et al. (2000) investigated the effect of the summer heat island of the western part of the Greater Athens area (Greece) on cooling energy and peak power using DBES tool DOE2.1.E and

measured values of temperature and other meteorological data at selected sites. Depending on the locations, the cooling energy and peak demand could increase by as much as 100 %.

Santamouris et al. (2001) used the climatic measurements from almost 30 urban and suburban stations as well as specific measurements performed in 10 urban canyons in Athens to assess the impact of the urban climate on the energy consumption of buildings. It was found that for the city of Athens, where the mean heat island intensity exceeded 10 °C, the cooling load of urban buildings might be doubled, and the peak electricity load for cooling purposes might be tripled especially for higher setpoints. During the winter period, the heating load of centrally located urban buildings was found to be reduced up to 30 %.

Kolokotroni et al. (2006) also used the measurements to identify the UHII in London (UK). They claimed that the energy demand for cooling of the rural reference office was 16 % smaller compared to that of an identical urban office for a typical hot week. The impacts were close for an extreme hot week.

Watkins et al. (2002) measured the simultaneous hourly air temperature in London (UK) continuously for a year at 80 locations, on a radial grid covering an area of 500 square miles. They presented that the central areas of London were significantly warmer than the surrounding areas (2 K warmer over the year). It was found that the urban cooling load was up to 25 % higher over the year, and the annual heating load was reduced by 22 %. Minimal CO_2 was emitted at a rural location among all locations. The net rate of increase of CO_2 with temperature was found to be 2.8 %/K.

Chan (2011) collected the field measurements in the summer months to determine the corresponding UHII in Hongkong (China). Then, the Morphing method developed by Belcher et al. (2005) was adopted to produce a new TMY weather file for building thermal simulations accounting for the UHI effect. It was found that there was around a 10 % increase in air-conditioning demand caused by the UHI effect in both a residential building and an office building.

Kolokotroni et al. (2012) presented the results of a computational study on the energy consumption and related CO_2 emissions for heating and cooling of an office building within the UHI of London, currently and in the future. 20 urban weather files were developed according to future climate change scenarios. It was predicted that heating load decreased, cooling load and overheating hours increased as the office location moved from rural to urban sites and from present to future years. Future cooling requirements might lead to a five-fold increase of CO_2 emissions.

Radhi and Sharples (2013) investigated the UHI effect in Bahrain. The annual total urban cooling degree day (CDD) value was up to 17 % higher than the rural CDD value. A sharp increase of up to 10 % in electricity consumption for air-conditioning occurred in urban regions from April to October.

Li et al. (2014a) studied the interactions between UHI effect and air-conditioning energy consumption in Beijing. They presented that electric air-conditioning energy consumption resulting from the comprehensive influence of microclimate accounted for 11.28 % of total summer electricity consumption and this percentage reached 20.4 % during the peak load period in Beijing in 2005. In turn, the increased air-conditioning energy consumption contributed to the increase of UHII.

Sun and Augenbroe (2014) presented the UHI effect on two routine applications of building energy simulation: (1) predicting the magnitude of energy use and (2) predicting energy savings based on case studies of office buildings in 15 representative cities across different climate zones in the U.S. The results showed that ignorance of the UHI effect remarkably underestimated buildings total energy use in hot climate zones where cooling energy use was dominant, yet causing overestimation in cold climate zones where heating energy use was prevalent. In mild climate zones, the UHI effect only had a moderate effect because the effects on cooling and heating mostly averaged out. When building simulation was used to assess energy savings that was measured as the ratio to the corresponding baseline such as in a comparative analysis of retrofit measures, the UHI effect was less of a factor.

Magli et al. (2015) used two weather datasets to analyse the UHI effect in Modena (Italy). The first set of data was collected by a weather station located in the city centre of Modena, while the second set of data was collected from another station, located in the surrounding area of the city, near to the studied building. They were associated to a case study of a university library. 10 % increase in cooling energy consumption was reported for the building located in the urban area compared to that located in the rural area.

Liu et al. (2017) generated new TMY weather files for different micro-scale areas in Singapore based on recent years' weather data. Based on the results, the dry bulb temperature of the new TMY was 1–2 °C higher, while the energy consumption prediction increased from 3.25 % to 11 %.

Skelhorn et al. (2016) employed an interdisciplinary approach to measure and model fine-scale microclimate changes due to greenspace and explore the implications for building energy demand in Manchester (UK). Both the modelled and measured microclimate data were used to develop a series of weather files for building energy modelling of three commercial building types. The results showed that the effect of the summer UHI alone increased the air conditioning load between 9 % and 12 %. Adding 5 % more mature trees in the urban case reduced the hourly air temperature by 1.0 °C under peak UHI conditions. In July a reduction of 2.7 % of chiller energy was estimated due to the combination of reduced UHI peak hours and the shading of eight additional trees.

Cui et al. (2017) analysed a long-term measured weather dataset from 1961 to 2014 for ten rural stations and seven urban stations in Beijing (China) to understand the detailed temporal and spatial characteristics of the UHI effect in Beijing. The results showed that the UHII can reach to 8 °C during the winter night. The UHI effect in Beijing led to an approximately 11 % increase in cooling load and 16 % decrease in heating load in the urban area compared with the rural area, whereas the urban heating peak load decreased 9 % and the cooling peak load increased 7 % because of the UHI effect.

Ignatius et al. (2016) evaluated the UHI effect on a hypothetical office block plan with hundreds of urban layouts in Singapore. An annual temperature profile was generated for each scenario using Screening Tool for Estate Environment Evaluation. It was found that the local average temperature and peak afternoon period from these scenarios could differ $1-2$ °C and $1.2-3.5$ °C respectively when compared to the meteorological station data, which could lead approximately to an 8 % difference in the predicted cooling load, 20 % in external conduction gain, and 17 % in fresh air intake gain.

Palme et al. (2017) investigated the UHI effect in four important South American Pacific coastal cities, with microclimate simulation. The results indicated that when UHI was incorporated, an increase in energy demand between 15 % and 200 % could be expected.

Salvati et al. (2017) studied the UHII in Barcelona (Spain), the densest Mediterranean coastal city, and its impact on cooling demand of residential buildings. The urban temperatures were measured. The maximum average UHII was found to be 2.8 °C in winter and 1.7 °C in summer, reaching 4.3 °C at street level. Simulations performed with EnergyPlus indicated that UHII increased the sensible cooling load of residential buildings by around 18 % – 28 %, depending on UHII, amount of solar gains and cooling setpoints.

Zinzi and Carnielo (2017) used the urban temperature measurements to evaluate the UHI effect in Roma (Italy). The results indicated that a UHII up to 8 °C was detected, with maximum monthly averages equal to 2 °C. The urban heat island increased the building cooling energy needs by 12 % in the peripheral neighbourhood, and by up to 46 % in the city centre, with respect to the undisturbed zone. Guattari et al. (2018) also investigated the UHI effect in Roma with the urban measurements. The results showed an average increase of cooling energy demand of about 30 % and an average reduction of heating energy demand of about 11 %.

Toparlar et al. (2018) used commercial CFD software ANSYS Fluent 15.1 to generate the urban microclimate and EnergyPlus to evaluate the building's energy consumption for Antwerp (Belgium). The results demonstrated that compared to the air temperatures in the rural area, on average, air temperatures at the urban sites away and close to the park were 3.3 °C and 2.4 °C higher, respectively. This led to an additional monthly cooling demand of up to 90 %.

Yang et al. (2020) compared continuous measurements of hourly air temperature and relative humidity for three years in 10 neighbourhoods of Nanjing (China), to the suburban meteorological stations. The annual mean UHII ranged from 0.4 °C to 2.2 °C in the night-time (19:00 – 06:00), and from 0.3 °C to 0.9 °C in the daytime (07:00 – 18:00). The heat islands could increase the cooling demand of residential (office) buildings by $12 - 24\,\%$ ($9 - 14\,\%$) and reduce heating demand by $3 - 20\,\%$ ($5 - 20\,\%$), leading to an increase of $2 - 5\,\%$ ($2 - 6\,\%$) in annual total demand.

1.4.3. *Coupling of a microclimate simulation tool and a DBES tool*

Based on the review article (Lauzet et al., 2019), the coupling of a microclimate simulation tool and a DBES tool is categorised into chaining, week coupling and strong coupling. For strong coupling, both UCM and DBES solvers run at the same time to converge to a consistent result and go through the next simulation timestep. For weak coupling, solvers of the UCM and DBES tools run in an iterative way to go ahead to the next simulation timestep. These two coupling methods consider the effect of the microclimate on the building, as well as the effect of the building on the microclimate (e.g. the anthropogenic emissions released outside due to air-conditioning or heating systems such as heat pumps), which is a double-way coupling.

On the contrary, the chaining method is a one-way coupling method. The UCM simulation is performed for the study period and its results are provided into the weather files used in a DBES tool, without feedback. Although the double-way coupling method taking the interactions between HVAC systems and the microclimate into account is more realistic, it is more complex and requires the UCM to deal with such heat sources and also allowing the user-defined parameters. In this thesis, ENVI-met is used, which does not contain such interactions. Besides, in order to simplify the problem, the chaining method is adopted, meaning only the effect of the microclimate on the building's energy performance is considered. To be clearer, it should be noted that in the thesis below, if not particularly indicated, the 'coupling' means the 'chaining method'.

As abovementioned, the key point in the coupling of a microclimate simulation tool and a DBES tool is modifying the weather input file from the original one (e.g. the meteorological data from rural stations) to the new one (which considering the urban microclimate). The weather file introduced in DBES tools usually comprises of 8 760 hours of various climatic values such as outdoor temperature, solar radiation, etc. It strongly influences heat and cooling loads calculation. However, it is time costing to perform microclimate simulation in UCM tools. For example in the study of Yang et al. (2012), it took 168 hours to simulate only 3 days in ENVI-met. Thus, a method generating the hourly weather file from UCM tools is needed.

Yang et al. (2012) presented a method for the quantitative analysis of building energy performance under any given urban contexts by linking the microclimate model ENVI-met to EnergyPlus. The full microclimatic factors such as solar radiation, longwave radiation, air temperature, air humidity, and wind speed were considered in their proposed scheme. However, the simulated period was only 3 days, and it was not extended to the whole year.

Flor et al. (2004) reported an estimation method to evaluate building energy loads for a given urban context by using the outputs of an urban canyon model as the inputs of a building thermal simulation program.

Bouyer et al. (2011) established a coupling simulation platform for building energy evaluation in an urban context by integrating a home-developed thermoradiative code into Fluent. This work focused on a typical week of January (the coldest month as the standard meteorological climate of 8 French cities) and one in July (the warmest month). The results were not extended to an annual hourly weather file.

Chan (2011) used the Morphing method developed by Belcher et al. (2005) to produce design weather data for building thermal simulations that account for changes of climatic condition. Morphing involves shifting and stretching the climatic variables in the present-day weather time series to produce new weather time series that encapsulate the average climate change, whilst preserving the physically realistic weather sequences of the source data. The common algorithms used for morphing the weather data x_n are (i) a shift; (ii) a linear stretch; (iii) a combination of shift and stretch, as listed below:

$$x_\mathrm{n} = x_0 + \Delta x_m \tag{1-18}$$

$$x_\mathrm{n} = \alpha_m x_0 \tag{1-19}$$

$$x_\mathrm{n} = x_0 + \Delta x_m + \alpha_m \times (x_0 - \langle x_0 \rangle_m) \tag{1-20}$$

where x_0 is the existing hourly climatic variable, Δx_m is the absolute change in monthly mean climatic variable for the month m, α_m is the fractional change in monthly mean climatic variable for month m, $\langle x_0 \rangle_m$ is the climatic variable x_o average over month m.

A shift (1-18) adds a monthly change to the current hourly weather data parameter. This method is mainly used to adjust atmospheric pressure. Equation (1-19) is to stretch current hourly weather data by scaling the current hourly data with a relative monthly mean change of the weather data, e.g. the wind speed. For the combination of a shift and a stretch (1-20), a current hourly weather data is shifted by adding an absolute monthly mean change and stretched by a monthly diurnal variation of the parameter. This approach is applied to adjust the dry bulb air temperature. It uses the measured monthly difference of the diurnal mean, minimum and maximum dry bulb air temperatures in order to integrate predicted variations of the diurnal cycle.

Ren et al. (2014) presented a method to construct urban hourly weather data by adopting the 'morphing' approach considering UHI effect. The method starts with the surrounding rural weather as the 'baseline climate' and an Urban Canopy Model is used to provide the differences in the monthly average values of major climate parameters due to urban heat islands. The 'baseline climate' is then morphed to generate the urban hourly weather file for building simulations. It was demonstrated that the constructed hourly weather data agreed well with the observations.

Liu et al. (2017) proposed a method to generate new TMY weather files for different micro-scale areas in Singapore based on recent years' weather data. They used a correlation equation between the urban texture variables (building, pavement and greenery) and the temperature for Singapore's urban areas to generate the local urban air temperature. This method was also used in the study of Ignatius et al. (2016).

Salvati et al. (2015) used UWG to simulate the microclimate in the Mediterranean region for one year. The building energy performance was evaluated by EnergyPlus afterwards. The weather input file was improved with local outdoor air temperature and radiation. It was presented that UHI effect led to an average increase in energy demand from 10 % up to 35 %, according to different urban densities.

Palme et al. (2017) coupled UWG with a building simulation engine to generate a representative urban weather file in EPW format which can be directly used in DBES. However this work only gave a microclimate simulation of one week, not providing a methodology to generate an annual weather file.

Tsoka et al. (2018) presented a computational method for assessing the urban climate's effect during the creation of typical weather years for dynamic building energy calculations. Microclimate simulations for 12 representative days (one for each month) were performed by ENVI-met. The results

were used as inputs in Meteonorm stochastic weather generator so as to create an urban specific weather dataset, which was finally compared with a reference stochastically created weather dataset reflecting climatic conditions at a meteorological station.

Castaldo et al. (2018) obtained hourly values of dry bulb temperature, direct and diffuse solar radiation, and wind speed, for one day in summer and winter by applying ENVI-met to a case study, and further generated the hourly values of these parameters for the entire year by performing the sinusoidal interpolation of the air temperature and solar radiation and the linear interpolation of the wind speed. However, the sinusoidal interpolation of the air temperature is not a satisfying assumption.

Stamatis Zoras et al. (2017) developed a model to predict hourly microclimatic data in a region for a whole day by employing Fourier analysis of past (measured) and future (simulated from a CFD analysis) microclimate data of a limited period (sunlight hours). Their method is able to assess building energy performance due to exterior micro-climate improvement, simultaneously, for about 200 buildings.

1.4.4. *Conclusions*

This section reviewed the well-known urban climate simulation models; some studies about the quantitative evaluation of the UHI effect on the building energy performance and the methods of coupling of the microclimate simulation tools with a DBES tool, especially for the generation of an hourly weather input file. Through this review, it can be inferred that an annual site-specific weather file generation method accounting for the microclimate effect, which can provide local hourly air temperature, is still needed. Few studies presented the UHI effect on the building energy performance by coupling a microclimate simulation tool with a DBES tool for Chinese cities, particularly even less for Wuhan. These issues will be investigated in chapter 4.

1.5. Review of building LCA

LCA is considered as a promising tool to quantitatively evaluate the building's environmental impacts, which has already been widely used in the building industry (Abd Rashid and Yusoff, 2015). The background systems such as the electricity production mix are essential boundary conditions in LCA applications. This mix might affect the environmental impacts of materials fabrication in the building construction stage. During the operation stage, electricity use is one major energy consumption factor, and its environmental impacts are strongly influenced by the electricity production mix. A building can have a long lifespan of more than 50 years. The electricity production mix might evolve during its lifespan, which is not considered by the static LCA method. In recent years, dynamic LCA (DLCA) has become an emerging research field as it incorporates time-dependent variables (Yang and Chen, 2014). The review is presented by the following two parts:

- introduction of LCA,

- electricity production mix in LCA background.

1.5.1. *Introduction of LCA*

LCA is a tool used for the quantitative assessment of materials used, energy flows and environmental impacts of a product or a system throughout its life (i. e. cradle to grave) from raw material acquisition, processing, manufacturing, use and finally its disposal or recycling (ISO 14040:2006, 2006). The concept of life cycle studies has developed over the years, initially in industry during the 1970s and in the building sector (Kohler, 1986) in the 1980s. In the recent years, life cycle studies have focused on the quantification of energy and materials used and wastes released into the environment throughout the life cycle (Sharma et al., 2011). LCA is subject to ISO 14040 adopted by the International Organization for Standardization (ISO) as an environmental management standard in 1990s to focus on the establishing methodologies for LCA (ISO 14040:2006, 2006). It defines the LCA methodology into four phases: goal and scope definition, life cycle inventory analysis, life cycle impact assessment and life cycle interpretation, as shown in Figure 1.12.
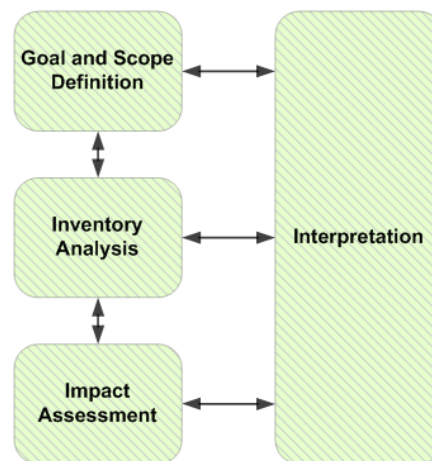
Figure 1.12: Four phases in LCA framework

(1) Goal and scope definition

In this first phase, the aim and scope of the study needs to be defined to set out the context and explain how and to whom the results are to be communicated. The depth and breadth of LCA can differ considerably depending on the goal. The functional unit, the system boundaries, the assumptions and limitations and quality criteria for inventory data should be defined in this phase.

- **Functional unit**

Functional unit defines the quantification of identified functions of the selected product to ensure comparability (ISO 14040:2006, 2006). Various functional units have been used in the literature, such as building elements (Jönsson, 2000) or weight of materials (Venkatarama Reddy and Jagadish, 2003). However, limiting the functional unit of LCA to a building material or component might ignore the various functions of a building such as thermal comfort or indoor air quality. Thus multiple functional units have been adopted by many researchers to do the case studies. Verbeeck and Hens (2010) used kg, m^3, m^2 or m, for building materials and kW for system components as functional units. A square

meter (1 m^2) of floor area is the most used functional unit for building LCA (Abd Rashid and Yusoff, 2015). Ortiz-Rodríguez et al. (2010) added a certain number of occupants to 1 m^2 to form a functional unit and Blengini and Di Carlo (2010) restrained the area to the heated areas only. The functional units are defined based on different goals of LCA, such as volume (Bonamente and Cotana, 2015), heat delivery (Rosenbaum et al., 2015) and heated floor area (Takano et al., 2015).

- **Lifespan**

The lifespan of a building is also an important parameter to be considered in an LCA study, due to the important environmental impacts generated during the use stage. In general, lifetime is assumed and not based on a calculation method. For residential buildings, the lifespan varies from 30 to 100 years (Adalberth, 1997 ; Oyarzo and Peuportier, 2014 ; Rossi et al., 2012); for commercial buildings, it is considered between 40 and 75 years (Cole and Kernan, 1996 ; Kofoworola and Gheewala, 2009 ; Van Ooteghem and Xu, 2012). But for both, a lifetime of 50 years is the most used. A statistical analysis of U.S. residential buildings was conducted by Aktas and Bilec (2012) and it reported 61 years as the average lifetime. Wang et al. (2018) estimated the average lifespan of buildings in China through literature review, field investigation and calculation, revealing that the average building lifespan in China is 25 - 35 years, due to various reasons such as poor quality of buildings, demolishing buildings to pursue commercial profits, area redevelopment and poor government planning, etc., which is far shorter than the designed lifespans required by the government (50 years for ordinary buildings and 100 years for important buildings) (MOHURD, 2019).

- **System boundaries**

The system boundary determines which process should be included within LCA and it should be consistent with the goal of the study (ISO 14044:2006, 2006). In the most cases, the cradle-to-grave system boundary which starts from pre-use stage to end-of-life use stage is most used, as shown in Figure 1.13. For building product analysis and construction process analysis, the cradle-to-gate system boundary and gate-to-gate system boundary are often used respectively (Abd Rashid and Yusoff, 2015).

Pre-use Stage		**Construction Stage**		**Use Stage**		**End-of-Life**
• Raw material acquisition • Manufacturing • Transportation to site	→	• Energy consumption during construction (Transportation & operation of machines/tools to site)	→	• Operating energy • Maintenance & replacement	→	• Demolition • Recycling potential • Landfill • Re-use
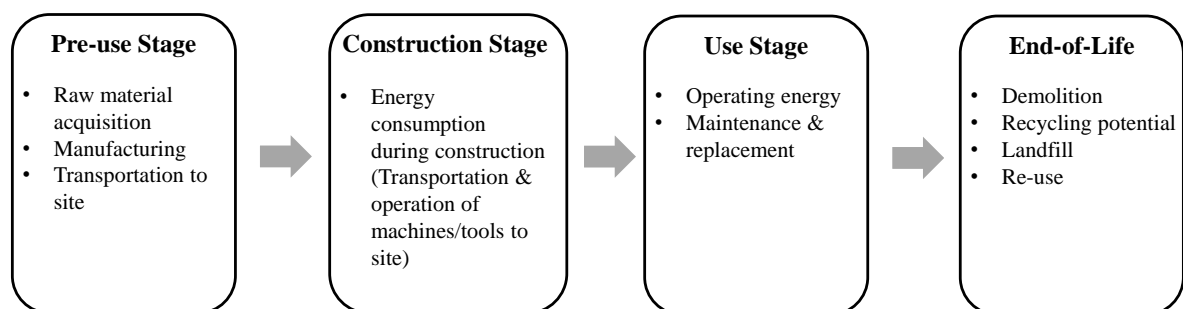
Figure 1.13: Cradle-to-grave system boundary used in building's LCA research (Abd Rashid and Yusoff, 2015)

(2) Inventory analysis

LCI analysis is the second phase of LCA, aiming at creating an inventory of flows including raw resources or materials, energy by type, water, and emissions to air, water and land by specific substance from and to nature for a product system. In building LCA, LCI can be very complex due to the numerous materials and processes involved during a building's lifespan.

In the construction stage of a building, the materials data are collected from the bill of quantities (Iyer-Raniga and Wong, 2012) or estimated from building sketches and field measured data (Blengini and Di Carlo, 2010). Regarding the transportation data, various approaches have been adopted, for example average distances from personal communication with designer and constructor (Blengini and Di Carlo, 2010). In Blengini's another case study (Blengini, 2009), the Buwal 250 database was used as the source for transport operations. Other methods such as nearest manufacturer or the national average distance are also used (Ochsendorf et al., 2011). Assumptions between the manufacture and the site can be also an option (Ortiz-Rodríguez et al., 2010). Peuportier et al. (2013) suggested that a 5 % surplus was added in the total amount of materials in order to account for on-site processes, broken elements and purchased quantities. In reality this ratio can be even higher (e.g. to 10 %).

The use stage is considered as the most important stage due to the large amounts of energy used for heating, cooling, DHW and the specific electricity, and environmental impacts generated by the building. Various DBES tools have been developed in several countries to simulate the energy consumption (e.g. electricity and natural gas) in the building. The primary energy and secondary energy are essential in the inventory analysis in LCA.

The lifespans of the building components are different from that of the building. The refurbishment can be observed as retrofitting, refurbishment, renovation, repair or restoration in different studies or reports. This stage usually mainly considers the replacement of windows, roofs, doors, paintings (Ortiz-Rodríguez et al., 2010). In some studies the thickening of the insulation layer is also considered, such as insulating cement (Brás and Gomes, 2015) or extruded polystyrene foam (XPS) (Stazi et al., 2012). Beccali et al. (2013) studied the energy retrofit such as more efficient boiler and photovoltaic plant. Favi et al. (2017) proposed an approach of sensitivity analysis for LCA of building retrofit measures aiming at establishing the impact of input data uncertainties on the output variance.

In the end-of-life stage, the recycling or reuse of building materials is regarded as a potential way to reduce the environmental impacts. The aluminium and steel materials are often considered as recyclable materials and the others are landfilled or incinerated. Energy consumed by machineries are evaluated during demolition and average transportation data to landfill or recycling centre will be included in this stage (Abd Rashid and Yusoff, 2015).

(3) Impact assessment

This phase aims at evaluating the significance of potential environmental impacts based on the LCI flow results (ISO 14044:2006, 2006), in the boundary defined by the goal and scope definition stage. Classical life cycle impact assessment (LCIA) consists of the following mandatory elements:

- selection of impact categories, category indicators, and characterisation models;

- the classification stage, where the inventory parameters are sorted and assigned to specific impact categories;

- impact measurement, where the categorised LCI flows are characterised, using one of many possible LCIA methodologies, into common equivalence units that are then summed to provide an overall impact category.

Two main methods are used to assess the environmental impacts: problem-oriented method (midpoints) and damage-oriented method (endpoints), depending on the method of accounting for the environmental relevance of category indicators, as shown in Figure 1.14 (European Commission-Joint Research Centre-Institute for Environment and Sustainability, 2010).
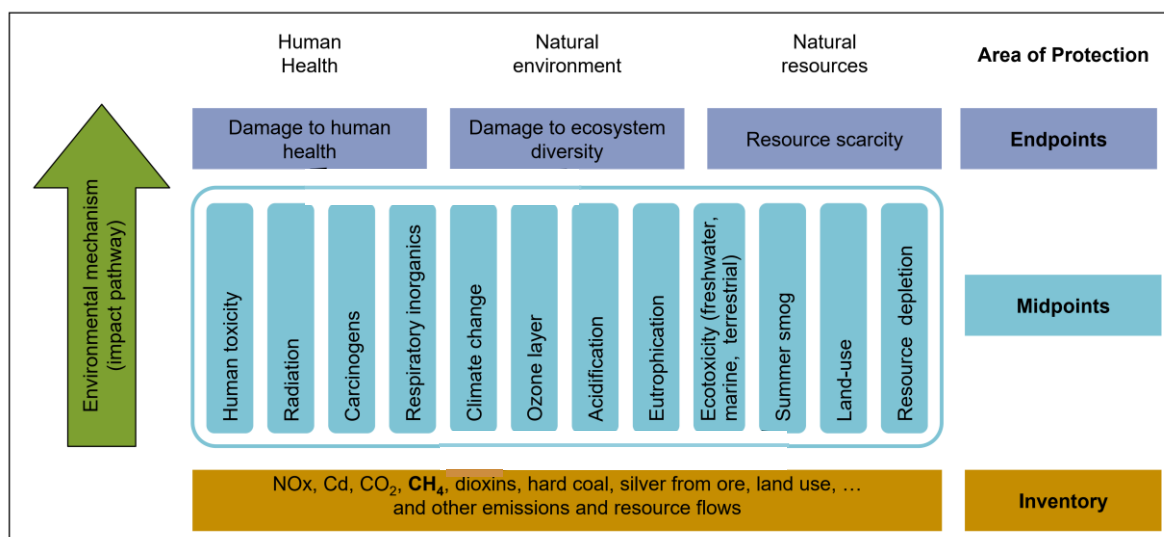
Figure 1.14: Schematic steps from inventory to category endpoints(European Commission-Joint Research Centre-Institute for Environment and Sustainability, 2010)

A midpoint approach is more related to elementary flows. Midpoints are considered to be links in the cause-effect chain (environmental mechanism) of an impact category, prior to the endpoints (Bare et al., 2000). Ozone depletion potentials, global warming potentials, and photochemical ozone (smog) creation potentials are the common used midpoints characterisation factors. Midpoint modelling includes points where it is possible to derive the characterisation factors and express the significance of emissions or extractions with a greater level of certainty and reliability (Bare and Gloria, 2008).

An endpoint approach aims at assessing the potential damage at the end of the chain. This depends on the type of receptor (human health, natural environment, and natural resources), geographical scale (global, regional and local), magnitude and priority of abatement (high, medium and low priority) as well as the impact medium (air, water, soil and resources) (Goedkoop et al., 2008). An endpoint approach allows better-controlled and knowledgeable weighing process and is easier to explain. However, due to the complex characterisation process, more assumptions and the requirement for high quality data, this method brings a larger uncertainty.

Ortiz et al. (2009) suggested that the midpoints can be assessed using CML 2002 baseline method, EDIP 97 and EDIP 2003 and IMPACT 2002+ and the endpoints can be assessed using Eco-indicator 99 and IMPACT 2002+. In fact, these two approaches are complementary, thus in many studies they are recommended to be combined for the environmental impacts assessment.

Various LCI databases have been developed to help study the environmental impacts caused by construction materials. Each LCI database is rather regional, because they are developed by a company or organism located in a specific country or territory, and the modelled processes are based on its manufacturing characteristics. Thus, when investigations carry out a study using an LCI database from another country, the results may well be incorrect (Martínez-Rocamora et al., 2016). In Europe, there are several LCI databases such as ecoinvent[8] developed by the Swiss Centre for Life Cycle Inventories, ELCD [9] supported by the European Commission, GaBi Database [10] by PE INTERNATIONAL. Eco-Profiles[11] is an LCI database specialised in plastic materials developed by PlasticsEurope. In North America, U.S. Life Cycle Inventory Database[12] was developed in 2001 by the National Renewable Energy Laboratory of the U.S. Department of Energy. Athena database[13] is used by Athena Impact Estimator in Canada. There are also Input–Output databases for specific countries: the Dutch Input-Output, EU and Danish Input-Output, Japanese Input-Output and US Input-Output. In China, the Chinese Reference Life Cycle Database (CLCD) (Liu et al., 2010) is a widely used LCI database, which is integrated into LCA software eBalance[14]. Various materials (Hong et al., 2015 ; Hong et al., 2016 ; Hong et al., 2017 ; Hong et al., 2019 ; Wang et al., 2019b ; Ji et al., 2020) were studied in China by applying LCA method and developed the Chinese Process-based Life Cycle Inventory Database (CPLCID) based on raw material data collection from the manufacturers and uncertainty analysis. Other LCI databases e.g. Sino-Center and CAS-RCEES are also reported (Wang et al., 2016).

---

[8] https://www.ecoinvent.org/database/database.html

[9] https://eplca.jrc.ec.europa.eu/ELCD3/index.xhtml

[10] http://www.gabi-software.com/international/index/

[11] https://www.plasticseurope.org/en

[12] https://www.nrel.gov/lci/index.html

[13] https://www.nrel.gov/lci/index.html

[14] http://www.athenasmi.org/our-software-data/lca-databases/

(4) Interpretation

This is the final phase for building LCA, in which the results from the impact assessment are analysed and the conclusion of LCA should be given. The robustness and sensitivity of the results are also often studied to evaluate the reliability of the study. The interpretation should include:

- identification of significant issues based on the results of the LCI and LCIA;

- evaluation of the study considering completeness, sensitivity and consistency checks;

- conclusions, limitations and recommendations.

1.5.2. *Electricity production mix in LCA background*

The electricity consumption in buildings is highly variable, with seasonal variation due to space heating or cooling, weekly variation due to professional activities and daily variation due to home appliances and lighting (Roux et al., 2016b). To meet the energy demand, the electricity production mix also varies, especially for a region such as Hubei Province (China), where hydropower highly depending on the seasons occupies a large share. During the long lifespan of a building, the choice of the electricity production mix might strongly influence the environmental impacts evaluation results in building LCA. Current practice in LCA is to use an annual average electricity supply mix based on a documented reference year (Itten et al., 2012). However, some studies considered the influence of variation in the electricity production mix.

Dandres et al. (2017a) considered the marginal GHG emissions caused by load migrations inside the electric grid instead of only considering the average emissions of the electric grid's prior load migrations. Marginal generation is the source of electricity which is supplied to meet increased demand or reduced to compensate for lower demand. Results showed that load migrations made it possible to minimise marginal GHG emissions of the cloud computing service. Olkonnen and Syri (2016) examined the spatially and temporally explicit marginal emissions of the Finnish, Nordic, and European electrical grids on an hourly basis until 2030, which combined time-resolved building electrical usage with time-resolved grid electricity production,

Roux et al. (2016b) applied LCA to an energy-efficient house in France, by using an annual average electricity supply mix and hourly data in 2013. The results showed that the use of an annual average mix instead of hourly mix data led to underestimation of potential impacts up to 39 % for abiotic depletion potential and 36 % for global warming potential when combining all end-uses. Furthermore, Roux et al. (2017) developed an attributional dynamic method and a marginal dynamic method integrating grid-building interaction in LCA of buildings and districts. The proposed electricity system models allow a more precise and representative evaluation of electricity supply related impacts in LCA compared to standard practices.

Roux et al. (2016a) evaluated life cycle impacts of a low-energy single family house located in France, integrating climate change and evolution of the energy mix on the long term (at 2050). The electricity production mix evolved for 2020 (present), 2030 (mid-term) and 2050 (long-term) in France.

The results showed that the carbon footprint of the house (total life cycle) varied from +21 % to +43 % for the electric heating alternative, -7 % to +4 % for the gas boiler alternative, -6 % to +15 % for the PV alternative depending on climate change intensity and evolution of the energy mix.

Collinge et al. (2018) assessed the differences between regional average- and marginal-electricity generation mixes as well as the variability between predicted and observed energy consumption of a conventional green building and a Net-Zero Energy Building (NZEB). Two static and four dynamic LCA models were evaluated for both buildings. It was reported that the most appropriate models significantly modified the use-phase global warming potential impacts relative to the static LCA (49 % greater impact for the conventional green building and 45 % greater reduction for the NZEB).

Su et al. (2019) used DLCA to a residential building located in Jiangsu Province (China). The proposed DLCA framework for buildings enabled the incorporation of dynamic assessment elements (DAEs) into the static LCA framework. They changed the basic inventory database to a dynamic one by considering the long-term electricity production mix forecasted by three scenarios (energy-saving, low-carbon, and enhanced low-carbon) (ERINDRC, 2009). The ecological damage index and resource depletion index values in the low-carbon scenario were respectively 16.0 % and 8.9 % lower than those in the energy-saving scenario, and the values in the enhanced low-carbon scenario were respectively 10.7 % and 5.4 % lower than those in the low-carbon scenario. The results showed that optimising the energy mix had an obvious influence on improving the environmental performance of the case study.

Negishi et al. (2019) evaluated the impacts of climate change on a French building using DLCA. As an essential factor in DLCA, two future production mix scenarios were considered: one with a high nuclear share of 50 % in 2050 and another with a low nuclear share of approximately 5 % in 2050, the remainder being satisfied by renewable resources and natural gas. The future mix was modelled by varying the mix composition without changing the current technologies, which represents a limiting assumption.

Walzberg et al. (2019) stated that ignoring temporal aspects of both the production and consumption sides of complex socio-technical systems may lead to errors. They showed that the wrong assumption regarding the nature of power demand led to sub-optimal results for demand-side strategy: the use of an average electricity mix slightly increased GHG emissions, whereas applying a marginal mix decreased emissions by 10 %.

1.5.3. *Conclusions*

This section presented an introduction to the building LCA and some studies concerning how electricity production mix affects the environmental impacts in building LCA. Through the review, it can be inferred that few LCA databases coupled to a DBES tool are available in China. Few building LCA studies considered the local energy mix in China. The evolution of energy mix influences a lot the evaluation results, however, few studies took this into account. Thus, a contextualised LCI database in Chinese context will be presented and the influence of the energy mix on the

environmental impacts of the building in China on spatial and temporal scales will be discussed in chapter 5.

1.6. Case study in Wuhan, China: HSJG

The investigation of the abovementioned three boundary conditions will be applied to a case study in Wuhan (China) which is presented in this section.

1.6.1. *General information about Wuhan and HSJG*

Wuhan, the capital city of Hubei Province, China (N 29°58' – 31°22', E 113°41' – 115°05'), is located in the eastern part of Jianghan Plain and the middle reaches of Yangtze river. Its topography is dominated by relatively flat land between 22 m and 27 m above sea level except the hilly areas sporadically distributed in suburban districts. Water body occupies a high percentage (>20 %) of its territory. Wuhan has a population over 10 millions and its urban area covers a total area of 8 494 km², with 13 municipal districts and 3 state-level development zones, accounting for 4.6 % of the total area of Hubei Province. Wuhan's climate is humid subtropical with an average annual temperature of approximately 16.9 °C with abundant rainfall (annual average precipitation is 1 140 – 1 265 mm) and four distinctive seasons. Spring and autumn are generally mild, summer is hot and humid and winter is cold and dry. The location of Wuhan in China and the remote sensing image of Wuhan is shown in Figure 1.15 (a) and (b) (Huang et al., 2019).

The studied building is situated on the intersection between Zhongbei road and Donghu Xi road of Wuchang District, with latitude of 30°32' North and longitude of 114°20' East. This area is a business and commercial centre, mixed with many recently built high-rise office, commercial and residential buildings and old buildings, as shown in Figure 1.15 (c). This area lies south by east with an angle of 20°. The simulated high-rise building is the unit 2 of the #2 (#2.2) building in Haishan Jingu (HSJG) block. HSJG consisting of 1 office building (#1) and 3 residential buildings (#2, #3 and #4) is a project providing housing, offices and shopping. It is integrated with GCHP systems to supply heating, cooling and DHW for the habitants. The overall effect plan is shown in Figure 1.15 (d).
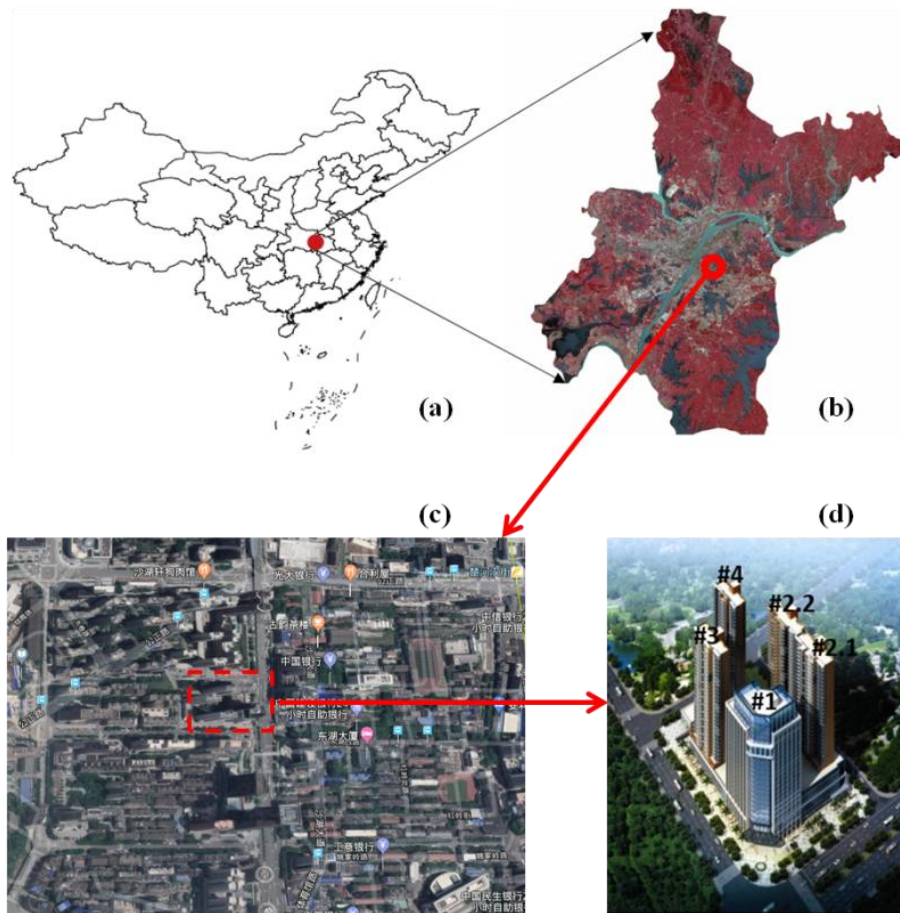
Figure 1.15: (a) Location of Wuhan in China (Huang et al., 2019), (b) remote sensing image of Wuhan (Huang et al., 2019), (c) surrounding area of the studied building and (d) HSJG block

1.6.2.   Case description

1.6.2.1.   Geometric information

Instead of the whole block, only the building #2.2 is studied, and the other buildings including one office building (#1), and three residential buildings (unit 1 of #2 (#2.1), #3 and #4) are regarded as obstructions. The plans of all buildings are shown in Figure 1.16 – Figure 1.18. In the studied building #2.2, each floor consists of four apartments named A, B, C, D (from west to east) and aisle. These buildings lay south by east with an angle of 20°.

There is a connected commercial centre under the buildings #1, #2.1, #3 and #4, acting as obstructions in simulation. There are 6 floors in the centre under #1 and #3 buildings for a total height of 18 m. The heights under #4 and #2.1 are 9 m and 27 m (with respectively 3 floors and 9 floors). They are indicated in the overall effect plan of the block and modelled as obstructions. The height, number of floors and function in simulation of each building are summarised in Table 1-1. The distances and orientations between every pair of buildings are listed in Table 1-2 to model the whole block.
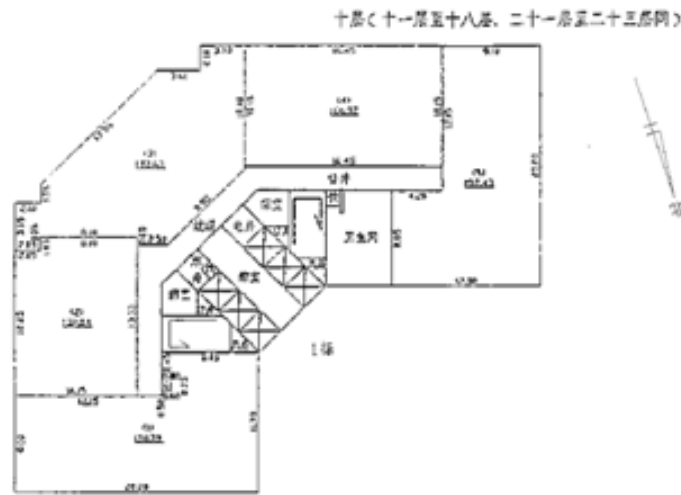
Figure 1.16: Plan of building #1
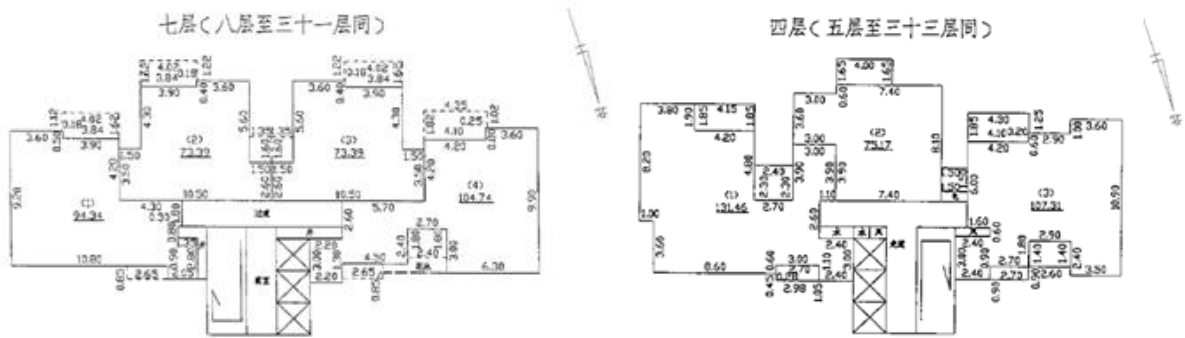
Figure 1.17: Plan of building #3 (left) and #4 (right)
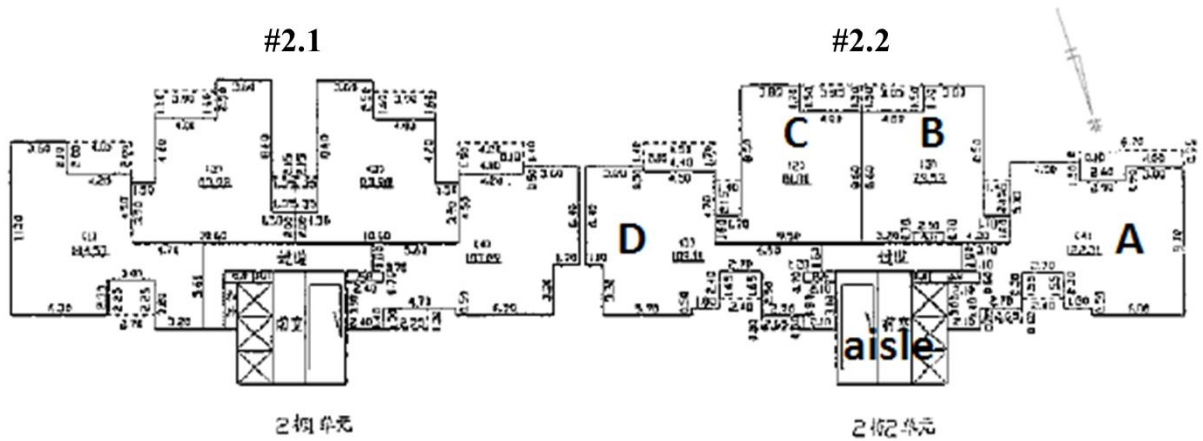
Figure 1.18: Plan of building #2.1 (left) and #2.2 (right)

Table 1-1   *Description of buildings*

Number of building	Number of floors (–)	Height (m)	Function in the simulation
#1	23	102	Obstruction
#2.1	34	102	Obstruction
#2.2	34	102	To be simulated
#3	31	102	Obstruction
#4	33	102	Obstruction
Commercial centre between #1 and #3	6	18	Obstruction
Commercial centre between #1 and #2.1	9	27	Obstruction
Commercial centre under #3 and #4	3	9	Obstruction

Table 1-2   *Distance and orientation between each pair of buildings*

Two buildings	Distance between two buildings (m)	Orientation
#1 – #2.1	14	north – south
#2.1 – #2.2	1.5	east – west
#2.2 – #4	8	east – west
#4 – #3	16	north – south
#3 – #1	18.5	east – west

1.6.2.2.   Envelope description

The thermal parameters of the wall material are listed in Table 1-3. The wall composition and its thermal resistance R are shown in Table 1-4. The parameters of windows and doors are listed in Table 1-5 and Table 1-6.

Table 1-3   *Thermal parameters of the building materials*

Material	Density (kg/m^3)	Conductivity (W/m.K)	Specific heat (J/kg.K)
Aerated concrete block	700	0.22	1 050
Cement mortar	1 800	0.93	1 050
Ceramic tile	2 700	1.99	850
Concrete	2 500	1.74	980
Emulsified asphalt perlite	300	0.093	1 550
XPS	25	0.03	1 380
Extruded Polystyrene Foam Board	30	0.042	1 380
Fine aggregate concrete	2 100	1.28	920
Insulation mortar	250	0.06	1 050
Marble	2 800	2.91	920

Table 1-4 **Wall description of building #2.2**

External wall (from outside to inside):	Intermediate floor (from top to bottom):
Ceramic tile 1 cm + Cement mortar 2 cm	Cement mortar 2 cm
Insulation mortar 4 cm	XPS 3 cm
Aerated concrete block 20 cm	Fine aggregate concrete (C15) 20 cm
Total thickness 27 cm; *R*=1.61 m². K/W	**Total thickness 25 cm; *R*=1.18 m². K/W**
Ground floor (from inside to ground)	**Roof (from outside to inside):**
Marble 2 cm	Ceramic tile 1 cm + Cement mortar 3 cm
Cement mortar 2 cm	Emulsified asphalt perlite 4 cm
Extruded Polystyrene Foam Board 4 cm	XPS 4 cm
Concrete (C10) 20 cm	Concrete (C10) 20 cm
Total thickness 28 cm; *R*=1.09 m². K/W	**Total thickness 32 cm; *R*=1.91 m². K/W**
Internal wall (in one apartment):	**Internal wall (partition wall):**
Aerated concrete block 10 cm	Aerated concrete block 20 cm
Total thickness 10 cm; *R*=0.45 m². K/W	**Total thickness 20 cm; *R*=0.91 m². K/W**

Table 1-5 **Parameters of windows**

Windows	Size (width ×height in cm)	Glazing	Vertical and horizontal U_w W/(m².K)	Solar factor (–)	Window basement (m)	Window depth(m)
Master bedroom	145 × 160, 283 × 160	Double low-emissivity glazing with insulating aluminium alloy frame	1.7	0.6	0.7	0.2
2nd bedroom	145 × 125				0.9	
Living room	300 × 225				0.1	
Kitchen	129 × 69				0.9	

Table 1-6 **Parameters of doors**

Doors	Size (width×height in cm)	Material and thickness (cm)	U_w (W/(m².K))[15]	Solar factor (–)
Between living room and master bedroom/2nd bedroom	80 × 205	Plain wood, 4.5	7	0.19
Between living room and bathroom/kitchen	70 × 205			
Entry door to the apartment located in the living room	82 × 196	Plain wood, 8		

---

[15] A default value is used, which has a minor influence on the total energy simulation

Thermal bridges are related to the heat losses in the thermal simulation. In this study, based on the building structure, the thermal bridges' characteristics are described in Table 1-7. Building finishes have a small influence on the thermal behaviour of buildings. The default values are used: solar absorptivity and reflection coefficient are 0.6 and 0.4 respectively, and infra-red emissivity is 0.9.

Table 1-7   Thermal bridge of building #2.2

Top floor	Intermediate floor
Windows (using insulating aluminium alloy frame can prevent the heat from leaking through the window frame)	**Shear wall** (roof is covered by an insulation layer and the heat cannot dissipate between the shear wall and the roof)
Ground floor	**Doors**
	0

1.6.2.3.   Residential schedules

According to the Chinese standard *Design standard for energy efficiency of residential buildings in hot summer and cold winter zone JGJ 134-2010* (MOHURD, 2010), the heating and cooling

thermostat setpoints are 18 °C and 26 °C for the whole year. The natural ventilation is 1 ach (air change per hour) because residents in Wuhan prefer opening windows for ventilation, and the infiltration ventilation is 0.2 ach. The internal heat gain is 4.3 W/m^2 for all days. The occupancy is 0.02 person/m^2 from 8h00 to 17h00 from Monday to Friday and the rest of the time, it is 0.04 person/m^2.

1.6.2.4. Zone definition

In Pleiades, the building is decomposed into a certain number of zones for the software to calculate the thermal performance. A zone is a volume with a homogeneous thermal behaviour for the study of temperature evolution and energy load. The temperature in a zone is unique. Criteria such as the use of room and the corresponding occupancy, the location of the room (orientation and level), internal gains and control systems are often used to divide the zones.

The studied building was modelled in the author's previous work (Pei, 2015), the zones definition was based on the following criteria:

- the bottom floor, connected to the underground space (not heated or cooled);

- the top floor, exchanging heat with the ambient through the roof and external wall;

- the 15th floor, where the experimental data were collected in the work (Pei, 2015);

- the other floors were modelled as several zones by the height and direction;

- the aisle was a single zone which was neither heated nor cooled.

The apartment C of the 15th floor was divided into three zones: the living room, the master bedroom and the rest of the rooms (including a bedroom, a kitchen and a WC). The apartment B of the 15th floor was also defined as one zone and apartments A and D were integrated as the north zone of floor 15. The detailed zone definition is shown in Table 1-8.

Table 1-8   Zone definition in building #2.2

Zone number	Zone name	Consist	Floors	Area (m^2)
1	floor 1	Apartment A, B, C, D	1	366
2	aisle	Aisle	1 – 34	1905
3	floor 2-6 north	Apartment A, D	2 – 6	1093
4	floor 2-6 south	Apartment B, C	2 – 6	739
5	floor 7-14 north	Apartment A, D	7 – 14	1748
6	floor 7-14 south	Apartment B, C	7 – 14	1183
7	floor 15 C-living room (15)	Apartment C-living room	15	37
8	floor 15 C-master bedroom (15)	Apartment C-master bedroom	15	14
9	floor 15 C-rest rooms (15)	Apartment C-bedroom, WC, kitchen	15	22
10	floor 15 B	Apartment B	15	75
11	floor 15 north	Apartment A, D	15	219
12	floor 16-25 north	Apartment A, D	16 – 25	2186
13	floor 16-25 south	Apartment B, C	16 – 25	1479
14	floor 26-33 north	Apartment A, D	26 – 33	1748
15	floor 26-33 south	Apartment B, C	26 – 33	1183
16	floor 34 north	Apartment A, D	34	219
17	floor 34 south	Apartment B, C	34	148

1.6.2.5.   Modelling result

The 15th floor plan of building #2.2 is shown in Figure 1.19 as an example, and the plan of each floor is similar. The areas surrounded by dotted lines are the balconies functioning as integrated shadings in the simulation. Windows and doors are shown in blue and brown lines on the walls correspondingly. The 1st floor is shown in Figure 1.20 with surroundings. Figure 1.21 represents the 3D view of the whole HSJG block from the south view. The grey obstacles are set as obstructions. Building #2.2 divided into different zones with different colours is shown in Figure 1.22. The blue obstructions are not considered as zones.
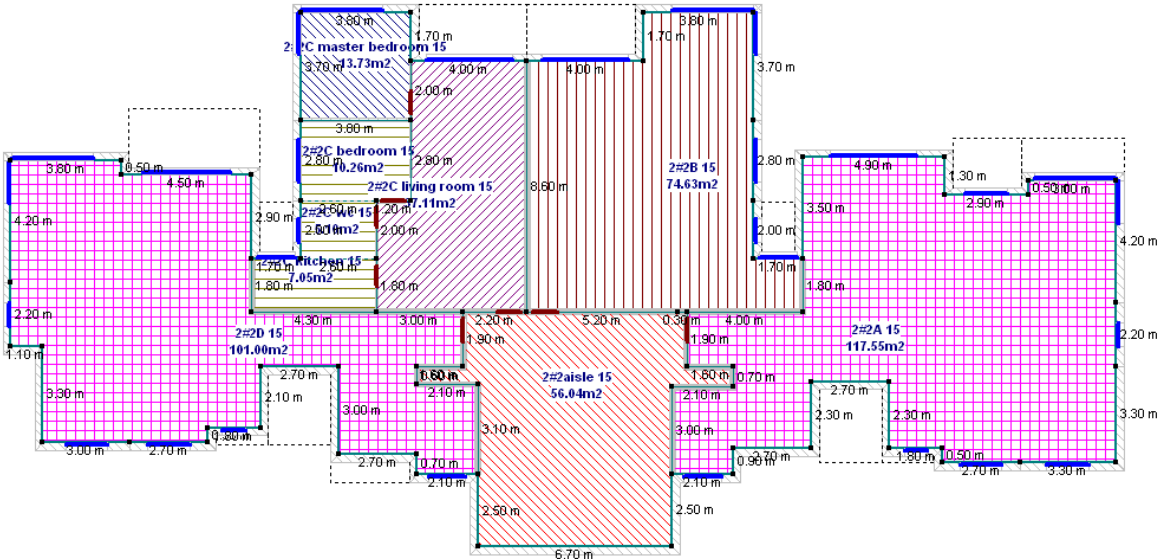
Figure 1.19: 15th floor plan of building #2.2
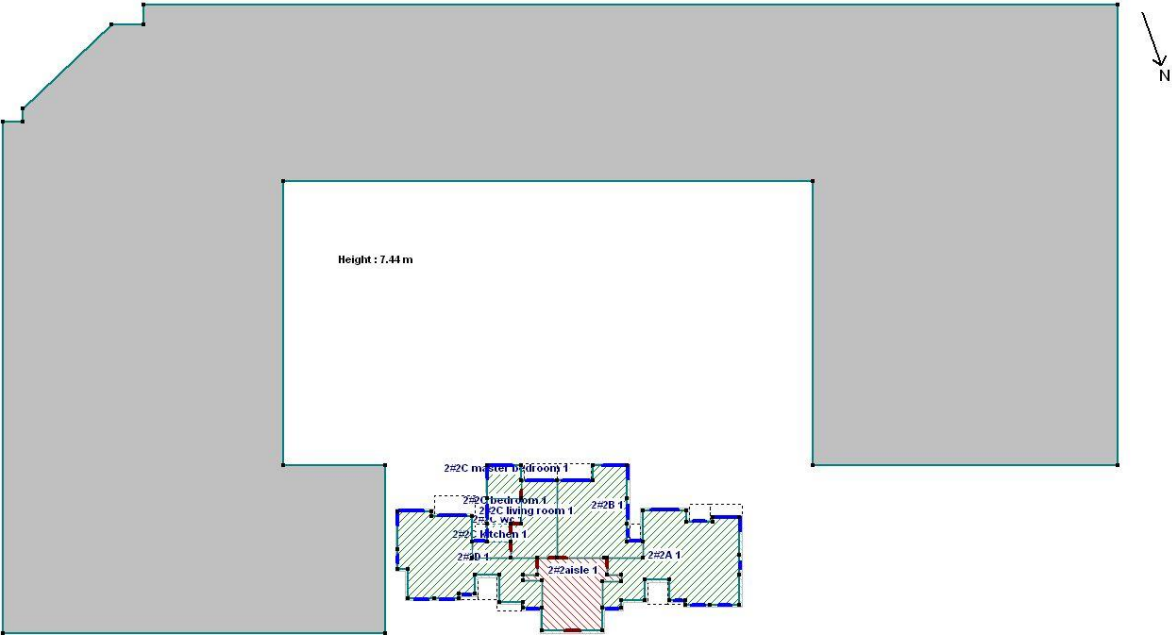
Figure 1.20: 1st floor plan of building #2.2 and its surroundings
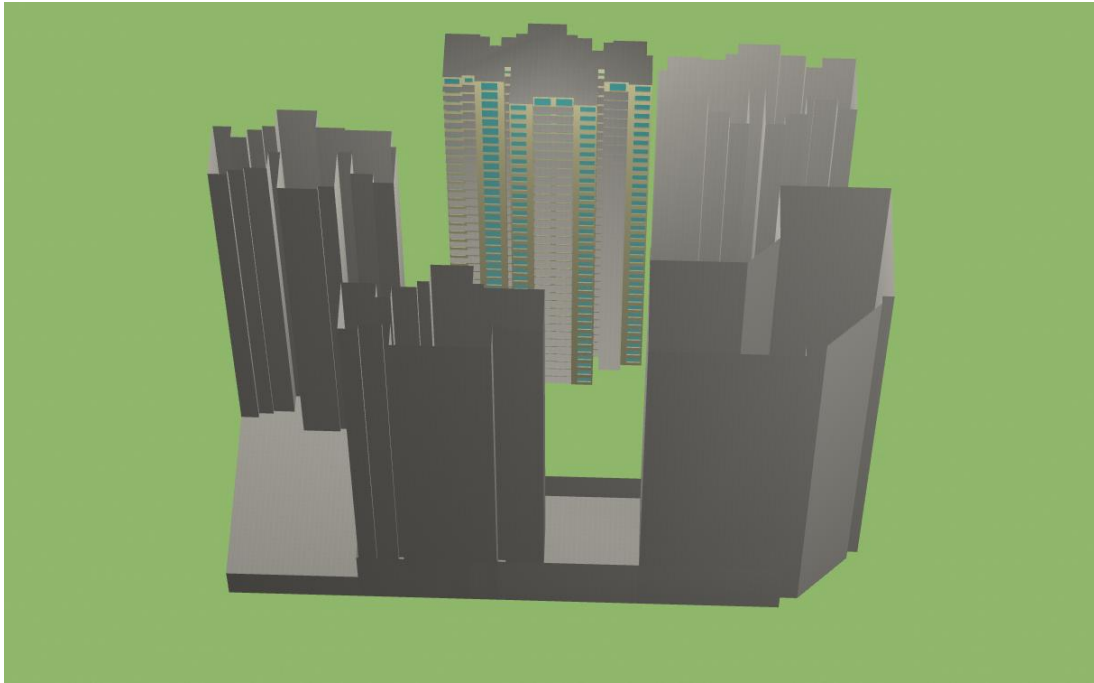
Figure 1.21: South view of HSJG
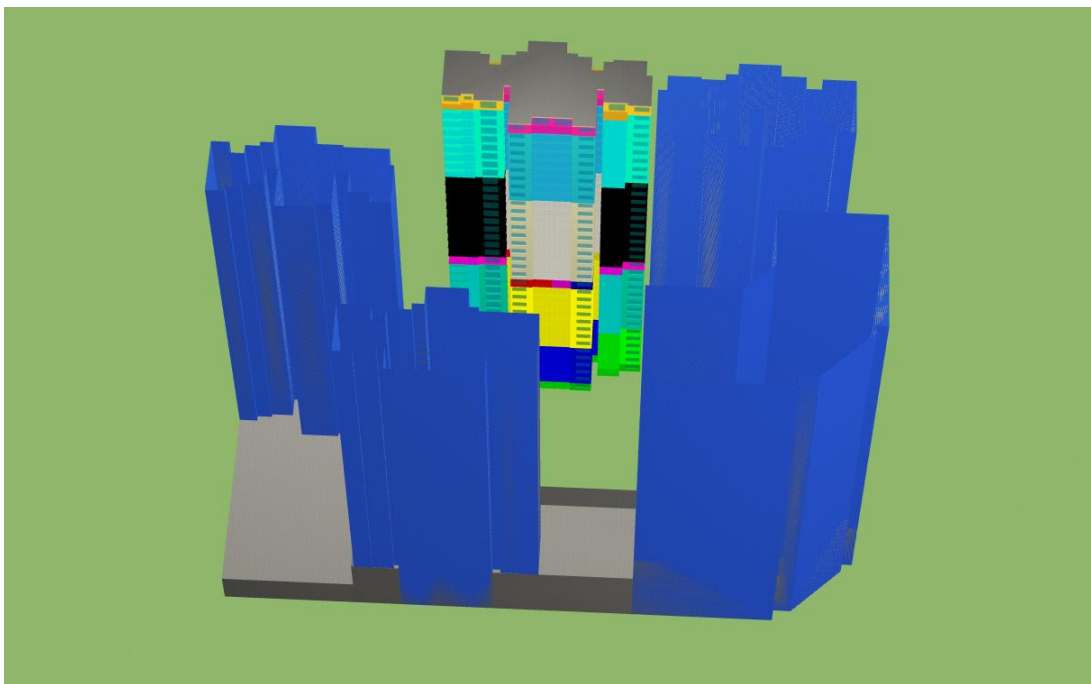
Figure 1.22: South view of HSJG and its zones

1.7. Conclusions of chapter

1.7.1. *Objectives of thesis*

Urbanisation process in China makes the Chinese building construction sector very active. This leads to a high pressure on resources, as well as future environmental impacts such as energy and GHG emissions during a building's long lifespan. The highest potential reduction of these impacts corresponds to decisions made during the building's design phase. Evaluating environmental impacts can help designers progress towards sustainable construction by comparing alternatives and optimising architectural or urban projects. This process can be accomplished with the aid of the computer simulation/evaluation tools. The environmental impacts of a building depend on many interacting aspects, so that a systemic evaluation tool like LCA is appropriate. But this requires to define relevant boundary conditions.

The thesis aims at improving the quantitative evaluation methodology of the building's environmental impacts based upon DBES and LCA, by refining three boundary conditions: the ground, the microclimate around the building, and the background systems in LCA. The proposed method is expected to be applied to the DBES tool COMFIE and the building LCA tool EQUER, but it could be applied to other tools.

The first objective is to propose a GCHP model equipped with a large-scale boreholes field, representing a good compromise between calculation time and accuracy and implement it in Pleiades. The second objective is to develop a methodology for quantitative evaluation of the microclimate's effects on the building's energy performance. Afterwards, the UHI effects on the building energy performance in Wuhan will be investigated. The third objective is to perform the environmental impacts evaluation by LCA methodology, accounting for the local background systems (e.g. the electricity production mix) in China and different provinces with local energy mix features. The temporal evolution of the background systems is taken into consideration as well.

1.7.2. *Methodology and outline of thesis*

In this thesis, the environmental impacts evaluation of a building is based on the DBES model ***COMFIE*** and building LCA model ***EQUER***, by considering the three abovementioned boundary conditions. These models are integrated in the commercial software ***Pleiades***. The methodology of the thesis is illustrated in Figure 1.23.

In chapter 2, a calculation time reduction method for a large-scale boreholes GHE is presented in order to overcome the challenge of the long simulation time, which is developed in ***Matlab***. This method is based on the FLS model and the 2D heat conduction equation, consisting of a series of sub-method to simplify the calculation. The calculation speed and accuracy of the proposed model are discussed.
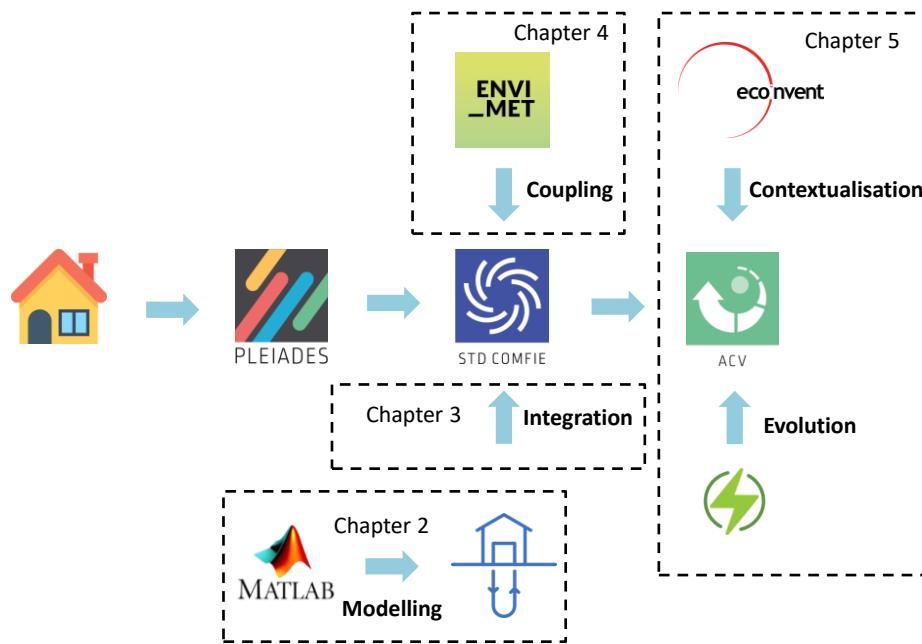
Figure 1.23: Schematic of the methodology in this thesis

In chapter 3, the GHE model is coupled to a steady-state semi-empirical heat pump model based on simplified cycle analysis and the whole GCHP model is integrated in ***COMFIE*** in Delphi environment. The proposed model is applied to the studied case to verify its accuracy and speed. This model is used to improve the system performance.

In chapter 4, a method to generate the local typical weather years' hourly data reflecting the microclimate is introduced. This method allows DBES tools to perform the dynamic simulation with more accurate local weather data. The coupling method of the microclimate simulation tool ***ENVI-met*** and the DBES model ***COMFIE*** is presented, aiming at quantitatively evaluating the microclimate's effect on building energy performance. The results of the case study using the proposed method are presented, considering the UHI effect in Wuhan.

In chapter 5, LCA is performed for the studied building, considering background systems e.g. the Chinese electricity production mix and a regional electricity production mix for Hubei province. Its environmental impacts are evaluated. A contextualised LCI database is developed based on the LCI database ***ecoinvent***, which can be helpful for other researchers to perform LCA in the Chinese context. Moreover, the influence of electricity production mix on the environmental impacts of the building on spatial and temporal scales are investigated for five different regions in different climate zones and four future energy mix scenarios. This LCA methodology accounting for the local energy mix features and future evolution is considered to provide more reasonable results for a Chinese building with a long lifespan.

In chapter 6, the results are summarised and finally some recommendations and perspectives are given for this thesis.

Chapter 2. Development of a large-scale vertical GHE model for fast calculation

The integration of a GCHP model with a DBES model can provide more accurate evaluation results regarding exchanging heat with the ground, which constitutes one boundary condition in building energy simulation. However, this process requires a fast simulation, especially when aiming at optimising the system performance in the design phase, which is a great challenge for the GCHP systems with a large-scale boreholes GHE. This chapter presents a global model to solve this problem.

Résumé du chapitre

Le sol constitue une condition aux limites du bâtiment et de certains de ses systèmes de chauffage / refroidissement, qui influence sa performance énergétique. Cette condition aux limites est prise en compte en particulier dans le cas des pompes à chaleur verticales, GCHP, pour lesquelles le sol sert de source ou de puits de chaleur. Afin de progresser vers des bâtiments plus économes en énergie, ces systèmes GCHP sont une solution prometteuse, en particulier dans le cas des bâtiments urbains avec une surface au sol limitée pour l'installation d'échangeurs horizontaux. Les bâtiments urbains nouvellement construits en Chine sont généralement de grande hauteur et leurs charges énergétiques sont importantes, ce qui implique de grands échangeurs verticaux, GHE, avec de nombreux forages. L'optimisation de la conception et du fonctionnement des échangeurs thermiques à grande échelle est un facteur clé pour réduire la consommation d'énergie de ces systèmes. Cela nécessite une évaluation rapide du facteur de réponse thermique du champ de forage. Toutefois, les modèles disponibles ne sont pas appropriés en raison de leur temps de calcul ou de leur complexité.

Pour surmonter ce défi, ce chapitre présente un nouveau modèle global combinant le modèle de source à ligne finie (FLS), l'équation de conduction thermique bidimensionnelle (2D) et une nouvelle méthode à trois points. La méthode à trois points a été proposée pour évaluer la température de la paroi du forage (qui est un paramètre essentiel dans le modèle GHE) sur la base du modèle FLS. Il utilise la moyenne de la température calculée en trois points caractéristiques le long de la paroi du forage pour représenter la température moyenne de la paroi du forage (et éviter ainsi un calcul intégral). Le champ de forage est trié en catégories de distance croissantes pour éviter des calculs répétés, chacun étant simulé avec des pas de temps variables. L'équation de conduction thermique 2D est utilisée pour déterminer les cas où les interactions entre les forages sont négligeables et à quelle fréquence les interactions doivent être recalculées. Les facteurs de réponse thermique du GHE peuvent alors être déterminés par la méthode des trois points à une vitesse rapide en n'effectuant que les calculs nécessaires.

Le temps et la précision du calcul du modèle global ont été évalués dans Matlab. La méthode à trois points a montré une bonne précision à la fois pour des temps courts et longs à différentes distances radiales, tandis qu'elle reste sous la forme d'une seule intégration pour garder un temps de calcul raisonnable. Le calcul du facteur de réponse thermique pour un champ carré de 26×26 sondes pour 1 année simulée a pris 4 secondes, montrant un facteur de réduction du temps de calcul d'environ 1 000 000 et des erreurs relatives inférieures à 4 % par rapport au modèle de référence à double intégration. Pour 20 années simulées, le modèle proposé n'a pris qu'une minute. Il convient à différentes configurations de champs de sonde. Sa précision et sa vitesse sont des caractéristiques clés pour son intégration dans les outils de simulation énergétique des bâtiments.

Abstract

The ground constitutes a boundary condition for buildings and some of their heating/cooling systems, which influences its energy performance. This boundary condition is particularly considered in the GCHP system, in which the ground serves as heat source or sink. In order to progress towards more energy efficient buildings, vertical GCHPs are a promising solution, especially in the case of urban buildings with limited ground area for the installation of horizontal GHEs. The new-built urban buildings in China are usually high-rise and their energy loads are large, resulting in large GHEs with numerous boreholes. Optimisation of both the design and operation of large-scale boreholes heat exchangers is a key factor to reduce energy consumption of such systems. This requires a fast evaluation of the thermal response factor of the boreholes field. Available models are not appropriate due to their computation time or complexity.

To overcome this challenge, this chapter presents a new global model combining the FLS model, the 2D heat conduction equation, and a newly developed three-points method. The three-points method was proposed to evaluate the borehole wall temperature (which is an essential parameter in the GHE model) based on the FLS model. It uses the average temperature of three points along the borehole wall to represent the borehole wall temperature (which thus avoids an integral calculation). The boreholes field is sorted in increasing distance categories to avoid repeated calculations, each being simulated with varying timesteps. The 2D heat conduction equation is used to determine when interactions between boreholes are negligible and how often the interactions have to be recalculated. The thermal response factors of the GHE can then be computed by the three-points method quickly by only performing the necessary calculations.

The calculation time and accuracy of the global model were evaluated in Matlab. The three-points method showed a good accuracy for both short and long term at different radial distances, meanwhile it remains in the form of a single integration to keep a reasonable computation time. The thermal response factor calculation for a square field of 26 × 26 boreholes for 1 simulated year took 4 seconds, showing a calculation time reduction factor of around 1 000 000, and relative errors smaller than 4 % compared to the reference double integration model. For 20 simulated years, the proposed model took only 1 minute. It is appropriate for various boreholes configurations. Its accuracy and speed are key features for its integration into the DBES models.

2.1.   Introduction

Buildings constitute one of the main energy consuming sectors and it is essential to optimise their energy performance. According to China Building Energy Use 2018 (Jiang et al., 2018), building energy consumption accounted for approximately 20 % of the total primary energy consumption in 2016 in China. Vertical GCHP systems have been used in the buildings sector at a large scale in China because of their energy efficiency (Ikeda et al., 2017) and environmental friendliness (Yang et al., 2010b). A vertical GCHP system mainly consists of a vertical GHE, heat pumps and distribution units. The vertical GHE exchanges heat with the ground that serves as a heat source or heat sink, respectively in winter and summer.

Buildings can be equipped with large-scale boreholes GHEs which may contain hundreds of boreholes due to their high energy loads (Gultekin et al., 2019). The optimisation of the design and control of the GCHP systems can yield more energy efficient buildings (Zanchini and Jahanbin, 2018). A DBES tool integrating a vertical GCHP model can help building designers to achieve this goal. However, it can be difficult and time costing due to the large amount of calculations required for a large-scale boreholes GHE.

The simulation of a GHE mainly aims at predicting its returning fluid temperature and the ground temperature in the borehole field (Yang et al., 2010a). Fast and accurate calculation of these temperatures is essential for the long-term evaluation of the GCHP performance and the proper design of the system (Chen et al., 2019 ; Cimmino, 2018). The temperature variation of a point in the ground can be represented in a dimensionless form by introducing a proper thermal response factor, which is also called temperature response factor in some references (Fossa et al., 2020 ; Priarone and Fossa, 2016), giving the relation between the temperature variation and the overall heat extraction rate in the borehole field. The most utilised method to analyse a vertical GHE consisting of large-scale boreholes is firstly to use a heat transfer model of a single borehole to obtain the thermal response factor of one borehole, and secondly to apply Duhamel's superposition principle to evaluate the temperature responses caused by all the boreholes in the field (Yu et al., 2016).

As reviewed in chapter 1.3, the energy analysis models for one borehole can be divided into analytical models and numerical models. Although the numerical models (Yang and Li, 2014 ; Ozudogru et al., 2014 ; Biglarian et al., 2017 ; Naldi and Zanchini, 2019 ; Chen et al., 2020 ; Yu et al., 2020 ; Kerme and Fung, 2020) can take into account all the elements (including U-pipe, grout and ground) and offer more accurate results compared to analytical models using simplifying assumptions (Zarrella et al., 2011), they are very complex and they cannot be easily integrated into DBES tools. Many analytical models have been proposed (Li and Lai, 2015) such as the infinite line source model (Ingersoll and Plass, 1948), the FLS model (Zeng et al., 2002), the infinite cylinder source model (Deerman and Kavanaugh, 1991), the infinite composite-medium line source method (Li and Lai, 2012), the full scale model (Li et al., 2014b), and the transient quasi-3D entire time scale line source model (Zhang et al., 2016). These analytical models are more easily implemented in DBES tools. The FLS model is widely employed in GHE simulation for its simple mathematical form and relatively

good accuracy in long operation time simulation (Koohi-Fayegh and Rosen, 2014 ; Cui et al., 2016 ; Yu et al., 2016 ; Cimmino, 2018 ; Chen et al., 2019). In Zeng et al.'s study (Zeng et al., 2002), it is indicated that the middle point temperature and the integral mean temperature could be two representative borehole wall temperatures, and that the middle point is more often chosen for its convenience.

However, there are two main problems for the application of this method. The first problem is the conflict between accuracy and calculation speed of the FLS model. If the middle point temperature is used to represent the borehole wall temperature, the accuracy can be low when the operation time is long. If the integral mean temperature is used, the double integration form of the model (see equation (2-2) in section 2.1) increases the calculation complexity (Koohi-Fayegh and Rosen, 2014). The second problem is that the calculation load is massive when a large-scale boreholes field operates over a long time (e. g. a 26×26 boreholes field during 20 years) under dynamic loads. Long time scales (larger amount of data), varying loads (thermal history) and multiple boreholes (thermal interactions) are the three major challenges to obtain the optimal design of GHEs based on the operating performance simulation of GCHPs (Zhang et al., 2018a). The intensive computation makes this method not suited to be integrated into DBES tools.

It can be inferred from section 1.3.2 that although some efforts have been made on reducing the computation load, there is still a lack of a global, convenient and fast model to simulate the large-scale boreholes GHE, especially one which can be easily linked with the GCHP models and integrated into a DBES tool. This chapter presents a new global model that overcomes the abovementioned issues. Firstly, the GHE model is introduced by using the FLS model and the superposition method. Secondly, a novel method (the three-points method) to evaluate the borehole wall temperature is presented. Thirdly, a new model to quickly calculate the thermal response factor of the large-scale boreholes GHE is proposed, combining the FLS model, the two-dimensional (2D) heat equation and the three-points method, and then applied to a case study. Finally, the results are presented and discussed. It should be noted that in this chapter, if not particularly indicated, the time refers to the operation time of a borehole or a GHE from initial conditions where the ground temperature is uniform.

2.2. GHE heat transfer model

2.2.1. *Finite line source model*

In the FLS model, the ground is regarded as a homogeneous semi-infinite medium with constant thermophysical properties and a uniform undisturbed temperature which is usually obtained from references measurements or evaluated by a ground model, e.g. the model presented by Thiers (2008), accounting for various factors (e.g. absorption of solar radiation, rain, etc). The boundary of the medium, the ground surface, keeps a constant temperature during the considered period. The effects of underground water, air temperature variations and solar radiation are not taken into consideration in the heat transfer process of a borehole during the considered period. The radial dimension of the

borehole is neglected so that it may be approximated as a line-source stretching from the ground surface to the borehole depth.

Considering the effects of one borehole exchanging heat with the ground at a constant heat load q (positive values when a GHE extracts heat from the ground), the ground temperature T at any point at time t, as shown in Figure 2.1, is given by the FLS model (Zeng et al., 2002):

$$
\begin{aligned}
T(r,z,t) - T_0 &= \frac{-q}{2\pi\lambda_s} \cdot \frac{1}{2} \int_0^H \left\{ \frac{\text{erfc}\left(\frac{\sqrt{(r)^2 + (z-h)^2}}{2\sqrt{\alpha_s t}}\right)}{\sqrt{(r)^2 + (z-h)^2}} - \frac{\text{erfc}\left(\frac{\sqrt{(r)^2 + (z+h)^2}}{2\sqrt{\alpha_s t}}\right)}{\sqrt{(r)^2 + (z+h)^2}} \right\} \, \mathrm{d}h \\
&= \frac{-q}{2\pi\lambda_s} \, G(r,t,z)
\end{aligned}
\tag{2-1}
$$

where r is the radial distance to the borehole centre line; z is the vertical coordinate; T_0 is the undisturbed ground temperature; λ_s and α_s are respectively the thermal conductivity and thermal diffusivity of the ground; H is the borehole length; h is an integral variable along borehole length; G is the thermal response factor; and erfc denotes the complementary error function.
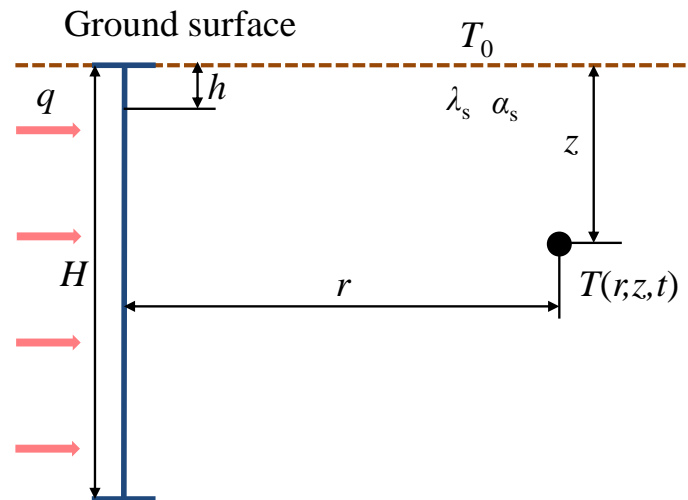
Figure 2.1: Temperature in the ground under the effect of one borehole

The integral mean temperature along the borehole length is considered to be a reasonable proxy to represent the borehole temperature (Zeng et al., 2002); this is called the double integration method in this chapter. Thus, considering the heat interaction between two boreholes, the borehole wall temperature T_b of a borehole at time t under the effect of the other borehole located at radial distance r with constant heat load q is given by:

$$T_{\text{b}}(r,t) - T_0 = \frac{-q}{2\pi\lambda_{\text{s}}} \frac{1}{2H} \int_0^H \int_0^H \left\{ \frac{\text{erfc}\left(\frac{\sqrt{(r)^2 + (z-h)^2}}{2\sqrt{\alpha_{\text{s}}t}}\right)}{\sqrt{(r)^2 + (z-h)^2}} \right.$$

$$\left. - \frac{\text{erfc}\left(\frac{\sqrt{(r)^2 + (z+h)^2}}{2\sqrt{\alpha_{\text{s}}t}}\right)}{\sqrt{(r)^2 + (z+h)^2}} \right\} \text{d}h \, \text{d}z = \frac{-q}{2\pi\lambda_{\text{s}}} G_{2\text{i}}(r,t)$$

(2-2)

where $G_{2\text{i}}(r,t)$ is the thermal response factor of a borehole wall temperature under the other borehole's effect using the double integration method. Considering a special case for the self-effect of one borehole, the borehole wall temperature response under the effect of its own heat load can be calculated by setting $r = r_{\text{b}}$, where r_{b} is the borehole radius.

2.2.2. *Superposition principle*

In the DBES model COMFIE, the time-varying heating and cooling loads are step-wise constant values. Here we assume that the energy load of the building is uniformly distributed to each borehole, which means the heat loads of all boreholes during a timestep are identical:

$$q_{1,m} = q_{2,m} = \cdots = q_{i,m} = \cdots = q_{N_{\text{b}},m} = q_m = \frac{Q_{\text{GHE}}(m)}{N_{\text{b}} \times H}$$

(2-3)

where $q_{i,m}$ is the lineic heat load of ith boreheole in a GHE consisting of N_{b} identical boreholes at timestep m; q_m is the lineic heat load of a single borehole; and $Q_{\text{GHE}}(m)$ is the heat load of the GHE field at timestep m.

The borehole wall temperature in a large-scale boreholes GHE could be evaluated by employing the superposition principle to the FLS model. The superposition principle consists of the temporal superposition and spatial superposition. The time-varying heating and cooling loads are step-wise constant values in this study, as shown in Figure 2.2 (a). In fact, the heat load has an effect on both the current time and the future, as shown in Figure 2.2 (b). For one borehole without the effects of other boreholes, its borehole wall temperature at timestep m is determined by employing temporal superposition to equation (2-2):

$$T_{\text{b}}(m) - T_0 = \sum_{k=1}^{m} \frac{q_{k-1} - q_k}{2\pi\lambda_{\text{s}}} \frac{1}{2H} \int_0^H \int_0^H \left\{ \frac{\text{erfc}\left(\frac{\sqrt{(r_{\text{b}})^2 + (z-h)^2}}{2\sqrt{\alpha_{\text{s}}(t_m - t_{k-1})}}\right)}{\sqrt{(r_{\text{b}})^2 + (z-h)^2}} \right.$$

$$\left. - \frac{\text{erfc}\left(\frac{\sqrt{(r_{\text{b}})^2 + (z+h)^2}}{2\sqrt{\alpha_{\text{s}}(t_m - t_{k-1})}}\right)}{\sqrt{(r_{\text{b}})^2 + (z+h)^2}} \right\} \text{d}h \, \text{d}z$$

(2-4)
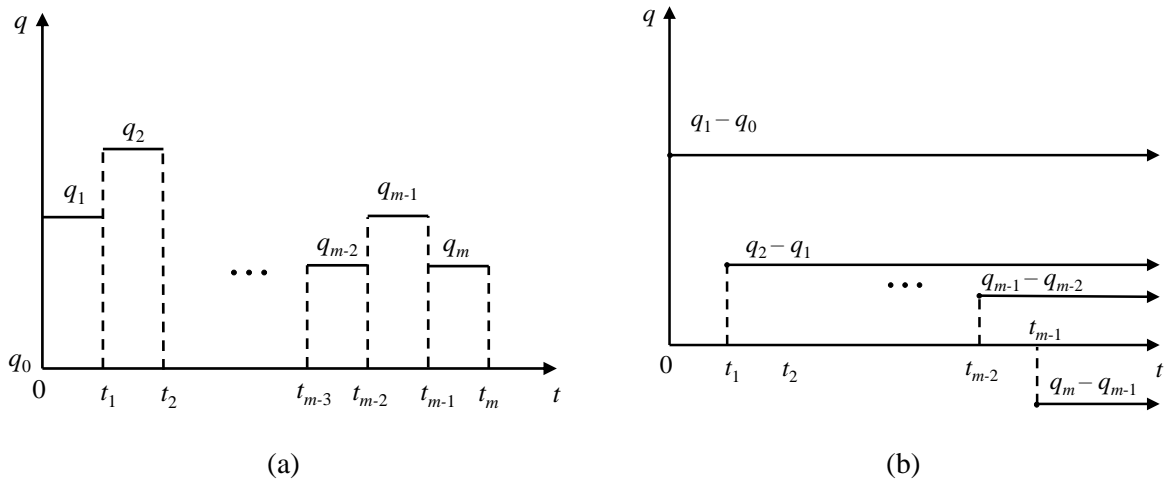
Figure 2.2: Temporal superposition principle for the timesteps of one borehole heat load: (a) the step-wise heat load and (b) heat load increment for various time intervals

The spatial superposition considers the effects of other boreholes on the calculated borehole, as shown in Figure 2.3. The borehole wall temperature of the jth borehole at timestep m can be determined by applying the spatial superposition to equation (2-4):

$$T_{b,j}(m) - T_0 = \sum_{i=1}^{N_b} \sum_{k=1}^{m} \frac{q_{k-1}-q_k}{2\pi\lambda_s} \frac{1}{2H} \int_0^H \int_0^H \left\{ \frac{\mathrm{erfc}\left(\frac{\sqrt{(r_{i,j})^2+(z-h)^2}}{2\sqrt{\alpha_s(t_m-t_{k-1})}}\right)}{\sqrt{(r_{i,j})^2+(z-h)^2}} - \frac{\mathrm{erfc}\left(\frac{\sqrt{(r_{i,j})^2+(z+h)^2}}{2\sqrt{\alpha_s(t_m-t_{k-1})}}\right)}{\sqrt{(r_{i,j})^2+(z+h)^2}} \right\} \mathrm{d}h\,\mathrm{d}z$$

$$\qquad\qquad (2\text{-}5)$$

$$= \sum_{i=1}^{N_b} \sum_{k=1}^{m} \frac{q_{k-1}-q_k}{2\pi\lambda_s} G_{2i}(r_{i,j}, t_m - t_{k-1})$$

where i is the ith borehole in the boreholes field; k is the kth timestep; q_k is the heat load of each boreheole at timestep k; $r_{i,j}$ is the radial distance between borehole centre lines of ith boreheole and j^{th} boreheole, and $r_{i,j} = r_b$ when $i = j$; t_m is the time at timestep m.
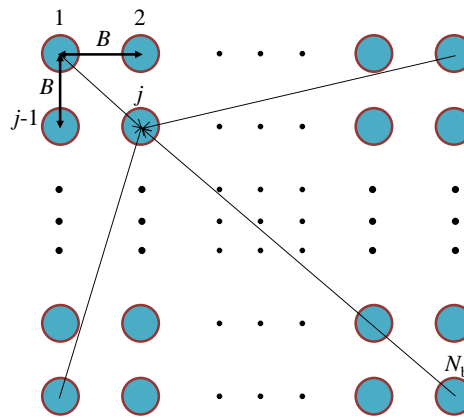
Figure 2.3: A square boreholes field consisting N_b boreholes and the spatial superposition principle

Equation (2-5) shows that the calculation of one borehole wall temperature can be costly due to its double integration form, the large number of boreholes N_b, and the large number of timesteps m. The calculation load of the GHE needs to be multiplied by a factor of N_b because this calculation needs to be performed for each borehole, which brings a huge difficulty to model the GHE in the DBES tools. Thus, a global model is presented in the following section to solve this problem.

2.3. Global model for fast calculation of thermal response factor

2.3.1. *Case description*

To illustrate the proposed model, a case study is introduced in Table 2-1, assuming that the ground is siliceous rock; its thermophysical properties and undisturbed temperature are taken from (Wang et al., 2019a). The default duration of one timestep is 1 hour, but it can be changed as needed.

Table 2-1   ***Main parameters of the case study***

Component	Parameter	Value	Unit
GHE	Layout	26×26	–
	Number of total boreholes N_b	676	–
	Borehole spacing B	4	m
	Borehole length H	133	m
	Radius for the borehole r_b	0.11	m
Ground	Ground thermal conductivity λ_s	2.635	W/m.K
	Ground thermal diffusivity α_s	1.23×10^{-6}	m^2/s
	Undisturbed ground temperature T_0	19	°C
Building load	Heat flux q	50	W/m

2.3.2. *Three-points method*

In Zeng et al.'s study (Zeng et al., 2002), they indicated that the middle point ($z = 0.5H$) temperature and the integral mean temperature could be two representative borehole wall temperatures. The middle point is mostly chosen because it can reduce the double integration equation to a single integration equation; this is called the middle point method in this chapter. Using the middle point temperature as the borehole wall temperature, the borehole wall temperature T_b of a borehole at time t under the effect of the other borehole located at radial distance r with constant heat load q is given by:

$$T_b(r,t) - T_0 = \frac{-q}{2\pi\lambda_s}$$

$$\cdot \frac{1}{2} \int_0^H \left\{ \frac{\text{erfc}\left(\frac{\sqrt{(r)^2 + \left(\frac{H}{2} - h\right)^2}}{2\sqrt{\alpha_s t}} \right)}{\sqrt{(r)^2 + \left(\frac{H}{2} - h\right)^2}} - \frac{\text{erfc}\left(\frac{\sqrt{(r)^2 + \left(\frac{H}{2} + h\right)^2}}{2\sqrt{\alpha_s t}} \right)}{\sqrt{(r)^2 + \left(\frac{H}{2} + h\right)^2}} \right\} dh \qquad \textbf{(2-6)}$$

$$= \frac{-q}{2\pi\lambda_s} G_m(r,t)$$

where $G_m(r,t)$ is the thermal response factor of a borehole wall temperature under the other borehole's effect using the middle point method.

However, we found that the difference between these two representative temperatures can be non negligible. For two typical boreholes with parameters in Table 2-1, the considered borehole wall absolute temperature differences between using the middle point method and the double integration method under the effect of the other borehole at different radial distances and times are shown in Figure 2.4 (a). For the self-effect of the borehole ($r = r_b = 0.11$ m), the absolute temperature difference is over 0.23 °C at $t = 1$ year. It increases with time and can reach over 1.0 °C when after 25 years; the corresponding relative difference of the thermal response factor is larger than 6 %, as shown in Figure 2.4 (b). For a certain t, although the relative difference of the thermal response factor becomes larger when the radial distance r increases, the borehole wall absolute temperature difference decreases, because the absolute value becomes smaller. For $t = 25$ years, the borehole wall absolute temperature differences are larger than 0.7 °C, within a radial distance of 10 m, meaning the borehole wall temperature is not accurately evaluated by using the middle point method.
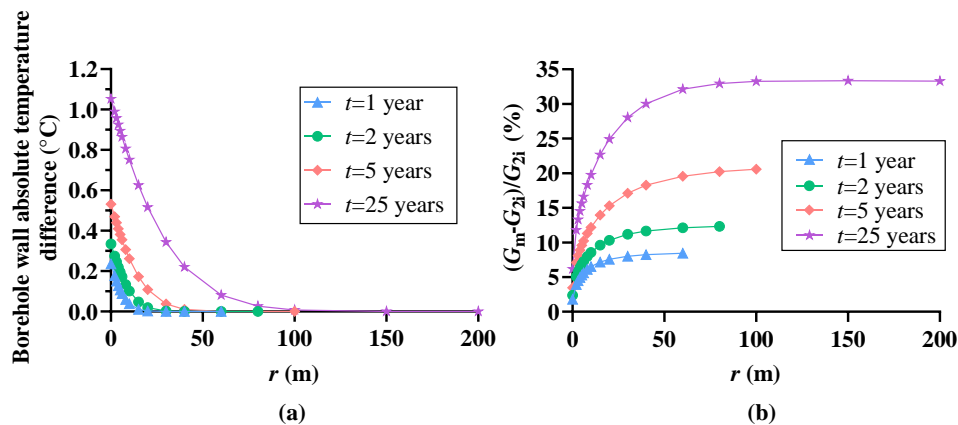
Figure 2.4: (a) Borehole wall absolute temperature difference and (b) relative difference of the thermal response factor between using the middle point method and the double integration method under the effect of another borehole located at radial distance r

The borehole wall temperature evolution under the self-effect with depth at different times is shown in Figure 2.5 (a). The borehole wall temperature tends to remain constant around the middle. However, it varies sharply at the top and bottom of the borehole due to the finite length of the borehole. Only using the middle point temperature cannot represent the borehole wall temperature, especially when time is long (beyond 1 year), because it does not consider the top and bottom parts. If the integral mean temperature is used, the single integration will become double integration, see equation (2-2), in the calculation, which will sharply increase the computational time. Thus, a method that gives a good calculation accuracy and keeps the single integration form is needed.

In the proposed method, three typical points (P_{top}, P_{middle} and P_{bottom}) are chosen instead of only one middle point, as shown in Figure 2.5 (b), and the average temperature of these three points is used to represent the borehole wall temperature. The three points are the middle point and two points symmetrical to the middle point located in the top and bottom areas, so the effects of the borehole top, middle and bottom can be all taken into consideration. This method is called the three-points method for the borehole wall temperature calculation in this chapter.
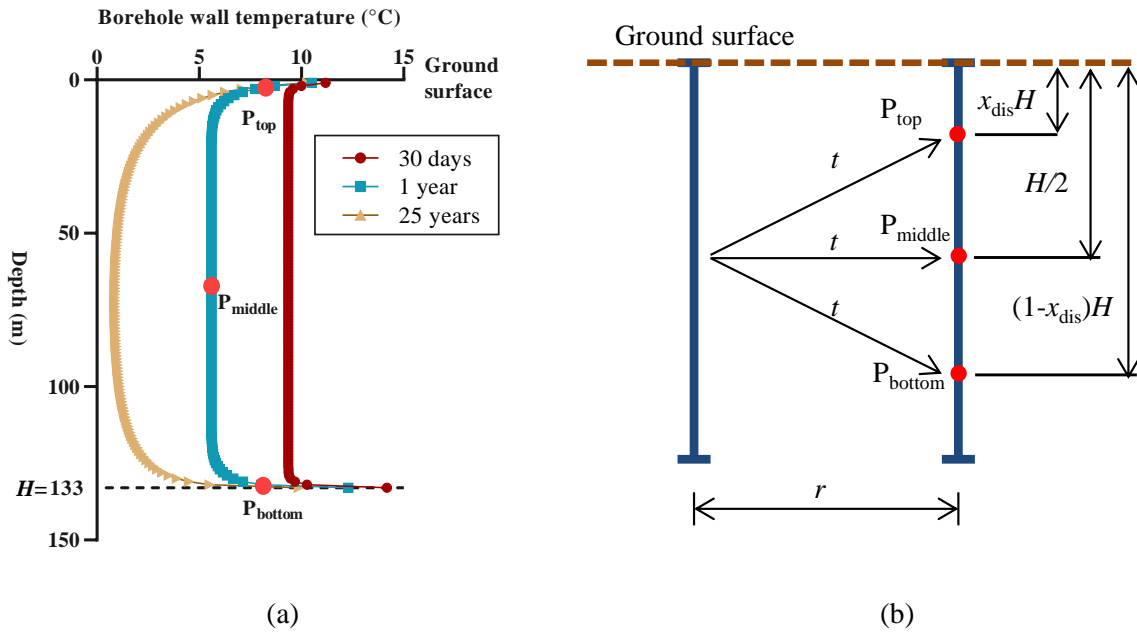
Figure 2.5: (a) Borehole wall temperature evolution under the self-effect with depth at different times (b) the three-points method to calculate a borehole wall temperature under the other's effect

The top and bottom points are located at H_{top} and H_{bottom} respectively. Although the borehole wall temperature T_b at time t under the effect of another borehole at radial distance r varies with depth, assuming a constant heat load q is a necessary approximation to apply the FLS model. This leads to the following equation:

$$T_b(r,t) - T_0 = \frac{-q}{2\pi\lambda_s} \cdot \frac{1}{3}\{G(r,t,H_{top}) + G(r,t,H/2) + G(r,t,H_{bottom})\} = \frac{-q}{2\pi\lambda_s} G_{3p}(r,t) \qquad \textbf{(2-7)}$$

where $H_{\text{top}} = x_{\text{dis}}H$, $H_{\text{bottom}} = (1 - x_{\text{dis}})H$; x_{dis} is the location factor of the top point; and $G_{3\text{p}}(r,t)$ is the thermal response factor of a borehole wall temperature under the other borehole's effect using the three points method.

In order to apply this method, it is essential to determine the location factor x_{dis}. Firstly, we identified the optimal x_{dis} for different radial distances r (0.11 m to 200 m), time t (30 minutes to 25 years) and borehole depth H (20 m to 200 m). Then we assumed that x_{dis} is an exponential function of these three parameters:

$$x_{\text{dis}} = \max\left(a_1 + a_2\left(1 - e^{(-a_3 \cdot t)}\right) + a_4\left(1 - e^{(-a_5 \cdot r)}\right) + a_6\left(1 - e^{\left(-\frac{H-a_7}{a_7}\right)}\right), a_8\right) \tag{2-8}$$

The coefficients a_1 to a_8 were finally obtained by using an exponential regression method ($a_1 = 0.0459$, $a_2 = 0.0605$, $a_3 = 2.08 \times 10^{-8}$, $a_4 = 0.0431$, $a_5 = 0.0725$, $a_6 = -0.035$, $a_7 = 133$). Moreover, x_{dis} was constrained to a minimum ($a_8 = 0.052$).

Using the three-points method and considering the superposition method, $T_{\text{b},j}(m)$ is given by:

$$T_{\text{b},j}(m) - T_0 = \sum_{i=1}^{N_{\text{b}}} \sum_{k=1}^{m} \frac{q_{k-1} - q_k}{2\pi\lambda_{\text{s}}}$$
$$\cdot \frac{1}{3}\{G(r_{i,j}, t_m - t_{k-1}, x_{\text{dis}}H) + G(r_{i,j}, t_m - t_{k-1}, H/2) + G(r_{i,j}, t_m$$
$$- t_{k-1}, (1 - x_{\text{dis}})H)\} \tag{2-9}$$

$$= \sum_{k=1}^{m} \frac{q_{k-1} - q_k}{2\pi\lambda_{\text{s}}} \sum_{i=1}^{N_{\text{b}}} G_{3\text{p}}(r_{i,j}, t_m - t_{k-1})$$

2.3.3. *Distance category simplification*

For a borehole in a square field of N_{b} boreholes at a certain timestep as shown in Figure 2.3, the interactions with other boreholes are calculated based on the radial distance. This requires N_{b} evaluations of $G_{3\text{p}}$, as shown in equation (2-9). If it is used to calculate the outlet fluid temperature of the GHE at a certain timestep, $G_{3\text{p}}$ will be calculated $N_{\text{b}} \times N_{\text{b}}$ times. However the calculation of $G_{3\text{p}}$ at a certain timestep is only a function of the radial distance $r_{i,j}$ between boreholes i and j. Identical radial distances will bring unnecessary repetition of calculation of $G_{3\text{p}}$: for the same $r_{i,j}$, $G_{3\text{p}}$ only needs to be calculate once.

Thus, the idea of distance category simplification is to identify all the possibilities of $r_{i,j}$ (entitled distance category in the following, each distance category corresponds to a specific radial distance), and calculate the corresponding $G_{3\text{p}}$. Then, in order to calculate each borehole's wall temperature, only the number of times each distance category occurs needs to be identified (that is the number of times other boreholes located at the radial distance from the considered borehole are found); afterwards the accumulation needs to be performed to determine $G_{3\text{p}}$ for each distance category. For a square field of N_{b} boreholes, there exist N_{d} radial distance possibilities in total. The number of times $G_{3\text{p}}$ evaluated is

reduced by a factor $\frac{N_b \times N_b}{N_d}$, which is a significant calculation time reduction. A similar idea is also found in other references e.g. (Claesson and Javed, 2011).

An example of a square 3×3 boreholes field is shown in Figure 2.6. There exist 5 radial distance possibilities between a pair of boreholes: B, $\sqrt{2}B$, $2B$, $\sqrt{5}B$ and $\sqrt{8}B$. Considering the radial distances between borehole 1 and the other boreholes, B occurs twice: from 1 to 2 and from 1 to 3; $\sqrt{2}B$ occurs once: from 1 to 5; $2B$ occurs twice: from 1 to 3 and from 1 to 7; $\sqrt{5}B$ occurs twice: from 1 to 6 and from 1to 8; $\sqrt{8}B$ occurs once: from 1 to 9. Combining the self-effect, the borehole wall temperature of borehole 1 under all boreholes' effects at timestep m is given by:

$$
\begin{aligned}
T_{b,1}(m) - T_0 = \sum_{k=1}^{m} \frac{q_{k-1} - q_k}{2\pi\lambda_s} &(G_{3p}(r_b, t_m - t_{k-1}) + 2 \cdot G_{3p}(B, t_m - t_{k-1}) \\
&+ G_{3p}(\sqrt{2}B, t_m - t_{k-1}) + 2 \cdot G_{3p}(2B, t_m - t_{k-1}) \\
&+ 2 \cdot G_{3p}(\sqrt{5}B, t_m - t_{k-1}) + G_{3p}(\sqrt{8}B, t_m - t_{k-1}))
\end{aligned}
\tag{2-10}
$$

Similarly, other boreholes' temperatures can be derived from the number of times each radial distance occurs.
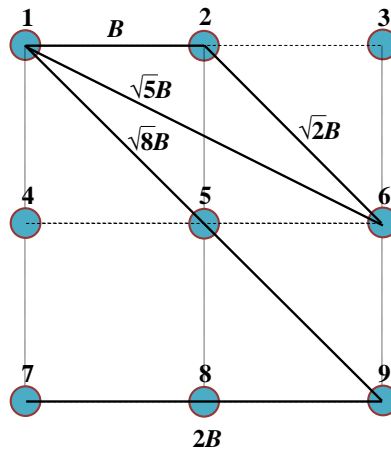
Figure 2.6: Radial distance possibilities between boreholes in a square 3×3 boreholes field

For a square field, the radial distances between borehole 1 and the other boreholes contain all possible radial distances between any pair of boreholes in the field. The first step of this distance category simplification method is to calculate $r_{1,j}$ from $j = 1$ to $j = N_b$, and identify and sort them into N_d categories of increasing radial distances. Then for the calculated borehole j, all the boreholes in the field can be converted to N_d categories, as shown in Figure 2.7, where r_n is the radial distance of the nth distance category, $N_{j,n}$ is the number of times the distance category n occurs for borehole j. The next step is to count $N_{j,n}$ from $j = 1$ to $j = N_b$ and from $n = 1$ to $n = N_d$.
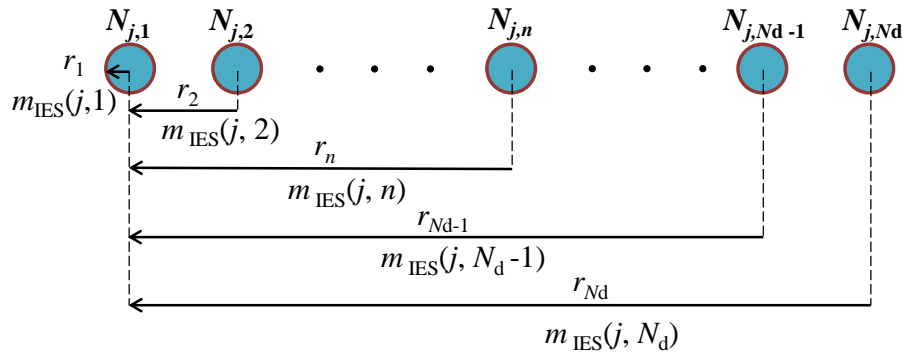
Figure 2.7: Borehole field converted to distance categories from borehole j

By knowing all $N_{j,n}$, equation (2-9) can be converted to:

$$
\begin{aligned}
T_{\mathrm{b},j}(m) - T_0 &= \sum_{k=1}^{m} \frac{q_{k-1} - q_k}{2\pi\lambda_{\mathrm{s}}} \sum_{n=1}^{N_{\mathrm{d}}} N_{j,n} \cdot G_{3\mathrm{p}}(r_n, t_m - t_{k-1}) \\
&= \sum_{k=1}^{m} \frac{q_{k-1} - q_k}{2\pi\lambda_{\mathrm{s}}} G_{3\mathrm{p,borehole}}(j, t_m - t_{k-1})
\end{aligned}
$$

(2-11)

where $G_{3\mathrm{p,borehole}}(j, t_m - t_{k-1})$ is the thermal response factor of jth borehole's wall temperature under all boreholes' effects at time $t_m - t_{k-1}$ using the three-points method.

2.3.4.   *Thermal response factor of GHE*

The thermal response factor of the whole GHE at time t_m using the three-points method is given by:

$$
G_{3\mathrm{p,GHE}}(t_m) = \sum_{j=1}^{N_{\mathrm{b}}} G_{3\mathrm{p,borehole}}(j, t_m)
$$

(2-12)

Similarly, the thermal response factors of the jth borehole's wall temperature under all boreholes' effects and the whole GHE at time t_m using the middle point method and double integration method are:

$$
G_{\mathrm{m,borehole}}(j, t_m) = \sum_{n=1}^{N_{\mathrm{d}}} N_{j,n} \cdot G_{\mathrm{m}}(r_n, t_m)
$$

(2-13)

$$
G_{2\mathrm{i,borehole}}(j, t_m) = \sum_{n=1}^{N_{\mathrm{d}}} N_{j,n} \cdot G_{2\mathrm{i}}(r_n, t_m)
$$

(2-14)

$$
G_{\mathrm{m,GHE}}(t_m) = \sum_{j=1}^{N_{\mathrm{b}}} G_{\mathrm{m,borehole}}(j, t_m)
$$

(2-15)

$$G_{2i,\text{GHE}}(t_m) = \sum_{j=1}^{N_b} G_{2i,\text{borehole}}(j, t_m) \qquad \textbf{(2-16)}$$

2.3.5. *Initial effect simplification*

The next step is to consider how to simplify the calculation of G_{3p} for numerous timesteps. The evolution of G_{3p} with time is presented in Figure 2.8 for different radial distances during one year. There are two potential methods to reduce the computational complexity: the initial effect simplification (IES) and the time averaging simplification (TAS).
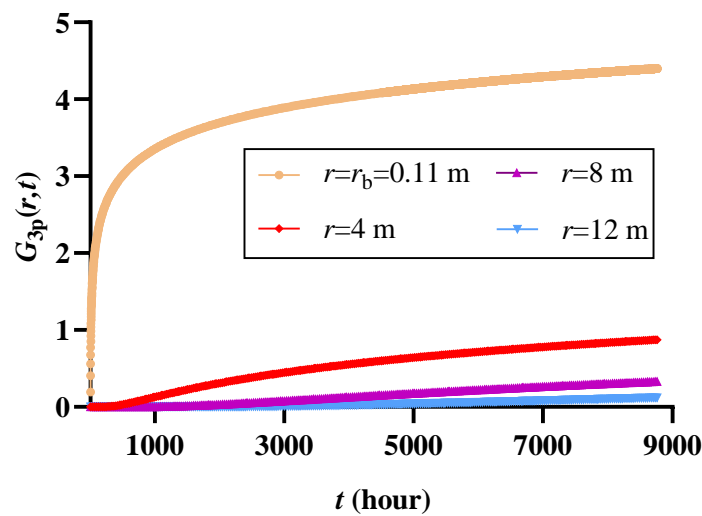
Figure 2.8: G_{3p} vs t for different r

According to Figure 2.8, at a certain time, t, the larger r is the smaller G_{3p} is. This means that for one borehole, the closer the other boreholes, the larger influence they have. Before $t = 500$ h, G_{3p} is nearly 0 when r equals to 4 m, 8 m and 12 m. Only the borehole itself ($r = r_b = 0.11$ m) has an effect on its wall temperature. That is to say the effects of other boreholes do not reach the considered borehole wall before this time. The further the other borehole, the later it starts to affect the considered borehole. The G_{3p} calculations concerning all the other boreholes are not necessary because they are negligible. As time goes on, more and more boreholes need to be taken into consideration.

For a field converted to distance categories as presented above, other boreholes located at distance category n start to have a non-negligible effect on borehole j from timestep $m_{\text{IES}}(j,n)$ onwards. $m_{\text{IES}}(j,n)$ is the first timestep that fulfils the following condition:

$$\frac{\sum_{i=1}^{n} N_{j,i} \cdot G_{3p}(r_i, t_{m_{\text{IES}}(j,n)})}{\sum_{i=1}^{N_d} N_{j,i} \cdot G_{3p}(r_i, t_{m_{\text{IES}}(j,n)})} < 1 - \varepsilon_{\text{IES}} \qquad \textbf{(2-17)}$$

where ε_{IES} is the tolerance of the initial effect simplification method, which is set at 0.5 % in this chapter. For borehole j, before timestep $m_{\text{IES}}(j,n)$, the effects of distance categories 1 to n - 1 contribute to over 1 - ε_{IES} (99.5 %) of the total effect of all distance categories. Figure 2.7 illustrates how the initial effect simplification fits into distance categories.

For different boreholes, $m_{\text{IES}}(j,n)$ is different due to the different distance category distribution. In order to simplify the calculations, the minimal $m_{\text{IES}}(j,n)$ among all boreholes is chosen to represent the m_{IES} for distance category n (this conservative approach ensures that the tolerance is respected for all boreholes):

$$m_{\text{IES}}(n) = \min_{1 \leq j \leq N_{\text{b}}} m_{\text{IES}}(j,n) \tag{2-18}$$

In fact, only approximately 1/8 of the total boreholes (in total $N_{\text{b,sym}}$) need to be considered due to the symmetry of the squared field, as shown in Figure 2.9. Equation (2-18) can then be converted to:

$$m_{\text{IES}}(n) = \min_{1 \leq j \leq N_{\text{b,sym}}} m_{\text{IES}}(j,n) \tag{2-19}$$
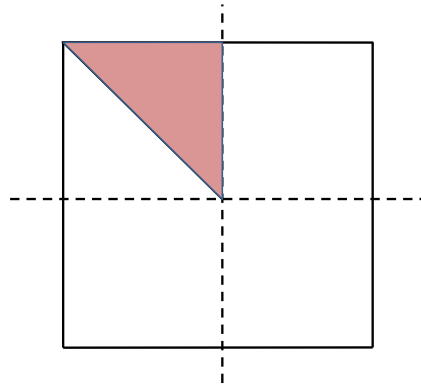
Figure 2.9: Calculated part (in red) of a square borehole filed after symmetry simplification

Before this timestep $G_{3\text{p}}(r_n,t)$ is negligible, and is therefore set at 0. This method is entitled initial effect simplification method and it can be expressed in the following equation:

$$G_{3\text{p}}(r_n, t) = \begin{cases} 0 & \text{if } t < t_{m_{\text{IES}}(n)} \\ G_{3\text{p}}(r_n, t) & \text{if } t \gg t_{m_{\text{IES}}(n)} \end{cases} \tag{2-20}$$

where $t_{m_{\text{IES}}(n)}$ is the time at timestep $m_{\text{IES}}(n)$.

It should be noted that the determination of m_{IES} requires knowing the values of $G_{3\text{p}}$, which is contrary to our goal to calculate $G_{3\text{p}}$. This problem will be solved by the simplified method to determine m_{IES} presented in section 2.3.7.

2.3.6. *Time averaging simplification*

Figure 2.8 shows that $G_{3\text{p}}$ increases sharply in the beginning and tends to stay stable as time goes. It can be inferred that the closer to the beginning of the operation, the more detailed calculation is

needed. Therefore, it is possible to divide the whole timespan into several periods (called averaging periods). In each averaging period, G_{3p} only needs to be calculated once every certain number of steps (called averaging ranges), because its variation for a specific radial distance during that time is negligible. For an averaging period p, its corresponding averaging range is l_p. The whole timespan is divided into p_{max} averaging periods. For example, the time averaging simplification of G_{3p} at the radius of a borehole during one year is shown in Figure 2.10. This method is named the time averaging simplification method.
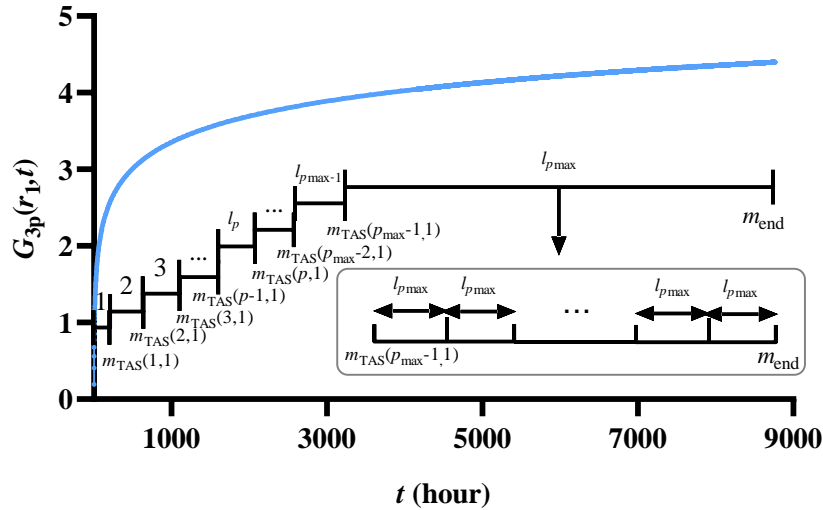
Figure 2.10: Time averaging simplification method at radial distance r_1

In averaging period 1 ($p = 1$), G_{3p} is calculated at each timestep ($l_1 = 1$); in averaging period 2 ($p = 2$), the averaging range l_2 is 2, is calculated every 2 timesteps; in the last averaging period (averaging period p_{max}), the curve slope is small, so G_{3p} only needs to be calculate every $l_{p_{max}}$ timesteps. In this study, the correspondence between p and l_p is set as shown in Figure 2.11.
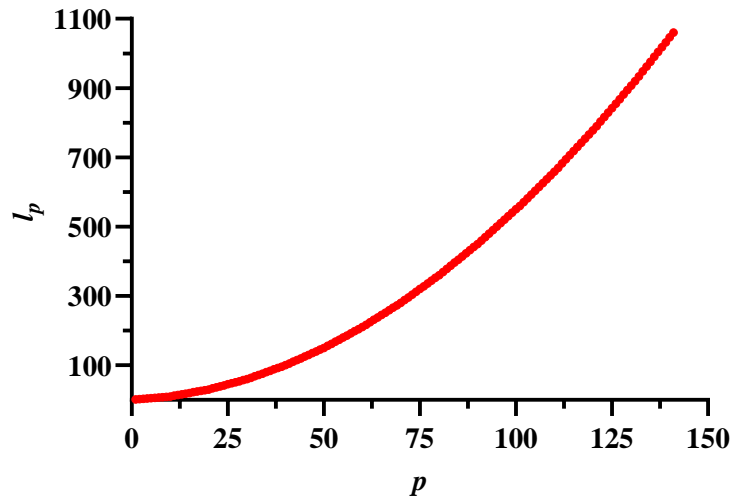
Figure 2.11: Correspondence between p and l$_p$

$m_{\text{TAS}}(p,n)$ is the timestep at the end of averaging period p for the nth distance category. It is determined by the following three steps:

1. Based on the distance category itself, G_{3p} is used to determine $m_{\text{TAS,dc}}(p,n)$ which is the first timestep that fulfils the following condition:

$$\frac{G_{3p}\left(r_n, t_{m_{\text{TAS,dc}}(p,n)+l_p}\right) - G_{3p}\left(r_n, t_{m_{\text{TAS,dc}}(p,n)}\right)}{\left(G_{3p}\left(r_n, t_{m_{\text{TAS,dc}}(p,n)+l_p}\right) + G_{3p}\left(r_n, t_{m_{\text{TAS,dc}}(p,n)}\right)\right)/2} < \varepsilon_{\text{TAS}} \tag{2-21}$$

where ε_{TAS} is the tolerance of the time averaging simplification method, which is set at 0.5 % in this study.

Equation (2-21) indicates that unlike $m_{\text{IES}}(j,n)$ that depends on the position of the borehole, $m_{\text{TAS,dc}}(p,n)$ is not related to $N_{j,n}$, thus it only needs to be applied to the first borehole which includes all the distance categories.

2. Based on the total effects of all distance categories for one borehole, $G_{3p,\text{borehole}}$ is used to determine $m_{\text{TAS,bh}}(p,j)$ which is the first timestep that fulfils the following condition:

$$\frac{G_{3p,\text{borehole}}\left(j, t_{m_{\text{TAS,bh}}(p,j)+l_p}\right) - G_{3p,\text{borehole}}\left(j, t_{m_{\text{TAS,bh}}(p,j)}\right)}{\left(G_{3p,\text{borehole}}\left(j, t_{m_{\text{TAS,bh}}(p,j)+l_p}\right) + G_{3p,\text{borehole}}\left(j, t_{m_{\text{TAS,bh}}(p,j)}\right)\right)/2} < \varepsilon_{\text{TAS}} \tag{2-22}$$

Using the symmetry of the square field, the maximal $m_{\text{TAS,bh}}(p,j)$ among all $N_{\text{b,sym}}$ boreholes is chosen to represent m_{TAS} for distance category n:

$$m_{\text{TAS,bh}}(p,n) = \max_{1 \le j \le N_{\text{b,sym}}} m_{\text{TAS,bh}}(p,j) ; n = 1, 2, 3, \dots, N_{\text{d}} \tag{2-23}$$

3. $m_{\text{TAS}}(p,n)$ is the smallest value between $m_{\text{TAS,dc}}(p,n)$ and $m_{\text{TAS,bh}}(p,n)$, as shown below:

$$m_{\text{TAS}}(p,n) = \min\left(m_{\text{TAS,dc}}(p,n), m_{\text{TAS,bh}}(p,n)\right) \tag{2-24}$$

Similar to m_{IES}, the determination of m_{TAS} also requires knowing the values of G_{3p}. The flowing section 2.3.7 illustrates how to solve this problem.

2.3.7. *Two-dimensional heat equation*

Based on these two simplification methods, G_{3p} does not need to be calculated for each distance category at each timestep. The computation time can be drastically saved. If we want to use the two simplification methods above, the timesteps for simplification (m_{TAS} and m_{IES}) have to be determined before the calculation of G_{3p}. Using equation (2-17), (2-21) and (2-22) to calculate m_{TAS} and m_{IES} requires to firstly calculate G_{3p}, which is contrary to our aim. Therefore, another method is needed to replace G_{3p} in these equations to identify m_{TAS} and m_{IES}.

The 2D heat equation describes how the distribution of heat evolves over time in a solid medium in two dimensions. Considering the axial symmetry, the temperature variation at radial distance r and at time t from uniform initial conditions under a line heat source input at $r = 0$ and $t = 0$ (also called Dirac delta function) is given by (Wang et al., 2007):

$$\theta_{\text{he}}(r, t) = \frac{\exp\left(-\frac{r^2}{4\alpha_s t}\right)}{4\alpha_s \pi t} \tag{2-25}$$

Equation (2-25) gives the heat propagation under an infinite line source of Dirac delta function, with a simple mathematic form. It represents the theoretical heat propagation speed. Although in this study the borehole is regarded as a finite line source under a step-wise heating load, it can reasonably be represented by equation (2-25) which in reality, is a conservative approach.

The heat propagation of Dirac delta distribution under different times and radial distances is shown in Figure 2.12. It takes a certain time for the heat to propagate to a certain radial distance, which is similar to the heat transfer process from a borehole to the other in this study. Accounting for the similarity, the simplicity and the conservativeness, it is possible to use θ_{he} calculated by the 2D heat equation instead of G_{3p} in equation (2-17), (2-21) and (2-22) to evaluate m_{TAS} and m_{IES}.

As abovementioned, the heat transfer process of a borehole is under a constant heat flux q during each timestep. Using the 2D heat equation, the wall temperature variation of borehole j considering all the effects of the boreholes (each borehole under a line heat source of a constant initial unit of heat flux) located at distance category n and timestep m can be calculated by:

$$\theta_{\text{he},j}(r_n, m) = \sum_{k=1}^{m} \frac{\exp\left(-\frac{r_n^2}{4t_k \alpha_s}\right)}{4\alpha_s \pi t_k} \cdot N_{j,n} \tag{2-26}$$

Combining equation (2-17) with equation (2-26), $m_{\text{IES}}(j,n)$ is the first timestep that satisfies the following condition:

$$\frac{\sum_{i=1}^{n} \theta_{\text{he},j}(r_i, m_{\text{IES}}(j,n))}{\sum_{i=1}^{N_d} \theta_{\text{he},j}(r_i, m_{\text{IES}}(j,n))} < 1 - \varepsilon_{\text{IES}} \tag{2-27}$$
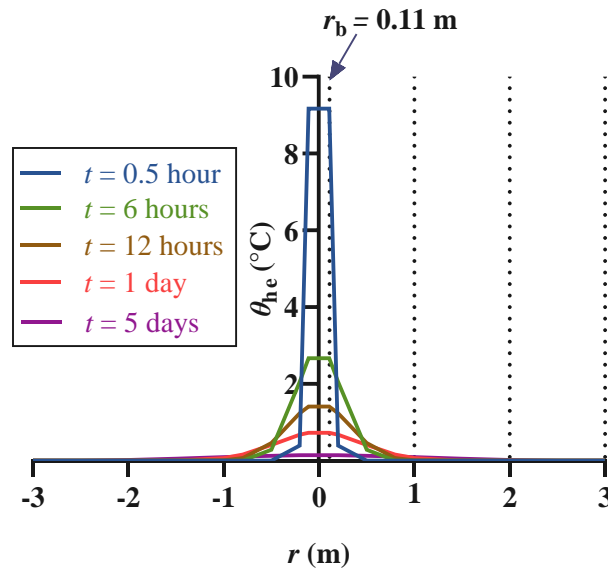
Figure 2.12: Heat propagation calculated by the 2D heat equation

Then $m_{\text{IES}}(n)$ can be determined by equation (2-19).

As explained in the time averaging simplification method, $m_{\text{TAS}}(p,n)$ is determined by the following steps:

1. *Determine $m_{TAS,dc}(p,n)$ by:*

$$\frac{\theta_{\text{he},1}\left(r_n, t_{m_{\text{TAS,dc}}(p,n)+l_p}\right) - \theta_{\text{he},1}\left(r_n, t_{m_{\text{TAS,dc}}(p,n)}\right)}{\left(\theta_{\text{he},1}\left(r_n, t_{m_{\text{TAS,dc}}(p,n)+l_p}\right) + \theta_{\text{he},1}\left(r_n, t_{m_{\text{TAS,dc}}(p,n)}\right)\right)/2} < \varepsilon_{\text{TAS}} \qquad \textbf{(2-28)}$$

2. *Determine $m_{TAS,bh}(p,n)$ by equation (2-23) and the following equation :*

$$\frac{\sum_{j=1}^{N_{\text{d}}} \theta_{\text{he},j}\left(r_n, t_{m_{\text{TAS,bh}}(p,n)+l_p}\right) - \sum_{j=1}^{N_{\text{d}}} \theta_{\text{he},j}\left(r_n, t_{m_{\text{TAS,bh}}(p,n)}\right)}{(\sum_{j=1}^{N_{\text{d}}} \theta_{\text{he},j}\left(r_n, t_{m_{\text{TAS,bh}}(p,n)+l_p}\right) + \sum_{j=1}^{N_{\text{d}}} \theta_{\text{he},j}\left(r_n, t_{m_{\text{TAS,bh}}(p,n)}\right))/2} < \varepsilon_{\text{TAS}} \qquad \textbf{(2-29)}$$

3. *Determine $m_{TAS}(p,n)$ by equation (2-24).*

Using m_{TAS} and m_{IES} calculated by equation (2-27), (2-28) and (2-29), $G_{3\text{p}}$ is calculated sooner and more often than needed, ensuring accuracy.

Equation (2-26) can be easily solved due to its simple mathematical form. Thus, the proposed method can quickly calculate m_{TAS} and m_{IES}, and afterwards the calculation time of $G_{3\text{p}}$ will be largely reduced.

2.3.8. *Summary of proposed model*

The fast calculation model for the thermal response factor of a large-scale boreholes GHE is shown in Figure 2.13. It contains four main steps:

1. *Convert the field into distance categories*

The N_d distance categories and their radial distances r_n (n varying from 1 to N_d) are identified from the position of borehole 1 (top left borehole). The number of times each distance category $N_{j,n}$ occurs is then evaluated for each borehole in the field.

2. *Calculate the 2D heat equation*

$\theta_{he,j}$ is calculated for each distance category and all timesteps by applying equation (2-26) to all boreholes.

3. *Determine the simplification timesteps m_{TAS} and m_{IES}*

According to the results of step 2, equations (2-19) and (2-27) are used to obtain $m_{IES}(n)$ for all N_n distance categories. Equations (2-24), (2-28) and (2-29) are used to obtain $m_{TAS}(p,n)$ for each averaging period p and each distance category n.

4. *Calculate the thermal response factor*

x_{dis} is firstly calculated by equation (2-8) to be used in the three-points method. Based on the results of step 3, G_{3p}, $G_{3p,borehole}$ and $G_{3p,GHE}$ are calculated by equations (2-9), (2-11) and (2-12), respectively, for all distance categories and all timesteps.
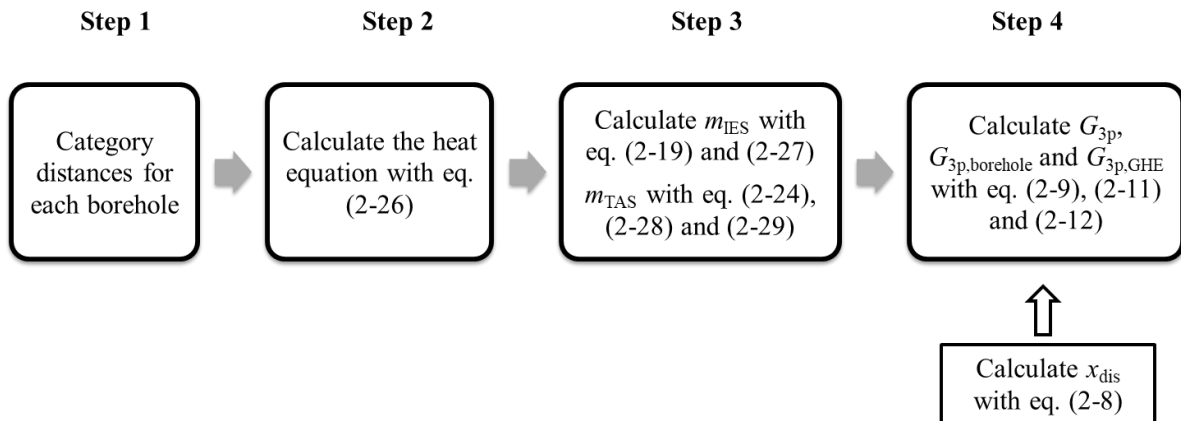
Figure 2.13: Flow chat of the global model for fast calculation of the thermal response factors

2.4. Results and discussion

2.4.1. *Three-points method accuracy*

The relative difference of the thermal response factor and the absolute temperature difference of the borehole wall between the three-points and the double integration methods for different times t and radial distances r are shown in Figure 2.14 (short term) and Figure 2.15 (long term). The relative difference is maintained under 4.7 %, instead of 34 % for the middle point method. For short periods, considering the self-effect ($r = r_b = 0.11$ m), the absolute temperature difference increases with time and the differences are all below 0.1 °C. Although the relative difference increases with r, the corresponding absolute temperature difference decreases, because the absolute value of G_{3p} decreases. For long periods, the absolute temperature difference decreases with r, and remains all below 0.15 °C. The best accuracy is observed for 25 years. The relative difference is reduced to less than 0.3 % and the absolute temperature difference is smaller than 0.01 °C. This is a large improvement compared to the maximal relative difference (over 30 %) and the maximal absolute temperature difference (over 1 °C) of the middle point method. The proposed three-points method shows a good accuracy, both for short term and long term evaluation.
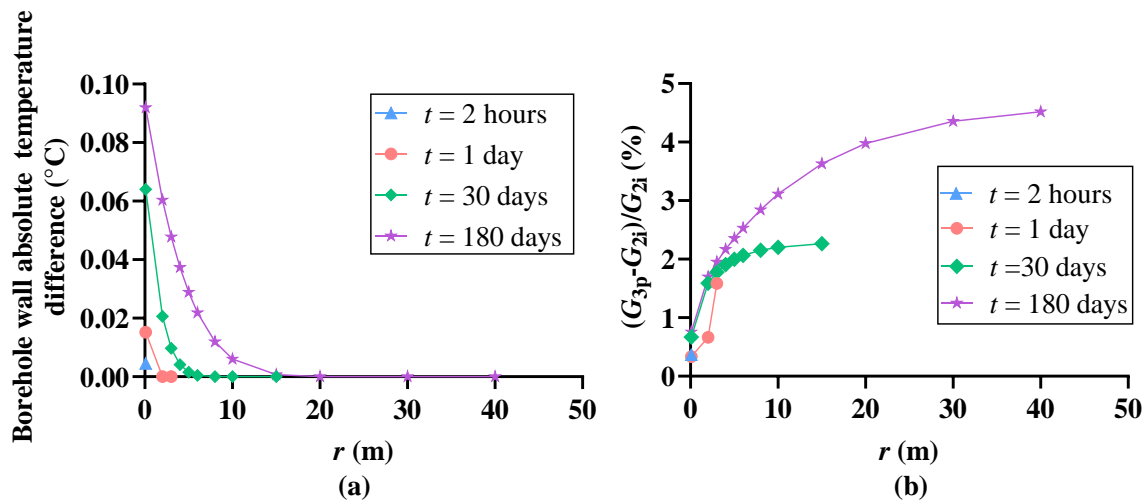
Figure 2.14: (a) Borehole wall absolute temperature difference and (b)relative difference of the thermal response factor between the three-points method and the double integration method for short periods (under 1 year)
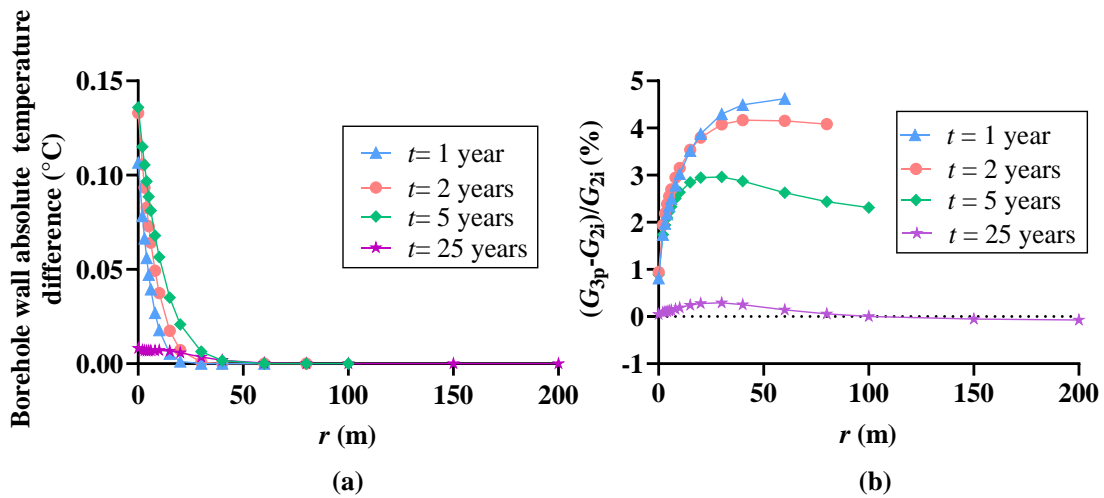
Figure 2.15: (a) Borehole wall absolute temperature difference and (b) relative difference of the thermal response factor between the three-points method and the double integration method for long periods (above 1 year)

2.4.2.   *Case study*

In order to deal with the long-time operation of 20 years, one year in this chapter contains 8 766 hours (($365 \times 3 + 366$) $\times$ 24 / 4), considering the leap year. The total number of timesteps is 175 320. The 676 boreholes contribute to 294 distance categories as shown in Figure 2.16. Distance category 1 has the smallest radial distance $r = r_b = 0.11$ m, and the largest radial distance r_{294} is between the first and last borehole (the diagonal of the square field) which equals to $\sqrt{(25B)^2 + (25B)^2} = 141.42$ m. Then $N_{j,n}$ is evaluated for all N_b boreholes.
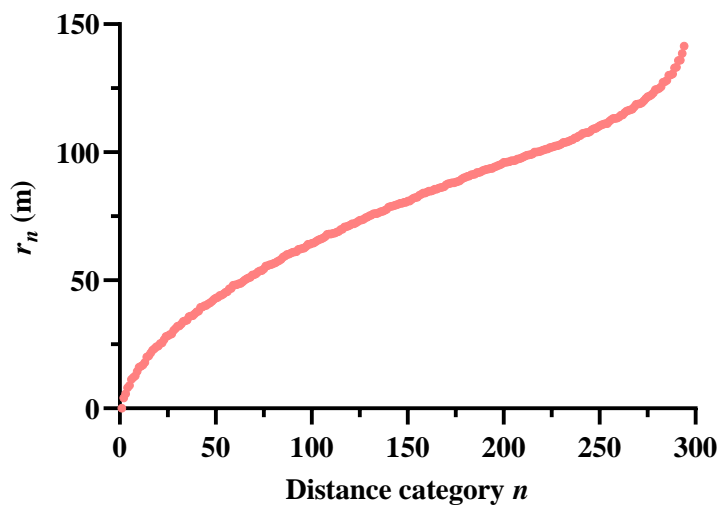
Figure 2.16: Distance categories and their radial distances

Four representative boreholes are chosen: top left corner borehole (borehole 1), top right corner borehole (borehole 13), bottom right corner borehole (borehole 325) and centre borehole (borehole 163) of the left top 1/4 field, as presented in Figure 2.17. The numbers of boreholes at different radial distance for these four boreholes are shown in Figure 2.18.
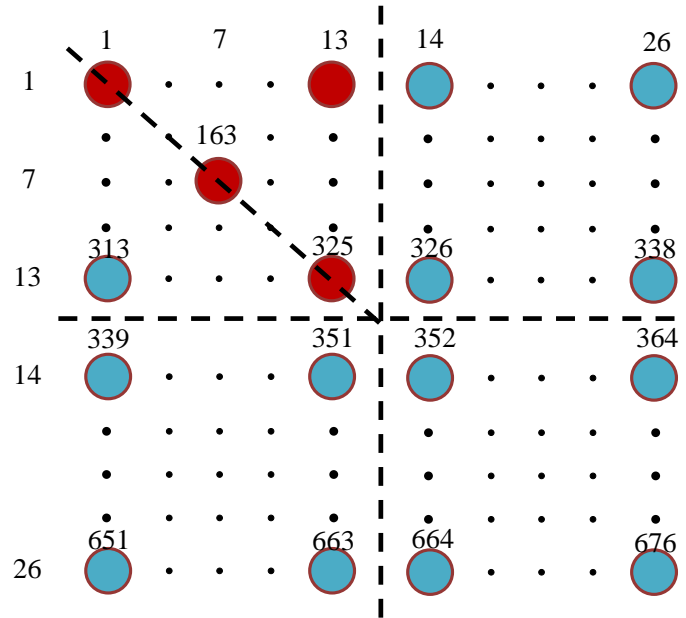
Figure 2.17: Four representative boreholes in the 26 × 26 square boreholes field
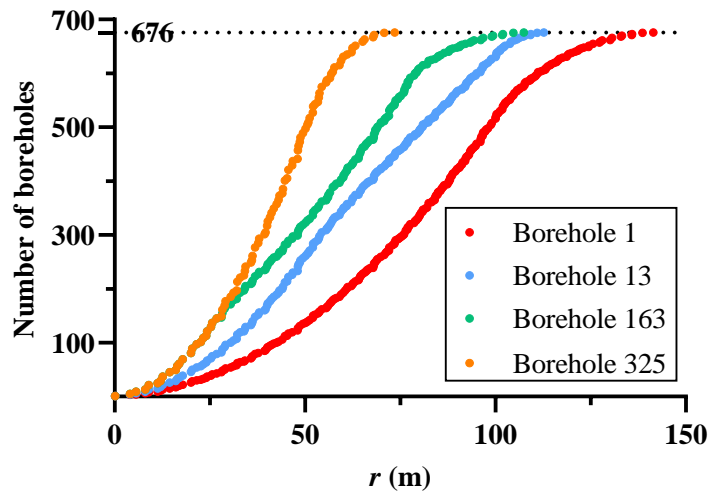
Figure 2.18: Number distribution of boreholes at a certain radial distance for borehole 1, 13, 163 and 325

m_{IES} for each distance category is calculated and shown in Figure 2.19. It can be inferred that distance category 1 starts to have an effect from the first timestep. m_{IES} increases with the radial

distance. When distance category is 210 (r_{210} = 98.06 m), m_{IES} is 174 809, which means that the effect of the boreholes at distance category 210 only need to be considered from timestep 174 809 onwards. It should be noted that the total number of timesteps for 20 years is 175 320; all the boreholes at distance categories from 211 to the last distance category 294 have negligible effects on the calculated borehole, so the thermal response factor of this part does not need to be evaluated, and calculation time can be massively saved.
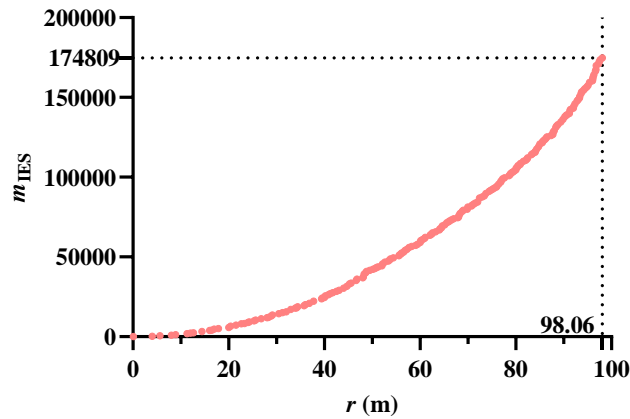
Figure 2.19: m_{IES} of different radial distances for 20 years operation

Figure 2.20 shows m_{TAS} for different distance categories. For r_1, from timestep 1 to $m_{TAS}(1,1) = 53$, G_{3p} is calculated every timestep; from timestep $m_{TAS}(1,1) + 1 = 54$ to $m_{TAS}(2,1) = 93$, G_{3p} is evaluated every 2 timesteps. From timestep $m_{TAS}(141,1) = 21\ 377$ to the last timestep 175 320, G_{3p} only needs to be determined every $l_p = 1\ 060$ timesteps (around 44 days). For a certain averaging range, m_{TAS} increases with the radial distance. For the largest distance category 294, the largest m_{TAS} is 172 955 for $p = 135$, and the corresponding l_p equals to 976. This means from timestep 172 955 to the last timestep 175 320, G_{3p} is calculated every 976 timesteps (around 40.6 days).
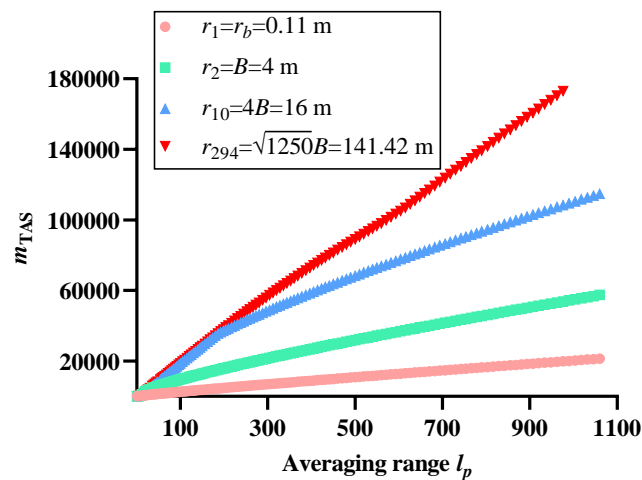
Figure 2.20: m_{TAS} of each averaging range at distance category 1, 2, 10 and 294

2.4.3. *Error analysis*

The three thermal response factors G_{3p}, $G_{3p,borehole}$ and $G_{3p,GHE}$ of the case study were compared to G_{2i}, $G_{2i,borehole}$ and $G_{2i,GHE}$. As abovementioned, G_{3p} gives the thermal response of one borehole wall caused by another borehole located at a certain radial distance at a certain time, $G_{3p,borehole}$ gives the thermal response of one borehole wall caused by all boreholes in the field at a certain time, and $G_{3p,GHE}$ gives the thermal response of the whole GHE at a certain time.

The absolute differences of the borehole wall temperature caused by G_{3p} and G_{2i} for distance categories 1, 2, 10, and 100 during 20 years of operation are shown in Figure 2.21 every 5 000 timesteps. The absolute differences are all under 0.15 °C, at the borehole radius ($r = r_{b} = 0.11$ m) during during 20 years of operation. The differences reduce with the radial distance. For $r = 4$ m, $r = 16$ m and $r = 64.5$ m, the absolute differences are smaller than 0.1 °C, 0.05 °C and 0.01 °C, respectively. Compared to the absolute temperature caused by the middle point method, as shown in Figure 2.4 (a), the three-points method shows a better accuracy for the calculation of the temperature response. The relative differences of $G_{3p,borehole}$ for borehole 1, 13, 163 and 325 are shown in Figure 2.22 every 500 timesteps. All relative differences are below 3 %, so it can be inferred that the proposed global model can give an accurate result for the temperature response of each borehole considering all the effects of the boreholes in the GHE field. Regarding the thermal response factor of the whole GHE, the relative differences every 500 timesteps are shown in Figure 2.23. The relative difference between $G_{m,GHE}$ and $G_{2i,GHE}$ reaches 23 %. However the relative difference of $G_{3p,GHE}$ is smaller than 3 %, indicating that the proposed model shows a better accuracy to predict the thermal response of the whole GHE as well.
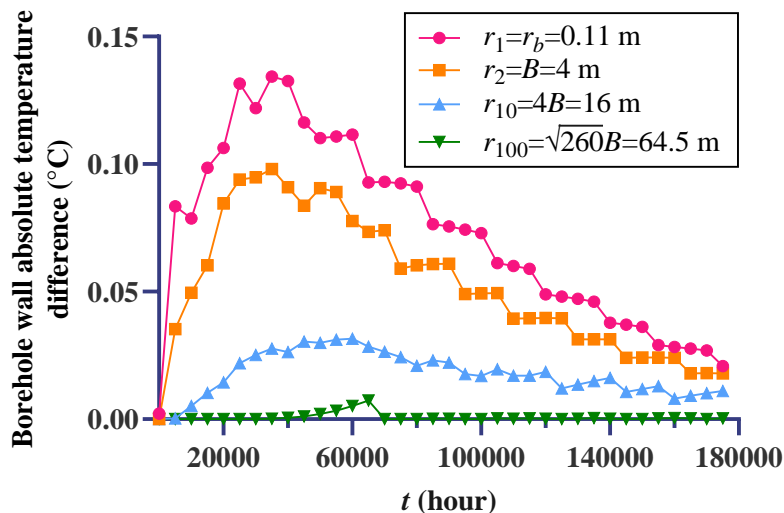
Figure 2.21: Absolute temperature differences of the borehole wall caused by G_{3p} and G_{2i} for distance category 1, 2, 10, and 100 during 20 years of operation
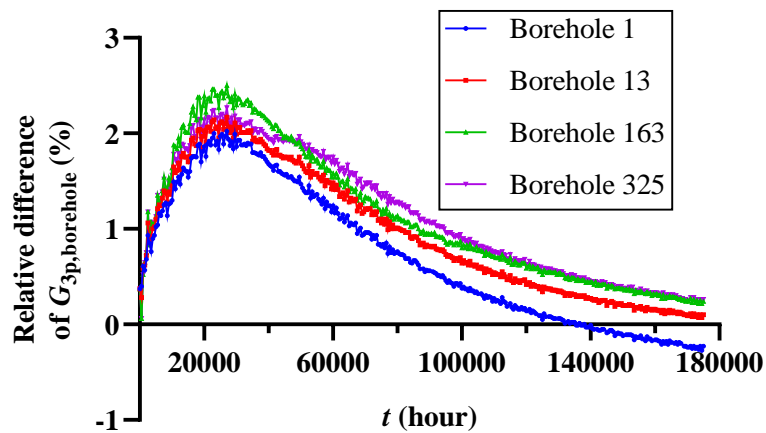
Figure 2.22: Relative differences of $G_{3p,borehole}$ ***for borehole 1, 13, 163 and 325 during 20 years of operation compared to*** $G_{2i,borehole}$
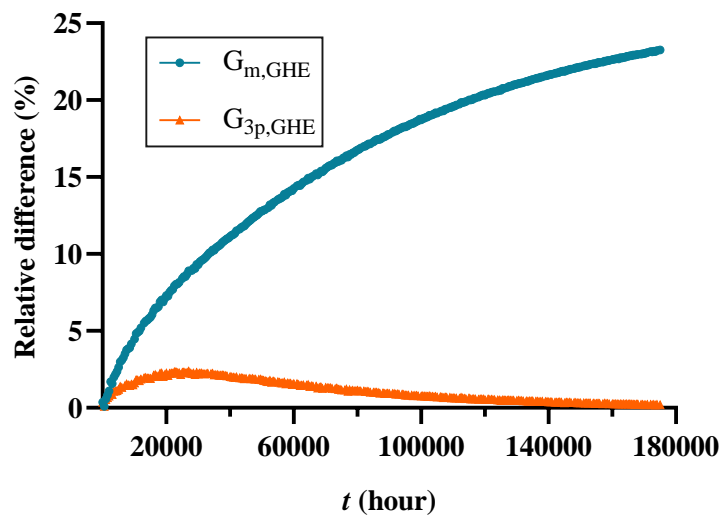
Figure 2.23: Relative differences of $G_{3p,GHE}$ ***and*** $G_{m,GHE}$ ***during 20 years of operation compared to*** $G_{2i,GHE}$

2.4.4. *Calculation speed*

The calculation time of the proposed model was compared to different calculation methods to analyse the calculation time reduction ability for the three main steps: distance category simplification, the three-points method and the initial effect simplification/time averaging simplification. The double integration method without distance categories uses equation (2-5). The double integration method with distance categories uses the form of equation (2-11) in which G_{3p} is replaced by G_{2i}. The three-points method with distance categories uses equation (2-11), without the initial effect/time averaging simplification. The proposed global model includes all the simplification methods. The calculation time of different methods is shown in Table 2-2. All methods were calculated in Matlab using a

computer with an Intel i7-6700 CPU and 16 GB RAM. In the proposed model, the parallel computing with 4 workers can be used. Its simulation time with and without parallel computing was also investigated.

Considering that the double integration method without distance category method is heavily time consuming, it is only possible to measure the calculation time for short simulated periods. It cost 1.4 hours in Matlab to simulate 10 hours of operation. Since the calculation time is linear to the simulated period for this double integration method, it was estimated that it would take almost 50 days to simulate 1 year. By applying distance category simplification to this method, the calculation time was significantly reduced to 1.7 hours, showing a calculation time reduction factor (CTRF) of approximately 700. The three-points method with distance categories cost 0.68 hour for 1 year simulated period, and it contributed to a CTRF of 2.5 compared to the double integration method with distance categories. The proposed global model only cost 4 seconds without parallel computing for 1 year simulated period, which meant the initial effect simplification and time averaging simplification gave a CTRF of 600. The parallel computing gave a CTRF of around 2. For 1 year simulated period, the overall CTRF of the proposed model with parallel computing was around 1 000 000 compared to the double integration method without distance categories, which was a huge improvement. Only 4 seconds of calculation time for a large-scale field of 26 × 26 boreholes for 1 year of operation makes it appropriate to simulate GHE systems in the DBES tools, especially in the design phase for buildings or vertical ground source heat pumps. Moreover, considering a long operation time of a GHE can be interesting. The proposed model cost about 1 minute with parallel computing and 2 minutes without parallel computing to simulate 20 years of operation, compared to nearly 1 000 days by the double integration method without distance categories, corresponding to a CTRF of around 1 600 000 and 760 000, respectively.

The calculation time of the proposed model using double integration instead of the three-points method was also investigated. It costs 1.5 minute and almost 4 minutes to simulate 1 year and 20 years respectively. It shows that by applying the three-points method in the initial effect simplification/time averaging simplification can give higher CTRFs, which are 24 for one year, 8.9 for 10 years and 4.4 for 20 years simulated period. Thus, the three-points method can further increase the calculation ability, and maintain high accuracy at the same time.

It should be noted that, although the proposed model is presented with a square field configuration, it is also suitable for other configurations such as L-shaped, box-shaped, U-shaped and even irregular. The distance category simplification can be applied to other configurations but the CTRF will vary depending on the shape of the field. The initial effect simplification/time averaging simplification only considers the distance categories, thus it can still simplify the calculation after the various configurations are converted into distance categories. In general, the proposed model can be widely adapted to engineering cases and DBES tools.

Table 2-2   ***Calculation time reduction of the proposed model for a 26 × 26 boreholes field***

Simulated period	**Calculation time**					
	Double integration method without distance categories (estimated)	**Double integration method with distance categories**	**Three-points method with distance categories**	**Proposed model with parallel computing using double integration method**	**Proposed model without parallel computing using three-points method**	**Proposed model with parallel computing using three-points method**
1 year	50 days	1.7 hours	0.68 hours	96 seconds	4 seconds	4 seconds
5 years	250 days	8.4 hours	3.4 hours	150 seconds	18 seconds	11 seconds
10 years	500 days	16.8 hours	6.9 hours	204 seconds	40 seconds	23 seconds
20 years	1000 days	33.5 hours	12.9 hours	230 seconds	114 seconds	53 seconds

2.5.   Conclusions and perspectives

2.5.1.   *Conclusions*

An increasing number of GCHP systems have been used to supply heating and cooling to energy efficient buildings. The optimisation of the design and operation of related large-scale boreholes heat exchangers requires to massively reduce the simulation time of these systems relatively to available models. The evaluation of annual energy consumption is based on the COP calculation which depends on the fluid temperature. Therefore, one of the most important steps to simulate the GHE is to identify the borehole wall temperature (which is required to evaluate the fluid temperature). However, the middle point temperature of the borehole wall is not accurate for long operation time, and the double integration form of the integral mean borehole wall temperature brings calculation complexity. Moreover, large-scale boreholes GHE models cannot be practically used in building simulation tools due to the interactions between the boreholes, and the large number of timesteps to be simulated, resulting in high computation cost. This chapter presents a global model to quickly and accurately evaluate the thermal response factor of a large-scale boreholes GHE, combining the FLS model, the 2D heat conduction equation, and a newly developed three-points method.

The three-points method is introduced to determine the representative borehole wall temperature. It considers three points located at the top, middle and bottom of the borehole and uses the average of these three points to represent the borehole wall temperature, avoiding the non-negligible errors of using the borehole middle point temperature for a long operation time. The equation to determine the positions of these three points is given and applied to different radial distances, times and borehole depths. The results show that the relative differences of the thermal response factor of the GHE

between the proposed method and the double integration method are below 3 % for all cases, which is a huge improvement compared to the middle point method for which errors as high as 23 % are observed. This three-points method shows a good accuracy for both short and long time at different radial distances, meanwhile it remains in the form of a single integration to keep a reasonable computation time. Besides, the position determination equation can be applied to different borehole configurations due to its universality.

In the global model, the first step is to sort the large number of boreholes in increasing distance categories. In the second step, the 2D heat conduction equation determines when interactions between boreholes are negligible and when detailed calculations are needed. In the third step, the 2D heat conduction equation evaluates how often the interactions have to be recalculated. In the last step, the thermal response factors are computed by the three-points method. An example of a 26×26 square borehole matrix is studied in this chapter. The results show that the proposed model can give accurate results for G_{3p}, $G_{3p,borehole}$ and $G_{3p,GHE}$, meanwhile the calculation time for one simulated year decreases by a factor of around 1 000 000 to only 4 seconds comparing to the double integration method without any simplification. In this case, simulating 20 years of operation only requires 1 minute. The proposed model is suitable not only for a square borehole configuration, but also for other configurations such as L-shaped, box-shaped, U-shaped and even irregular. Its universality and calculation speed facilitate its integration into building energy simulation tools to optimise the design and operation of GCHP systems.

2.5.2. *Perspectives*

Some perspectives can be proposed in this topic. The model focuses on a square field, which can be extended to other shapes. In the assumptions, the heating load is uniformly distributed to each borehole. The model could be improved by considering a non-uniform distribution of the heating load. The comparison of the proposed model and some experimental results can be a complementary validation providing more information about the accuracy of the model.

Chapter 3. Modelling of a GCHP system for building energy simulation

This chapter is dedicated to integrate the large vertical GHE model presented in chapter 2 in a heat pump model, and implement it in COMFIE. The proposed model can be used as a design aid to optimise the performance of GCHP system.

Résumé du chapitre

Les systèmes GCHP verticaux sont largement utilisés pour fournir le chauffage et le refroidissement des bâtiments en Chine, en raison de divers avantages tels que l'efficacité énergétique et la réduction des émissions de GES. L'optimisation de la conception et du contrôle des systèmes GCHP peut produire des bâtiments plus économes en énergie. Un outil DBES intégré dans un modèle GCHP vertical peut être utile comme aide à la décision des concepteurs de bâtiments, et intéressant pour les chercheurs afin d'étudier ses performances globales, surtout s'il peut rapidement évaluer un champ de sondes à grande échelle.

En utilisant le modèle GHE décrit au chapitre 2, ce chapitre présente un modèle GCHP complet qui peut fournir des resultants au pas de temps horaire. Le modèle de PAC eau-eau est un modèle semi-empirique en régime permanent basé sur une analyse de cycle thermodynamique simplifiée ; il prend en compte les conditions à pleine charge et à charge partielle. Le modèle de PAC utilise 6 paramètres concernant le compresseur, 2 paramètres concernant les échangeurs de chaleur et 1 concernant la vanne d'expansion. Le modèle GHE est lié au modèle de PAC par sa température de fluide de sortie, qui est déterminée par le facteur de réponse thermique et la charge énergétique du GHE. L'ensemble du modèle GCHP est intégré dans l'outil SED COMFIE, dans un co-environnement Matlab-Delphi.

Ce modèle a été appliqué à l'étude d'un champ de sondes 26×26 à Wuhan (Chine). Pour une simulation avec un pas de temps d'une demi-heure sur un an, le temps de calcul spécifique du modèle GCHP proposé était de 4 secondes sur les 8 minutes nécessaires pour l'ensemble du bâtiment : le modèle GCHP n'a pas augmenté le temps de calcul de façon notable. Les performances de la pompe à chaleur ont été étudiées pour différents paramètres de conception concernant l'espacement des trous de forage et la profondeur de forage, par exemple pour améliorer les performances du système. Ce modèle a également été appliqué pour une simulation pluriannuelle et les résultats ont indiqué que, si le système n'est utilisé qu'en mode chauffage, sa performance diminue avec l'année. La prise en compte de la climatisation et de la production d'eau chaude sanitaire est proposée en perspective. Le modèle proposé peut être utilisé comme outil de soutien à la conception pour optimiser les performances du système, dans les phases de conception et d'exploitation, sur la base d'un COP évalué par simulation horaire prenant en compte les charges dynamiques du bâtiment.

Abstract

Vertical GCHP systems are widely used to supply heating and cooling for buildings in China, due to various advantages such as energy efficiency and reduced GHG emissions. The optimisation of the design and control of GCHP systems can yield more energy efficient buildings. A DBES tool integrating a vertical GCHP model can be useful for building designers' decisions, and interesting for researchers to study the overall performance of a GCHP system, especially if it can provide fast calculation for a large-scale boreholes field.

Using the GHE model described in chapter 2, this chapter presents a whole GCHP model that can provide hourly simulation. The water-water HP model is a steady-state semi-empirical model based on a simplified thermodynamics cycle analysis; it considers full load and part load conditions. The HP model is described by 6 parameters regarding the compressor, 2 parameters regarding the heat exchangers and 1 parameter regarding the expansion valve. The GHE model is linked to the HP model by its outlet fluid temperature, which is determined by the thermal response factor and the energy load of the GHE. The whole GCHP model is integrated in the DBES tool COMFIE, in a Matlab-Delphi co-environment.

This model was applied to the case study with a 26×26 boreholes field in Wuhan, China. For half-hourly simulation during 1 year, the specific calculation time of the proposed GCHP model was 4 seconds out of the 8 minutes required for the whole building: the GCHP model did not increase noticeable calculation time. The heat pump performance was investigated for different design parameters regarding the borehole spacing and the borehole depth, as an example to improve the system performance. This model was also applied for a multi-year simulation and the results indicated that, if the system is used only in the heating mode, its performance decreases with time. Accounting for cooling and domestic hot water production is proposed as a perspective. The proposed model can be used as a supporting tool to optimise the system performance in the design and operation phases, based on COP evaluated by hourly simulation accounting for the dynamic loads of the building.

3.1. Introduction

As introduced in chapter 1, buildings are one of the main energy consumption contributors in China and it is essential to optimise their energy performance. An increasing number of vertical GCHPs have been used to heat or cool buildings in China, not only because of its energy efficiency and environmental friendliness, but also the much smaller land area they require compared to ground heat pumps with horizontal tubes. In order to achieve a more accurate evaluation of the energy consumption for Chinese buildings, this type of heat pump system should be integrated in the DBES tools. It can be beneficial to building designers' decision making, and interesting for researchers to study the overall performance of a GCHP system.

A typical vertical GCHP system basically consists of three sub-systems: (1) the heat distribution system in the building; (2) the heat pump (HP) system; and (3) the vertical ground heat exchanger (GHE) system. The ground serves as a heat source to provide heat to the building in winter and a heat sink to receive heat from the building in summer.

As a key component in the GCHP system, the GHE plays an important role in the system performance. A GHE usually consists of one or numerous boreholes, depending on the building loads. The recently-built Chinese buildings are usually high and dense in population, leading to large heating and cooling loads. Consequentially a large-scale boreholes GHE is required. A fast calculation model of a large-scale boreholes GHE was developed and presented in chapter 2. However, it only deals with the calculation of the thermal response factor of the GHE.

This chapter presents an integrated vertical GCHP system with a large-scale boreholes field in China. Each subsystem is presented in detail. The integration algorithm of the GHE, the heat pump, the distribution system and the building is illustrated. The integrated model is applied to the case study presented in section 1.4 with a large GCHP system consisting of a 26 × 26 boreholes field. The system performance of the GCHP is estimated for different design parameters. The DBES model COMFIE integrating the proposed GCHP model can provide a better evaluation for the buildings equipped with this type of system, and can be used as a design tool to improve the building's energy efficiency as well.

3.2. Model description

3.2.1. *General model*

The heat transfer process in a GCHP system for heating is shown in Figure 3.1. In this chapter, a water-water heat pump is considered. The building model calculates the building heating load Q_b. This heating load is met by the heat flow Q_{dis} exchanged with the distribution model. The water on the condenser side circulates at a mass flowrate $\dot{m}_{cd}$. The inlet and outlet temperatures of the distribution unit and the condenser are respectively $T_{in,dis}$, $T_{out,dis}$, $T_{in,cd}$ and $T_{out,cd}$, respectively. The heat flux exchanged in the condenser is Q_{cd}. On the evaporator side, the fluid is a 30 % volume ethylene glycol

water solution with a mass flowrate $\dot{m}_{ev}$. Similarly, the inlet and outlet temperatures of the GHE and the evaporator are respectively $T_{in,GHE}$, $T_{out,GHE}$, $T_{in,ev}$ and $T_{out,ev}$. The heat flux exchanged in the evaporator is Q_{ev}. The work input of the compressor is W.
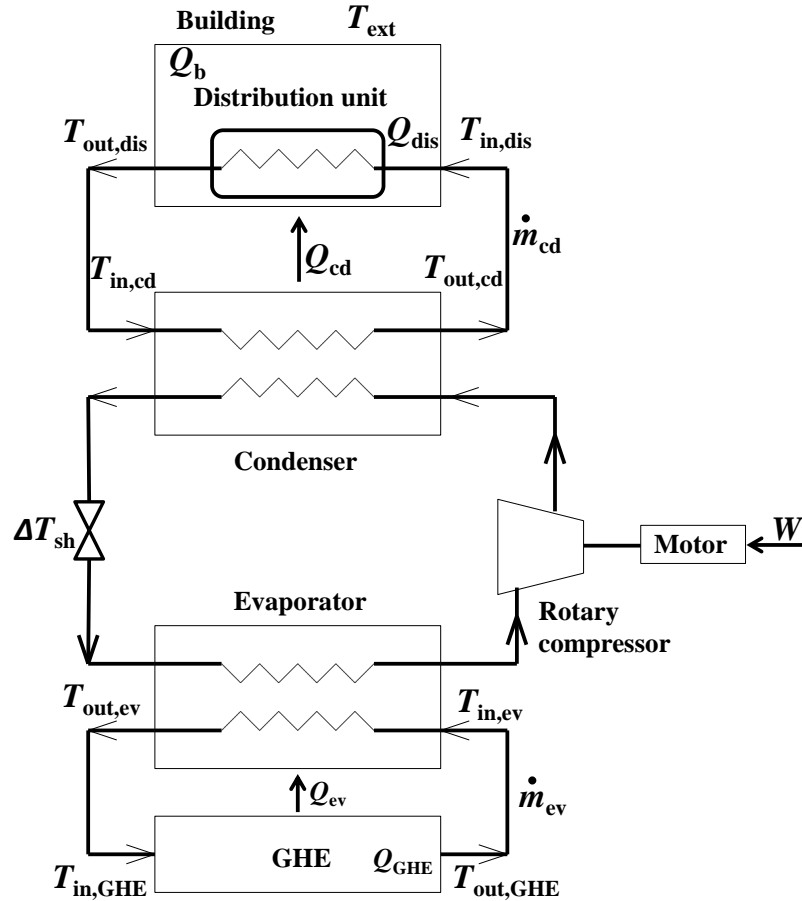
Figure 3.1: Schematic of the energy flows in the GCHP system in the heating mode

3.2.2. *Building model*

The DBES model COMFIE is used to evaluate the energy load. It has been briefly presented in section 1.1.3. Considering that the aim is to integrate a GCHP model in COMFIE, this chapter focuses on the GCHP model implementation. The detailed description of COMFIE model is not presented here; it can be found in Peuportier and Blanc-Sommereux's article (1990).

3.2.3. *Heat distribution model*

In this model, the flowrate in the condenser is maintained at a constant value, and the varying heating load is satisfied by adjusting the inlet and outlet temperatures of the heat distribution model. The efficiency of the heat distribution model is set as 1, and there is no loss between the heat distribution unit and the condenser:

$$Q_{cd} = Q_{dis} = Q_b \tag{3-1}$$

$$T_{\text{out,cd}} = T_{\text{in,dis}} \qquad \textbf{(3-2)}$$

$$T_{\text{in,cd}} = T_{\text{out,dis}} \qquad \textbf{(3-3)}$$

The inlet water temperature of the heat distribution unit $T_{\text{in,dis}}$ is assumed to be 20 °C and 75 °C when the external air temperature T_{ext} is respectively 15 °C and -5 °C, respectively. $T_{\text{in,dis}}$ is assumed to be linear[16] with T_{ext} when $T_{\text{ext}} \leq 15.7$ °C (corresponding to $T_{\text{in,dis}} = 18$ °C) and $T_{\text{in,dis}}$ is constant (18 °C) when $T_{\text{ext}} > 15.7$ °C (it is assumed that there is no heating load when $T_{\text{ext}} > 15.7$ °C):

$$T_{\text{in,dis}} = \begin{cases} -2.75T_{\text{ext}} + 61.25 & \text{if } T_{\text{ext}} \leq 15.7 \,°C \\ 18 & \text{if } T_{\text{ext}} > 15.7 \,°C \end{cases} \qquad \textbf{(3-4)}$$

The outlet water temperature of the heat distribution system is given by:

$$T_{\text{out,dis}} = T_{\text{in,dis}} - \frac{Q_{\text{dis}}}{\dot{m}_{\text{cd}} \cdot c_{\text{p,w}}} \qquad \textbf{(3-5)}$$

in which $c_{\text{p,w}}$ is the specific heat capacity of water.

3.2.4. *Heat pump model*

The work regarding the HP modelling has been continued since the thesis of Filliard (2009) in our group. An HP model with a rolling piston type rotary compressor based on the HP model with scroll compressor presented by Jin and Spitler (2003) was developed. The model is a steady-state semi-empirical model based on a simplified cycle analysis and it considers full load and part load conditions. The reason that the behaviour of the heat pump can be regarded as steady-state is that its time constant is assumed to be small compared to that of the building (Filliard et al., 2009).

3.2.4.1. **Compressor model**

The GCHP in this chapter contains a rolling piston type rotary compressor. Figure 3.2 shows how this type of compressor works. A rolling piston is fixed on an eccentric shaft rotating in a stationary cylinder. The shaft is off-centre so that rolling piston rolls around the cylinder wall. The tolerance between the rotor and cylinder is very close. A spring-loaded blade is set into the slot of the cylinder. The blade moves up and down in such a way that it will be always in positive contact with the rolling piston while it rotates. The blade is machined in such a way that it restricts the fluid flow between the intake and discharge side. This blade separates the suction and compression parts of the compressor. The rolling piston is directly connected to the motor shaft, so it rotates at the same speed as the motor.

In the beginning of compression, suction port is open and the compression chamber is blocked by rolling piston itself. The trapped fluid (refrigerant) is then getting progressively compressed by the decreasing annular space between the rolling piston and cylinder. When the rolling piston rotates, the fluid ahead of the rolling piston is compressed and is pushed towards the compression chamber. The pressure increases until compressed fluid forced out through discharge valve. At the end of

---

[16] https://www.abcclim.net/regulation-loi-eau-pompe-a-chaleur.html

compression, the compressed fluid is discharged. The cycle continues, in this way low-pressure fluid is compressed and delivered at the output of the rotary compressor.
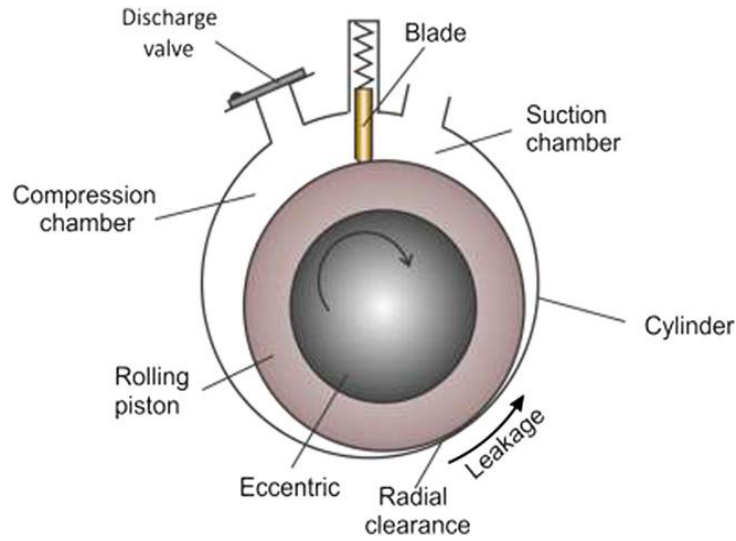
Figure 3.2: Schematic of a rolling piston type rotary compressor (Gasche et al., 2012)

The HP model is based on the parameter estimation and thermodynamic cycle. Jin and Spitler (2003) proposed a method to describe the compressor with few parameters.

The geometry of the compressor can be described by 'built-in' pressure ratio or internal pressure ratio π_i:

$$\pi_i = \frac{P_{dis}}{P_{suc}} \qquad (3\text{-}6)$$

where P_{dis} is the internal discharge pressure and P_{suc} is the internal suction pressure.

Another related characteristic to the 'built-in' pressure ratio is the 'built-in' volume ratio, v_i, which is the ratio of the volume of the trapped gas pocket immediately after closing to the volume of trapped gas pocket immediately before opening to discharge. If the compression is assumed to be isentropic and the gas has a constant isentropic coefficient, the relationship between the 'built-in' pressure ratio and the 'built-in' volume ratio is:

$$\pi_i = v_i^{\gamma} \qquad (3\text{-}7)$$

where γ is the isentropic coefficient.

The 'external pressure ratio', which is the ratio of the condensing pressure (P_{cd}) to the evaporating pressure (P_{ev}), is also important:

$$\pi = \frac{P_{cd}}{P_{ev}} \qquad (3\text{-}8)$$

P_{ev} equals to P_{suc} in this model.

There are three compression modes depending on the difference between external pressure ratio and 'built-in' pressure ratio: design operation, over-compression and under-compression.

Figure 3.3 shows the ideal thermodynamic cycle of a rotary piston compressor under design operation. Under this mode, the 'built-in' pressure ratio equals to the external pressure ratio (i.e. the discharge pressure is equal to the condensing pressure). However, the system operates over a range of conditions where the external pressure ratio varies and does not match the internal pressure ratio.
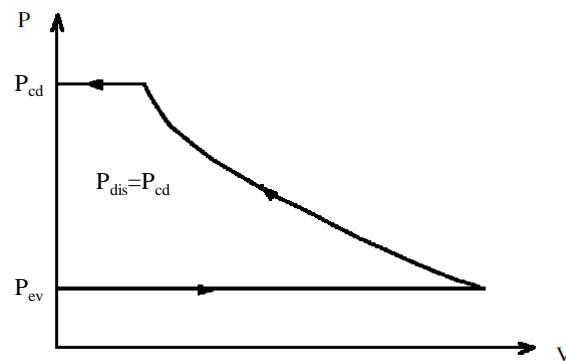
Figure 3.3: Thermodynamic cycle of a rolling piston type rotary compressor under design conditions (Jin and Spitler, 2003)

If the condensing pressure is lower than the discharge pressure, over-compression occurs. In this case, the trapped gas pocket is compressed above the condensing pressure and expands into the discharge as the port is uncovered. When this phenomenon occurs, the work provided is greater than the work necessary to bring the fluid into the equilibrium conditions of the refrigeration cycle, resulting in lost work. Figure 3.4 shows the thermodynamic cycle with over-compression. The lost work is represented by the shaded area.
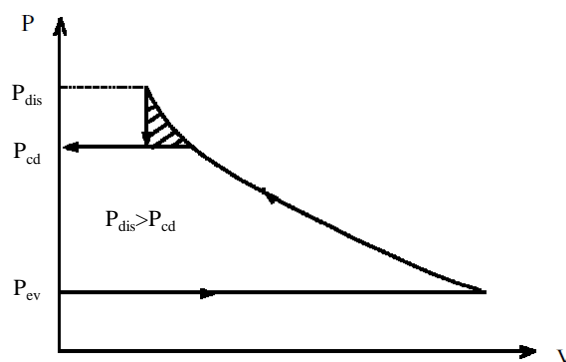
Figure 3.4: Thermodynamic cycle of a rolling piston type rotary compressor under over-compression conditions (Jin and Spitler, 2003)

When the condensing pressure is higher than the internal discharge pressure, under-compression occurs. In this case, the trapped gas pocket opens early to a higher pressure in the discharge line and

then must pump against this higher pressure for the remaining rotary motion of the scrolls, requiring higher torque than would have been required if the pressure had built up gradually to the condensing pressure. This operation mode is shown in Figure 3.5. The lost work is also represented by the shaded area.
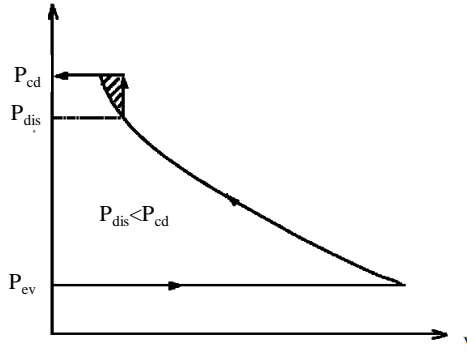
Figure 3.5: Thermodynamic cycle of a rolling piston type rotary compressor under under-compression conditions (Jin and Spitler, 2003)

Over-compression and under-compression therefore lead to energy over-consumption in the compressor. If the external pressure ratio matches the internal pressure ratio, the power consumption of the compressor in the isentropic process:

$$\dot{W}_t = \dot{W}_{is} = \frac{\gamma}{\gamma - 1} P_{ev} \dot{V}_r \left[\pi^{\frac{\gamma - 1}{\gamma}} - 1 \right] \tag{3-9}$$

where $\dot{V}_r$ is the refrigerant volume flow rate.

If the external pressure ratio does not match the internal pressure ratio, the power consumption will be higher than that of the isentropic process:

$$\dot{W}_t = \left[\frac{\gamma}{\gamma - 1} P_{ev} \dot{V}_r \right] \left[\frac{\gamma - 1}{\gamma} \frac{\pi}{v_i} + \frac{1}{\gamma} \pi_i^{\frac{\gamma - 1}{\gamma}} - 1 \right] \tag{3-10}$$

Instead of an isentropic process, a polytropic compression is considered in this model; thus a polytropic coefficient x_p is defined, and the calculation integrates this polytropic coefficient in replacement of the isentropic coefficient γ. This is to model the real compression process, taking into account heat losses and other irreversibilities.

Considering the electrical and mechanical efficiency of the compressor, the actual power input for the compressor is calculated by the following equation:

$$\dot{W} = \frac{\dot{W}_t}{\eta} + \dot{W}_{loss} \tag{3-11}$$

where η is the electromechanical efficiency and $\dot{W}_{loss}$ is the constant part of the electromechanical power losses.

Due to theoretically negligible re-expansion volumes, the refrigerant volume flowrate at the beginning of the compression, $\dot{V}_r$, is equal to the product of the volume of the pockets that seal the suction gas at the beginning the compression and the rotational speed. Thus, the refrigerant mass flowrate can be determined as:

$$\dot{m}_r = \frac{\dot{V}_r}{v_{\text{suc}}} \tag{3-12}$$

where v_{suc} is the specific volume at the suction state.

The leakage in the refrigerant flowrate of a rolling piston compressor can be calculated by (Gasche et al., 2012):

$$\dot{m}_{\text{leak}} = C_l \rho_{\text{leak}} \Delta P \tag{3-13}$$

where $\Delta P = P_{\text{cd}} - P_{\text{ev}}$, C_l is the compressor leakage rate and ρ_{leak} is the saturated density of the fluid in the compressor outlet conditions.

This leakage flow is subtracted from the flow calculated in equation (3-12) to obtain the actual mass flowrate of refrigerant.

The performance of the heat exchangers is described by their effectivenesses:

$$\varepsilon_{\text{ev}} = \frac{T_{\text{out,ev}} - T_{\text{in,ev}}}{T_{\text{out,ev}} - T_{\text{ev}}} = 1 - \exp\left(-\text{NTU}_{\text{ev}}\right) \tag{3-14}$$

$$\varepsilon_{\text{cd}} = \frac{T_{\text{out,cd}} - T_{\text{in,cd}}}{T_{\text{cd}} - T_{\text{in,cd}}} = 1 - \exp\left(-\text{NTU}_{\text{cd}}\right) \tag{3-15}$$

where ε_{ev} and ε_{cd} are the effectiveness of the evaporator and the condenser, respectively; T_{ev} and T_{cd} are the evaporation and condensation temperatures, respectively; NTU_{ev} and NTU_{cd} are the numbers of transfer units (NTU) of the evaporator and the condenser, respectively.

$$\text{NTU}_{\text{ev}} = \frac{U_{\text{ev}} A_{\text{ev}}}{\dot{m}_{\text{ev}} \cdot c_{\text{p,wg}}} \tag{3-16}$$

$$\text{NTU}_{\text{cd}} = \frac{U_{\text{cd}} A_{\text{cd}}}{\dot{m}_{\text{cd}} \cdot c_{\text{p,w}}} \tag{3-17}$$

where U_{ev} and U_{cd} are the global heat transfer coefficients for the evaporator and condenser respectively, W/(m^2.K), and A_{ev} and A_{cd} are the surface areas where the heat transfer takes place for the evaporator and condenser respectively, m^2.

To summarise, in order to describe the HP system, 6 parameters regarding the compressor ($\dot{V}_r$, C_l, v_i, x_p, $\dot{W}_{\text{loss}}$ and η) and 2 parameters regarding the heat exchangers (effectiveness of evaporator ε_{ev} and condenser ε_{cd}) are necessary. An additional parameter is the overheat temperature at the outlet of the evaporator ΔT_{sh}. In this study, it was fixed at 7 °C (sensitivity analyses on this parameter determined that it was not of primary influence on the model precision).

3.2.4.2. Parameter identification of case study

Due to a lack of data from the HP manufacturer in the case study, the corresponding parameters of the HP were estimated by scaling the existing parameters from the previous work of our group. This will lead to an estimation of the real HP performance and not an accurate COP value. In the previous study, a water-water geothermal HP was used. This heat pump was designed for small houses with a capacity under 10 kW, which is much smaller compared to the large GCHP system in this chapter (needs to supply the heating load of the whole HSJG block, approximately 5 000 kW). The scale ratio is the mass flow rate ratio of the condenser between the case study (200 kg/s) and previous work (0.3 kg/s), as listed in Table 3-1. Then, the energy exchanged at the condenser and evaporator can be determined by the thermodynamic cycle analysis of the refrigerant. The coefficient of performance (COP) is:

$$\text{COP} = \frac{Q_{\text{cd}}}{\dot{W}} \tag{3-18}$$

Table 3-1   Parameters of the HP model in the case study by scaling the reference HP

Component	Parameters	Symbol	Value in case study	Value in previous study	Scale	Unit
Compressor	Refrigerant volume flow rate	$\dot{V}_r$	0.831	1.25×10^{-3}	$\frac{200}{0.3}$	m³/s
	Compressor leakage rate	C_l	0.0101	1.32×10^{-4}	$(\frac{200}{0.3})^{\frac{2}{3}}$	m³.Pa/s
	'Built-in' volume ratio	v_i	2.99	2.99	1	–
	Polytropic coefficient	x_p	1.20	1.20	1	–
	Electro-mechanical power losses	$\dot{W}_{\text{loss}}$	1.49	0.17	$(\frac{200}{0.3})^{\frac{1}{3}}$	kW
	Electro-mechanical efficiency	η	0.98	0.98	1	–
Heat exchanger	Evaporator effectiveness	ε_{ev}	0.83	0.83	1	–
	Condenser effectiveness	ε_{cd}	0.99	0.99	1	–
Expansion valve	Overheat temperature at the outlet of the evaporator	ΔT_{sh}	7	7	1	°C

3.2.4.3. Operation model

The full load is calculated by the presented heat pump model in section 3.2.4.2. When the building load is smaller than the full capacity of the HP, the inverter-driven compressor method is used to control the HP heating capacity. The inverter partial load operating model used is based on a corrective factor, the partial load factor (PLF), applied to the COP at full load, COP_{fl}:

$$PLF = \frac{\text{Part load performance}}{\text{Full load performance}} = \frac{COP_{pl}}{COP_{fl}} \qquad \textbf{(3-19)}$$

where COP_{pl} is the COP at partial load. PLF is calculated according to the partial load ratio (PLR), which is defined by the ratio of the building heating load, Q_b, and the heating capacity at full load, $Q_{cd,fl}$:

$$PLR = \frac{Q_b}{Q_{cd,fl}} \qquad \textbf{(3-20)}$$

Below the full load, two operating conditions exist which are distinguished by the reference partial charge rate PLR_{ref} (the corresponding PLF is PLF_{ref}), as shown in Figure 3.6. Above PLR_{ref}, the compressor regulates its rotation frequency in order to adapt the heat delivered to the condenser to satisfy the heating load. This is called the "inverter mode". Below PLR_{ref}, the compressor can no longer lower its rotation frequency and then operates in "on/off mode".
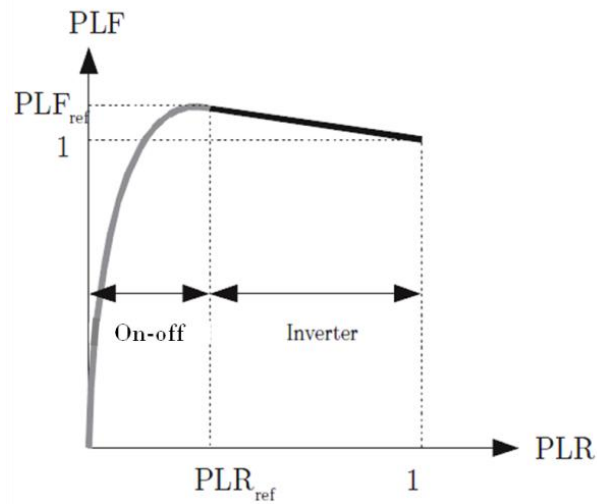
Figure 3.6: HP inverter function model (Filliard, 2009)

In "inverter mode" (PLR $\geq$ PLR_{ref}), the system performance increases linearly when PLR decreases. In "on-off" mode (PLR $<$ PLR_{ref}), the performance of HP significantly reduces with PLR:

$$PLF = \begin{cases} \dfrac{PLR}{PLR + \alpha}\beta; & PLR < PLR_{ref} \\[2ex] \dfrac{PLF_{ref} - 1}{PLR_{ref} - 1}PLR + \dfrac{PLR_{ref} - PLF_{ref}}{PLR_{ref} - 1}; & PLR \geq PLR_{ref} \end{cases} \qquad \textbf{(3-21)}$$

where α is the fraction of the monitoring part in the power, which usually varies from 1 % to 5 % according to the technologies and characteristics of the HP (Filliard, 2009); and $\beta = PLF_{ref} \times (PLR_{ref} + \alpha) / PLR_{ref}$. In this thesis, $PLR_{ref} = 0.5$, $PLF_{ref} = 1.1$, $\alpha = 0.01$ and $\beta = 1.01$, as adopted in Filliard's thesis (2009) and the previous study in our group. That is to say that at 50 % of full load of the heat pump, we consider that the performance is increased by around 10 % compared to the performance at full load.

3.2.5. *GHE model*

The link between the GHE model and the heat pump model is the temperature at the evaporator inlet (equal to $T_{out,GHE}$ if no heat loss is considered). The configuration of a square boreholes field consisting of N_b boreholes is shown in Figure 2.3. Each borehole is equipped with double U-tube in parallel connection. In COMFIE, the time-varying heating and cooling loads are step-wise constant values. Here we assume that the energy load from the building is uniformly distributed to each borehole, which means the heat load of each borehole at timestep m is identical:

$$q_m = \frac{Q_{GHE}(m)}{N_b \times H} = \frac{Q_{ev}(m)}{N_b \times H} \tag{3-22}$$

where $Q_{GHE}(m)$ and $Q_{ev}(m)$ are respectively the heat load of the GHE field and the evaporator at timestep m; H is the borehole's depth.

The GHE model focuses on calculating its outlet fluid temperature $T_{out,GHE}$, which at timestep m can be determined by:

$$T_{out,GHE}(m) = \frac{\sum_{j=1}^{N_b} T_{out,j}(m)}{N_b} \tag{3-23}$$

where $T_{out,j}(m)$ is the outlet fluid temperature of the jth borehole at timestep m.

Based on the assumption that the mean fluid temperature of the jth borehole at timestep m, $T_{fl,j}(m)$, is the average temperature of the inlet and outlet fluid temperature and the energy balance equation:

$$T_{fl,j}(m) = \frac{T_{out,j}(m) + T_{in,j}(m)}{2} \tag{3-24}$$

$$q_m H = \frac{\dot{m}_{ev} c_{p,wg}(T_{out,j}(m) - T_{in,j}(m))}{N_b} \tag{3-25}$$

$T_{out,j}(m)$ can be calculated by:

$$T_{out,j}(m) = T_{fl,j}(m) + \frac{N_b q_m H}{2\dot{m}_{ev} c_{p,wg}} \tag{3-26}$$

where $c_{p,wg}$ is the specific heat capacity of water-glycol solution.

$T_{fl,j}(m)$ is determined by the borehole wall temperature of the jth borehole $T_{b,j}(m)$ at timestep m and the thermal resistance R_b:

$$T_{fl,j}(m) = T_{b,j}(m) - q_m \cdot R_b \tag{3-27}$$

The borehole wall temperature can be determined by the FLS model, and represented by the integral mean temperature. The heating load has an effect on both the current time and the future. Considering all boreholes' effects, the borehole wall temperature of the jth borehole at timestep m can be determined by applying the superposition principle:

$$
\begin{aligned}
T_{\text{b},j}(m) - T_0 = \sum_{i=1}^{N_{\text{b}}} \sum_{k=1}^{m} \frac{q_{k-1} - q_k}{2\pi\lambda_{\text{s}}} \frac{1}{2H} \int_0^H \int_0^H &\left\{ \frac{\operatorname{erfc}\left(\frac{\sqrt{\left(r_{i,j}\right)^2 + (z-h)^2}}{2\sqrt{\alpha_{\text{s}}(t_m - t_{k-1})}} \right)}{\sqrt{\left(r_{i,j}\right)^2 + (z-h)^2}} \right. \\
&\left. - \frac{\operatorname{erfc}\left(\frac{\sqrt{\left(r_{i,j}\right)^2 + (z+h)^2}}{2\sqrt{\alpha_{\text{s}}(t_m - t_{k-1})}} \right)}{\sqrt{\left(r_{i,j}\right)^2 + (z+h)^2}} \right\} dh \, dz
\end{aligned}
\tag{3-28}
$$

$$
= \sum_{i=1}^{N_{\text{b}}} \sum_{k=1}^{m} \frac{q_{k-1} - q_k}{2\pi\lambda_{\text{s}}} G\left(r_{i,j}, t_m - t_{k-1}\right)
$$

where i is the ith borehole in the boreholes field (interacting with the jth borehole under consideration); k is the kth timestep; t_m is the time at timestep m; $r_{i,j}$ is the distance between the ith borehole and the jth borehole, and $r_{i,j} = r_{\text{b}}$ when $i = j$; h and z are the integration variables; λ_{s} and α_{s} are the thermal conductivity and diffusivity of the ground, respectively; T_0 is the initial ground temperature; G is the thermal response factor (G-function) of one borehole under the effect of another borehole; and erfc denotes the complementary error function. Combining equations (3-23) to (3-28), $T_{\text{out,GHE}}(m)$ can be expressed by a G-function of the whole GHE, G_{GHE}:

$$
\begin{aligned}
T_{\text{out,GHE}}(m) &= \frac{\sum_{j=1}^{N_{\text{b}}} \sum_{i=1}^{N_{\text{b}}} \sum_{k=1}^{m} \frac{q_{k-1} - q_k}{2\pi\lambda_{\text{s}}} G\left(r_{i,j}, t_m - t_{k-1}\right)}{N_{\text{b}}} - q_m \cdot R_{\text{b}} \\
&\quad + \frac{N_b q_m H}{2\dot{m}_{\text{ev}} C_{\text{p,wg}}} + T_0 \\
&= \frac{\sum_{k=1}^{m} \frac{q_{k-1} - q_k}{2\pi\lambda_{\text{s}}} G_{\text{GHE}}(t_m - t_{k-1})}{N_{\text{b}}} - q_m \cdot R_{\text{b}} + \frac{N_{\text{b}} q_m H}{2\dot{m}_{\text{ev}} C_{\text{p,wg}}} + T_0
\end{aligned}
\tag{3-29}
$$

For a large boreholes field, the calculation of G_{GHE} can be complex and time costing. As presented in chapter 2, a fast calculation method was developed and implemented in Matlab. G_{GHE} at timestep m corresponds to $G_{\text{3p,GHE}}(t_m)$ in chapter 2.

The calculation of $G_{\text{3p,GHE}}$ is off-line and a text file containing the results of $G_{\text{3p,GHE}}$ is generated. This text file constitutes an input when integrating the GHE model and the heat pump model in COMFIE.

The heat transfer inside the borehole mainly depends on the borehole thermal resistance R_b. The 2D model presented in section 1.3.1.2 is used here to calculate the borehole thermal resistance. It is defined by the sum of the pipe thermal resistance R_p and the borehole-to-pipe thermal resistance R_{bp}:

$$R_b = \frac{R_p}{N_l} + R_{bp} \qquad \text{(3-30)}$$

where N_l is the number of U-pipe legs.

One of the widely used expression for R_b of a single U-tube borehole (Hellström, 1991) and of a double U-tube borehole (P. Conti et al., 2016) are:

$$R_b = \begin{cases} \dfrac{1}{4\pi\lambda_b} ln\left[\dfrac{r_b^2}{2x_c r_o}\left(\dfrac{r_b^4}{r_b^4 - x_c^4}\right)^{\sigma}\right] + \dfrac{R_p}{2}\,; for\ single\ U-tube \\[4mm] \dfrac{1}{8\pi\lambda_b}\left[\begin{matrix} ln\left(\dfrac{r_b}{r_o}\right) + 2\,ln\left(\dfrac{r_b}{\sqrt{2}x_c}\right) + ln\left(\dfrac{r_b}{2x_c}\right) \\[2mm] -\sigma\,ln\left(\dfrac{r_b^8 - x_c^8}{r_b^8}\right) \end{matrix}\right] + \dfrac{R_p}{4}\,; for\ double\ U-tube \end{cases} \qquad \text{(3-31)}$$

where x_c is the half spacing between legs of U-tube; λ_b is the thermal conductivity of the grout; dimensionless variable σ is defined as $(\lambda_b - \lambda_s)/(\lambda_b + \lambda_s)$.

The pipe thermal resistance R_p can be caculated by summing the conductive and convective resistances:

$$R_p = \frac{1}{2\pi\lambda_p} ln\left(\frac{r_o}{r_i}\right) + \frac{1}{2\pi r_i h_f} \qquad \text{(3-32)}$$

$$h_f = \frac{Nu \cdot \lambda_f}{2r_i} \qquad \text{(3-33)}$$

$$Nu = \begin{cases} 4.36 \ \text{ for } Re \leq 2300 \\ 0.0149Re + 4.356 \text{ for } 2300 < Re < 10000 \\ 0.023Re^{0.8}Pr^{1/3} \ \text{ for } Re \geq 10000 \end{cases} \qquad \text{(3-34)}$$

where λ_p is the thermal conductivity of the pipe; λ_f is the thermal conductivity of the fluid; r_o and r_i are the outside and inside radius of the pipe; h_f is the convective heat transfer coefficient.

3.2.6. *Backup resistance*

The studied heat pump is equipped with two electric backup resistances of 1 500 kW. They are used when the heat pump capacity is too low to meet the building heating load. In this case, a first backup is turned on, and if it is not sufficient, both are used.

3.2.7. *Integration of different components*

The algorithmic diagram of the integration of the GHE model and the HP model into COMFIE in the Delphi-Matlab co-environment is shown in Figure 3.7. With the heating load calculated by the building model, the heat distribution model determines the inlet and outlet fluid temperatures of the

distribution system which correspond respectively to the outlet and inlet fluid temperatures of the condenser. The inlet fluid temperature and the heat flow of the condenser are then transferred to the HP model as inputs.

In the HP model, by knowing the inlet fluid temperatures of the condenser $T_{in,cd}$ and the evaporator $T_{in,ev}$ (initial value equals to the undisturbed temperature), the 9 input parameters describing the HP system in Table 3-1 and the properties of the working fluid (which is also an input), it is possible to determine the energy exchanged in the evaporator and the inlet and outlet fluid temperatures of the evaporator, as well as the work of the compressor and COP of the heat pump at full load, based on the thermodynamic cycle. It is an iterative process, the calculated energy flow through the evaporator and condenser replacing the former ones (the initial values are given by guess) until the variation between two iterations are smaller than 0.1 %. Then, PLR is calculated and other parameters (e.g. the energy flow of the heat exchangers) are derived under the part load condition.

The energy exchanged in the evaporator is equal to the heat extracted from the ground, which is an input for the GHE model. By using G_{GHE} calculated by Matlab, the GHE model calculates its outlet fluid temperature which is compared to the inlet fluid temperature of the evaporator calculated by the HP model. An iterative process is performed for these temperatures to converge (until the temperature difference is smaller than 0.1 °C). At each timestep of the simulation, a balance point between different systems is achieved to describe the overall system performance.

In COMFIE, the dynamic energy simulation of the building is performed for one year (52 weeks). The integrated GCHP model is designed for one year as well, but it can be extended to a multi-year simulation, in order to investigate the system performance operating for a long time. This process only requires an input of the heat load of each borehole which is used in equation (3-29) during the previous years.

Taking a 3-year simulation as an example, the simulated period of 3 years is divided into two parts: the present year (titled "year_0") and the previous 2 years (titled "year_-1" and "year_-2"). It is assumed that the heating load is identical in all three years. Year_-2 is firstly simulated and its heat load q of each borehole during year_-2 is an output of the GCHP model. It is recorded in a text file then regarded as an input for the simulation of year_-1. Similarly, the heat load q of each borehole during year_-1 is recorded as well and finally used with that during year_-2 together in the simulation of year_0. It should be noted that, a n-years simulation requires a 1-year simulation for n times to obtain q, thus the calculation time in total will be n times longer.
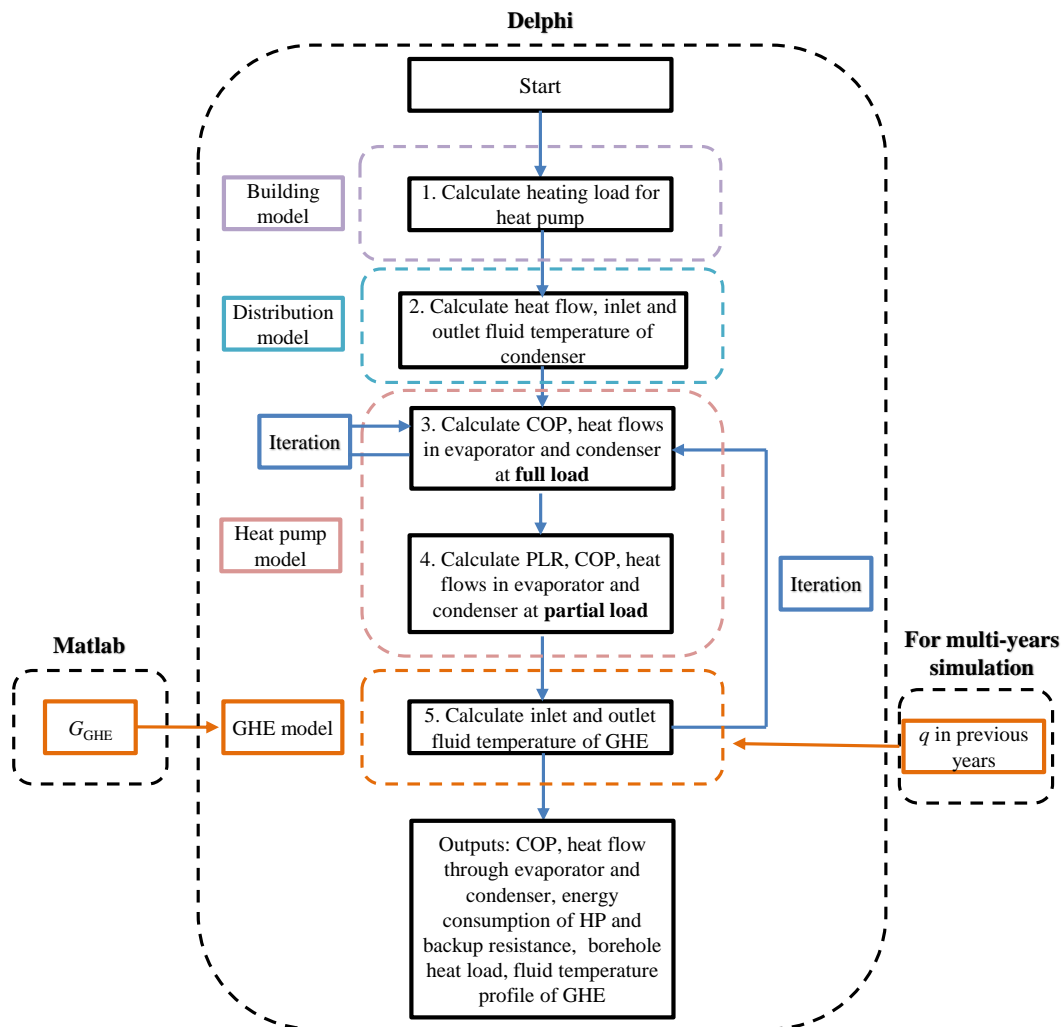
Figure 3.7: Algorithmic diagram of integrating GHE with HP to building simulation tool

3.3. Case study

The GCHP model (detail information in Table 3-2) was applied for the case study presented in section 1.4, but with several differences: the building was redefined with 6 thermal zones (5 for habitants, 1 for the aisle space) in total, instead of 17 zones, to reduce the complexity in GCHP simulation; the internal gain was 15 W/m^2 from 7h00 to 9h00 and from 20h00 to 22h00 everyday and 5 W/m^2 in the rest time, instead of 4.3 W/m^2 for all day. The other parameters were identical. The heating load of the case study is multiplied by 10 to approximate the heating load of the whole HSJG block, which is supplied by the large-scale boreholes field.

To illustrate the proposed model, a case study is introduced, assuming that the ground is siliceous rock (Wang et al., 2019a). The default duration of one timestep is 0.5 hour, but it can be changed as needed.

Table 3-2 **Main parameters of the case study**

Component	Parameters	Description	Value	Unit
GHE	N_b	Number of borehole	26 × 26	–
	B	Borehole spacing	4	m
	H	Borehole length	133	m
	r_b	Borehole radius	0.110	m
	r_o	Outside radius of the pipe	0.025	m
	r_i	Inside radius of the pipe	0.02	m
	x_c	Half spacing between U-tube legs	0.035	m
	λ_p	Thermal conductivity of pipe	0.41	W/m.K
	λ_b	Thermal conductivity of grout	1.69	W/m.K
	R_b	Borehole thermal resistance	0.147	m.K/W
	Type of borehole connection		Parallel	–
	Type of tube		Double-U	–
Ground	λ_s	Ground thermal conductivity	2.635	W/m.K
	α_s	Ground thermal diffusivity	1.23×10^{-6}	m^2/s
	T_0	Undisturbed ground temperature	19	°C
Heat pump	m_{cd}	Mass flow rate at condenser	200	kg/s
	m_{ev}	Mass flow rate at evaporator	200	kg/s
	$C_{p,w}$	Specific heat capacity of water	4 180	J/kg.K
	$C_{p,wg}$	Specific heat capacity of water-glycol solution	3 590	J/kg.K
	Refrigerant		R410a	–

3.4. Results and discussion

3.4.1. *One year simulation*

The calculation of G_{GHE} for 1-year operation in Matlab using a computer with an Intel i7-6700 CPU and 16 GB RAM cost 4 seconds. The half-hourly dynamic energy simulation of the building with and without the proposed GHE model in COMFIE both cost 8 minutes. Therefore, for a 1-year simulation, the calculation time of a large 26 × 26 boreholes field is almost negligible. The heating load is shown in Figure 3.8. The peak heating load is 4 755 kW. The COP of the heat pump system is

illustrated in Figure 3.9. It should be noted that the COP here is the COP of the heat pump (the backup resistance is not included), not the whole system. It can be inferred that the heat pump system operates at a COP of over 3.5 for 91 % of the whole year, which shows a good efficiency. The average COP of the heating period (total heat energy exchanged in the condenser divided by the total electricity consumption of the compressor) is 4.56. $T_{out,GHE}$ varies between 7.22 °C and 16.84 °C.
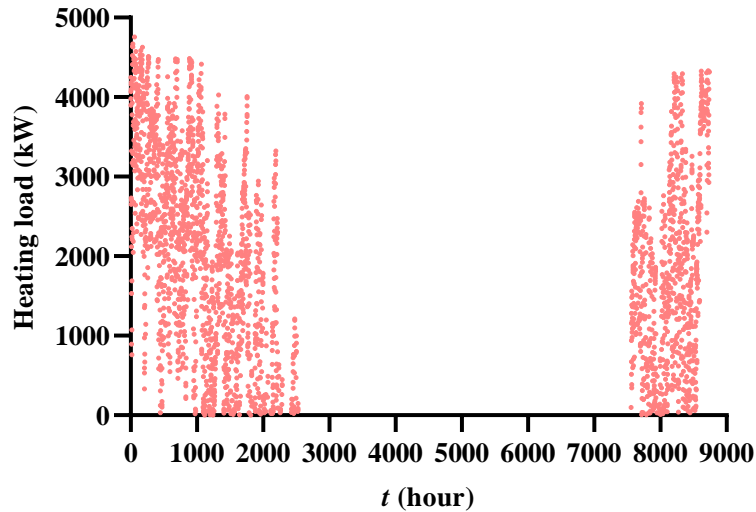
Figure 3.8: Heating load of the case study
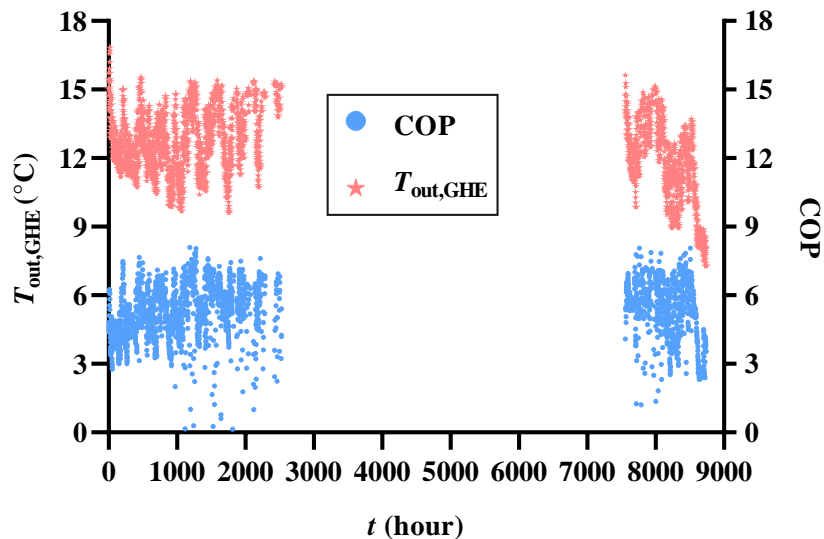
Figure 3.9: COP and T$_{out,GHE}$ of the case study

The proposed model was applied to different boreholes' spacings, B (from 3 m to 8 m, $H = 133$ m), and various depths, H (90 m, 110 m, 133 m, 150 m and 170 m, $B = 8$ m) to study the heat pump's energy efficiency. The COP differences are shown in Figure 3.10 and Figure 3.11. On the

whole, COP increases with B. The average COP increases from 4.46 ($B = 3$ m) to 4.65 ($B = 8$ m). Moreover, the influence of B on COP decreases with B. Larger H shows a better heat pump performance. The average COP is 4.77 for $H = 170$ m, improving the performance of the heat pump by 8 %, compared to 4.40 for $H = 90$ m.
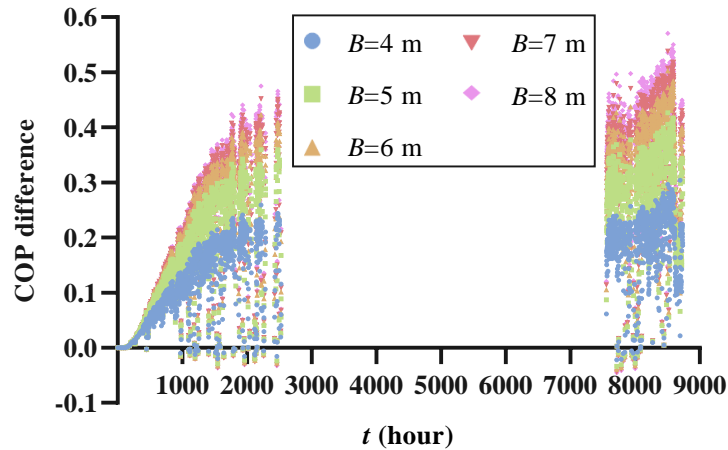
Figure 3.10: COP difference of different B and same H = 133 m compared to base value (3 m)
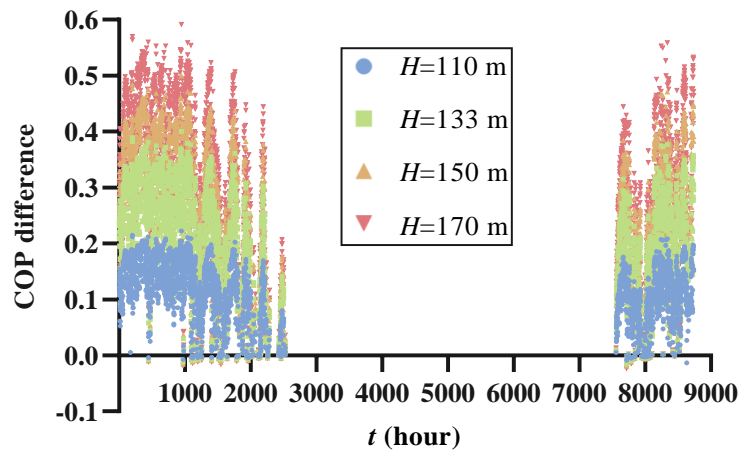
Figure 3.11: COP difference of different H and same B = 8 m compared to base value (90 m)

The electricity consumptions of the heat pump and the backup resistance are shown in Figure 3.12 and Figure 3.13. For $H = 133$ m, the electricity consumption of the heat pump decreases with B. The decrease becomes smaller when B gets larger. The same trend is found in the backup resistance as well. The total electricity consumption when $B = 8$ m is 1 491 MWh, which is 4 % smaller than when $B = 3$ m. For $B = 8$ m, larger H values show better performances. The total electricity consumption for $H = 90$ m is 1 611 MWh; the heat pump and the backup resistance consume 1 415 MWh and 196 MWh, respectively. The electricity consumption decreases with H, and similarly, a larger

reduction is observed for small H values. For $H = 170$ m, the total electricity consumption is reduced by 10 % compared to $H = 90$ m. Although larger B and H values show a better performance, larger land area and higher initial investment costs are required to install the GHE. The proposed model can help the designers to achieve a balance between performance and cost.
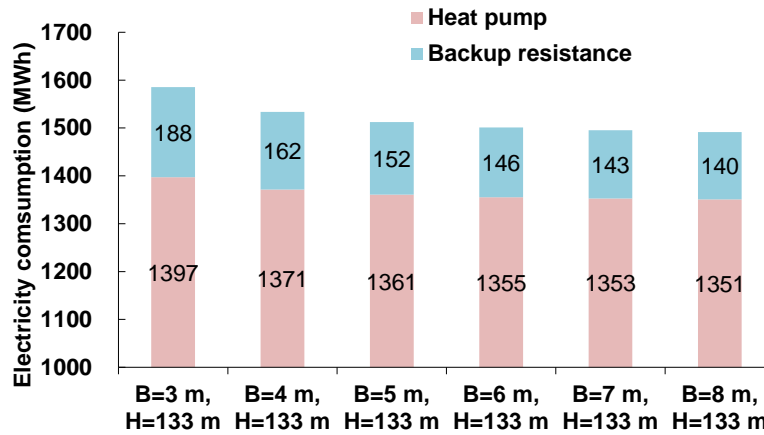
Figure 3.12: Electricity consumptions of the heat pump and the backup resistance for different B
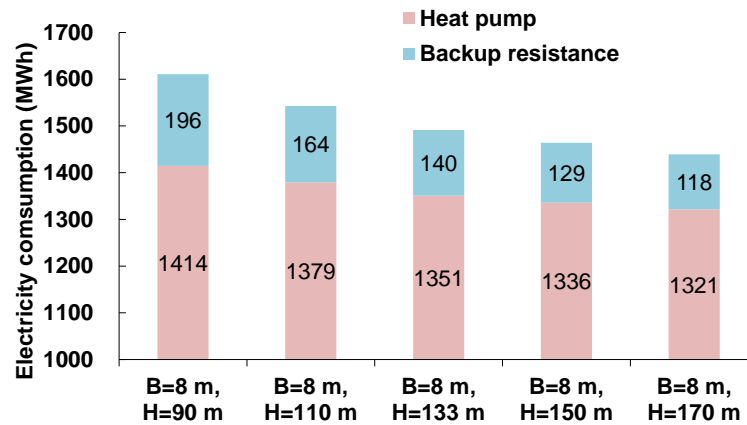
Figure 3.13: Electricity consumptions of the heat pump and the backup resistance for different H

3.4.2. *Multi-year simulation*

A 4-year simulation was performed for the GCHP model in Table 3-2. The heat load of each borehole during the simulated 4 years is shown in Figure 3.14. It can be inferred that, as only the heating mode is considered in this first step, the borehole heat load decreases with time. The yearly average borehole heat loads of year 1 to year 4 are 18.2 W/m, 17.8 W/m, 17.1 W/m and 16.3 W/m. This is consistent with the fact that the GCHP system is only used for heating, thus the heat exchange between the borehole and ground becomes weaker due to the continuous heat extraction from the ground.
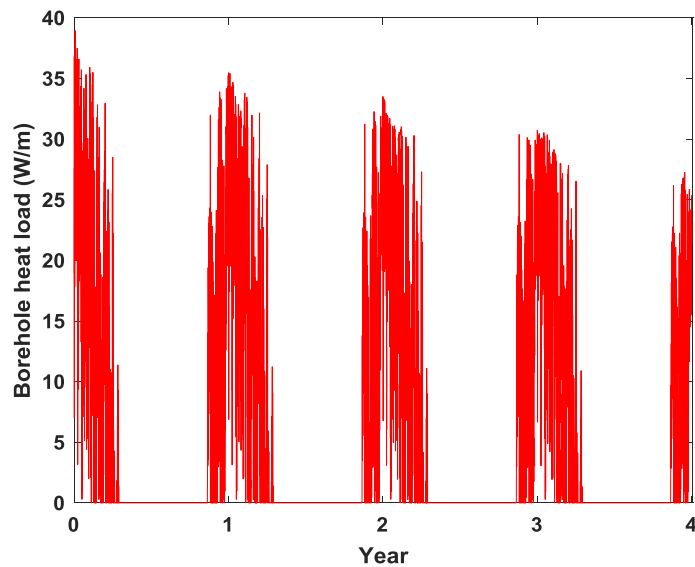
Figure 3.14: Heat load of each borehole during a simulated period of 4 years

The outlet fluid temperature of the GHE is shown in Figure 3.15. $T_{out,GHE}$ decreases with time. In the 4th year, $T_{out,GHE}$ is below 0 °C. This might cause a low temperature of the ground near the GHE, resulting inappropriate working conditions for it. Therefore, the simulation was not extended to the 5th year. It should be noted that, in reality of the case study, both heating and cooling exist and they have a similar order of magnitude. The slight difference might lead to a long term decrease of performance. It can be interesting to study the long term performance of the GCHP system under such conditions. The COP of the GCHP is shown in Figure 3.16. The average COP of the heating period decreases with time as well, which is 4.56, 4.25, 4.00 and 3.69 for year 1 to 4, respectively. The performance of the GCHP is affected if only heating mode is considered in the simulation.
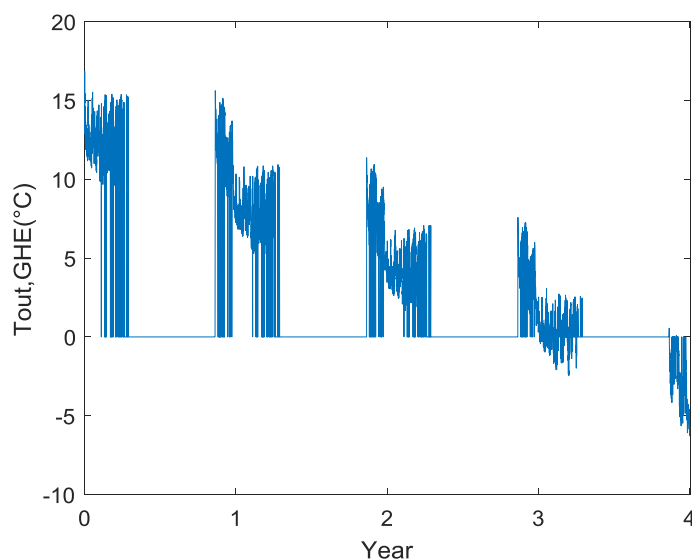
Figure 3.15: $T_{out,GHE}$ during a simulated period of 4 years
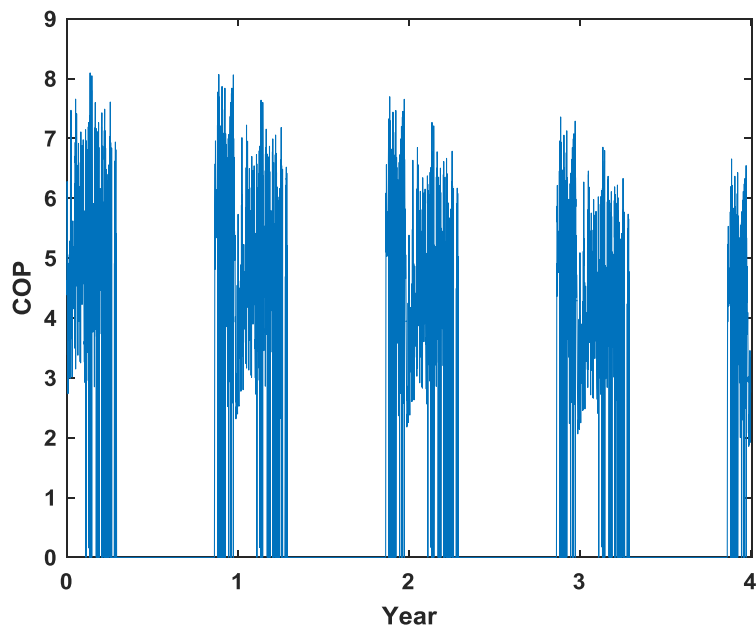
Figure 3.16: COP during a simulated period of 4 years

The electricity consumptions of the heat pump and the backup resistance during the 4 years are shown in Figure 3.17. The total electricity consumption increases from 1534 MWh to 2057 MWh, in which the heat pump system consumes from 1371 MWh to 1624 MWh and the backup resistance consumes from 163 MWh to 433 MWh. The share of the consumption of the backup resistance in the total increases from 11 % to 21 %. It can be inferred that with the decrease of the performance of the GCHP system, more consumption of the backup resistance is needed, which lowers the overall performance of the system.
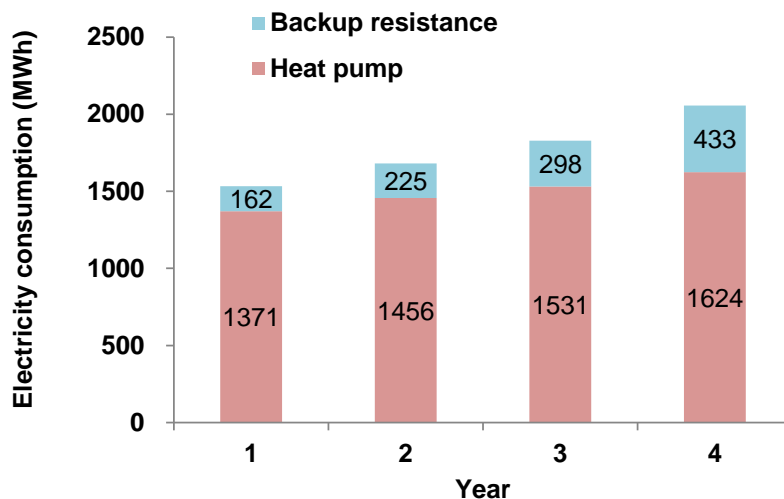
Figure 3.17: Electricity consumptions of the heat pump and the backup resistance during a simulated period of 4 years

3.5.   Conclusions and perspectives

3.5.1.   *Conclusions*

The building sector is a main energy consumption sector, and it is essential to improve its energy performance. The use of geothermal in the buildings is one promising solution. A DBES tool providing a fast simulation of the building integrated with a geothermal heat pump is beneficial for the building design and comprehensive performance analysis. This chapter presents the modelling of a large-scale boreholes GHE associated with a heat pump. This GCHP system was integrated in the DBES tool COMFIE. The finite line source model and the superposition model were used in the GHE model and its *G*-function was calculated off-line in Matlab. Then, the *G*-function was input and used by the GHE model integrating an existing heat pump model in COMFIE (Delphi environment). A case study containing a large 26×26 boreholes field in China allowed to test its usability and simulation speed. The off-line calculation of the *G*-function only cost 4 seconds. The GHE model did not bring noticeable extra calculation time for this case study. The heat pump system performance was analysed under different *B* and *H* values. The results showed that the average COP increased with both *B* and *H*. The total electricity consumption of $B = 8$ m, $H = 133$ m was reduced by 6 % compared to $B = 3$ m, $H = 133$ m. This model was also extended for a multi-year simulation. The results showed that the performance of the GCHP system decreased with time when only heating is considered. The main contributions of this study are: (1) the modelling of a large GHE with fast calculation speed, which is an efficient model that can be used in other DBES tools; (2) the integration of a GCHP model into COMFIE, which is helpful to the building designers to improve building efficiency; (3) a system performance optimisation, which is beneficial for the design of GHEs.

3.5.2.   *Perspectives*

The power consumption of the pumps should be considered in this chapter, thus more accurately predicting the performance for the whole GCHP system. The distribution model is a simplification model, which can be improved if more data are available. The parameter identification of a large-scale heat pump is based on the scaling rules, which can be more accurately obtained if the datasheets are available from the manufacturer. More representative technologies regarding the compressor should be modelled, especially for the large-scale heat pump. This GCHP model should be extended for cooling and DHW production as well. The long term performance of the GCHP system under both heating and cooling conditions should be studied. On top of reference model validation, the accuracy of the whole model could be validated experimentally.

Chapter 4.   Effects of microclimate on building energy performance

---

Urbanisation brings to the urban areas different climate characteristics by replacing natural surroundings with urban settlements, compared to the rural areas where the meteorological input data are normally collected for DBES. As an essential boundary condition in DBES, the microclimate might cause noticeable differences in the simulation results. This chapter is dedicated to quantitatively evaluate the microclimate's effects (particularly the UHI effect) on building energy performance, by coupling the microclimate simulation tool ENVI-met and the DBES tool COMFIE.

Résumé du chapitre

L'urbanisation modifie l'environnement urbain qui présente en conséquence des caractéristiques climatiques différentes par rapport aux zones rurales. L'évaluation de la performance énergétique du bâtiment est principalement basée sur un fichier météorologique contenant 8 760 heures de données climatiques, p. ex. température et humidité de l'air. En tant que condition aux limites essentielle, la précision du fichier d'entrée météorologique influence directement les résultats de la simulation. Dans les méthodes existantes, ce fichier météorologique est généralement collecté en zone rurale, ce qui ne peut pas refléter le microclimat autour du bâtiment et peut provoquer des différences notables. Un effet du climat urbain bien connu est l'effet d'îlot de chaleur urbain (*Urban heat island*, UHI), décrivant l'écart entre la température de l'air urbain et la température de l'air rural. Ce chapitre vise à évaluer quantitativement les effets du microclimat (en particulier l'effet UHI) sur la performance énergétique du bâtiment.

L'outil de simulation du microclimat ENVI-met est d'abord présenté et utilisé pour obtenir les paramètres du microclimat. Le temps de simulation du microclimat est long pour un PC standard, il n'est donc pas possible d'obtenir les données horaires du microclimat pour toute l'année. Ainsi, une méthode de génération de fichier météorologique spécifique au site est proposée, permettant de simuler uniquement un jour représentatif à chaque saison. Ensuite, la méthodologie de couplage d'ENVI-met et de COMFIE est présentée pour effectuer une simulation plus précise sous l'effet UHI.

La méthodologie proposée a été appliquée à l'étude de cas à Wuhan (Chine), qui a été présentée au chapitre 1. Une quartier de 660 m × 660 m a été modélisé et la simulation du microclimat a été effectuée pendant quatre jours représentatifs par ENVI-met. L'intensité de l'îlot de chaleur urbain (*Urban heat island intensity*, UHII) horaire a été obtenu en appliquant la méthode proposée et un ensemble de fichiers météorologiques spécifiques au site considérant l'effet UHI généré pour 4 orientations et 6 hauteurs. Ce nouvel ensemble de fichiers météorologiques locaux a permis une simulation plus précise, concernant différentes températures de l'air pour des zones thermiques d'orientations et de hauteurs différentes. L'UHII moyenne annuelle à une hauteur de 3 m a été estimé à 0,45 °C. La simulation utilisant le fichier EPW (*EnergyPlus Weather*) d'origine a montré des besoins de chauffage plus élevés de 3,5 %, des besoins de refroidissement plus petits de 3,9 % et une consommation d'énergie totale plus petite de 0,2 %, par rapport à la simulation de référence. Si seul le fichier météorologique à 3 m de hauteur au sud était utilisé, les besoins de chauffage diminueraient de 5,4 % et les besoins de refroidissement augmenteraient de 6,9 % par rapport au fichier EPW.

Abstract

During urbanisation, the urban environment is altered and shows different climate characteristics compared to the rural areas. The building energy performance evaluations are mainly based on a weather file containing 8 760 hours of climate data (e.g. air temperature and humidity). As an essential boundary condition, the accuracy of the weather input file directly influences the simulation results. Usually, this weather file is usually collected in rural regions, which cannot reflect the microclimate around the building and might cause noticeable differences. One well-known urban climate phenomenon is the urban heat island (UHI) effect, describing the fact that the urban air temperature is higher than the rural air temperature. This chapter aims at quantitatively evaluating the microclimate's effects (particularly the UHI effect) on the building energy performance.

The microclimate simulation tool ENVI-met is presented and used to obtain the microclimate's parameters. The microclimate simulation time is too long for a standard PC to obtain the hourly microclimate data for the whole year. Thus, a site-specific weather file generation method is proposed, allowing simulating only one representative day in each season. Afterwards, the coupling methodology of ENVI-met and the DBES tool COMFIE is presented to perform a more accurate simulation under the UHI effect.

The proposed methodology was applied to the case study in Wuhan (China), which was presented in chapter 1. A district area of 660 m × 660 m was modelled and the microclimate simulation was performed for four representative days by ENVI-met. The hourly urban heat island intensity (UHII) was obtained by applying the proposed method and a set of site-specific weather files considering UHI effect was generated for 4 orientations and 6 heights. This new set of local weather files yielded a more precise simulation, concerning different air temperatures for the thermal zones of different orientations and heights. The yearly average UHII at the height of 3 m was estimated to be 0.45 °C. The simulation using the original EPW (EnergyPlus Weather) file showed a heating load 3.5 % larger, a cooling load 3.9 % smaller and a total energy load smaller 0.2 %, compared to the reference simulation. When only the weather file at the height of 3 m in the south was used, the heating load decreased by 5.4 % and the cooling load increased by 6.9 % compared to the EPW file.

4.1. Introduction

4.1.1. *Urbanisation and UHI*

As presented in chapter 1, China is moving towards urbanisation and this process will last for decades. Taking Wuhan, the largest city in central China, as an example, its land area has been transforming to construction land in the last ten years, as shown in Figure 4.1 (Huang et al., 2019). As the numbers of buildings and occupants increase, the local climate in the urban areas is altered. The microclimate around a building is an essential boundary condition that affects the building thermal performance, due to the heat exchange processes happening at the external surface of the building. In the urban areas, the urban heat island (UHI) effect is a well-known phenomenon among the microclimate features and can be quantitatively described by the urban heat island intensity (UHII), which is the urban air temperature minus the rural air temperature. Occasionally, the urban air temperature can be lower than the rural air temperature, which is called the urban cool island (UCI) effect, and the temperature difference is the urban cool island intensity (UCII).
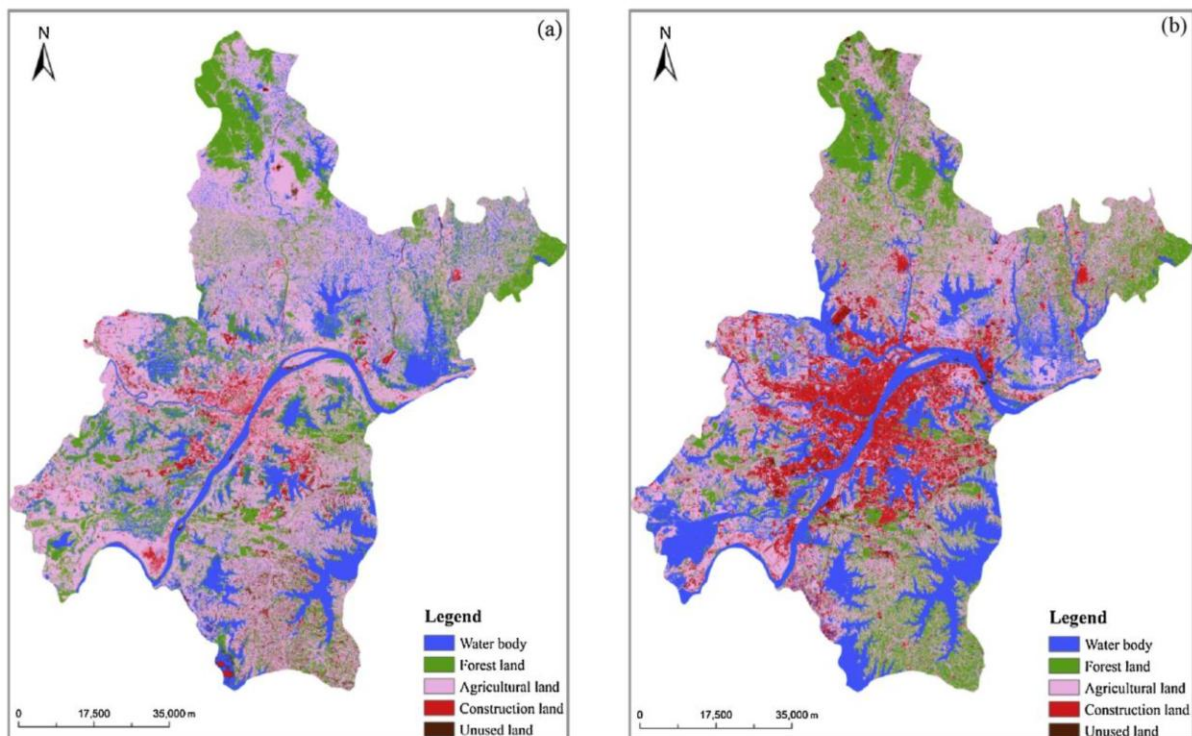
Figure 4.1: Land use of Wuhan in (a) 2005 and (b) 2015 (Huang et al., 2019)

Residential and commercial buildings account for large energy consumption and CO_2 emissions, as well as other environmental impacts. DBES tools are widely used by building designers and engineers to investigate the energy saving potential through applying different design plans, involving building equipments and operating scenarios. As an essential boundary condition for DBES, the accuracy of the weather file comprising 8 760 hours of various climatic parameters such as air

temperature and solar radiation, strongly influences the simulation results. In the present DBES tools, the mostly used weather file format is Typical Meteorological Year (TMY) (Hall et al., 1978) format, which consists of 12 Typical Meteorological Months (TMM) from the past decades (McLeod et al., 2012). These data usually come from the meteorological stations located in the peripheral zones, which have a significantly different morphological form from the urban areas composed of dense buildings. In the literature review of this thesis, many studies indicated the UHI effect usually leads to a larger cooling load and a smaller heating load. The energy performance evaluation of the buildings in urban area might bring non-negligible errors if TMY weather file is directly used as the boundary condition in the DBES tool. A weather input file considering the local microclimate can yield a more accurate evaluation of building energy performance, especially in the urban areas where the UHI effect is observed.

The aim of this chapter is to quantitatively evaluate the microclimate's effects on the building energy performance, based on the DBES tool COMIFE, which also uses a yearly weather file containing hourly climate data for 52 weeks. The urban climate parameters are mainly obtained by measurement or simulation. In this thesis, the microclimate simulation tool ENVI-met is used to evaluate the microclimate parameters, instead of measurements. However, the microclimate simulation time is quite long for a standard PC, so that it is not possible to obtain the hourly microclimate data for the whole year in a timely manner. A method for the hourly microclimate parameters generation could be beneficial. Afterwards, the microclimate simulation tool should be coupled to COMFIE in order to quantitatively evaluate the microclimate's effects on the building energy performance.

Therefore, this chapter proposes a site-specific weather file generation method accounting for hourly microclimate parameters for a TMY, allowing to simulate only one representative day in each season. The coupling methodology of ENVI-met and COMFIE is presented to perform a more accurate simulation of the building energy performance under the UHI effect. Finally, the effects of UHI on the energy performance of the case study presented in chapter 1 are quantitatively investigated.

4.1.2. *Introduction to ENVI-met*

ENVI-met is a three-dimensional (3D) numerical model initially developed by Bruse and Fleer (1998) to analyse microclimates through the fundamental laws of fluids and thermodynamics. The main difference between ENVI-met and large-scale atmospheric models used for the prediction of the daily weather or future climate conditions is the temporal and spatial model resolution (Huttner, 2012). The interactions between buildings, soil, vegetation and atmosphere can be simulated with a typical spatial resolution between 0.5 m and 10 m and a timestep of 1 - 10 s. Every single plant and every urban structure can explicitly be simulated, making ENVI-met the perfect tool for urban planners, architects and urban climatologists who want to simulate the meteorological components of the urban environment (Huttner, 2012). This model has been validated by several studies (Ayyad and Sharples, 2019 ; Elwy et al., 2018 ; López-Cabeza et al., 2018 ; Sharmin and Steemers, 2017 ; Tsoka et al., 2018 ; Yang et al., 2013) for different cities with different microclimate conditions.

The model structure of ENVI-met is shown in Figure 4.2. In order to accurately determine the microclimate, the height of the model should be high enough, however this brings a computation complexity. In ENVI-met, a simplified one-dimensional (1D) model is used to initialise the upper boundary of the main 3D model. It considers the whole height H divided into two layers: from 0 to the main model height z, it is identical to the cells division of the main model; from z to $H = 2500$ m, it is divided into 15 cells with a telescoping height (higher cell with larger spacing).
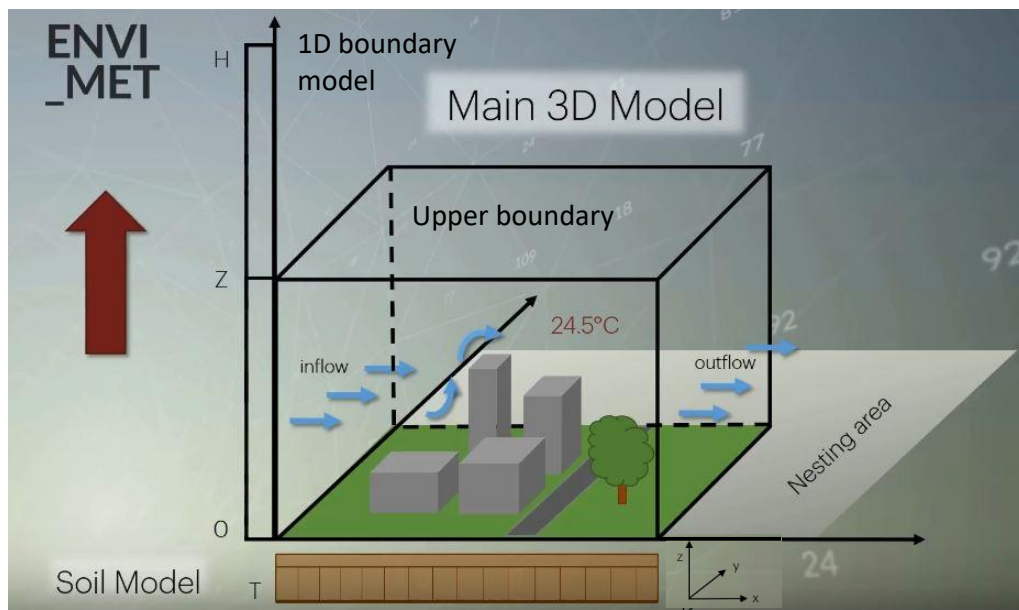
Figure 4.2: Structure of ENVI-met model

The main 3D model is divided into a rectangular grid consists of $I \times J \times K$ cells with dimensions $\Delta x \times \Delta y \times \Delta z$. Buildings, vegetation and the digital elevation model are constricted to this rectangular grid. This means that a cell is either fully occupied by one of these obstacles or not at all. On the horizontal surface, Δx and Δy (usually from 0.5 m to 10 m) are constant for all the cells. On the vertical direction Δz can be defined from four types (Yang, 2012), as shown in Figure 4.3. Generally, the cell close to the ground surface should have a smaller dimension, in order to have a more accurate simulation of the interactions between the ground and the atmosphere. The dimension of the higher cells can be larger to save the simulation time. The nesting area is an option to the main model in order to reduce the boundary effects, where only the surface type can be defined instead of the plants and the buildings.

The outflow boundary of the main 3D model is a free boundary. The upper boundary is a "forced boundary" with the values calculated by the 1D boundary model. The inflow boundary can be set as "open", "forced" or "cyclic". In the open lateral boundary condition, the values of the next grid point close to the border are copied to the border for each timestep. In the forced boundary condition, the values of the 1D model or from the forcing data are copied to the border. In the cyclic lateral boundary condition, the values of the downstream model border are copied to the upstream model border.

(a) Constant Δz
(bottom cell is dividied into 5 subcells)

(b) Telescoping Δz

(c) Telescoping Δz
(telescope from n^{th} cell)

(d) Constant Δz
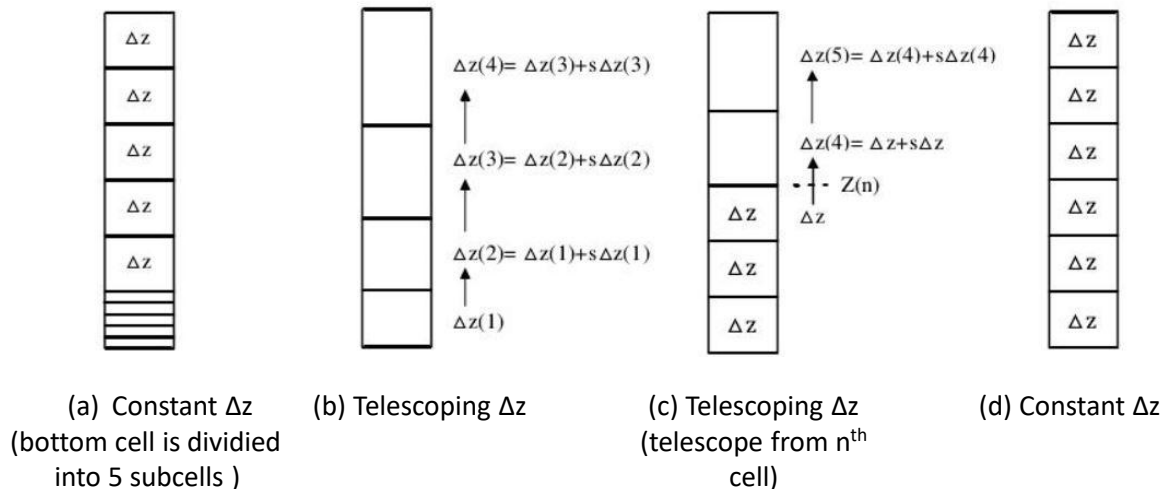
Figure 4.3: Four types of vertical grid in ENVI-met (Yang, 2012)

ENVI-met V4.4.4, the latest version, allows the users to simulate various meteorological conditions with their own data or EnergyPlus Weather (EPW) files by using the function ''full forcing''. The customisable meteorological variables include incoming direct and diffuse solar radiations, downward long-wave radiation, background concentration of particle/gas, as well as 1D vertical profiles of atmospheric parameters (such as air temperature, specific humidity, wind speed and direction). These 1D meteorological profiles (from the ground surface to 2 500 m height) are used as the lateral and top inflow boundaries of the main model (3D). Usually, the atmosphere profile information is obtained from radiosonde observation. However, if there is a lack of such information, the observed data from meteorological station at ground level can be interpolated temporally and spatially to the full 1D profile. The methods of interpolation are illustrated as follows: the assumption of neutral stratification of atmosphere is used for air temperature profile (constant potential temperature for all levels); simple logarithmic interpolation is applied for the vertical wind profile calculation; wind direction is kept constant at all levels; the humidity profile of atmosphere is interpolated linearly, according to the observed data at ground level and the input specific humidity at 2 500 m above ground. It should be noted that the air temperature in "FOX file (see Figure 4.4)", $T_{air,fox}$, is converted into potential temperature based on atmosphere pressure and temperature recorded in the EPW file with the following equation (4-1):

$$T_{air,fox} = T_{air,EPW}^{abs} \left(\frac{P_0}{P}\right)^{0.286}$$
(4-1)

where $T_{air,EPW}^{abs}$ is the absolute air temperature (K) in EPW file, P_0 is the reference pressure (100 000 Pa in ENVI-met) and P is the atmosphere pressure (Pa) in EPW file.

A FOX file recording the user-defined meteorological parameters is generated to be used in the microclimate simulation. The format of a FOX file is shown in Figure 4.4.

```
<date> 01.01.2018 </date>          ─── Date and time
<time> 01:00:00 </time>
<dataSrc> EPW </dataSrc>
<dataType> orig </dataType>
<radSurface> horizontal </radSurface>
<dirRad> 0.00000 </dirRad>         ─── Direct horizontal radiation (Wh/m²)
<difRad> 0.00000 </difRad>              Diffuse horizontal radiation (Wh/m²)
<lwRad> 261.64029 </lwRad>              Longwave radiation (Wh/m²)
<lClouds> -999.00000 </lClouds>
<mClouds> -999.00000 </mClouds>    ─── Cloud (cannot be set at the same time with radiation)    Background concentration (mg/m³)
<hClouds> -999.00000 </hClouds>
<precipitation> 0.00000 </precipitation>
<atmPressure> 1020.00000 </atmPressure>    ─── Precipitation and atmosphere pressure (hPa)
<backgroundpollutants> 0.00000,0.00000,0.00000,0.00000,0.00000,0.00000,0.00000,0.00000,0.00000 </backgroundpollutants>
<profileData type="matrix-data" dataI="5" dataJ="3" signcount="5">
    0.0000,   274.8903,      0.0000,      0.0000,    7.1602       From left to right: Height (m), Potential temperature (K),
   10.0000,   274.8903,     -0.2819,     -0.1026,    7.1602       U of wind (m/s), V of wind (m/s), Specific humidity (g/kg)
 2500.0000,   274.8903,     -0.6199,     -0.2256,    7.1602
</profileData>
</impulse>
<impulse>
   <date> 01.01.2018 </date>       ─── Next timestep
   <time> 01:30:00 </time>
```

Figure 4.4: Structure and format of the full forcing file (.FOX) in ENVI-met 4.4.4

The soil model divides a 2 m depth of the soil into 14 non-equidistant layers, as illustrated in Figure 4.5. The closer to the surface, the smaller the layer depth is. The user can define different components for these 14 layers based on reality. This model is a 1D model only considering the heat and water transfer in the vertical direction. More detailed information about other models (e.g. building model, radiation model) used in ENVI-met can be found on its website (https://www.ENVI-met.com/) and in dedicated references (Bruse and Fleer, 1998 ; Huttner, 2012).
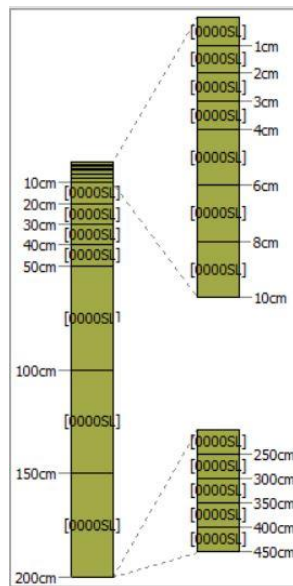
Figure 4.5: Vertical grids layout of the soil model in ENVI-met

4.2. Methodology

4.2.1. *Site-specific weather file generation method*

To identify the local microclimate's effects on the building energy performance, COMFIE is used for DBES. The simulation of buildings' energy performance requires a yearly file containing hourly values of meteorological data. However, as a complex dynamic numerical microclimate model, the simulation of ENVI-met for even one day brings a heavy calculation load (around one day in our study). It is not possible to obtain the hourly microclimate effects for one year with a standard PC, especially if the energy performance optimisation of a building or a block is needed in the design-phase. Thus, the key point for the integration of the DBES simulation tool and the microclimate tool is to propose a method which can generate a "site-specific weather file" containing the hourly microclimate's effects appropriately in reasonable simulation time.

The reference typical weather file for DBES in COMFIE in this chapter is an EPW format file downloaded from the website of EnergyPlus[17]. It is a TMY format file composed of 12 TMMs, which can appropriately represent the typical meteorological parameters in the past decades. This file also records the extreme air temperature weeks in summer and winter and the average air temperature weeks for all four seasons, which is convenient to analyse the representative days of the four seasons. The other reason why EPW file is chosen is that it can be directly and easily imported in the full-forcing function in ENVI-met to generate the forcing file for microclimate simulation. In this chapter, if not especially indicated, spring refers to March, April and May; summer refers to June, July and August; autumn refers to September, October and November; winter refers to December, January and February.

The proposed site-specific weather file generation method considering the local microclimate consists of four steps:

1. One representative day of the representative week (extreme hot/cold week for summer/winter and average week for spring/autumn, which are directly given in EPW file) of each season is chosen based on air temperature: extreme hot day in summer (ex-summer), extreme cold day in winter (ex-winter) and average days in spring (av-spring) and autumn (av-spring);

2. Then these four representative days are simulated in ENVI-met to obtain the local microclimate parameters and the UHIIs;

3. The hourly UHIIs are obtained with linear interpolation for 24 hours between each two representative days;

4. The air temperature of the site-specific weather file is generated by adding the hourly UHII to the original EPW file.

The algorithm of the proposed method is shown in Figure 4.6.

---

[17] https://energyplus.net/weather-location/asia_wmo_region_2/CHN/CHN_Hubei.Wuhan.574940_SWERA
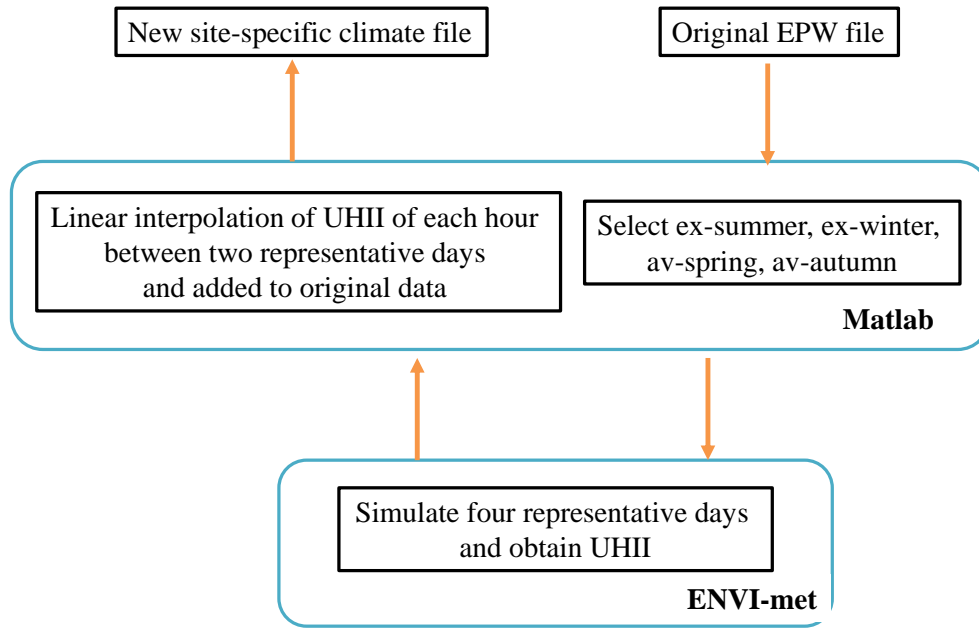
Figure 4.6: Algorithm of the proposed method to generate the site-specific weather file

In step 1, in order to determine the representative day of the representative week of each season, the average temperature of ith hour $T_{\text{av},i}$ of the representative week is firstly to be identified using equation (4-2):

$$T_{\text{av},i} = \frac{\sum_{j=1}^{7} T_i^j}{7} \quad i = 1 \dots 24 \tag{4-2}$$

where T_i^j is temperature of the ith hour of the jth day in the representative week.

The root mean square error (RMSE) and the mean absolute error (MAE) of each day for the 24 hours are calculated by:

$$RMSE_j = \frac{\sqrt{\sum_{i=1}^{24} (T_i^j - T_{\text{av},i})^2}}{24} \tag{4-3}$$

$$MAE_j = \frac{\sum_{i=1}^{24} |T_i^j - T_{\text{av},i}|}{24} \tag{4-4}$$

The day with the smallest RMSE is chosen as the representative day of each season; if RMSE is similar, the day with smaller MAE is selected.

In step 3, knowing the four representative days, the UHII of the ith hour of the jth day in the whole year can be calculated by linear interpolation:

$$\text{UHII}_i^j = \frac{\text{UHII}_i^{j_{\text{re2}}} - \text{UHII}_i^{j_{\text{re1}}}}{j_{\text{re2}} - j_{\text{re1}}} (j - j_{\text{re1}}) + \text{UHII}_i^{j_{\text{re1}}} \tag{4-5}$$

where j_{re1} and j_{re2} are the day numbers of the 1$^{\text{st}}$ and 2$^{\text{nd}}$ representative day.

It should be noted that the linear interpolation between two representative days to obtain the hourly UHII for the whole year is a highly simplified assumption. The hourly variation of UHII in cities is much more complex due to enormous factors such as the complicated urban synoptic and systems, various constructions and plants and climate conditions. The main aim of this study is to identify the UHI effect on the building energy demands for a long time (usually one year), rather than accurately estimate the UHI variation of one day. The assessment of the UHI effect on building energy demands for a long time mainly relies on the estimation of a general UHI feature, so there is a certain tolerance on the biases of hourly UHII (Yang et al., 2019).

4.2.2. *Coupling microclimate simulation tool with DBES tool*

As reviewed in section 1.4.3, the coupling of a microclimate tool and a DBES tool are classified into one-way coupling and double-way coupling. In this thesis, the coupling of ENVI-met and COMFIE is one-way coupling, meaning the simulation results of ENVI-met are transferred to COMFIE but without feedback. The key point in the coupling of a microclimate simulation tool and a DBES tool is modifying the weather input file from the original one (e.g. the meteorological data from rural stations) to the new one (which considers the urban microclimate). The reviewed coupling methods use one temperature file for the whole building.

In COMFIE, a building is usually modelled into thermal zones (as presented in section 4.1.2.4) and simulated according to the orientations and heights. However an identical temperature profile is used for the whole building, regardless of its height and zone orientation. In urban areas in China, the buildings are dense and high-rise. The temperature profile might be rather different in the different orientations, as well as along the height. Accurate simulation should consider these differences.

The coupling method proposed in this chapter considers the air temperature variation with height and orientation, based on the microclimate simulation results. The temperature profiles of four orientations (north, south, west and east) along N_h different heights (depending on the zone definition) are generated from the microclimate simulation tool ENVI-met. The temperature profiles are inputted in the weather tool Meteocalc (which is integrated in Pleiades) and corresponding site-specific weather files are generated and then used by COMFIE for building energy simulation. The whole coupling method is shown in Figure 4.7.
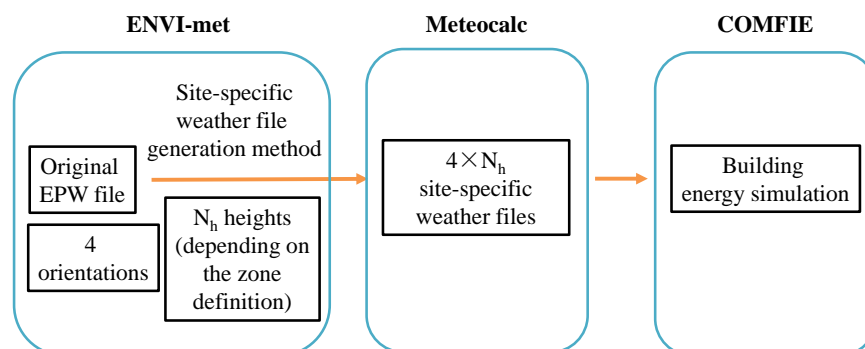
Figure 4.7: Method of coupling microclimate tool with the DBES tool

4.3. Case study

4.3.1. *Microclimate simulation configuration*

The basic geometric information about the case study and Wuhan city has been presented in section 1.6. Locating the studied building approximately in the centre, the total area for microclimate simulation is a region of 660 m × 660 m, as shown in Figure 4.8. Although it is very difficult to obtain the detailed surroundings information, it is still possible to get a rough picture of the surroundings including the heights of the buildings, the green areas and the roads by using Google Map and Google Earth. This information allows to apply a microclimate model e.g. ENVI-met to evaluate the site-specific climatic conditions. If detailed data of the surroundings can be obtained, a more accurate simulation can be performed. Accounting for the calculation speed and the model accuracy, $110 \times 110 \times 19$ cells were used in this study, with the resolution of 6 m in the horizontal directions. In the vertical direction, the solution of one cell is 6 m below 30 m (the first 5 cells) and afterwards the height of cell $n + 1$ is the height of cell n multiplied by 1.25 (n being the level of the cell from 6 to 19). This corresponds to method (c) in Figure 4.3. Besides, 8 empty cells were set at each border to increase the stability and accuracy of the simulation, which is the "nesting area" shown in Figure 4.2.
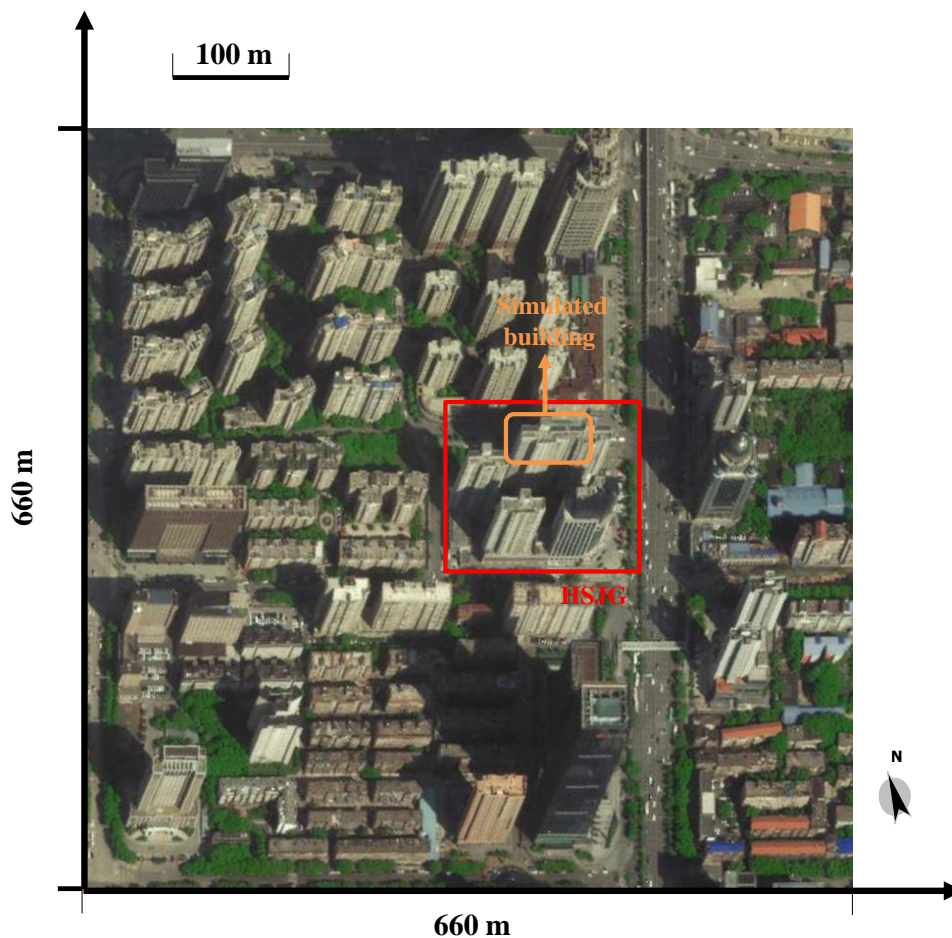
Figure 4.8: Simulated area in ENVI-met

The ground in the simulated area mainly contains four types of ground profiles: the brick road, the concrete field, the green field and the asphalt concrete road. The depths of the compositions of the ground profiles in ENVI-met are listed in Table 4-1 and the modelled figure is shown in Figure 4.9.

Table 4-1   Composition and its depth in the ground profiles in ENVI-met

Brick road	Concrete field	Green field	Asphalt concrete road
Brick: 0~3 cm	Concrete: 0~20 cm	Sandy loam: 0~40 cm	Asphalt: 0~10 cm
Concrete: 4~20 cm	Sand: 21~ 30 cm	Loam: 41~450 cm	Sand: 11~40 cm
Sand: 21~30 cm	Loam: 31~450 cm		Loam: 41~450 cm
Loam: 31~450 cm			
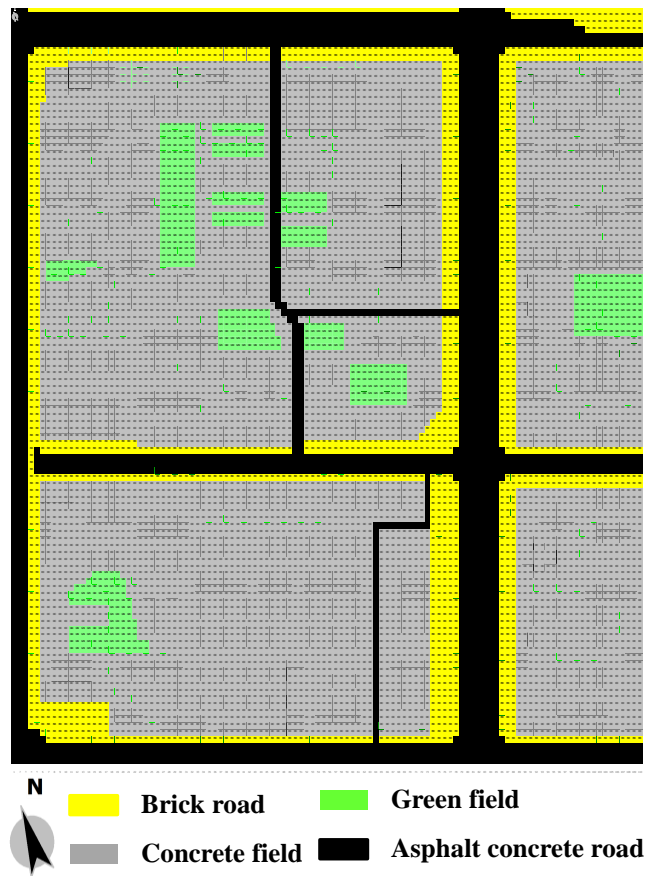
Figure 4.9: Ground profile of the simulated area in ENVI-met

Another soil parameter is the initial temperature and the relative humidity for the four layers of the soil: upper layer (0-20 cm), middle layer (20-50 cm), deep layer (50-200 cm) and bedrock layer (below 200 cm). Assuming the soil is semi-infinite and with unique physical properties, the soil temperature $T_{\text{soil}}(z,t)$ of depth z at time t can be calculated by (Thiers, 2008):

$$T_{\text{soil}}(z,t) = \overline{T_{\text{soil\_surf}}} + A_{\text{soil\_surf}} \cdot \exp\left(-\frac{z}{\delta(\omega)}\right) \cdot \sin\left(\omega \cdot t - \varphi_{\text{soil\_surf}} - \frac{z}{\delta(\omega)}\right) \qquad \textbf{(4-6)}$$

where

$$\delta(\omega) = \sqrt{\frac{2 \cdot \alpha_s}{\omega}} \tag{4-7}$$

$\overline{T_{soil\_surf}}$ is the average temperature of the soil surface, 19 °C in this chapter;

A_{soil_surf} is the amplitude of the oscillation of the temperature of the soil surface, 15 °C in this chapter;

ω is the pulsation of the oscillation of the temperature of the soil surface, rad/s, $\frac{2\pi}{8760\times3600}$ rad/s in this chapter;

φ_{soil_surf} is the phase shift of the temperature of the soil surface (the temperature peak is set at July 31, 14:00 in this chapter); it is equal to 2.07 rad;

α_s is the thermal diffusivity of the soil, 1.23×10^{-6} m^2/s in this chapter.

Then the soil temperatures of the upper layer T_{upper}, the middle layer T_{middle}, the deep layer T_{deep}, and the bedrock layer $T_{bedrock}$ are calculated by:

$$T_{upper}(t) = \frac{T_{soil}(0,t) + T_{soil}(0.1,t) + T_{soil}(0.2,t)}{3} \tag{4-8}$$

$$T_{middle}(t) = \frac{T_{soil}(0.2,t) + T_{soil}(0.3,t) + T_{soil}(0.4,t) + T_{soil}(0.5,t)}{4} \tag{4-9}$$

$$T_{deep}(t) = \frac{T_{soil}(0.5,t) + T_{soil}(1,t) + T_{soil}(1.5,t) + T_{soil}(2,t)}{4} \tag{4-10}$$

$$T_{bedrock}(t) = 19\ °C \tag{4-11}$$

With the abovementioned inputs, the soil temperatures of different layers and the surface are shown in Figure 4.10.
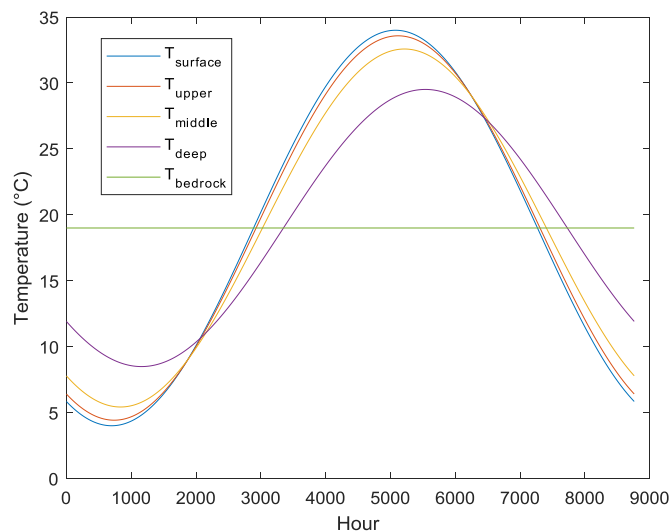
Figure 4.10: Soil temperatures of different layers

The corresponding soil relative humidities of the four layers in ENVI-met were calculated from (Wu et al., 2017), as listed in Table 4-2.

Table 4-2 **Soil relative humidity of case study in ENVI-met**

	Spring (Mar, Apr, May)	Summer (Jun, Jul, Aug)	Autumn (Sep, Oct, Nov)	Winter (Dec, Jan, Feb)
Upper layer (0-20 cm)	77 %	85 %	84 %	80.5 %
Middle layer (20-50 cm)	80.5 %	81 %	83 %	83 %
Deep layer (50-200 cm)	82 %	79 %	81 %	84 %
Bedrock layer (below 200 cm)	82 %	79 %	81 %	84 %

The plants in this area are shown in Figure 4.11. It should be noted that the density of the plants' leaves vary with the season in the simulation. Considering the aim of ENVI-met simulation is to obtain the outdoor air temperature, instead of the indoor thermal comfort or other parameters concerning the building envelope, the building's envelope configuration is not as important as other configurations, thus the envelopes of all the buildings are set to be identical, as shown in Table 4-3.
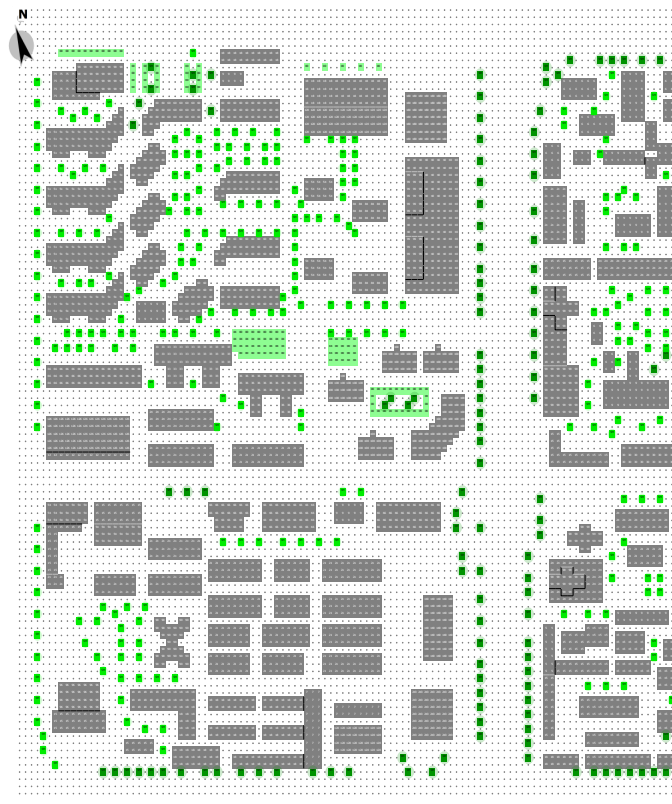
Figure 4.11: Vegetations in the simulated area in ENVI-met

Table 4-3   ***Wall configuration of the buildings in ENVI-met***

External wall	**Roof**
Ceramic tile 1 cm	Ceramic tile 1 cm
Insulation mortar 4 cm	Extruded Polystyrene Board (XPS) 4 cm
Aerated concrete block 20 cm	Concrete (C10) 20 cm

Receptors can be set at the nodes in the simulated area, recording the detailed simulation results for each height of the node on the vertical axis. In order to analyse the effects of the orientation on the building's energy performance, four receptors around the simulated building were used: North (N), West (W), South (S) and East (E), as illustrated in Figure 4.12.
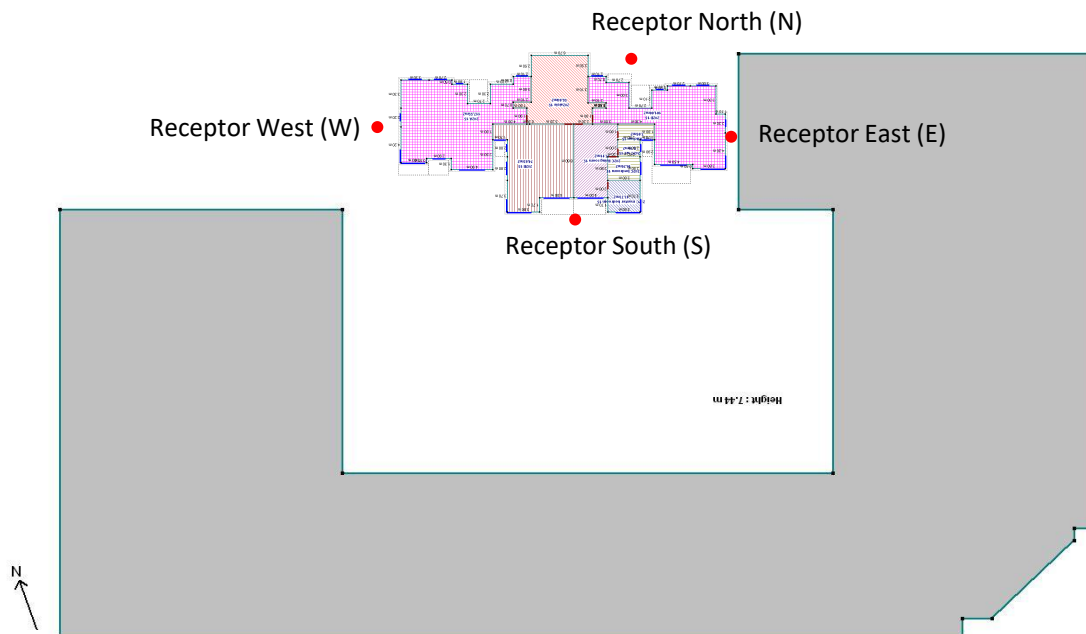
Figure 4.12: Four receptors around the case study

The simulated area was modelled in the submodel SPACES in ENVI-met. The whole 3D model is shown in Figure 4.13.

N

	Brick road		Green field
	Concrete field		Asphalt concrete road

Figure 4.13: 3D model of the simulated area

4.3.2.   *Weather file*

4.3.2.1.   **Original EPW file**

The EPW file downloaded from EnergyPlus website is *CHN_Hubei.Wuhan.574940_SWERA.epw*. According to the file, the site is located at the latitude of N 30.62° and longitude of E 114.13°. The main meteorological parameters are shown in Figure 4.14 to Figure 4.17.

The four representative weeks of the four seasons are shown in Table 4-4, which are directly indicated by the EPW file.

Table 4-4   Four representative weeks

	Summer	Winter	Spring	Autumn
	Extreme high	**Extreme cold**	**Average temperature**	**Average temperature**
Week	Aug 05-11	Jan 01-07	May 27-Jun 02	Nov 26-Dec 02
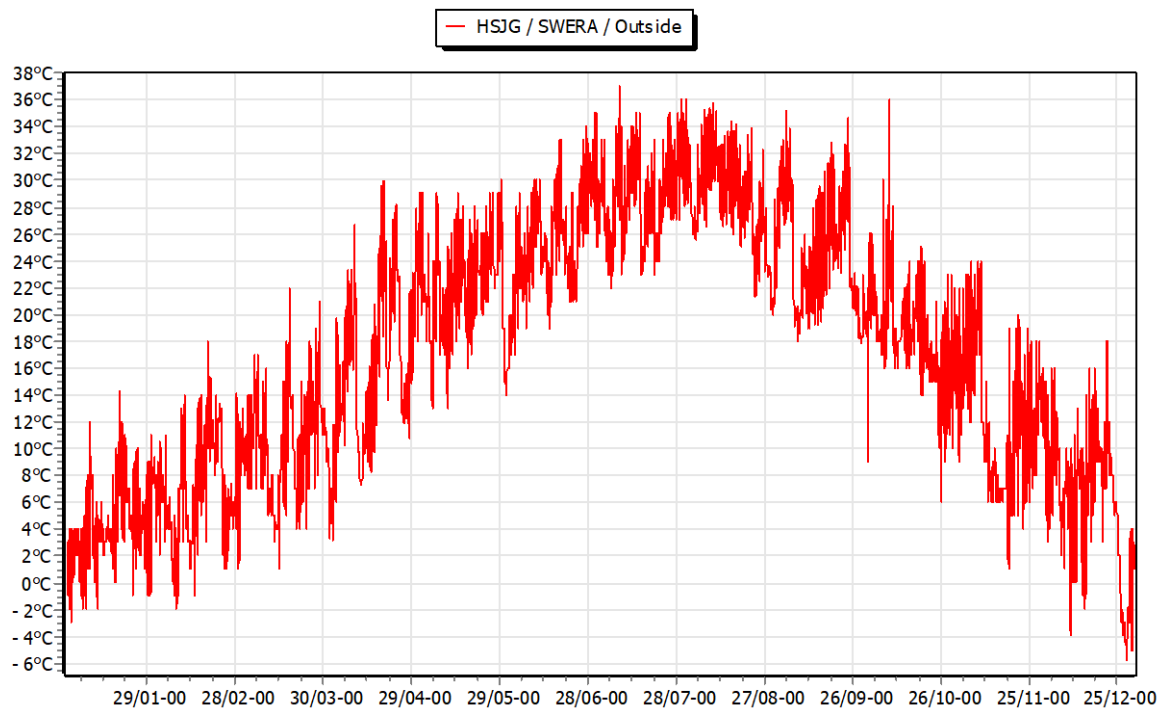
Figure 4.14: Air temperature in EPW file
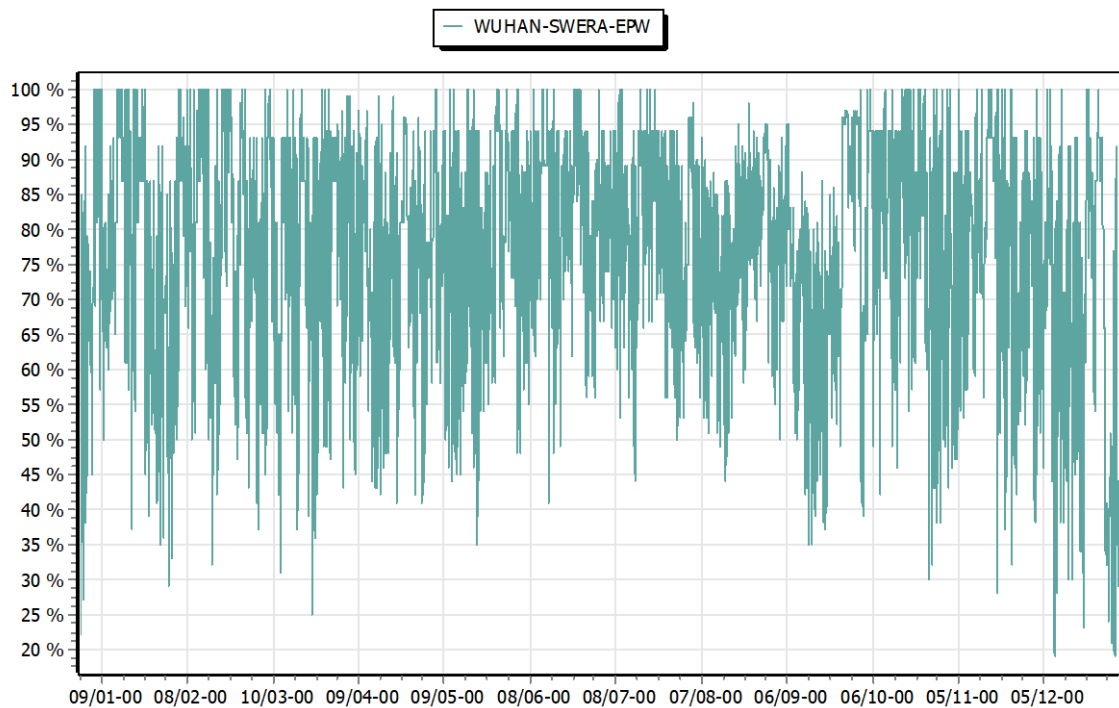
Figure 4.15: Relative humidity in EPW file
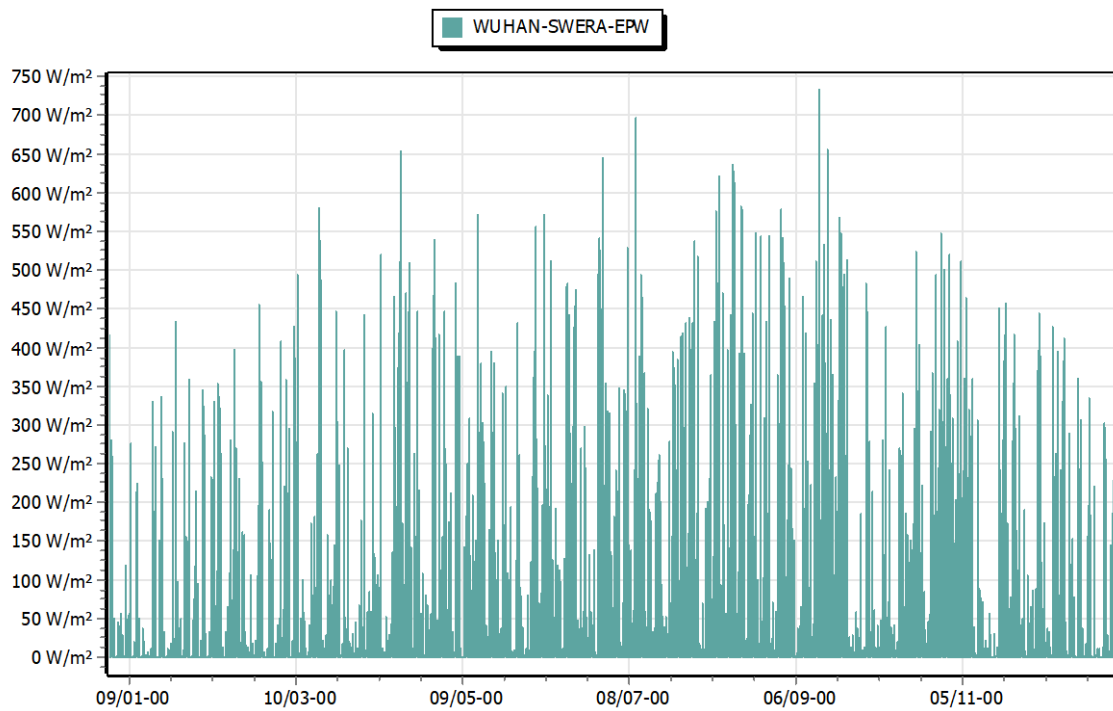
Figure 4.16: Direct horizontal irradiance in EPW file
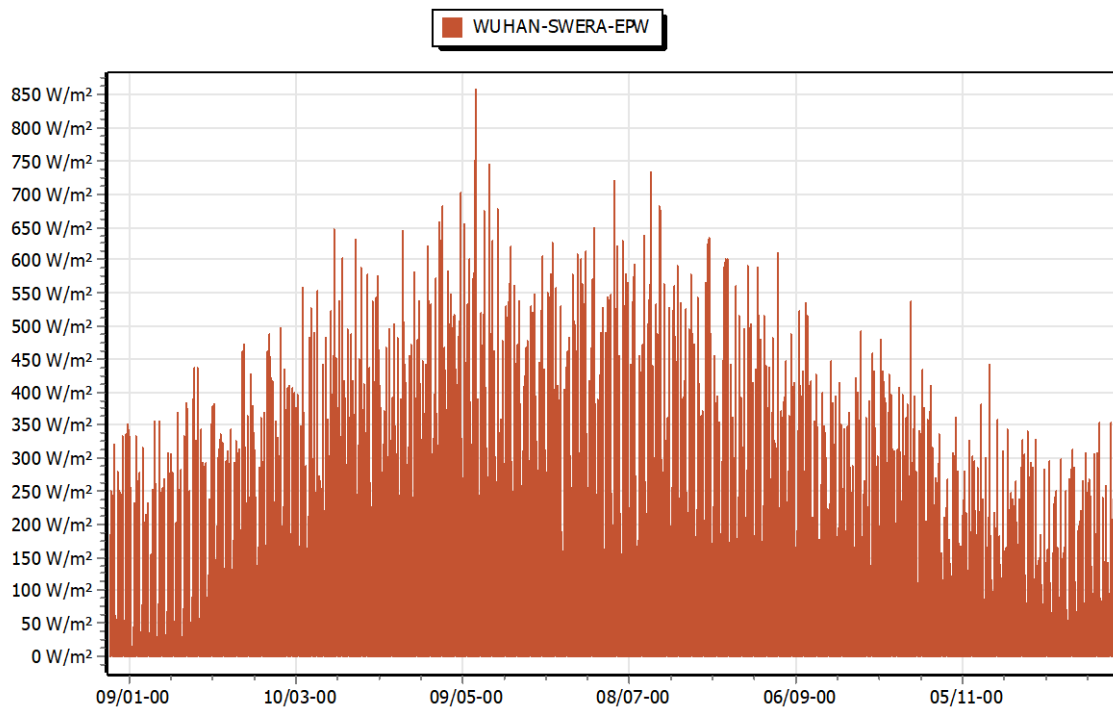
Figure 4.17: Diffuse horizontal irradiance in EPW file

4.3.2.2. Microclimate simulation weather file

Using the site-specific weather file generation method, the representative day of each season was selected for the microclimate simulation. The day of each week with the smallest RMSE was chosen as the representative day for each season. The results are shown in Table 4-5. The microclimate simulation has better accuracy with a buffering time, thus an extra day (48 hours in total) was used to obtain more precise simulation results.

Table 4-5   Representative days of each season

Season	Abbreviation	Representative day	RMSE (°C)	MAE (°C)
Summer Extreme hot	Ex-summer	Aug 09	0.82	0.76
Winter Extreme cold	Ex-winter	Jan 04	1.11	0.90
Spring Average temperature	Av-spring	Jun 02 (date is in June, but represents spring)	1.48	1.19
Autumn Average temperature	Av- autumn	Nov 30	1.25	1.02

4.3.2.3. Building energy simulation weather file

The building was described in detail in section 1.6. The temperature variation along the height could influence the energy loads of the building. Combining the zone definition and the height of ENVI-met cells，6 different heights were chosen for the DBES weather file generation. For example, the building level 2 – 6 is divided into two zones in section 1.6.2.4, as the north zone (contacts with north/west/south/east air) and south zone (contacts with south air). The vertical cells in ENVI-met record the air temperatures at 9 m and 15 m during the height of 6 to 18 m from level 2 to 6. Thus we use the average of the air temperatures at 9 m and 15 m to generate the weather input file for this two zones. Therefore, considering four orientations (N, W, S, E) and 6 heights (from #1 to #6), 24 DBES weather files were generated as inputs for the energy simulation, as illustrated in Table 4-6.

Table 4-6   The height of weather file for building energy simulation

Building level	Level height	Weather file number of 4 orientations	ENVI-met height by averaging the heights of vertical cells
1	3 m	N#1, W#1, S#1, E#1	3 m
2 – 6	6 – 18 m	N#2, W#2, S#2, E#2	(9 m + 15 m) / 2 = 12 m
7 – 14	21 – 42 m	N#3, W#3, S#3, E#3	(21 m + 27 m + 33.75 m + 42.19 m) / 4 = 31 m
15 – 25	45 – 75 m	N#4, W#4, S#4, E#4	(52.73 m + 65.92 m) / 2 = 59.3 m
26 – 33	78 – 99 m	N#5, W#5, S#5, E#5	82.4 m
34	102 m	N#6, W#6, S#6, E#6	103 m

4.4. Results and discussion

4.4.1. *Microclimate simulation results*

Figure 4.18 to Figure 4.21 show the potential air temperature maps of the simulated region for the four representative days at the height of 3 m at 13h00 (av-spring and ex-summer) and 14h00 (av-autumn and ex-winter) when the maximum UHII are observed. The northeast region containing the asphalt road and the southwest region respectively show the highest and lowest UHI effect on all these four days. On ex-summer and av-autumn, the UHI effect is obvious along the north-south asphalt road, in which the north part has a stronger UHI effect. The temperature surrounding HSJG can vary over 1.5 °C on ex-summer, particularly higher on the side of the north-south asphalt road, but on other days the temperature difference is not very large (< 0.5 °C).
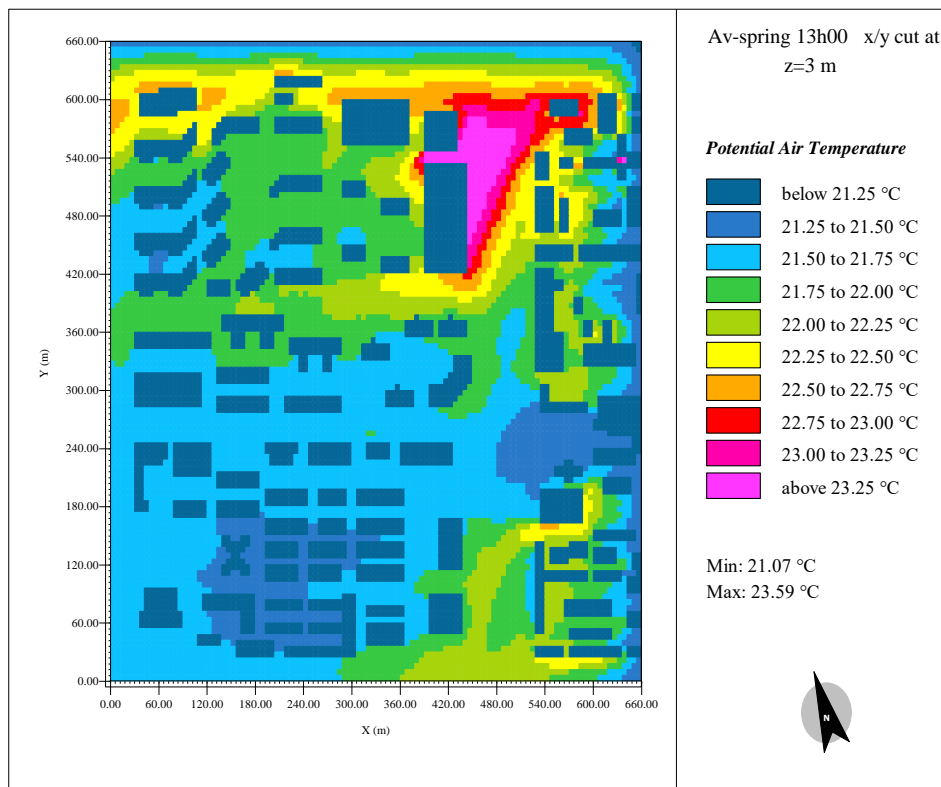
Figure 4.18: Potential temperature map of the simulated area for av-spring
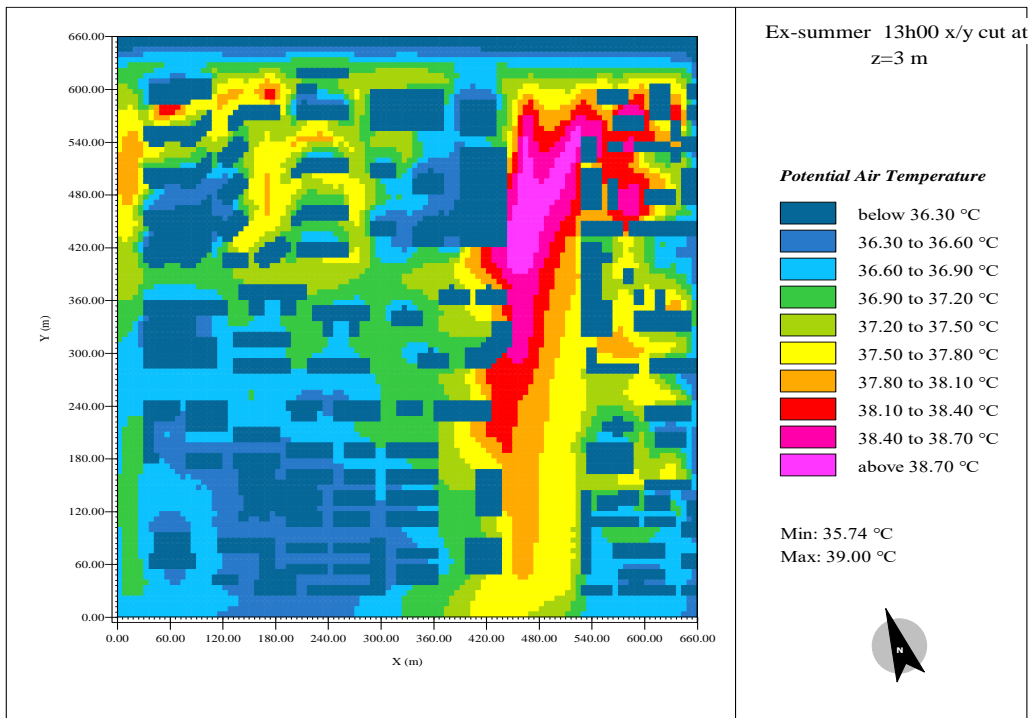
Figure 4.19: Potential temperature map of the simulated area for ex-summer
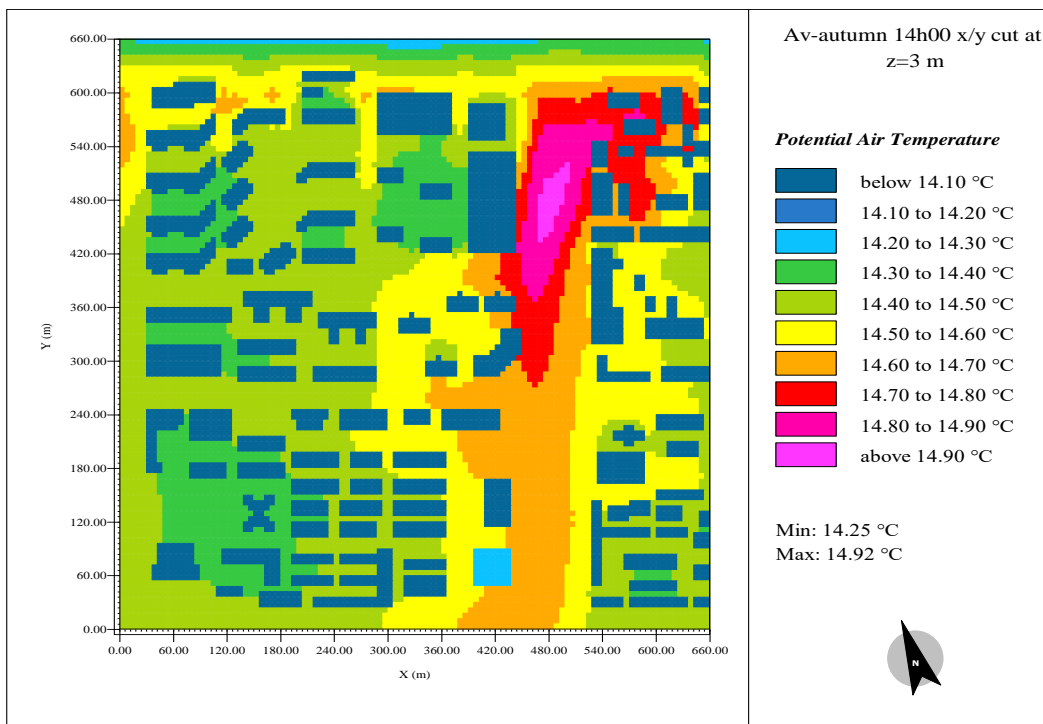
Figure 4.20: Potential temperature map of the simulated area for av-autumn
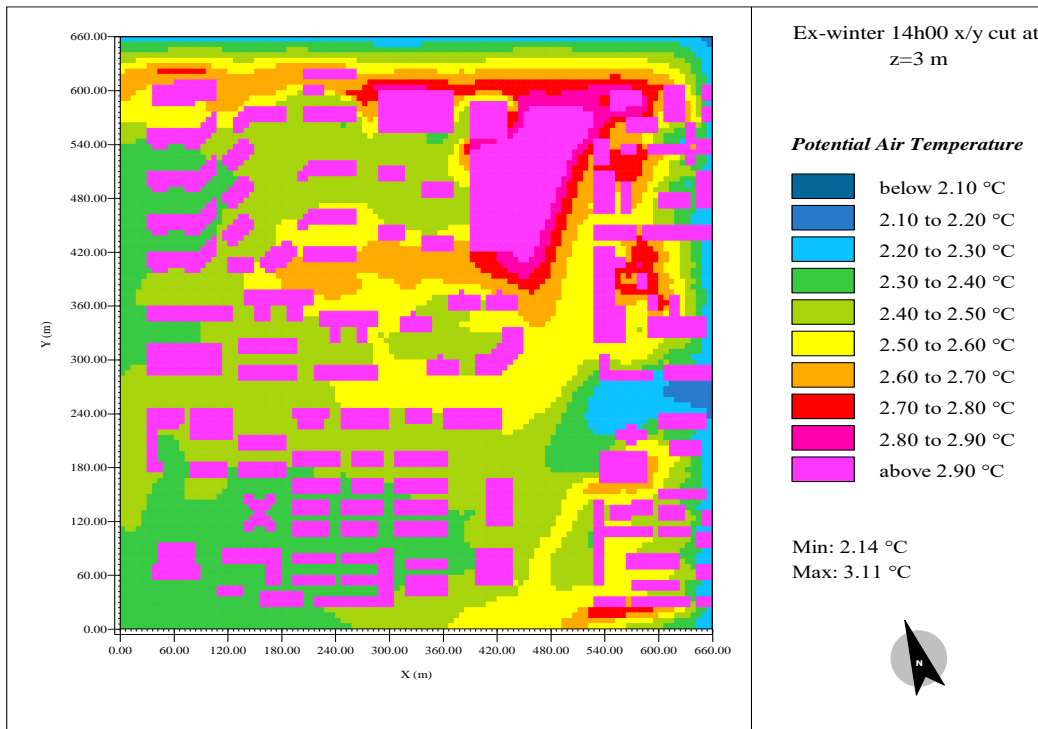
Figure 4.21: Potential temperature map of the simulated area for ex-winter

4.4.2. *Simulation results for the four representative days*

As abovementioned in equation (4-1), the air temperature in ENVI-met is the potential temperature. The heat island effect can be quantitatively described by UHII:

$$\text{UHII} = T_{\text{air,ENVImet}} - T_{\text{air,EPW}} \tag{4-12}$$

where $T_{\text{air,ENVImet}}$ is the air temperature converted from the potential air temperature in ENVI-met simulation and $T_{\text{air,EPW}}$ is the air temperature in EPW file.

The air temperature at the height of 3 m of the north receptor is shown in Figure 4.22. For av-spring, av-autumn and ex-winter, all the simulated air temperatures are higher than the input air temperatures. For ex-summer, in the morning there are several hours when the simulated air temperature is lower than the input air temperatures, meaning that there exists a "cool island" effect. However, the UHI effect starts to appear after 8h00, and it shows a maximal UHII of around 2.56 °C at 13h00. The average and maximal UHIIs of these representative days are listed in Table 4-7. It can be inferred that the maximal UHII occurs on the extreme hot summer day and the minimal UHII occurs on the average autumn day. For the average UHII during one day, it is observed that ex-summer > av-spring > ex-winter > av-autumn.

(a) Av-spring

(b) Ex-summer

(c) Av-autumn

(d) Ex-winter
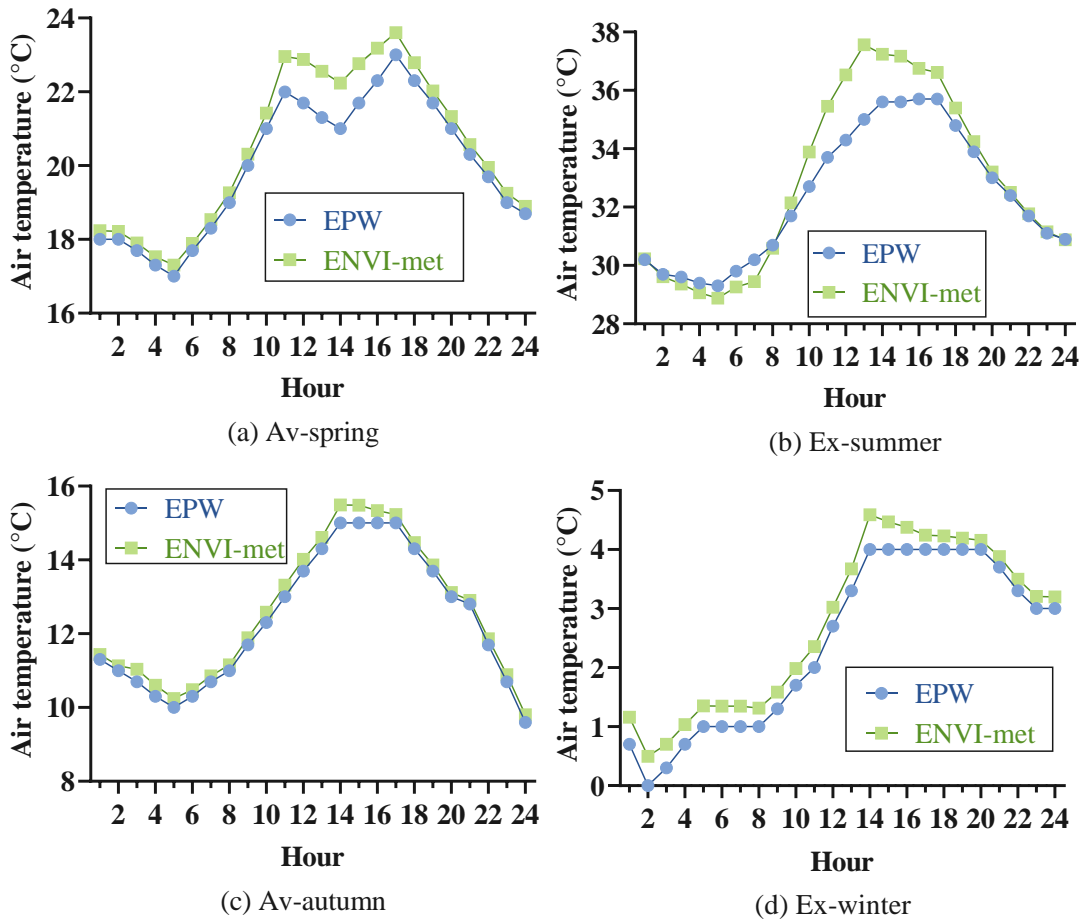
Figure 4.22: ENVI-met simulation results for the four representative days at the height of 3 m of the north receptor

Table 4-7   UHII$_{max}$ and UHII$_{ave}$ at the height of 3 m of the north receptor

Representative day	UHII$_{max}$ (°C)	UHII$_{ave}$(°C)
Av-spring	1.26	0.50
Ex-summer	2.56	0.51
Av-autumn	0.49	0.24
Ex-winter	0.59	0.32

Although some studies, e.g. Chan (2011), reported a similar UHII measurement trend as Figure 4.22, in urban areas, a larger UHI effect is usually observed during the night period compared to the day time, which is contradictory to Figure 4.22. A longer buffering time of 3 days was used to investigate the possibility of improving the results, e.g. the result of ex-summer is shown in Figure

4.23. These results showed a limited heat island effect at night, which may be due to numerical approximation of ENVI-met. It would be useful to perform calculations again using a more powerful computer allowing more precise simulation options to be chosen.
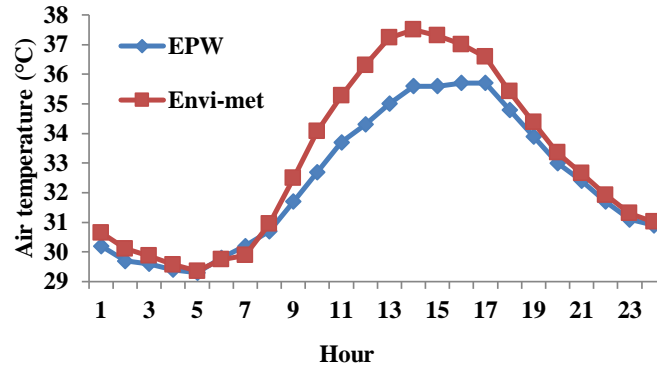
Figure 4.23: Simulation results of ex-summer with a buffering time of three days

The air temperature along the height of the north receptor was investigated, as shown in Figure 4.24. In general, the air temperature decreases with the height. If the UHII is larger (e.g. 12h00 on ex-summer), the air temperature decreases more sharply. The air temperature at the height #1 (3 m) is 1.9 °C higher than at height #6 (103 m). The opposite trend is observed for the hours of UCI effect, e.g. 6h00 on ex-summer: the air temperature increases from 29.26 °C to 29.42 °C along the height. A more accurate building energy simulation should include the air temperature variation along the height.

The air temperatures of the four orientations at 3 m are compared in Figure 4.25. The temperature difference is not quite large for av-autumn and ex-winter for the four receptors; however the difference can be noticeable from 10h00 to 14h00 on av-spring and from 8h00 to 16h00 on ex-summer. This means the orientation might have a larger influence on the cooling load than on the heating load; it will be discussed in section 4.4.4.
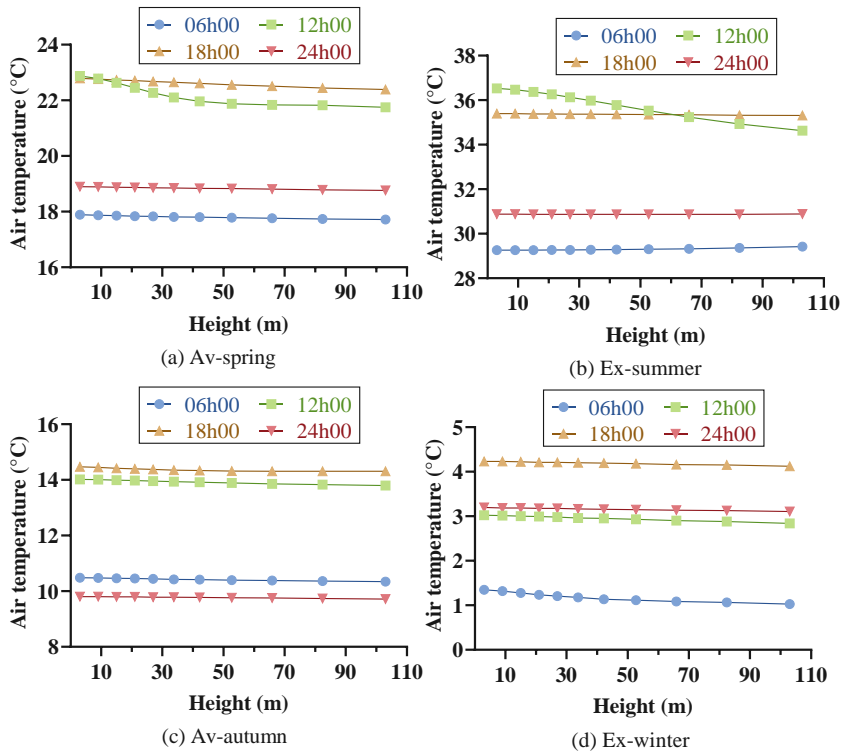
Figure 4.24: *Air temperature evolution along height for four representative days of receptor N*
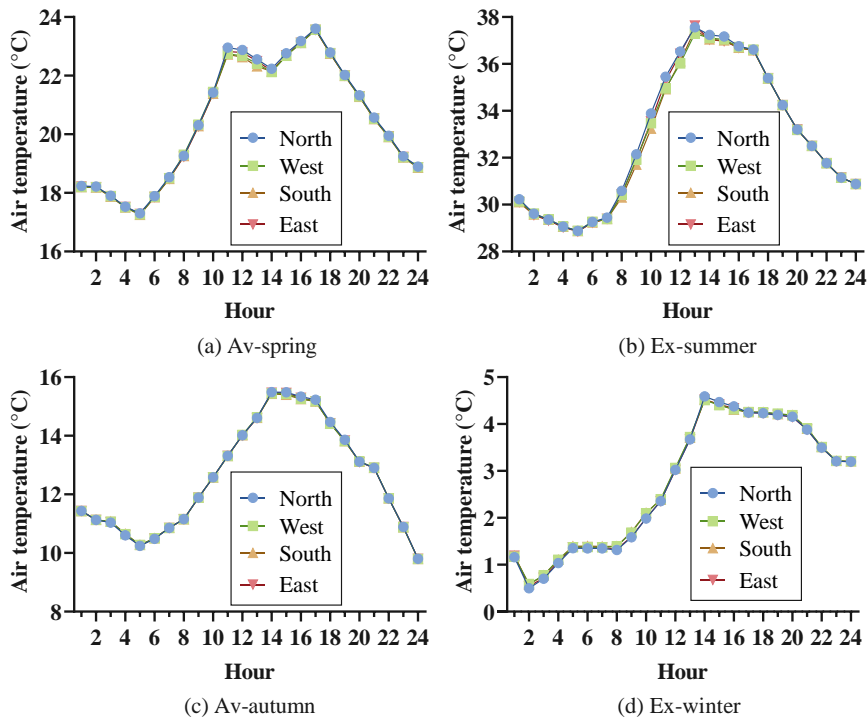
Figure 4.25: *Air temperature of the four orientations at height #1 for the four representative days*

4.4.3. *Generated weather files for COMFIE*

Applying the method illustrated in section 4.2, the meteorological files for building energy simulation in COMFIE were generated. The UHIIs of 6 different heights of four orientations were calculated and added to the original EPW file, meanwhile the other meteorological parameters were kept the same. In total 24 meteorological files considering the local microclimate effects were generated and were used to simulate the building's energy performance. The hourly temperature of N#1 is shown in Figure 4.26, compared to the original EPW. The yearly average UHII at the height of 3 m is estimated to be 0.45 °C (considering the average of four orientations).

The accumulations of hourly heat island or cool island intensity over TMY were calculated, namely urban heat island degree-hours (UHIdh) and urban cool island degree-hours (UCIdh) (Yang et al., 2018a), as shown in Figure 4.27. UHIdh and UCIdh measure how much and for how long the air temperature at a site is higher or lower than the reference suburb. At height #1, the values of UHIdh are ranked in the following order: summer > spring > autumn > winter in the north and east; summer > spring > winter> autumn in the west and south. For the number of UCIdh, at height #1 and #6, the following ranking is observed for all orientations: summer > autumn > spring > winter (in spring and winter there is nearly no UCI effect). For the whole year, at height #1, the order of the number of UHIdh is N#1 (3 740 °C hours) > E#1 (3 490°C hours) > W#1 (3 420°C hours) > S#1 (3 320°C hours). UHIdh decreases with the height. At height #6, the order changes to: S#6 (922 °C hours) > E#6 (902°C hours) > W#6 (874°C hours) > N#6 (873 °C hours). For the UCIdh of the whole year, at height #1, S#1 (205 °C hours) > E#1 (200 °C hours) > W#1 (180°C hours) > N#1 (164°C hours). UCIdh also decreases with height. At height #6, N#6 (123 °C hours) = E#6 (123°C hours) > S#6 (118°C hours) > W#6 (114 °C hours).

The ratio of UHI degree hours to degree hours of original EPW are presented in Figure 4.28, based on 18 °C for heating and 26 °C for cooling. This ratio indicates the potential of changing the heating/cooling load. For summer, N#1 has the largest ratio to affect cooling load, which is almost 4 % larger than the smallest of S#1. At the height #1, the ratio of four orientations in spring and autumn are in the identical order with the cooling load in summer. For winter, the four orientations have similar ratios, indicating the heating load is not strongly influenced by the orientation. The ratio decreases with the height. At height #6, the ratio drops below 1 % in winter and to around 6 % in summer. This indicates smaller effects are foreseen with the increase of the height.
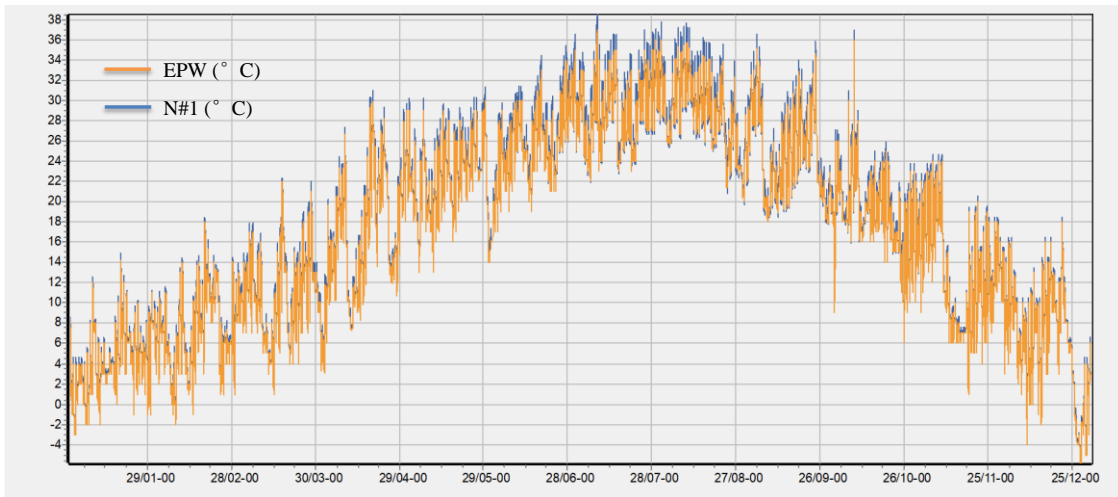
Figure 4.26: Air temperature of EPW and N#1
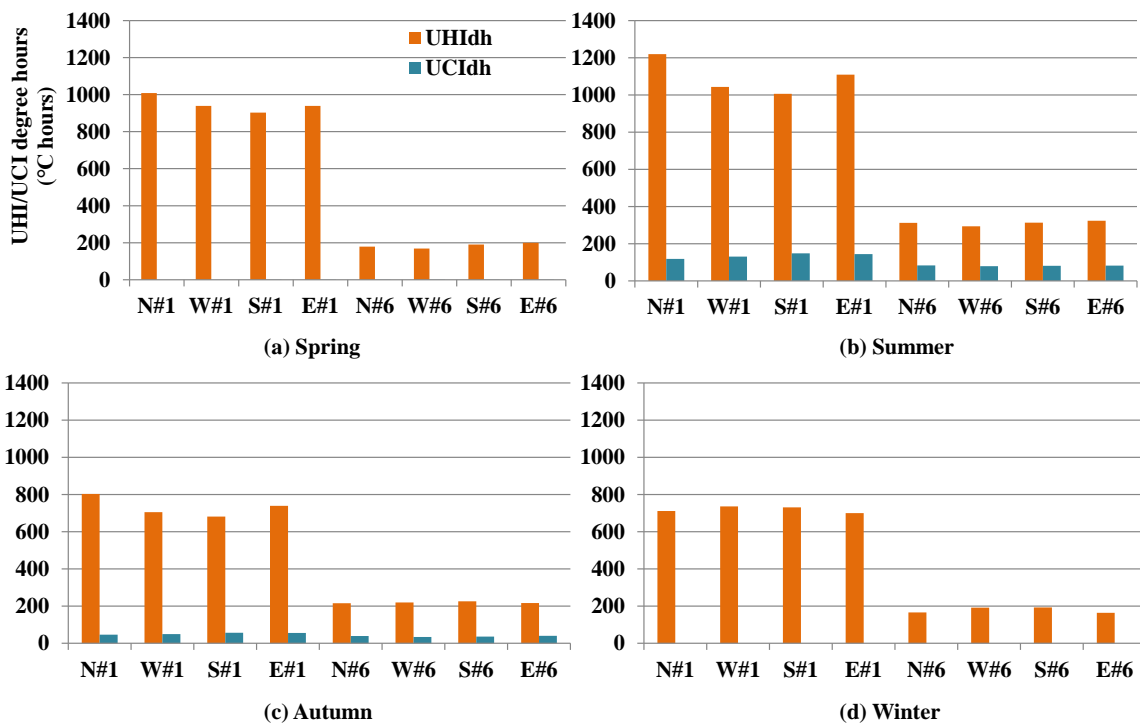
Figure 4.27: UHI/UCI degree hours of four orientations at the height #1 and #6 for four seasons
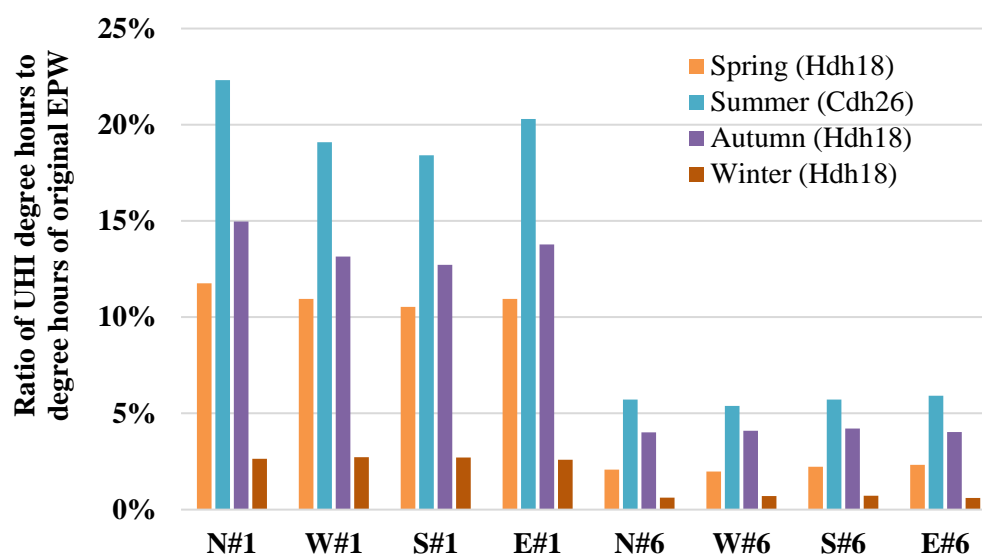
Figure 4.28: Ratio of UHI degree hours to degree hours of original EPW

4.4.4. *Building energy simulation results*

4.4.4.1. DBES with detailed microclimate data

As abovementioned, 24 meteorological files accounting for the local microclimate effects were generated and were used to simulate the building's energy performance, for different heights and orientations.

Based on the location of the receptors (see Figure 4.12) and the zone definition (see section 1.6.2.4), the south zones are mainly affected by the air in south, and the north zones are surrounded by the air in all the four orientations. To perform a precise energy performance simulation, the loads of each zone are calculated using the meteorological files according to the orientation and height, as shown in Table 4-8. The heating/cooling load of the north is the average of the corresponding simulation results from the four weather files of N, S, W and E and for the south zone, it is directly the simulation results from weather file S. Applying this method, the energy simulation results with detailed microclimate data were obtained: the total heating and cooling loads are 586 000 kWh (47.1 kWh/m^2) and 582 000 kWh (46.7 kWh/m^2), respectively. Since this simulation considers the air temperature variation with height and orientation, it can be regarded to be closer to the reality and it is used as a reference to compare the differences of other simulation results such as the simulation with the original EPW file.

Table 4-8   ***Meteorological files to calculate the energy load of each zone***

Zone number	Zone name	Weather file
1	floor 1	(N#1+S#1+W#1+E#1)/4
2	aisle	-
3	floor 2-6 north	(N#2+S#2+W#2+E#2)/4
4	floor 2-6 south	S#2
5	floor 7-14 north	(N#3+S#3+W#3+E#3)/4
6	floor 7-14 south	S#3
7	floor 15 C-living room (15)	S#4
8	floor 15 C-master bedroom (15)	S#4
9	floor 15 C-rest rooms (15)	S#4
10	floor 15 B	S#4
11	floor 15 north	(N#4+S#4+W#4+E#4)/4
12	floor 16-25 north	(N#4+S#4+W#4+E#4)/4
13	floor 16-25 south	S#4
14	floor 26-33 north	(N#5+S#5+W#5+E#5)/4
15	floor 26-33 south	S#5
16	floor 34 north	(N#6+S#6+W#6+E#6)/4
17	floor 34 south	S#6

4.4.4.2. Impact of orientation

The simulation results of different meteorological files were compared including the original EPW and the reference simulation. Figure 4.29 shows the simulated annual loads of different orientation at a height of 3 m. Compared to the reference simulation, the simulation with EPW file shows a heating load 3.6 % larger, a cooling load 3.9 % smaller and a total energy load 0.2 % smaller. This is mainly due to the temperature from EPW file which is collected in the rural areas such as in the airport. The UHI effect reduces the heating load in winter and increases the cooling load in summer. At the height of 3 m, the orientation slightly affects the heating load, with a variation of only 0.2 % between north and east. The orientation has a larger influence on the cooling load. Compared to the reference simulation, the north has a result 4.4 % larger, meanwhile the south only shows a 2.7 % increase. For the total energy load, the north has the biggest difference (1.1 %) and the south has the smallest (0.3 %). In general, the ranking of the accuracy according to the orientation is: south > west > east > north.
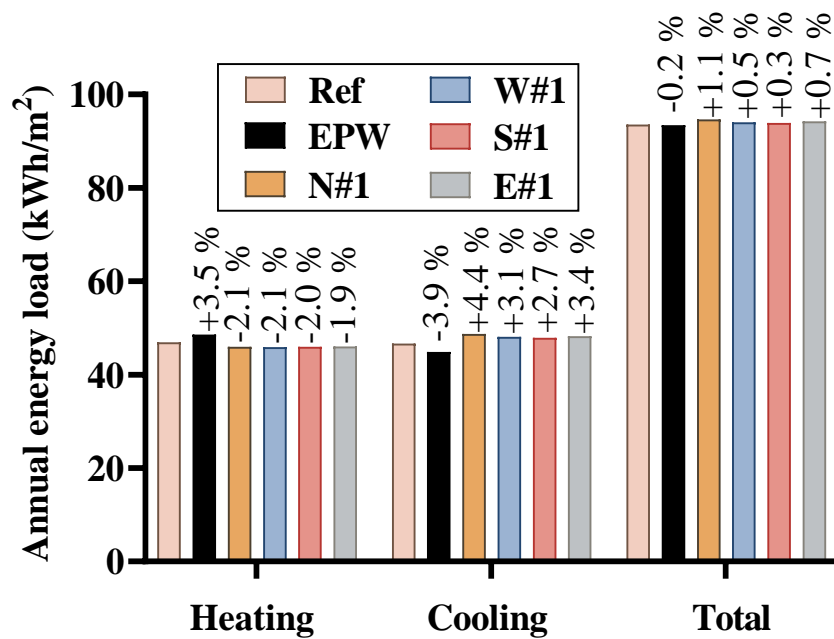
Figure 4.29: Energy loads for different orientations at the height #1

4.4.4.3. The impacts of height

According to Figure 4.24, the air temperature drops along the height, yielding different energy loads. As abovementioned, the south orientation has a more accurate simulation result than the other orientations. The building energy simulation results of different heights are illustrated in Figure 4.30. It can be inferred that compared to the reference simulation, the difference of the heating load increases from -2.0 % to +2.1 % and the cooling load decreases from +2.7 % to -2.2 % with height. S#3 shows a better accuracy in evaluating the heating and cooling load, with a +0.4 % and -0.8 % difference. The height has a minor influence on the total load, with a maximal difference of ±0.3 %. Compared to EPW, the differences of heating load and cooling load can reach to -5.4 % and +6.9 % for S#1. The smallest differences are from the largest height S#6, with differences of -1.4 % and +1.8 %. It can be indicated that the microclimate's effects on the low-rise buildings is larger than the high-rise buildings. In this study, S#4 is the best representative meteorological file which can obtain the closest result compared to the reference simulation. The simulation with the original EPW file did not consider the UHI effect, overestimating the heating load by 3.5 % and underestimating the cooling load by 3.9 %; however it can accurately predict the total energy load.

It should be noted that, in our case study, the heating and cooling loads are almost balanced, resulting in a minor difference in the total energy load due to the microclimate. However, its effect could be stronger in other climate zones where the difference between the heating and cooling loads is large.
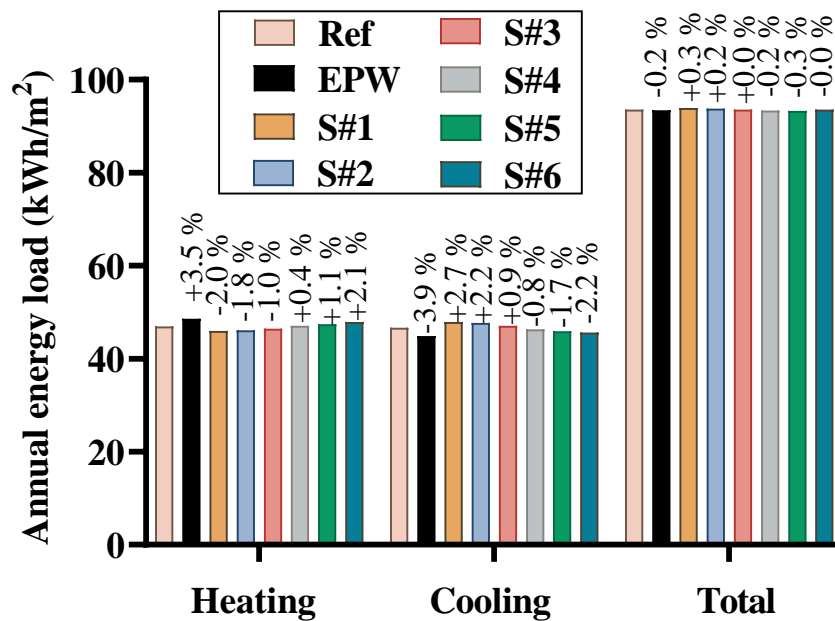
Figure 4.30: Annual loads of different heights for S orientation

4.5. Conclusions and perspectives

4.5.1. *Conclusions*

Certain microclimate conditions are observed in the city urban areas such as UHI effect, which are not reflected in the normal weather files used in the DBES tools. As an essential boundary condition of a building, the microclimate can influence the building energy simulation results. This chapter quantitatively analysed the UHI effect on the energy performance of a high-rise residential building located in a central business district in Wuhan, China. The main achievements of this study are:

1. A site-specific weather file generation method was proposed, accounting for the UHI effect, which can provide local hourly air temperature.

2. The method of coupling the 3D numerical microclimate simulation tool ENVI-met with the DBES tool COMFIE was introduced, allowing to provide relatively more accurate simulation results with local weather conditions.

3. Four representative days were chosen and simulated in ENVI-met. On ex-summer and av-autumn, the UHI effect was obvious along the north-south asphalt road; and the north part had a stronger UHI effect. For the average UHII during one day, the following ranking was observed: ex-summer > av-spring > ex-winter > av-autumn.

4. The site-specific weather files were generated considering the UHI effect for 4 orientations and 6 heights, based on the microclimate simulation results. For the whole year, at the height of 3 m, the order of the number of UHIdh is N#1 (3 740 °C hours) > E#1 (3 490°C hours) > W#1

(3 420°C hours) > S#1 (3 320°C hours). This order changed with the orientation and height. The yearly average UHII at the height of 3 m was estimated to be 0.45 °C.

5. The energy simulations of the case study were performed using the generated site-specific weather files. More precise energy simulation results were obtained considering the air temperature variation with height and orientation: the total heating and cooling loads were 586 000 kWh (47.1 kWh/m2) and 582 000 kWh (46.7 kWh/m2), respectively.

6. The simulation using the original EPW file showed a heating load 3.5 % larger, a cooling load 3.9 % smaller, and a total energy load 0.2 % smaller, compared to the reference simulation. If only the weather file at the height of 3 m in the south (S#1) is used, not considering the air temperature variation along the height (which is adopted in many studies), the heating load decreases by 5.4 % and the cooling load increases by 6.9 % compared to the EPW file. The microclimate's effects on the low-rise buildings is larger than the high-rise buildings.

7. At the height of 3 m, the orientation has a small effect on the heating load, but a larger influence on the cooling load. The heating load increases and the cooling load decreases with the height; however, the height barely influences the total load, because the heating and cooling loads are almost balanced.

4.5.2. *Perspectives*

This study investigated the influence of air temperature of the local microclimate of a residential building in a central business district. Other site-specific climate parameters such as relative humidity, solar radiation, longwave radiation and wind affecting the building energy loads were not considered in this study, which is an interesting topic in future research.

The method of generating the hourly UHII is based on the linear interpolation between four representative days in each season, which might not precisely evaluate the UHII for every hour. Although this is a good attempt to account for the local UHI effect on the building energy performance, a more accurate method generating the hourly UHII would be beneficial. Besides, measurements of the local climate parameters could be helpful to validate the simulation results. The energy performance of other uses of the building can also be investigated, such as the office buildings only operating in the daytime.

This study only evaluates the effects of local microclimate on the energy consumption of the building. However there are other environmental impacts such as CO_2 emissions, human health and biodiversity. Moreover, the environmental impacts of electricity are different in winter and summer. Although the total energy consumption is almost identical, the variations in the heating and cooling loads might influence the environmental impacts. This is another interesting topic to be investigated.

Chapter 5.   Environmental impacts of a building in China evaluated using LCA

The environmental impacts of buildings are generally evaluated using LCA. A building life cycle is related to other sectors like the manufacture of construction products, energy, water and waste treatment sectors. Assumptions regarding this background system constitute another boundary condition considered in this thesis, addressing particularly the local electricity production mix. The large area of China leads to regional specificities, regarding climate features as well as the electricity production mix. The energy mix evolves towards a more renewable structure, which might affect the evaluation results during the long lifetime of buildings. This chapter aims at determining the influence of the energy mix boundary condition on LCA results taking into account the spatial and temporal variations in China.

Résumé du chapitre

L'ACV est un outil largement utilisé pour évaluer les impacts environnementaux d'un bâtiment, qui est fortement connecté à ses systèmes d'arrière-plan, par exemple la fabrication des produits de construction, les procédés liés à l'eau et aux déchets, et le mix de production d'électricité. Le choix du mix énergétique influence les impacts tout au long de la durée de vie d'un bâtiment, incluant la fabrication des matériaux de construction, la consommation électrique des équipements de chauffage / refroidissement et la consommation électrique quotidienne des occupants. La grande superficie de la Chine entraîne des caractéristiques climatiques régionales ainsi que des variations spatiales du mix de production d'électricité. Les charges de chauffage et de refroidissement d'un bâtiment varient en fonction de son emplacement, donc les impacts environnementaux dus à l'electricité pour le chauffage et le refroidissement sont fortement affectés par la région. Par ailleurs, le mix de production d'électricité évolue vers une part plus importante d'énergies renouvelables en Chine, visant à réduire les impacts environnementaux tels que les émissions de CO_2. De nombreuses études utilisent un mix de production d'électricité statique dans l'ACV et l'évolution du système électrique n'est pas prise en compte. Cette hypothèse affecte la précision des résultats de l'évaluation ; en particulier la durée de vie d'un bâtiment est généralement supérieure à 50 ans, prériode dans laquelle le mix énergétique peut changer de manière significative.

Pour étudier cette question, cinq régions (Hubei, Pékin, Guangdong, Mongolie intérieure, Yunnan) dans cinq zones climatiques (été chaud et hiver froid, froid, été chaud et hiver chaud, froid sévère, doux) en Chine ont été sélectionnées. Les caractéristiques du mix énergétique de ces villes sont différentes, et ces caractéristiques se refléteront également à l'avenir. Quatre scénarios futurs pour la Chine ont été adoptés : trois axés sur la réduction des émissions de carbone et un proposant une part élevée d'énergies renouvelables. Ces scénarios nationaux ont été déclinés à l'échelle locale pour ces cinq régions.

Dans une première étape, une simulation énergétique dynamique a été réalisée pour le cas d'étude présenté au chapitre 1 sous les climats de ces cinq villes, afin d'obtenir les charges énergétiques au stade d'utilisation du bâtiment. L'approche ACV a ensuite été appliquée, en contextualisant la base de données ICV avec différents mix locaux de production d'électricité. Les impacts environnementaux ont été comparés entre l'utilisation de chaque mix énergétique local et l'utilisation du mix énergétique moyen national, dans l'approche statique (le futur scénario n'est pas pris en compte) et l'approche dynamique (le futur scénario est pris en compte).

Les résultats ont indiqué que les différences entre les impacts environnementaux de la phase de construction utilisant la base de données locale par rapport à ceux utilisant la base de données contextualisée avec le mix énergétique moyen national étaient inférieures à 8 %. Ces différences ont une faible influence sur les impacts environnementaux sur toute la durée de vie, car la phase d'utilisation en est le principal contributeur. Pour l'ensemble du cycle de vie, l'utilisation du mix moyen national dans l'approche statique peut estimer de façon relativement précise certains indicateurs environnementaux dans certaines provinces. Cependant pour la plupart des provinces, elle a apporté

des différences non négligeables, telles que la surestimation du PRG d'un facteur 5 au Yunnan. L'approche statique peut entraîner des différences significatives par rapport à l'approche dynamique pour la plupart des indicateurs d'impact environnemental. Les différences dépendent fortement des scénarios futurs prévus et montrent également des caractéristiques régionales. Par exemple, dans le Guangdong, la différence de GWP peut atteindre environ 900 % dans le scénario ELC (scénario bas carbone amélioré, scénario futur selon lequel davantage d'efforts seront consentis en matière de réduction de la consommation d'énergie et de technologies énergétiques propres), néanmoins elle était relativement petite dans le Yunnan dans le scénario LC (scénario à faible émission de carbone, un scénario futur selon lequel des politiques supplémentaires seront prises concernant la réduction des émissions de carbone/de la consommation d'énergie, moins forte que le scénario ELC). Les variations spatiales et temporelles du mix de production d'électricité ont des impacts très importants sur les résultats de l'ACV.

Les deux autres conditions aux limites concernant le sol et le microclimat ont également été étudiées dans ce chapitre. Dans l'étude de cas de Wuhan, la plupart des indicateurs environnementaux au stade de l'utilisation sont surestimés de 13 % si le modèle GCHP n'est pas utilisé. Les effets UHI sont par contre négligeables.

Ce chapitre révèle l'influence du choix du mix sur l'évaluation de la performance environnementale, en particulier utiliser le mix énergétique local au lieu du mix énergétique moyen national en Chine, ainsi que la prise en compte de l'évolution énergétique future. Le choix du mix de production d'électricité est essentiel pour évaluer avec précision les impacts environnementaux d'un bâtiment à longue durée de vie.

Abstract

LCA is a widely used tool to assess the environmental impacts of a building, which is highly connected to its background systems, e.g. the manufacture of construction products, water and waste related processes, and the electricity production mix. The choice of energy mix influences the impacts throughout a building's lifespan, such as building materials fabrication, electricity use for heating/cooling equipments and daily electricity consumption of occupants. The large area of China leads to regional climate features as well as electricity production mix. The heating and cooling loads of a building vary with its location, therefore the environmental impacts due to the electricity used for heating and cooling are strongly affected by the region. Besides, the electricity production mix evolves towards a more renewable content in China, aiming at reducing the environmental impacts such as CO_2 emissions. Many studies use a static electricity production mix in LCA and the evolution of electric system is not considered. This assumption affects the precision of the results; especially, the lifespan of a building is usually over 50 years, during which the energy mix might significantly change.

To study this question, five regions (Hubei, Beijing, Guangdong, Inner Mongolia, Yunnan) in five climate zones (hot summer and cold winter, cold, hot summer and warm winter, severe cold, mild) in China were selected. The energy mix features in these regions are different, and will continue to be different in the future. Four future scenarios for China were considered: three focusing on the carbon emissions reduction and one proposing a high renewable energy share. These national scenarios were extended to the local scale for these five regions.

In a first step, dynamic building energy simulation was performed for a case study in the climates of these five regions, to obtain the energy loads in the building's use stage. LCA approach was afterwards applied under local context, by contextualising the LCI database with different local electricity production mixes. The changing in environmental impacts were compared when using each local energy mix and the national average energy mix, in the static approach (the future scenario is not considered) and the dynamic approach (the future scenario is considered).

The results indicated that the differences of the environmental impacts of the construction stage using the local database compared to that using the database contextualised with national average energy mix were lower than 8 %. These differences had a small influence on the environmental impacts in the whole lifespan, because the use stage is the main contributor. For the whole life cycle, using a national average mix in the static approach could reasonably estimate some environmental indicators in some provinces. However for most provinces, it brought non-negligible differences, such as the overestimation of GWP which reached a factor 5 in Yunnan. The static approach might cause huge differences compared to the dynamic approach for most environmental impact indicators. The differences highly depended on the predicted future scenarios and showed regional features. For example, in Guangdong, the difference of GWP could reach around 900 % in the ELC scenario (enhanced low carbon scenario, a future scenario in which more efforts will be made on the energy consumption reduction and clean energy technologies), nevertheless it was relatively small in Yunnan in the LC scenario (low carbon scenario, a future scenario in which extra policies will be made

regarding the carbon emissions/energy consumption reduction, weaker than the ELC scenario). Both the spatial and temporal variations of the electricity production mix have very important impacts on the LCA results.

The other two boundary conditions regarding the ground and the microclimate were investigated in this chapter as well. In the case study in Wuhan, most environmental indicators in the use stage were overestimated by 13 % if the GCHP model was not used. However, the effects of the UHI were negligible.

This chapter reveals the influence of the choice of energy mix on the assessment of environmental performance, in particular using local energy mix instead of national average energy mix in China, as well as considering future energy evolution. The choice of electricity production mix is essential in accurately evaluating then environmental impacts of a building with a long lifespan.

5.1.   Introduction

China is a large country with an area of about 9.6 million km^2. About 98 % of the land area stretches between a latitude of 20°N and 50°N, from the subtropical zones in the south to the temperate zones in the north. The regional climate characteristics are different and China is divided into five zones by the national standard *GB 50176-2016 Code for thermal design of civil building* (MOHURD, 2016): severe cold (SC), cold (C), hot summer and cold winter (HSCW), mild (M), and hot summer and warm winter (HSWW), as shown in Figure 5.1. The zoning criteria are based mainly on the average temperatures in the coldest and hottest months of the year. The number of days on which daily average temperature is below 5 °C or above 25 °C is counted as complementary indices.
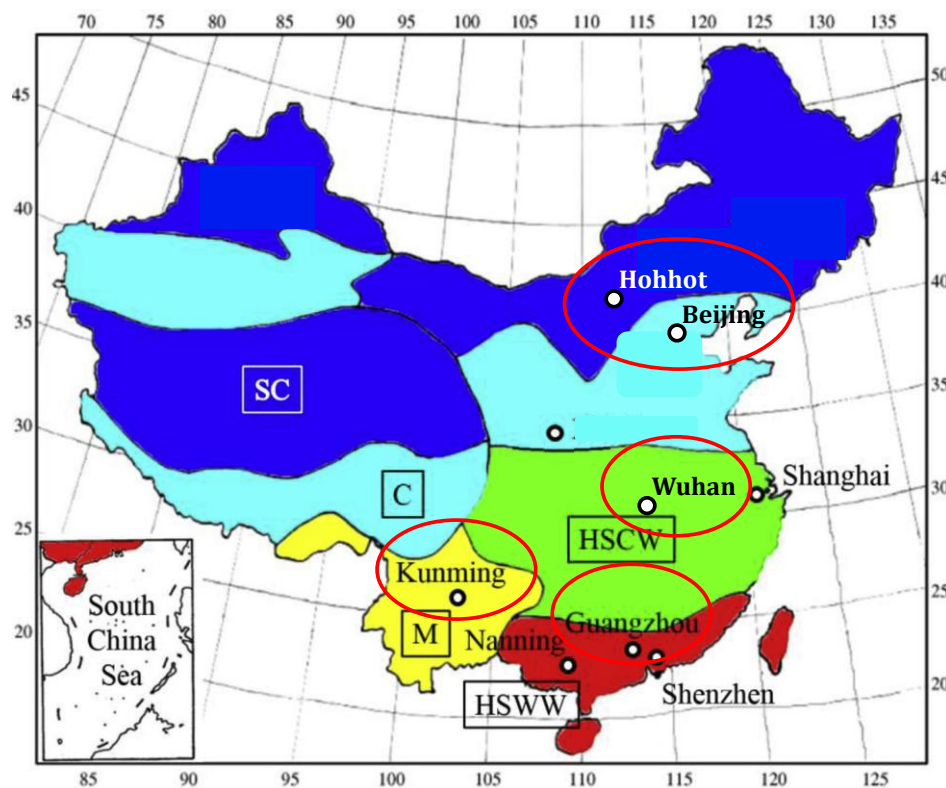
Figure 5.1: Five climate zones and representative cities on a map of China (Lai et al., 2018)

On a spatial scale, the energy performance of a building highly depends on the climate, leading to a large difference of energy consumption (e.g. heating and cooling) during its lifespan between different climate zones. Moreover, the electricity production mix varies with the climate zone as well, due to the natural energy resource distribution and other factors such as energy policies and strategies. Related environmental impacts therefore differ with the location by affecting the materials fabrication processes involving electricity, because some materials e.g. concrete, steel, etc. are produced locally, and the electricity used during a building's lifespan.

On a temporal scale, to achieve the goals of low carbon society and energy structure transition, the evolution of energy mix in the future is foreseen in China, by increasing the share of renewable energy and reducing the fossil fuel power. The environmental impacts of electricity will vary during this evolution. This is a key factor affecting the accuracy of evaluation during a long lifespan (normally over 50 years) of a building.

As mentioned in section 1.2.3, LCA is widely used in the building sector to evaluate building's environmental impacts and the electricity production and grid is an important background system in this method. In many related studies (Wu et al., 2012 ; Yang et al., 2018b ; Su et al., 2020 ; Xie et al., 2020a), the electricity production mix adopted for LCA cases in China is either a national average or static, or both, which cannot reflect the regional energy mix characteristics and its future evolution. This might lead to non-negligible errors in the evaluation of LCA impacts.

This chapter is dedicated to throw a light on this topic. The first objective of this chapter is to generate LCI databases under the Chinese context and even regional (province scale) context. The second objective is to evaluate the environmental impacts of the case study located in Wuhan (Hubei), taking into account the local context for the evolution of the energy mix, and the two boundary conditions presented in previous chapters as well. Another objective is to evaluate the effects of the spatial and temporal variations of the electricity production mix on the environmental impacts of a Chinese building, by applying the LCA method.

5.2. Electricity production mix in China

5.2.1. *Spatial scale*

An unbalanced distribution of natural resources e.g. wind energy, hydropower and fossil fuels exists in China, resulting in an electricity production mix variation according to the location. In 2015, as shown in Figure 1.7 in chapter 1, wind power is more abundant in Inner Mongolia, leading to a share of around 12 %. Hydro power can provide more than 80 % of the total energy in a province along Yangtze river such as Yunnan. Larger share of nuclear is observed in the coastal provinces e.g. Guangdong, which can reach 20 %. In Beijing, the capital city of China, nearly all the electricity is generated by thermal power plants. The energy mix of Wuhan (Hubei), where the case study in this thesis is located, consists of mainly thermal power (63 %) and hydro power (36 %), small wind power/solar power and no nuclear power. In 2015, the Energy Research Institute (ERI) of the National Development and the Reform Commission of China (NDRCC) released the report: *China 2050 high renewable penetration scenario and road map study*, giving a scenario for high renewable energy penetration (HRE) in future China (ERINDRC, 2015). It reported the installed capacity of each technology by region in China, as shown in Figure 5.2. Northern, northwestern and northeastern parts of China are foreseen to have a large share of wind energy due to their abundant wind resources and large potential land for wind. More solar power plants will be installed in north, northwest and south China. Fossil fuel power will still contribute to a certain share in central China.

Biogas
Fuel Oil
Natural gas
Hydropower
Nuclear power
Solar energy
Straw and stalk
coal
Municipal solid waste
Wind power
Geothermal energy
Wave energy
Wood pellets
Pumped hydro storage
Chemical energy storage
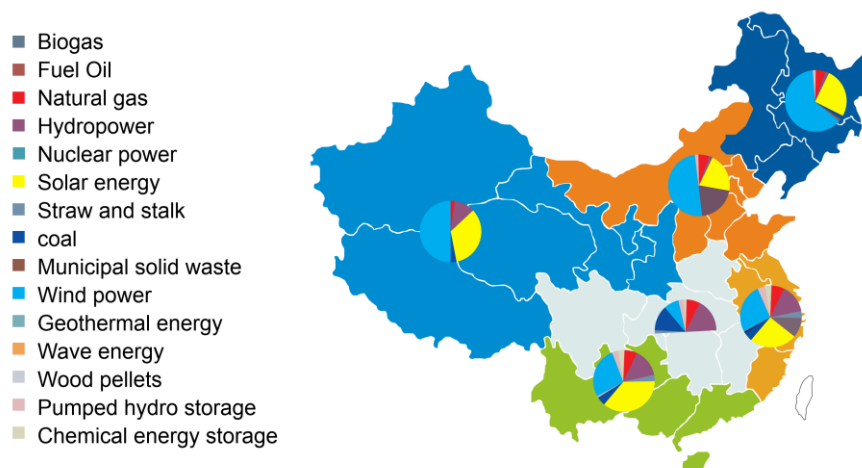
Figure 5.2: Regional installed capacity under HRE scenario in 2050 (ERINDRC, 2015)[18]

Accounting for the climate zone and the renewable energy features, one city is chosen for one climate zone (therefore, they do not cover the whole electricity production in China but are rather representative of climate conditions). Their energy mixes are as shown in Table 5-1 (data source: *China Electricity Industry Annual Development Report 2019*[19], *local government report*[20], National Bureau of Statistics of China [21], Guangdong power exchange centre [22] and local electric power association[23,24]). The locations of the cities are shown in Figure 5.1. Hohhot (in climate zone SC) is in Inner Mongolia (NM) province where the electricity production mainly relies on thermal power and its wind power capacity is relatively high. Beijing (BJ) in climate zone C is the capital of China, where much less land is planned for renewable energies, thus it is almost fully supplied by thermal power. Wuhan (in climate zone HSCW) is in Hubei (HU) province, where the *Three Gorges Dam* is located, leading to a high capacity of hydro power. Guangzhou (in climate zone HSWW) is the capital city of Guangdong (GD); the province has the highest nuclear share. Kunming (in climate zone M) is in Yunnan province where the power generation is dominated by hydro power, and the total of wind energy and solar energy is relatively high (9 %). The national average energy mix is mainly dominated by thermal power and hydro power. The share of solar power is around 3 %, which is higher than that in Hubei, Guangdong and Beijing. These five provinces have different energy mix features, making them appropriate to present the effects of energy mix on a spatial scale. The abbreviation for the energy mix of a province/the nation in 2019 is expressed by PROVINCE/Nation-2019.

---

[18] The capacity data for the central region of China are not completely given in the figure.

[19] https://www.cec.org.cn/detail/index.html?1-284218

[20] https://shoudian.bjx.com.cn/html/20200201/1039132.shtml

[21] https://www.huaon.com/story/515726

[22] http://news.bjx.com.cn/html/20200227/1048396.shtml

[23] http://www.nmgzzqdlhyxh.com/List.asp?ClassID=3&AnclassID=20&ID=353

[24] http://www.yppta.com.cn/pc/front/cms/articleDetail?articleId=2888d570514d11ea899000163e0d22fc&categoryId=1c56e564750211e88dc400163e003558

Table 5-1   *Five representative cities in different climate zones with their energy mix features*

City, province	*Climate zone*	*Energy mix in 2019*	*Energy mix features*
Hohhot, Inner Mongolia (NM)	SC	Thermal 84 %, wind 12 %, solar 3 %, hydro 1 %	Dominated by thermal power; High wind power
Beijing, Beijing (BJ)	C	Thermal 98 %, hydro 2 %	Dominated by thermal power; Low renewable power
Wuhan, Hubei (HU)	HSCW	Thermal 68 %, hydro 26 %, wind 3 %, solar 3 %	Dominated by thermal power; High hydro power
Guangzhou, Guangdong (GD)	HSWW	Thermal 70 %, nuclear 21 %, hydro 7 %, wind 2 %, solar 1 %	Dominated by thermal power; High nuclear power
Kunming, Yunnan (YN)	M	Hydro 82 %, thermal 9 %, wind 7 %, solar 2 %	Dominated by hydro power; Low thermal power
National average	-	Thermal 69%, nuclear 5 %, hydro 18 %, wind 5 %, solar 3 %	-

5.2.2.   *Temporal scale*

5.2.2.1.   **National scale**

The share of renewable energy in China is predicted to significantly increase in the future due to the coal power dominated energy mix structure and the urgent requirement for low carbon development. In 2009, ERI proposed three scenarios (the energy-saving (ES) scenario, the low-carbon (LC) scenario, and the enhanced low-carbon (ELC) scenario) concerning the carbon reduction to forecast the long-term energy mix in China by 2050 (ERINDRC, 2009). These scenarios are identified using the Integrated Policy Assessment model of China (IPAC) with variations in economy, population, technology, lifestyle, etc. taken into account (ERINDRC, 2009). The predicted electricity production is shown in Figure 5.3 and detailed data are listed in Table Annex-1. It should be noted that these three scenarios only provide data for 2020, 2035 and 2050. The other years were obtained by linear interpolation. The corresponding abbreviations are ES/LC/ELC-year.

The ES scenario describes the future society under the energy saving policies in 2009, without other particular policies on climate change. The LC scenario considers extra policies regarding carbon emissions reduction, energy structure optimisation and reduction of energy consumption. In the ELC scenario, more efforts will be made on the energy consumption reduction and clean energy technologies with the increase of Chinese economy, reduced cost and development of technologies. As foreseen, the total energy consumption and the fossil fuel energy will be the largest (resp. the lowest) in the ES (resp. ELC) scenario. Nuclear power will be very important due to its low carbon emissions in these scenarios. But it causes ionizing radiation, exhaust of resources and radioactive waste, which can also be evaluated using LCA in order to avoid replacing climate change by other impacts.
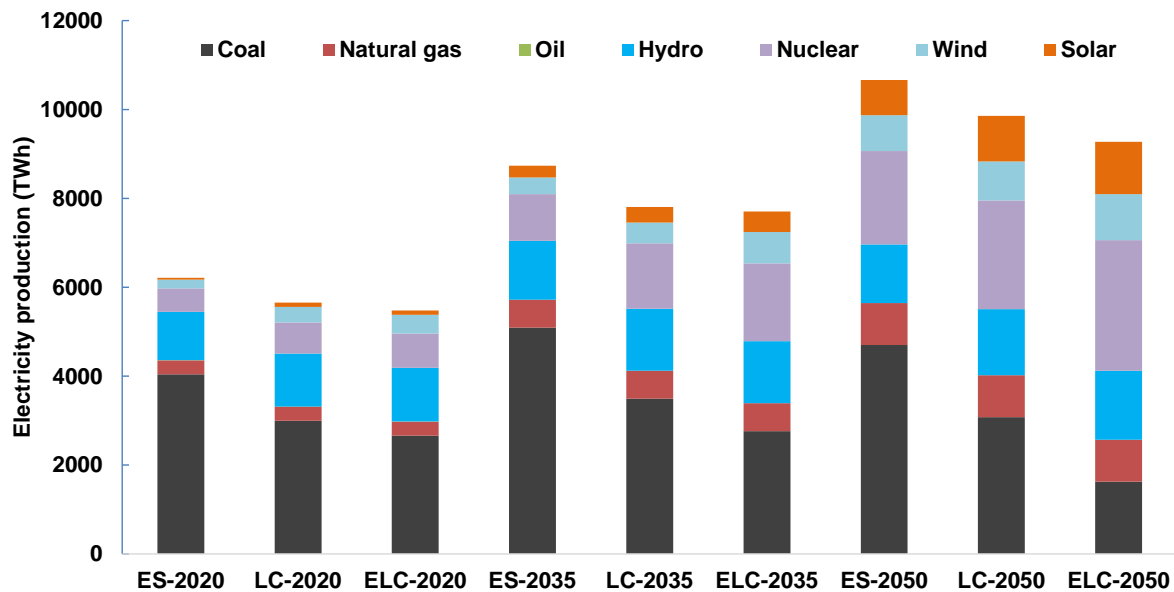
Figure 5.3: Power generation in ES, LC and ELC scenarios in China (ERINDRC, 2015)

In 2015, the same institute released the abovementioned HRE scenario (ERINDRC, 2015). The power generation in this scenario is shown in Figure 4.7. In 2050, China's total power generation will be 15.2 trillion kWh in 2050 in the HRE scenario, including 1 038 billion kWh generated by coal power, 466 billion kWh by natural gas power, 649 billion kWh by nuclear power, 2 187 billion kWh by hydro power, 5 350 billion kWh by wind power, 4 130 billion kWh by solar power and 1 100 billion kWh by biomass power. Renewable energy and NFFs energy will account for 85.8 % and 91 % of total power generation respectively. In this chapter, to simplify the study, ocean energy and geothermal energy are categorised with *other thermal power* (e.g. blast furnace gas treatment), and biomass pellets power, straw and stalks power and municipal solid waste power are categorised as *biomass power*. The corresponding abbreviation of one year in the HRE scenario is HRE-year.

The share of each technology in these four scenarios for China is shown in Figure 5.5. In the ES, LC and ELC scenarios, the main difference to the mix 2019 is that, the share of coal power will decrease and the share of nuclear power will increase in the future. In the ES and LC scenarios, the coal power will still be the most important technology. In ELC-2050, nuclear will replace coal to generate the most part of electricity. Solar power and wind power will largely increase while hydro power will slightly decrease. In the HRE scenario, wind power and solar power will be the two technologies supplying the most part of electricity from 2040. Wind power and solar power will contribute to 35.2 % and 28.3 % of the total production in 2050. The share of coal power will significantly decrease from 62.3 % in 2019 to 6.8 % in 2050 and the share of biomass will increase from 1.4 % to 6.3 %. Nuclear power will remain a small share under 5 %, and the share of hydro power will be around 15 %.

	2011	2015	2020	2025	2030	2035	2040	2045	2050
■ Ocean energy						4	4	4	4
■ Geothermal power						30	90	90	90
■ Biomass pellets power		6	12	18	28	46	80	180	202
■ Straw and stalks power	10	20	59	87	129	187	244	283	297
■ Biogas power	1	63	118	118	118	118	111	126	139
■ Municipal Solid Waste power	12	30	50	75	112	197	315	413	462
■ Solar power	5	61	228	718	1496	2445	3400	4214	4310
■ Wind power	97	252	753	1513	2595	3904	4741	5130	5350
■ Hydropower	889	1031	1221	1620	1794	1790	1851	2014	2187
■ Nuclear power	88	300	354	449	463	484	544	569	649
■ Oil power	2	2	2	2	2	2	2	2	2
■ Natural gas power	67	267	522	559	563	553	524	467	466
■ Coal power	3508	4223	4994	4868	4566	3263	2018	1387	1038

Figure 5.4: Power generation in high renewable energy scenario in China (ERINDRC, 2015)
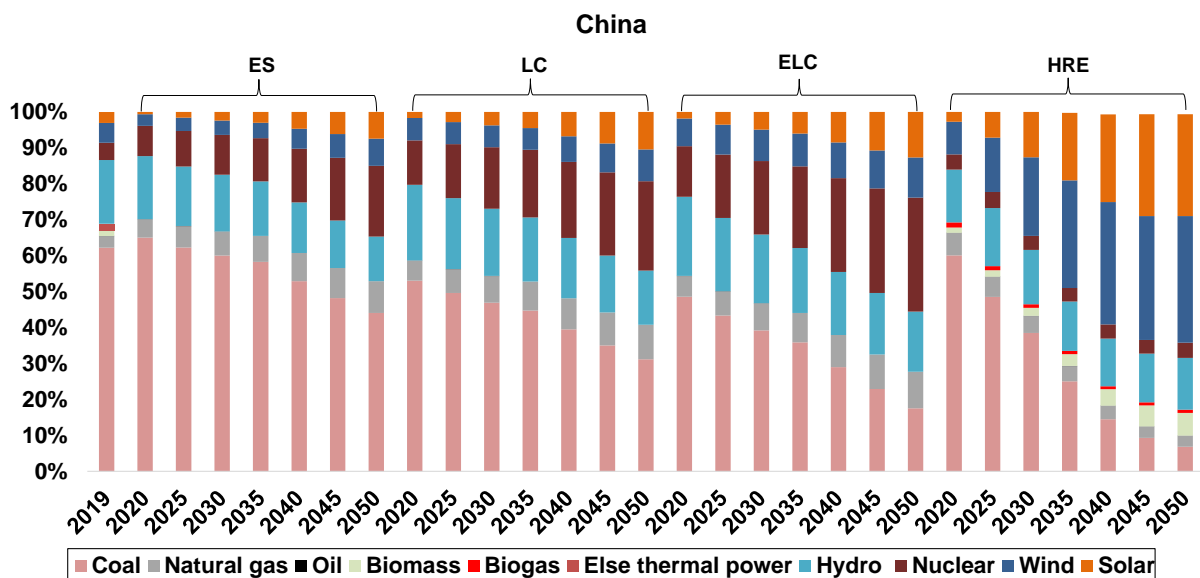
Figure 5.5: Future energy mix for China in four scenarios

5.2.2.2. Regional scale

These four abovementioned scenarios describe the future energy mix on the national level. The regional energy mix is not given by any according to our literature survey. The regional electricity production mix should respect its local energy mix features. As abovementioned, some provinces have more wind power resource and others have more hydro or nuclear. Therefore, this chapter proposes a method to obtain the local energy mix, based on the energy mix of 2019 and the future national scenario. This method assumes that the regional nuclear or renewable energy features (the share of the local nuclear or renewable energy electricity production to that of the nation in 2019) is constant in the future.

It should be noted that, some provinces import electricity from other provinces in China, for example, a part of the electricity produced in Inner Mongolia is transmitted to the north and east China. It is difficult to obtain the data of the interactions between provinces. To simplify the problem, the interactions are not considered; the electricity consumption mix is therefore assumed to be identical with the electricity production mix.

For one province, in a first step, the ratio $R_{i,2019}^k$ of its nuclear or renewable energy electricity production $E_{i,2019}^k$ to that of the nation $E_{i,2019}^{\text{nation}}$ of 2019 is calculated by equation (5-1), as well as the total electricity production ratio; the ratio $R_{i,j}^k$ is constant for the future year j (aiming at maintaining the nuclear or renewable energy features):

$$R_{i,j}^k = R_{i,2019}^k = \frac{E_{i,2019}^k}{E_{i,2019}^{\text{nation}}} \tag{5-1}$$

where i is the nuclear or renewable technology (hydro, wind, solar) or total; j is the year (from 2020 to 2050, every 5 years); k is the province (HU, BJ, GD, NM,YN).

The second step is to calculate the corresponding nuclear, renewable energy and total electricity production $E_{i,j}^k$ of each province in the future:

$$E_{i,j}^k = R_{i,j}^k \cdot E_{i,j}^{\text{nation}} \tag{5-2}$$

where $E_{i,j}^{\text{nation}}$ is the nuclear, renewable energy or total electricity production of the nation.

The third step is to calculate the thermal power electricity production $E_{\text{thermal},j}^k$, which supplies the remaining part in the total production $E_{\text{total},j}^k$ that nuclear and renewable energies cannot fulfil:

$$E_{\text{thermal},j}^k = E_{\text{total},j}^k - E_{\text{hydro},j}^k - E_{\text{nuclear},j}^k - E_{\text{wind},j}^k - E_{\text{solar},j}^k \tag{5-3}$$

In the fourth step, if the thermal power electricity production is calculated to be negative, meaning the nuclear + renewable energy produces more electricity than the total, the negative part is distributed on nuclear and renewable resources based on their own production ratios 5 years ago (meaning the latest ratios are used) in the total non fossil production. This step can be expressed by:

$$E_{i,j}^k$$

$$= \begin{cases} E_{i,j}^k & \text{if } E_{\text{thermal},j}^k > 0 \\ E_{i,j}^k + E_{\text{thermal},j}^k \cdot \dfrac{E_{i,j-5}^k}{E_{\text{hydro},j-5}^k + E_{\text{nuclear},j-5}^k + E_{\text{wind},j-5}^k + E_{\text{solar},j-5}^k} & \text{if } E_{\text{thermal},j}^k \leq 0 \end{cases} \qquad \textbf{(5-4)}$$

$$E_{\text{thermal},j}^k = \begin{cases} E_{\text{thermal},j}^k & \text{if } E_{\text{thermal},j}^k > 0 \\ 0 & \text{if } E_{\text{thermal},j}^k \leq 0 \end{cases} \qquad \textbf{(5-5)}$$

The final step is to determine the electricity production of each technology in thermal power. The future ratio of each technology in thermal power on the national scale is illustrated in Table 5-2. These ratios are assumed to be identical on the regional scale.

One general technology might contain several detailed sub technologies, as listed in Table 5-3. The shares of detailed sub technologies in each technology are considered identical for all the five provinces and the nation and they will not evolve with time.

By applying this method, the four scenarios on regional scale are shown in Figure 5.6 to Figure 5.10. The detailed production of each technology for each province is illustrated in Table Annex-2 - Table Annex-6.

In the ES, LC and ELC scenarios of Hubei, coal power will remain the largest contributor in the total power generation. The share of natural gas power will increase largely from 3.2 % in 2019 to 23.5 % in LC-2050. Hydro power is still important (varying from 18 % to 32 %) but the share will slightly drop with time. The wind and solar power will also become more important, reaching 6.8 % and 10.8 % in ELC-2050, respectively. In HRE-2050, the share of solar power will become the largest (24.2 %), followed by wind power (21.5 %) and hydro (20.9 %). The share of coal power will decrease to 13.3 %, compared to 61.6 % in 2019. The share of natural gas power will increase to 12.3 %. The renewable energy feature in HRE-2050 shows a balance between wind, solar and hydro.

The future energy mix of Beijing is shown in Figure 5.7. As analysed in section 5.2.2, the share of renewable energy is small in the energy structure of Beijing. In the future scenarios, this structure will be maintained. In the ES, LC and ELC scenarios, no wind energy will contribute and the share of solar energy is smaller than 1 %. Over 97 % of electricity will still be generated by thermal technologies, but a part of coal power will be replaced by natural gas. In the HRE scenario, the solar energy will be still minor. The share of coal power will decrease and more biomass power will be used, which will reach to 35.7 % in 2050.

Guandong being the province with the highest share of nuclear production in China in 2019, this trend is also observed in the ES, LC and ELC scenarios, as illustrated in Figure 5.8. As abovementioned, nuclear power will be more developed in these three scenarios on a national scale, resulting a huge increase of nuclear in Guangdong as well. There will be no more thermal power from LC-2040 and ELC-2030 and the corresponding nuclear share will be over 90 %. Hydro power will be the second contributor providing around 4 % of the total electricity in ELC-2050. In the HRE scenario,

the share of nuclear power is more stable varying from 16.6 % to 20 %. The shares of wind and solar will increase to 9.9 % and 6.2 % in 2050 respectively. The coal power will be less important and the biomass will contribute to 21.9 % of the total production.

The electricity of Inner Mongolia is mainly generated by thermal power and wind power in 2019. As shown in Figure 5.9, they will also be important in the ES, LC and ELC scenarios. The share of natural gas will increase and the share of coal will decrease, but still larger than 39 %. The wind and solar power will generate 24.6 % and 12.2 % of the total electricity in ELC-2050. In the HRE scenario, the thermal power will totally be replaced by wind and solar power from 2045, which will quickly increase respectively to 73.5 % and 25.7 % in 2050. The renewable energy feature in HRE-2050 shows a domination by wind and solar power.

The future mix of Yunnan is shown in Figure 5.10. The hydro power will generate more than half of the total in any scenario. Different from other cities, thermal power will increase in the ES, LC and ELC scenarios, because the capacity increase of hydro power and other renewable energies will not meet the increase of the total electricity consumption, the thermal power will therefore increase to fulfil the lacking part. The share of wind and solar will increase to 14.2 % and 5.7 % in ELC-2050. In the HRE scenario, the thermal power will be replaced by wind and solar from 2030, and only hydro, wind and solar will supply the electricity afterwards. The share of hydro, wind and solar will be 54 %, 35.9 % and 10.1 % respectively.

Table 5-2   ***Technologies in thermal power on the national scale in the ES, LC and ELC scenarios***

Scenario	Year	Coal	Natural gas	Oil	Biomass	Biogas	Thermal
ES	2020	92.68 %	7.23 %	0.09 %	0 %	0 %	100 %
	2025	91.22 %	8.73 %	0.06 %	0 %	0 %	100 %
	2030	90.01 %	9.97 %	0.03 %	0 %	0 %	100 %
	2035	88.99 %	11.01 %	0 %	0 %	0 %	100 %
	2040	87.10 %	12.90 %	0 %	0 %	0 %	100 %
	2045	85.19 %	14.81 %	0 %	0 %	0 %	100 %
	2050	83.26 %	16.74 %	0 %	0 %	0 %	100 %
LC	2020	90.41 %	9.50 %	0.09 %	0 %	0 %	100 %
	2025	88.23 %	11.72 %	0.06 %	0 %	0 %	100 %
	2030	86.35 %	13.62 %	0.03 %	0 %	0 %	100 %
	2035	84.72 %	15.28 %	0 %	0 %	0 %	100 %
	2040	82.02 %	17.98 %	0 %	0 %	0 %	100 %
	2045	79.28 %	20.72 %	0 %	0 %	0 %	100 %
	2050	76.49 %	23.51 %	0 %	0 %	0 %	100 %
ELC	2020	89.33 %	10.57 %	0.10 %	0 %	0 %	100 %
	2025	86.46 %	13.47 %	0.06 %	0 %	0 %	100 %
	2030	83.84 %	16.13 %	0.03 %	0 %	0 %	100 %
	2035	81.43 %	18.57 %	0 %	0 %	0 %	100 %
	2040	76.43 %	23.57 %	0 %	0 %	0 %	100 %
	2045	70.47 %	29.53 %	0 %	0 %	0 %	100 %
	2050	63.23 %	36.77 %	0 %	0 %	0 %	100 %
HRE	2020	86.75 %	9.07 %	0.03 %	2.10 %	2.05 %	100 %
	2025	85.00 %	9.76 %	0.03 %	3.14 %	2.06 %	100 %
	2030	82.75 %	10.20 %	0.04 %	4.87 %	2.14 %	100 %
	2035	74.74 %	12.67 %	0.05 %	9.85 %	2.70 %	100 %
	2040	61.26 %	15.91 %	0.06 %	19.40 %	3.37 %	100 %
	2045	48.53 %	16.34 %	0.07 %	30.65 %	4.41 %	100 %
	2050	39.83 %	17.88 %	0.08 %	36.88 %	5.33 %	100 %

Table 5-3   Detailed description of each technology in this study

Technology	*Detailed description*
Coal	Centralised power plant from coal
Natural gas	Conventional power plant (8.5 %) and combined cycle power plant (91.5 %)
Oil	Oil power plant
Biomass	Biomass power plant
Biogas	Biogas power plant
Else thermal	Treatment of blast furnace gas
Hydro	Run of river hydro (99.5 %) and pumped storage (0.5 %)
Nuclear	Pressure water reactor nuclear power plant
Wind	Onshore turbine<1 MW (15.7 %), 1-3 MW (45.7%), >3 MW (38.5 %)
Solar	Open ground multi-Si system (66.7 %), on-roof mono-Si (14.8 %), on-roof multi-Si (18.5 %)
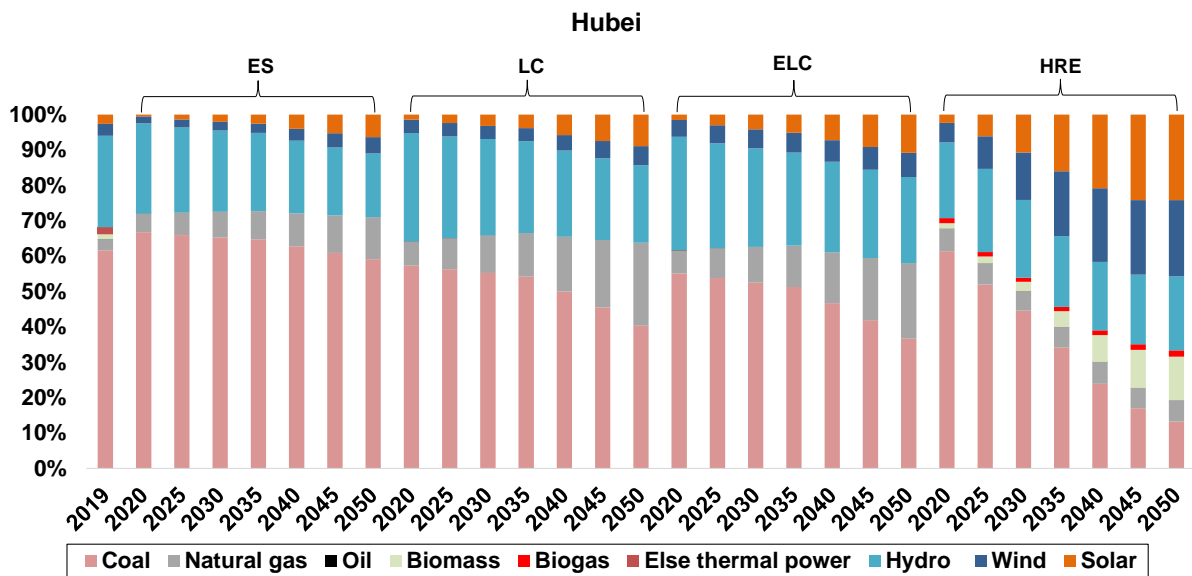
Figure 5.6: Future energy mix for Hubei
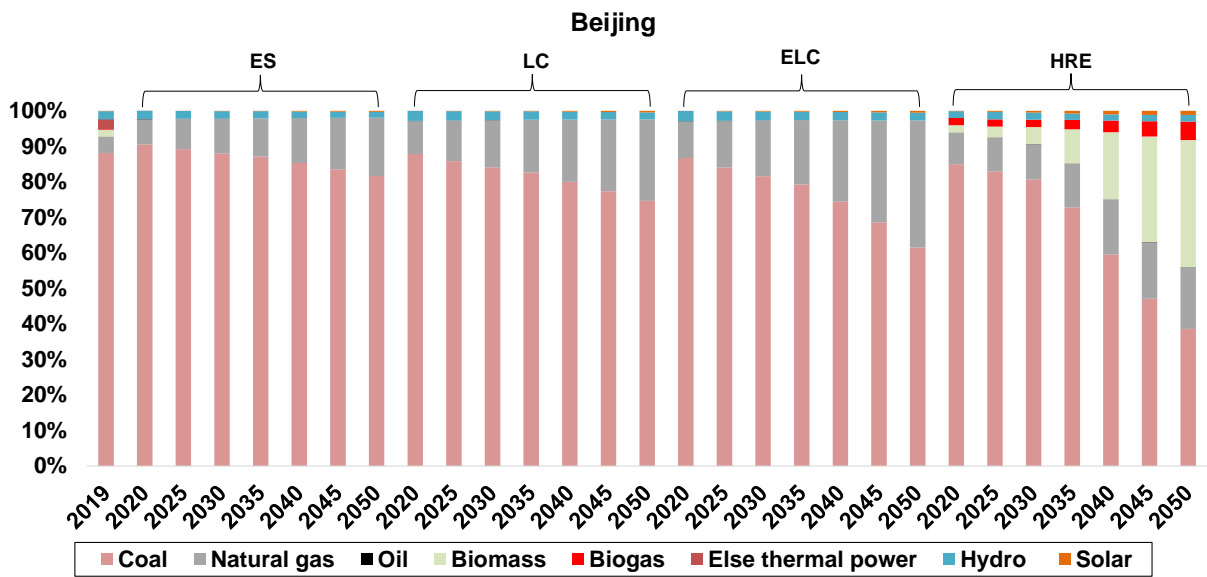
Beijing

Figure 5.7: Future energy mix for Beijing
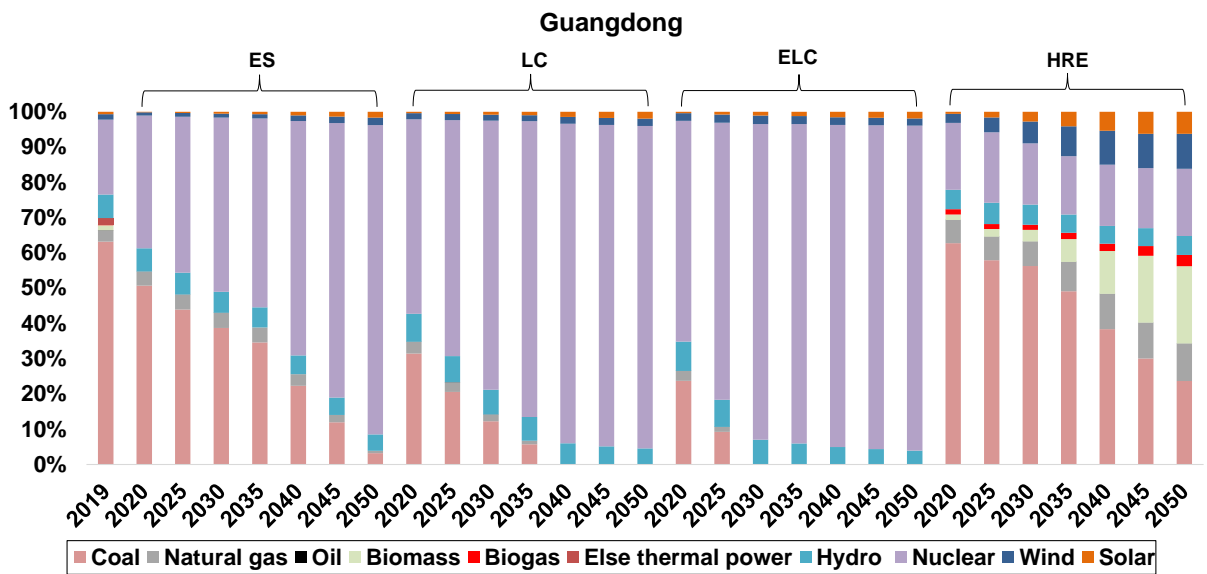
Guangdong

Figure 5.8: Future energy mix for Guangdong
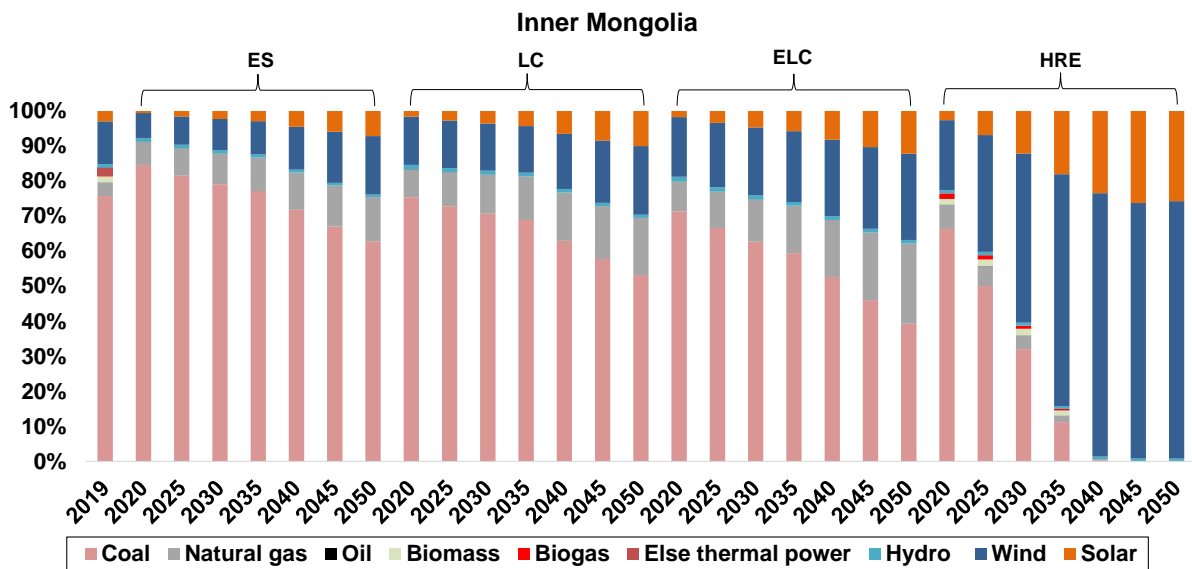
Figure 5.9: Future energy mix for Mongolia
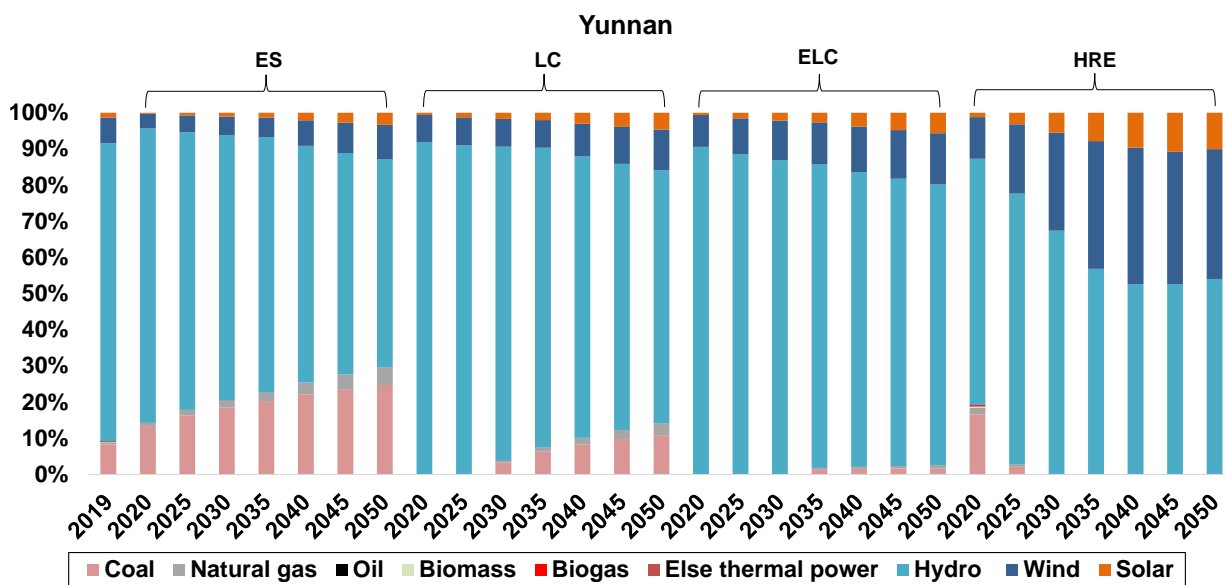
Figure 5.10: Future energy mix for Yunnan

5.3.   Methodology

5.3.1.   *General method*

The method is based on dynamic energy simulation and LCA of a building, as shown in Figure 5.11. The case study is assumed to be located in the five abovementioned regions in China with different climate conditions and energy mix. Environmental impacts are expressed per m^2 of useful area and per year, considering a building lifespan of 50 years which is the designed life expectancy

proposed by the government (MOHURD, 2019). European standards in civil engineering impose a lifespan of around 250 years for concrete building structures (Palacios-Munoz et al., 2019). Increasing the lifespan of buildings would decrease environmental impacts. A building life cycle is divided into four stages: construction (including the fabrication of products), use (including energy and water consumption), renovation and deconstruction (including waste treatment or possible recycling). Starting from the international ecoinvent database [25], data regarding the fabrication of building materials are contextualised considering the energy mix of year 2019 in different provinces as well as the national average energy mix: if the production of 1 kg of material requires electricity, the impacts of this electricity production are modified in order to correspond to the chosen mix. The dynamic building energy simulation tool COMFIE is used to evaluate the energy loads (e.g. heating/cooling load, domestic hot water (DHW) load and specific electricity load) in the use stage. The weather files of the cities are downloaded from EnergyPlus website[26,27,28,29,30]. The energy loads are then converted to electricity consumption by considering the efficiency of the energy supply equipments, and the yearly electricity consumption is assumed to be identical during the lifespan. The impacts of electricity are evaluated according to the national and local energy mixes, for 2019 and every five years from 2020 to 2050. The impacts of the other years are obtained by linear interpolation. The impacts of the electricity consumed in the years from 2050 to 2068 are identical to those of year 2050. The renovation stage concerns the replacement of materials and equipments at the end of their lives, which is assumed to have the same impacts as the construction stage, meaning they are not contexualised with the future energy mix even if they are replaced in the future years. The deconstruction stage does not involve any significant energy consumption, thus no contextualisation process is considered in this stage.

The effects of the energy mix on the environmental impacts can be then determined by comparing two approaches in the use stage: dynamic versus static energy mix approach. The dynamic energy mix approach uses the yearly evolving impacts of electricity according to the scenarios. On the contrary, the static energy mix approach considers constant impacts for all years, corresponding to the beginning year 2019. They are applied to four future energy scenarios (ES, LC, ELC and HRE) and five provinces (HU, BJ, GD, NM and YN), and compared to the national average energy mix to determine the spatial and temporal effects.

The building environmental impacts evaluation tool used in this chapter is EQUER. It assesses the environmental impacts of buildings by the LCA approach, developed since 1995 at École des Mines de Paris (Polster, 1995), and now integrated into the commercial software Pleiades. This tool has been completed to deal with neighbourhoods (Popovici, 2005 ; Herfray, 2011), by integrating several types of buildings, public spaces (roads, green spaces, etc.) and networks (water, district

---

[25] https://www.ecoinvent.org/home.html

[26] https://energyplus.net/weather-location/asia_wmo_region_2/CHN//CHN_Beijing.Beijing.545110_CSWD

[27] https://energyplus.net/weather-location/asia_wmo_region_2/CHN//CHN_Guangdong.Guangzhou.592870_CSWD

[28] https://energyplus.net/weather-location/asia_wmo_region_2/CHN//CHN_Nei.Mongol.Hohhot.534630_CSWD

[29] https://energyplus.net/weather-location/asia_wmo_region_2/CHN//CHN_Yunnan.Kunming.567780_CSWD

[30] https://energyplus.net/weather-location/asia_wmo_region_2/CHN/CHN_Hubei.Wuhan.574940_SWERA

heating, etc.). Its reliability was studied in several projects (Peuportier et al., 2004 ; Salmon et al., 2011 ; Lebert et al., 2014 ; Frischknecht et al., 2019).

The impact evaluation is based on the LCI database ecoinvent v3.4[31]. Ecoinvent database is a Swiss database with consistent and transparent, up-to-date LCI data. It is one of the most comprehensive international LCI databases containing the areas of agriculture, energy supply, transport, biofuels and biomaterials, bulk and chemicals, construction materials, packaging materials, basic and precious metals, metals processing and electronics as well as waste treatment. Common building materials such as concrete, insulation layers, etc. are included in the database.
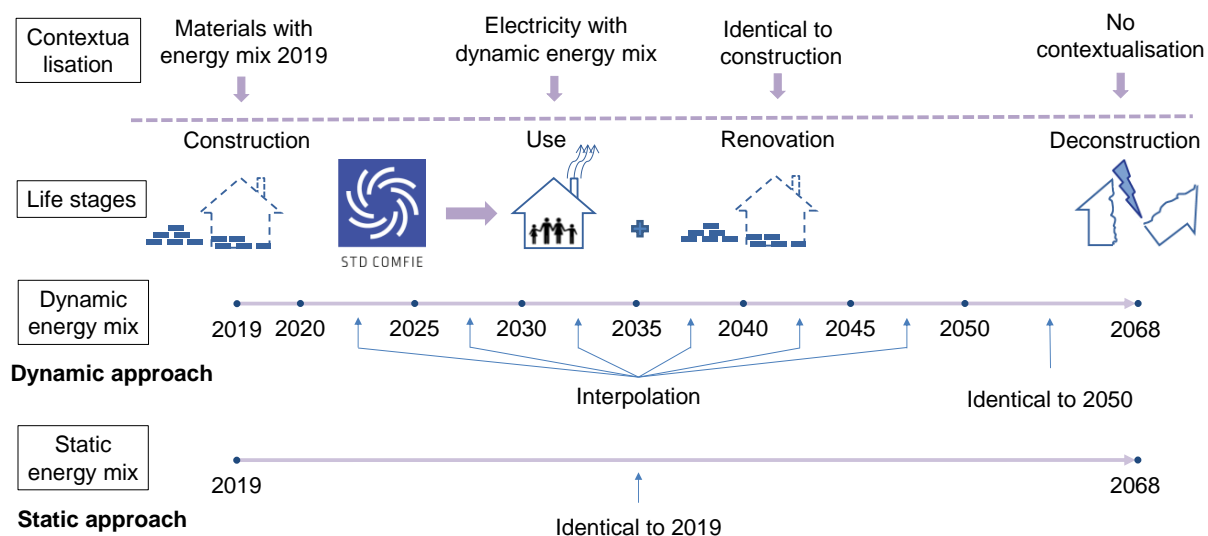
Figure 5.11: Illustration of the method in this chapter

5.3.2. *LCA method*

5.3.2.1. **Goal and scope**

The main goal of LCA in this study is to determine the effects of the spatial variations (five regions in five climate zones) and temporal variations (four future scenarios) of electricity production mix on environmental impacts of the case study presented in section 1.6.

The evaluation scope covers the entire life cycle (50 years) of the building, consisting of the construction stage (at the beginning of year 2019), the use stage (year 2019-2068), the renovation stage (depending on the lifespan of building materials and components) and the deconstruction stage (at the end of year 2068). The system boundaries consider the processes in the building (e.g. the heat pump system), upstream processes (e.g. materials fabrication) and downstream processes (e.g. landfill of materials at end-of-life). Focusing on the environmental impacts of the building, the daily transportation and waste generation are not considered.

---

[31] https://www.ecoinvent.org/database/older-versions/ecoinvent-34/ecoinvent-34.html

The functional unit is 1 m^2 over one year based on a lifespan of 50 years for a high-rise residential building located in the five regions in five climatic zones.

5.3.2.2.   Inventory analysis

The amount of each material is calculated in EQUER and the corresponding element in ecoinvent is used in the evaluation. The amounts of materials and equipments are summarised in Table 5-4. Besides the materials for the building construction, the GCHP system is included in this inventory. Based on the dynamic energy simulation results of the case study, the highest heating power is 554 000 kW, therefore a heat pump of 600 kW is estimated to be equipped. Available LCI data for a 30 kW heat pump in the ecoinvent database are multiplied by 20. It is also evaluated that 100 boreholes of 133 m and a hot water tank of 25 000 L are required. A decentralised ventilation system of 96 × 120 m^3/h is needed, which corresponds to 16 units of 6 × 120 m^3/h systems in ecoinvent v3.4. Some extra materials are estimated: for every 100 m^2, 34.8 kg copper, 105 kg steel, 21.8 kg polyvinyl chloride (PVC), 200 kg ceramic tile, 52 kg polyethylene (PE), 500 m cable for electricity and plumbing, 0.33 ton concrete for foundation and underground space are needed, and the total quantities are listed in Table 5-4.

In the assumptions, the materials transported to the construction site are 5 % higher than the needed materials in order to account for on-site processes, broken elements and superfluous purchased quantities. The materials are transported by truck. The building elements lifespans are 10 years for finishes, 20 years for the equipments, 30 years for windows and doors, and 50 years for the building itself. The materials and equipments are replaced at their end of life in the renovation stage. The distance from the material factories to the construction site is assumed as 100 km. The distance from the site to landfill plant in the deconstruction stage is 20 km. All deconstruction waste is assumed to be landfilled, which has little influence because end-of-life is a minor contributor to LCA of buildings compared to the use and construction stages (Lotteau et al., 2015), see section 5.4.3.1.

Regarding the energy consumption, there are four main uses to be considered: heating, cooling, DHW and specific electricity (including lighting). Heating, cooling and DHW are provided by the GCHP system driven by electricity. The COPs for heating, DHW and cooling are 3.1, 3 and 3.9, respectively, from *Technical regulations for ground-source heat pump systems* (MOHURD-Hubei, 2017) for Hubei province. The specific electricity is supplied by the electricity grid. The water network leakage is set at 20 %, and the hot and cold water consumptions are set at 40 liters/day/person and 100 liters/day/person. The total number of occupants in the building is 498.

Table 5-4   ***Materials and equipments in case study and corresponding LCA items in ecoinvent***

Name	LCI item in ecoinvent	Quantity of LCI item	Unit
Aerated concrete block	Aerated concrete block	2 884 380	kg
Borehole heat exchanger 133 m	borehole heat exchanger 133 m	100	unit
Cable 3 conductors	Cable 3 conductors	62 293	m
Cement mortar	Cement mortar	933 774	kg
Ceramic tile	Ceramic tile	329 894	kg
Concrete	Normal unreinforced concrete production, with cement CEM II/A	4 535 787	kg
Copper	Copper	4 341	kg
Double glazing window with aluminium frame	Double glazing window with aluminium frame	2 626	m²
Emulsified asphalt perlite	Expanded perlite	5 093	kg
External door wood - aluminium	External door wood - aluminium	222	m²
Extruded Polystyrene Board (XPS)	Extruded polystyrene	10 929	kg
Extruded Polystyrene Foam Board	Extruded polystyrene	509	kg
Fine aggregate concrete	Normal unreinforced concrete production, with cement CEM II/A	6 782 699	kg
Heat pump 600 kW	Heat pump 30kW	20	unit
Hot water tank	Hot water tank	25 000	L
Insulation mortar	Mortar	108 710	kg
Internal door wood	Internal door wood	1 101	m²
Marble	Stone	23 768	kg
Painting	Painting	63 347	m²
Polyethylene (PE) high density	Polyethylene (PE) high density	6 479	kg
PVC	PVC	2 714	kg
Steel	Steel	13 082	kg
Ventilation system - decentralised - 96 × 120 m³/h	Ventilation system - decentralised - 6 × 120 m³/h - steel ducts - without earth tube heat exchanger	16	unit

5.3.2.3.   Impact assessment

(1) Impact indicators

In EQUER, the environmental impact indicators for a building have been updated according to the progress of life cycle impact assessment knowledge. How they were chosen is detailed in Annex H in the PhD thesis of Pannier (2017). In Pleiades version 5.20.1.0, which was used in this chapter, 12 indicators are used to comprehensively evaluate a building's environmental impacts, as shown in Table 5-5.

- Global warming potential at 100 years. This indicator reflects the global warming potential of different greenhouse gases converted into ton CO_2 equivalent, for a period of 100 years.

- Acidification potential. This indicator is linked to acid rain and forests protection. It is expressed in kg sulfate equivalent.

- Cumulated energy demand. Primary energy analysis can consider different energy carriers (electricity, heat) on a consistent basis. The analysis goes up to the extraction of the fuel upstream phase (such as crude oil or uranium), or other resources (such as hydro power). It is expressed in MJ.

- Water used. The total water consumption throughout the life cycle of the building is measured in m^3.

- Non-radioactive waste creation. Non-radioactive waste can be divided into three categories: inert (class III), banal (class II) and dangerous wastes (class I). The value of this indicator depends on the type of waste and the cost of treatment.

- Eutrophication potential. This indicator is linked to the intake of substances acting as fertilisers (nitrates and phosphates) in surface waters. These fertilisers promote the growth of blue-green algae, whose decomposition is toxic to living organisms.

- Photochemical oxidant formation potential. Ozone decomposition of certain volatile organic compounds (VOCs) under the presence of sunlight contributes to the formation of ozone. This smog has adverse effects on the respiratory tract.

- Radioactive waste creation. Radioactive waste here is classified to Class A, B and C, and the amounts are expressed in dm^3.

- Land use. This factor indicates how much land is occupied in m².year.

- Abiotic depletion potential. This indicator reflects the depletion of the environment and fossil mineral resources. The calculation is performed according to the remaining stock and the rate of consumption of the current economy, expressed in antimony equivalent per kg.

- Ecotoxicity. This indicator reflects the damage caused by the ecotoxic emissions to ecosystems. It is expressed as a PDF.m².year, in which PDF means the Potentially Disappeared Fraction.

- Human toxicity. This indicator reflects the impacts on human health, expressed in years of life lost (Disability Adjusted Life Years, DALYs).

Table 5-5   ***12 environmental impact indicators in EQUER***

n°	Indicator	Unit	Level	Legend
1	Global warming potential (100 years)	kg CO_2 eq.	Midpoint	GWP
2	Acidification potential	kg SO_2 eq.	Midpoint	AP
3	Cumulative energy demand	MJ	Midpoint	CED
4	Water used	L	Midpoint	Water
5	Waste	kg	Midpoint	Waste
6	Eutrophication potential	kg PO_4 eq.	Midpoint	EP
7	Photochemical ozone production	kg ethylene eq.	Midpoint	POP
8	Radioactive waste	m^3	Midpoint	Rad.W
9	Land use	m².year	Midpoint	Land
10	Abiotic resources depletion potential	kg antimony eq.	Midpoint	ADP
11	Damage to biodiversity	PDF.m².year	Endpoint	Biodiv
12	Damage to human health	DALYs	Endpoint	Hum

(2) Environmental impacts of electricity generation technologies

Ecoinvent v3.4 provides life cycle inventories (i.e. quantities of raw materials used, pollutants emitted to the air, water and ground) corresponding to 1 kWh of electricity produced by different technologies at high voltage level (above 24 kV) for China and other countries (e.g. Swiss, France, etc.). It also includes inventories for grid infrastructure (transmission and distribution network) (Treyer and Bauer, 2016).

Life cycle impacts of 1 kWh delivered to the low voltage level (below 1 kV) by a given technology, I_i, include impacts related to electricity production using the technology and impacts related to the network infrastructure (Roux et al., 2016b), as expressed in :

$$I_i = C_f \times (LCI_i \times (1 + l) + LCI_{\text{network},i})$$

(5-6)

where C_f is the characterisation factor matrix, LCI_i is the life cycle inventory of one kWh produced by technology "i", $LCI_{\text{network},i}$ is the life cycle inventory of electricity network infrastructure per kWh supplied in China for technology "i", and l is the level of losses. l represents electricity lost during transmission in the transport network (national and interconnection high voltage network), conversion and transmission in the distribution network (national low and medium voltage network, below 24 kV). 2 % losses are accounted for the transport network and 4 % losses for the distribution network according to *China Electricity Industry Annual Development Report 2019*[32].

---

[32] https://www.cec.org.cn/detail/index.html?1-284218

Because the main aim of this study is to investigate the impacts of different energy mixes, it should be noted that each technology is assumed independent of time and region, thus the impacts of each technology is constant through a building's lifespan for all regions in China. All the technologies are located in Hubei, China in ecoinvent v3.4 database, except for nuclear and biomass, because the corresponding technologies in Hubei are not available in ecoinvent v3.4. Thus, the inventory of these technologies is based on Guangdong's location in ecoinvent in this chapter.

All technologies are considered to produce electricity at high voltage (above 24 kV), except for photovoltaic systems (considered to release electricity at low voltage). By accounting for the share of each technology, environmental impacts ($I_{\text{loc,year}}$) of 1 kWh supplied by the grid in a certain location (nation or province) and in a certain year is the sum of environmental impacts of each technology multiplied by its contribution in the mix:

$$I_{\text{loc,year}} = \sum_{i=1}^{n} R_{\text{loc,year}}^{i} \times I_i \qquad \textbf{(5-7)}$$

where $R_{\text{loc,year}}^{i}$ is the share of technology i in a certain location and in a certain year and n is the total number of technologies.

(3) LCI database contextualisation

The contextualisation process of a material is accomplished by replacing the electricity used in the material fabrication (e.g. the electricity in France) with local electricity in China which can be under a province context or the nation context. The other inventories except electricity related to this material are assumed to be the same, meaning that their impacts are considered identical in all Chinese contexts. For example, the impacts of one material in a certain location in China and in a certain year, $I_{\text{loc,year}}^{\text{material}}$, can be contextualised based on the French database:

$$I_{\text{loc,year}}^{\text{material}} = I_{\text{FR}}^{\text{material}} - E \times I_{\text{FR}} + E \times I_{\text{loc,year}} \qquad \textbf{(5-8)}$$

where $I_{\text{FR}}^{\text{material}}$ is the impacts of this material under French context, E is amount of electricity used in the material fabrication and I_{FR} is the impacts of one kWh electricity in France.

5.3.2.4. Interpretation

The interpretation phase mainly focuses on how the energy mix influences the LCI databases and LCA impacts of a building in China. The importance of appropriately choosing the energy mix is revealed as well. This will be discussed in the next section.

5.4. Results and discussion

5.4.1. *Energy simulation results*

The heating and cooling loads of the studied case located in different cities are shown in Figure 5.12. The heating load of Hohhot located in SC zone is the largest, reaching 116.9 kWh/m². The heating load of Guangzhou located in HSWW zone is small (2.4 kWh/m²). Kunming in M zone does not need to be heated for the whole year, on the contrary it has the largest cooling load of 117.1 kWh/m². The heating load (48.7 kWh/m²) of Wuhan in HSCW is slightly larger than the cooling load (44.9 kWh/m²). The C zone city Beijing has a heating load over 100 kWh/m² and a smaller cooling load of 25.1 kWh/m².
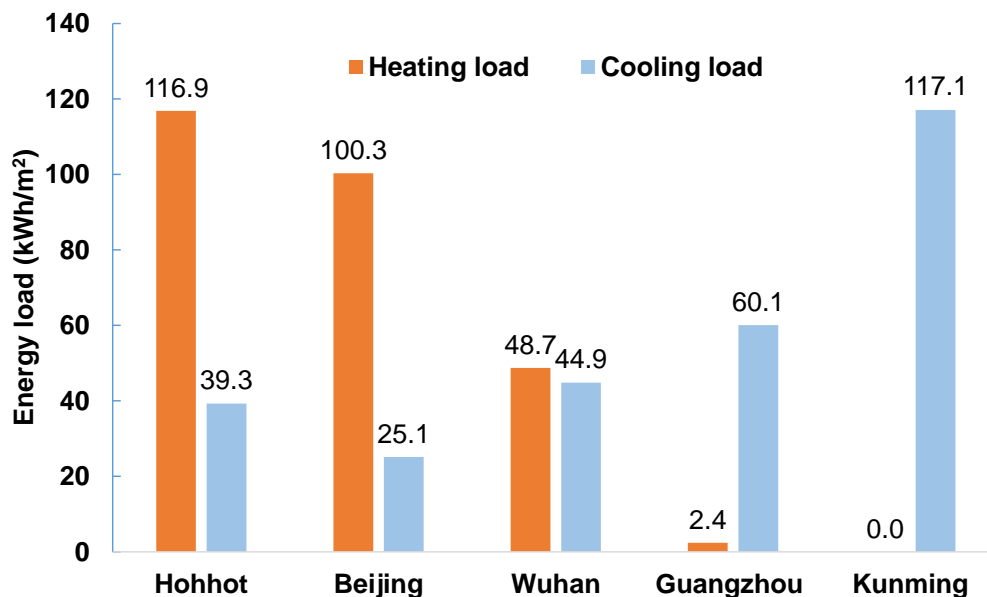
Figure 5.12: Energy performance of the studied case in the five cities

As abovementioned, heating, cooling and DHW are provided by the GCHP driven by electricity and the COPs for heating, cooling and DHW are 3.1, 3 and 3.9, respectively. The yearly final energy consumption is shown in Figure 5.13. The specific electricity consumption and the electricity consumption for DHW are estimated to be 468 007 kWh and 85 667 kWh per year respectively for all the five cities. The yearly total primary energy consumption of Guangzhou is the smallest 60.6 kWh/m² and Hohhot has the largest total consumption of 92.2 kWh/m².
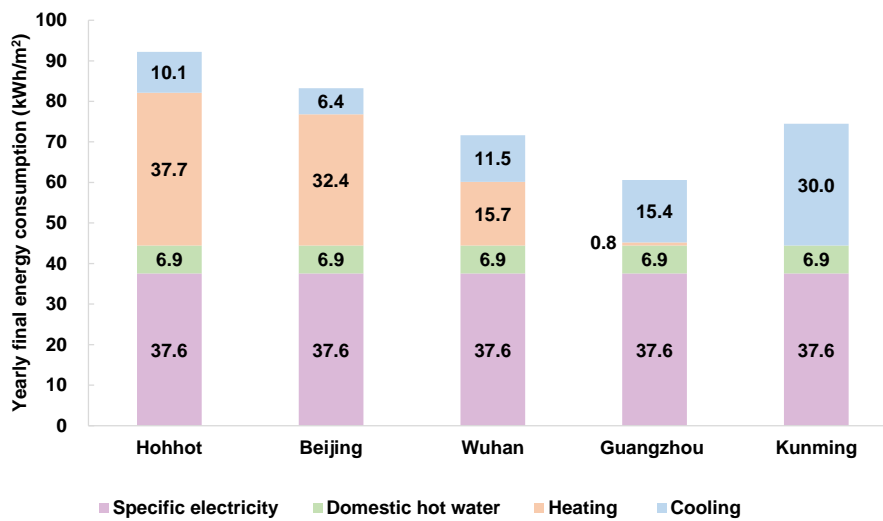
Figure 5.13: Total yearly final energy consumption per square meter for five cities (heated and cooled area of the building)

5.4.2.   *Contextualised database comparison*

5.4.2.1.   **Carbon footprint of energy mixes**

The environmental impacts of one kWh electricity were obtained after national and local contextualisation, as listed in Table Annex-7 - Table Annex-12. One of the most important environmental impacts is carbon emissions. The carbon footprints of the energy mix at the national and provincial levels are shown in Figure 5.14 - Figure 5.19. On average, 1 kWh electricity of the national average energy mix in 2019 emits 990 g CO_{2eq}; it emits 980 g, 1 391 g, 1 002 g, 1 201 g and 148 g CO_{2eq} for Hubei, Beijing, Guangdong, Inner Mongolia and Yunnan respectively. The energy mix of Beijing is dominated by thermal power, resulting in the highest CO_{2eq} emissions (40 % higher than the national average mix) among all five provinces. 82 % of electricity in Yunnan in 2019 is generated by hydro power, which is a much cleaner technology compared to thermal power, leading to the lowest emissions (85 % lower than the national average mix). The emissions ranking is Beijing > Inner Mongolia > Guangdong > Nation > Hubei > Yunnan.

In the future scenarios, on the national scale, the HRE scenario becomes the scenario with the lowest carbon content from 2030, and the emissions decrease to 169 g CO_{2eq} (17 % compared to 2019). In the ES, LC and ELC scenarios, the emissions of 2050 show a reduction of 27 %, 45 % and 64 % to 2019. In general, the emissions show a decreasing trend for all the provinces except Yunnan. This coincides with a part of hydro share that will be replaced by thermal power in Yunnan. The CO_{2eq} emissions of 1 kWh electricity in ES-2050, LC-2050, ELC-2050 and HRE-2050 of Yunnan are 415 g, 203 g, 53 g and 30 g, respectively, which are 280 %, 137 %, 36 % and 20 % of that in 2019. For Hubei, CO_{2eq} emissions are not significantly reduced in the ES scenario and a small increase is shown from 2020 to 2045. In the HRE scenario, the CO_{2eq} emissions are greatly reduced to 280 g in 2050, due to

the increased share of renewable energy. The carbon emissions of Beijing decrease in all four scenarios, and the HRE scenario indicates a larger reduction (around 48 %) in 2050 by replacing the share of coal power with biomass power compared to 2019. In Guangdong, the HRE scenario shows higher carbon emissions than other scenarios, because nuclear in the other three scenarios is significantly increased. The CO_{2eq} emissions of 1 kWh electricity in ES-2050, LC-2050, ELC-2050 and HRE-2050 of Guangdong are 65 g, 18 g, 18 g and 455 g, respectively, but this might cause more other impacts (e.g. radioactive waste). Inner Mongolia is a province with high wind and solar power potential, thus in the HRE scenario, the shares of wind and solar power are high, leading a low CO_{2eq} emissions of 48 g in 2050, which is only 4 % that of 2019. In the ES, LC and ELC scenarios, the increase of wind and solar power is much slower compared to the HRE scenario, consequentially the CO_{2eq} emissions are higher, with corresponding values of 1027 g, 914 g, 758 g. It can be inferred that the carbon emissions significantly vary with the location, and this difference could be magnified with the energy mix evolution in the future. The emissions ranking changes to Beijing > Inner Mongolia > Hubei > Nation > Yunnan > Guangdong in the ES, LC and ELC scenarios, and Beijing > Guangdong > Hubei > Nation > Inner Mongolia > Yunnan in the HRE scenario.
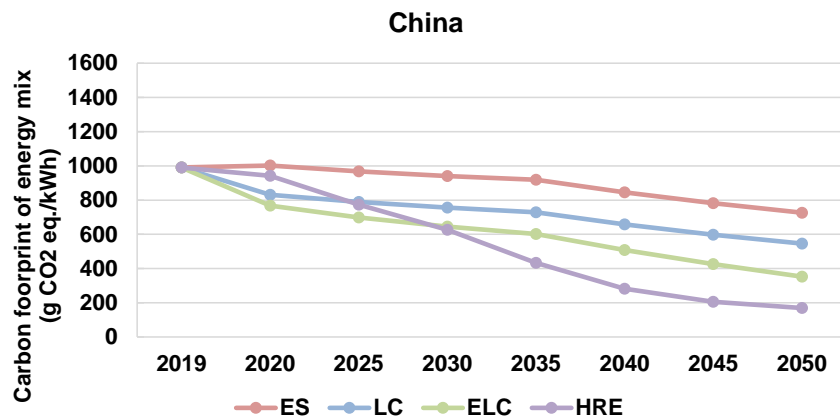
Figure 5.14: Carbon footprint of the national average energy mix
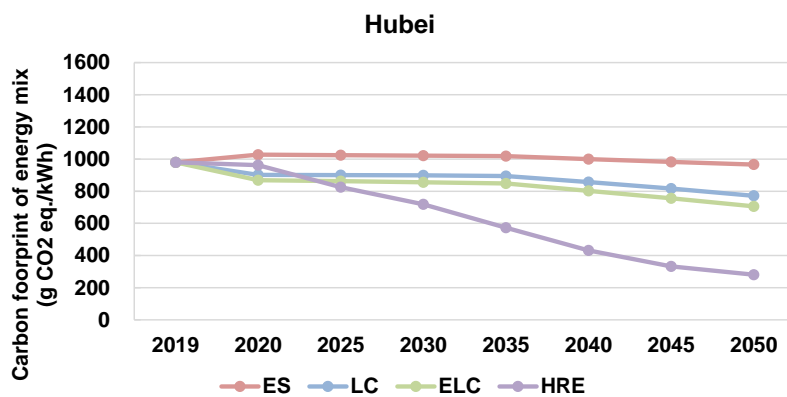
Figure 5.15: Carbon footprint of energy mix in Hubei
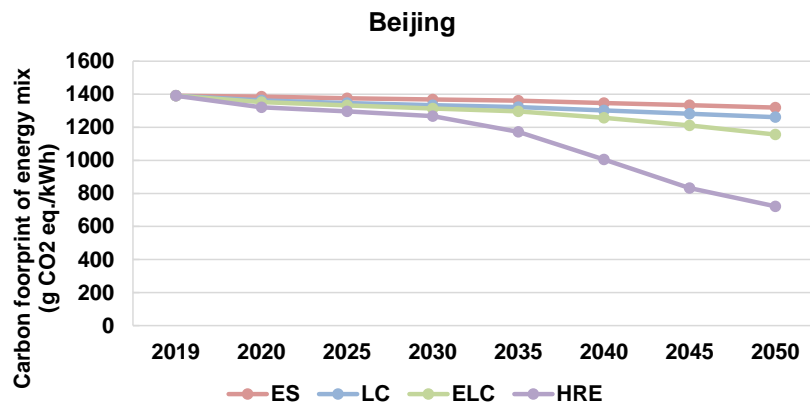
Figure 5.16: Carbon footprint of energy mix in Beijing
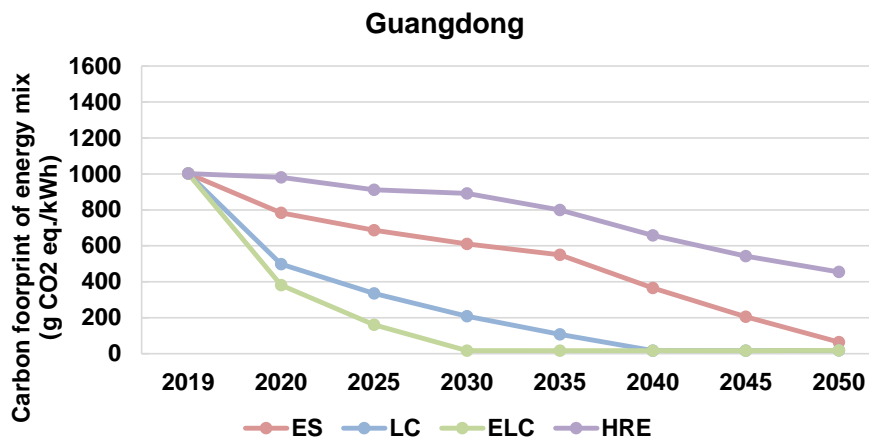
Figure 5.17: Carbon footprint of energy mix in Guangdong
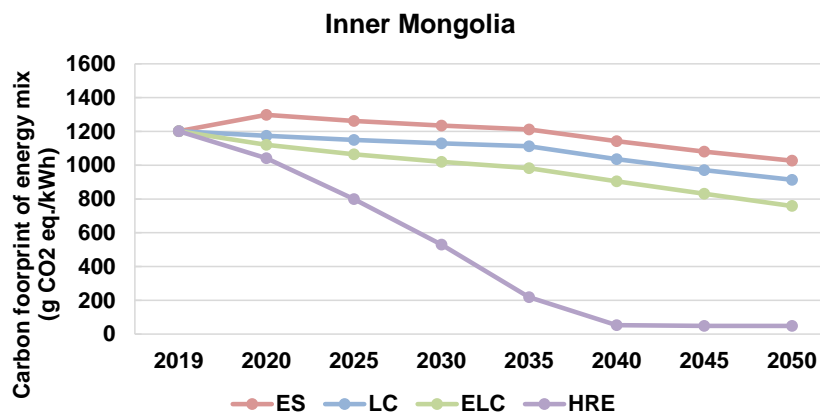
Figure 5.18: Carbon footprint of energy mix in Inner Mongolia
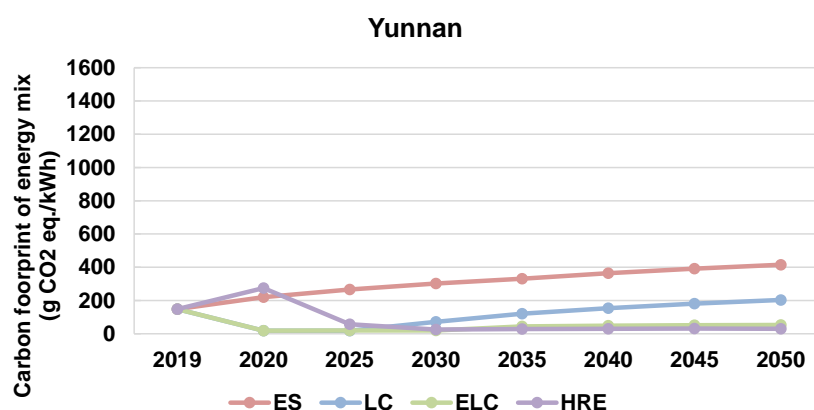
Figure 5.19: Carbon footprint of energy mix in Yunnan

5.4.2.2. Building materials

The building materials influence the construction stage and the renovation stage in a building's lifespan. The materials used in the studied case were contextualised under Chinese national and regional contexts by applying the method in section (3). The energy mix of each region used in contextualisation is for the year 2019. The effects of choosing local energy mixes compared to a nation average mix at the construction stage are shown in Figure 5.20. The original database contextualised for France is also illustrated, to present the contextualisation effects. The contextualised databases for Hubei and China are provided in Annex C and Annex D, which can be a reference for the researchers who work in building LCA in China.

Compared to the materials contextualised using a national average mix, the environmental impacts of the local database in China vary from -7.4 % (waste in Yunnan) to +6 % (radioactive waste in Guangdong). The impacts using the Yunnan database are the smallest and those of Beijing database are the largest (except radioactive waste). France has a nuclear dominated energy structure (over 70 %), thus the radioactive waste of the original French database is 23.5 % higher than the database contextualised with Chinese national average energy mix. However, it shows a reduction of 6 % in CO_{2eq} emissions and 4 % in acidification potential.

The choice of a contextualised database in China is not a key factor affecting the total environmental impact, because their differences are small and the construction and renovation stages are less important than the use stage (see Figure 5.21). However this importance, particularly for CO_2 emissions, might increase in the future with a longer lifespan because the construction and renovation stages will occupy larger shares in total impacts (e.g. less CO_2 emissions in the use stage in the future due to cleaner electricity presented in section 5.4.2.1).
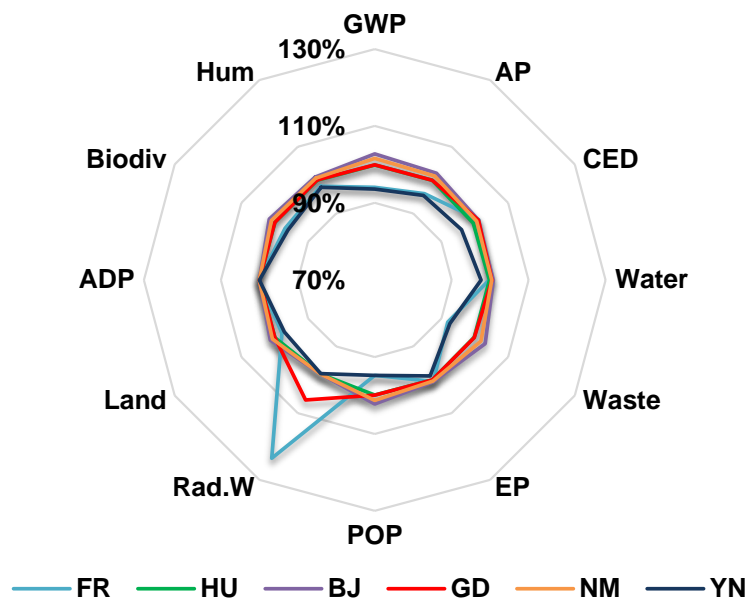
Figure 5.20: Effects of the construction stage with local energy mix 2019 compared to NATION-2019

5.4.3.   *LCA results for case study in Wuhan, Hubei*

5.4.3.1.   **Static approach**

In reality, the case study is located in Wuhan. This section aims at evaluating the environmental impacts of the studied case based on a local contextualised database, by using a static energy mix (HU-2019) in the use stage. The results correspond to a common LCA practice that does not account for the electricity system evolution in the future. The environmental impacts are given in Table 5-6. The contribution of each stage for the environmental impacts is shown in Figure 5.21.

In the whole lifespan of the building, nearly 53.4 kiloton CO_{2eq} are emitted and approximately 570 000 GJ of primary energy are consumed over 50 years, corresponding to 86 kg/m^2.year and 254 kWh/m^2.year. The use stage generates the most of the environmental impacts among the four stages: in 10 of the 12 impacts (except Rad.W and ADP). 84.1 % of CO_{2eq} is generated, 80.9 % of the primary energy and 96.5 % of water is consumed in this stage.

The construction stage contributes to most of the Rad.W (33.6 %), followed by the renovation stage (32.7 %) It is the second important stage for GWP (9.6 %), CED (9.6 %) and water (2.2 %). The renovation stage generates the most of ADP of 55.4 %. 7 indicators are the second largest in the renovation stage The deconstruction stage has a minor influence (< 1 %) on the total impacts for 10 indicators out of 12, except for waste (21.5 %) and radioactive waste (3.8 %). These results support the simplification made in this study for the deconstruction stage.
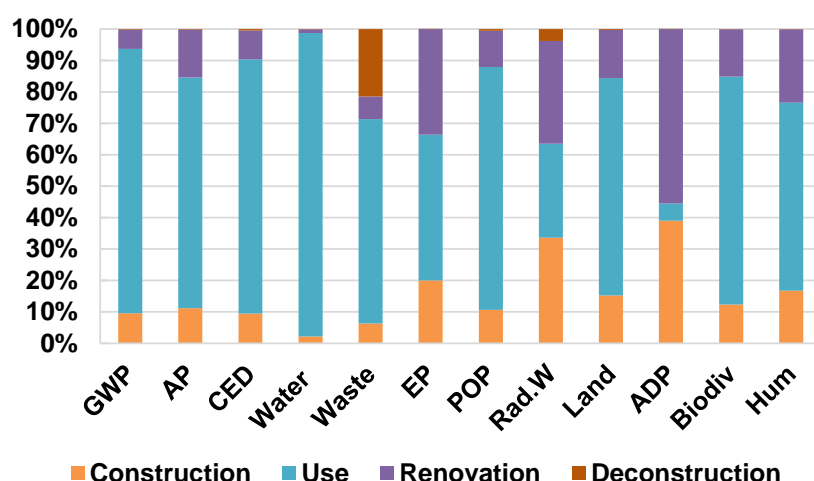
Figure 5.21: Contribution of each stage in the environmental impacts

Table 5-6   *Environmental impacts of the studied case by the static approach for a lifespan of 50 years*

Impact	Construction	Use	Renovation	Deconstruction	Total
GWP (t CO2 eq.)	5 110	44 900	3 280	96	53 400
AP (kg SO2 eq.)	49 400	325 000	67 200	1 020	444 000
CED (GJ)	53 800	461 000	52 200	2 880	570 000
Water (m³)	41 300	1 820 000	22 600	580	1 890 000
Waste (t)	4 640	47 600	5 250	15 700	73 300
EP (kg PO4 eq.)	11 100	25 900	18 700	21	55 700
POP (kg ethylene eq.)	16 300	118 000	17 700	874	153 000
Rad.W (dm³)	65	58	63	7	194
Land (m².year)	365 000	1 650 000	367 000	6 530	2 390 000
ADP (kg antimony eq.)	2 400	338	3 410	3	6 150
Biodiv (PDF.m².year)	2 840 000	16 600 000	3 450 000	32 100	22 900 000
Hum (DALYs)	32	116	45	0.2	193

The environmental impacts of the building components in the construction stage are shown in Figure 5.22. In this building, among all components in the construction stage, the equipment (heat pumps, boreholes, water tank, ventilation systems and cables) is the main source for 8 indicators in 12: AP (54 %), CED (23.1 %), Waste (34.6 %), EP (34.6 %), POP (35.7 %), ADP (66.1 %), Biodiv (46.8 %), Hum (61.1 %). The use of geothermal heat pumps obviously increases the environmental impacts in the construction stage. 15.2 % of CO_{2eq} emissions is due to the equipments, while 21.1 % is due to the building facades. The double glazing windows account for 13.1 % of the total primary energy.
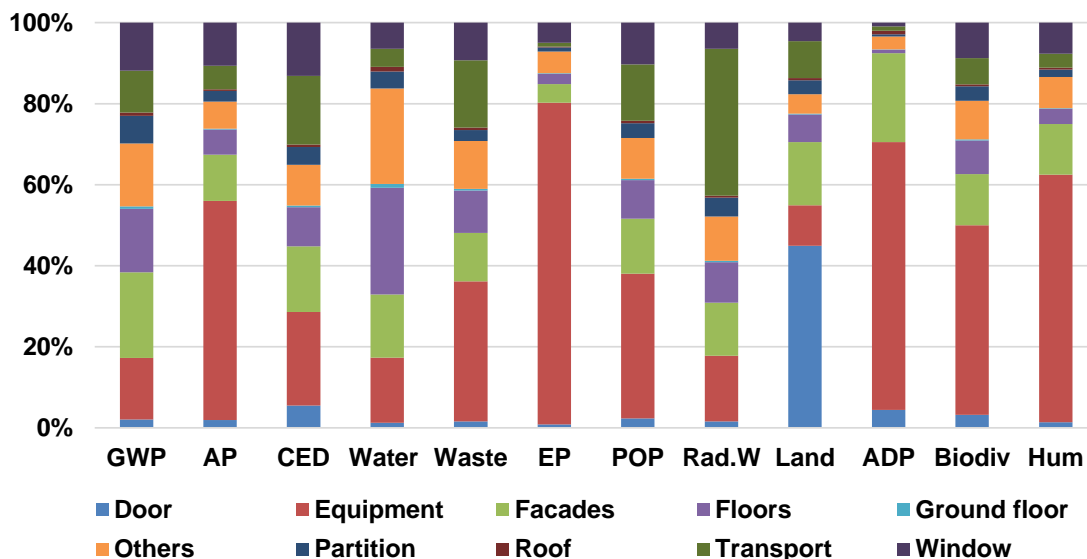
Figure 5.22: Environmental impacts of components in the construction stage

The impacts of each type of energy consumption in the use stage are presented in Figure 5.23. Specific electricity consumption causes nearly over 40 % in all impacts except Water and Rad.W. Specific electricity contributes 50.3 % of the total primary energy demand in this stage, meanwhile heating, cooling and energy for heating water consume 21 %, 15.4 % and 9.2 % respectively. They have similar shares in GWP, AP, Waste, POP, Land and Biodiv. The use of water has larger influence on Water, Rad.W, ADP and EP with corresponding values of 93.1 %, 69.6 %, 22.8 % and 20.4 % compared to heating and cooling. Generally, the specific electricity is the main contributor of the environmental impacts, thus eco-behaviours of the occupants (e.g. switch off the lights when leaving the room) are helpful to reduce the impacts.
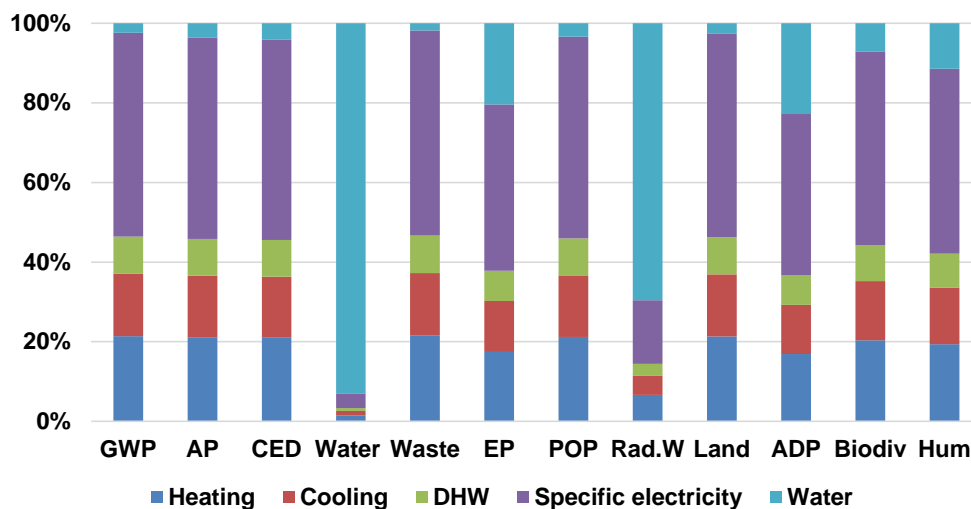
Figure 5.23: Environmental impacts of each consumption in the use phase

5.4.3.2.   Dynamic approach

Instead of the static approach, this section evaluates the environmental impacts of the studied case based on the dynamic approach. This approach only changes the environmental impacts of the use stage; the other three stages have the same impacts as the static approach. The environmental impacts are given in Table 5-7.

The CO_{2eq} emissions are estimated to be 53.9, 46.9, 44.5 and 31.2 kiloton for the ES, LC, ELC and HRE scenarios, respectively. The primary energy consumption is evaluated to be approximately 589 000, 561 000, 545 000 and 498 000 GJ for these four scenarios. These correspond to 86, 75, 71, 50 kg CO_{2eq}/m^2.year and 263, 250, 243, 222 kWh/m^2.year. The static approach overestimates the CO_{2eq} emissions and CED by 72 % and 14 % in the HRE scenario. A more detailed comparative analysis between static and dynamic approaches for Hubei is presented in section 5.4.4.2.

The contribution of each stage in the environmental impacts is shown in Figure 5.24. It can be inferred that from the ES to HRE scenario, the share of the use stage decreases, and the importance of the construction/renovation stage increases. For example, the construction stage emits 9.5 % of the total CO_{2eq} and consumes 9.1 % of the total primary energy in the ES scenario; these figures increase to 16.4 % and 10.8 % in the HRE scenario. The corresponding values in the use stage are 84.3 % and 81.5 % in the ES scenario, and 72.8 % and 78.1 % in the HRE scenario. However in the energy structure of Hubei, this level of variation is not huge; the choice of LCI database (Hubei database or national database) will not largely influence the total impacts.

Table 5-7   Environmental impacts of the studied case by the dynamic approach for a lifespan of 50 years

Impact	Use (ES)	Use (LC)	Use (ELC)	Use (HRE)	Total (ES)	Total (LC)	Total (ELC)	Total (HRE)
GWP (t CO2 eq.)	45 400	38 000	36 000	22 700	53 900	46 900	44 500	31 200
AP (kg SO2 eq.)	325 000	260 000	245 000	201 000	442 000	377 000	362 000	319 000
CED (GJ)	480 000	452 000	437 000	389 000	589 000	561 000	545 000	498 000
Water (m³)	1 826 000	1 807 000	1 801 000	1 762 000	1 892 000	1 874 000	1 867 000	1 829 000
Waste (t)	47 900	37 500	35 300	23 400	74 000	63 100	60 900	49 000
EP (kg PO4 eq.)	26 000	22 300	21 600	18 600	56 000	52 200	51 500	48 500
POP (kg ethylene eq.)	119 000	96 700	91 000	65 900	154 000	132 000	126 000	101 000
Rad.W (dm³)	59	58	58	65	195	194	194	200
Land (m².year)	757 000	651 000	639 000	5 730 000	1 500 000	1 390 000	1 380 000	6 470 000
ADP (kg antimony eq.)	362	387	409	586	6 170	6 200	6 220	6 400
Biodiv (PDF.m².year)	16 500 000	13 800 000	13 000 000	11 100 000	22 800 000	20 100 000	19 400 000	17 400 000
Hum (DALYs)	116	98	94	75	194	176	171	153
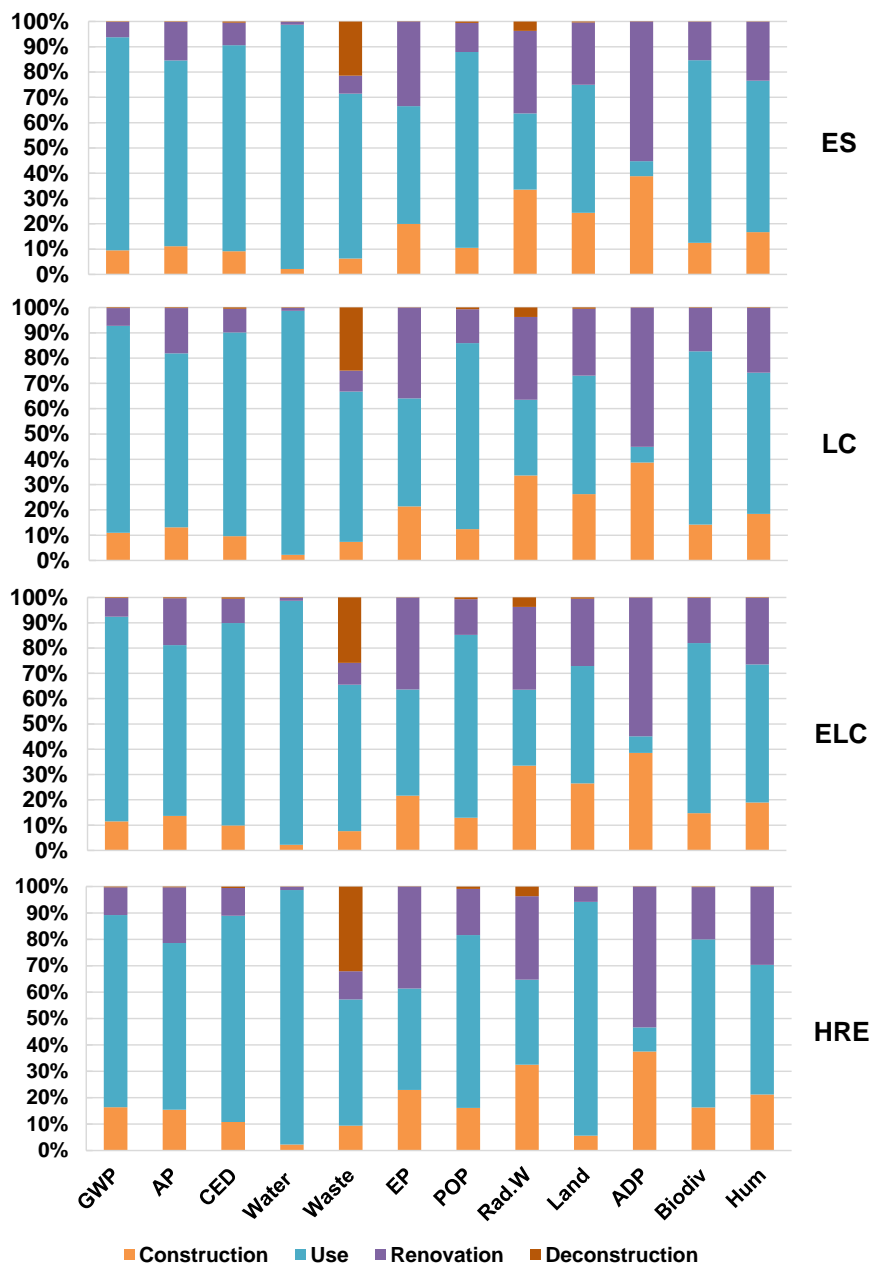
Figure 5.24: Contribution of each stage for the environmental impacts in the dynamic approach

5.4.4.   *Impacts of energy mix evolution*

5.4.4.1.   National static versus local static

This section compares the impacts of the local static (Local-S) energy mix 2019 and the national static (Nation-S) average energy mix 2019. The evolution of energy mix is not considered. The construction stage is identical for the same region, only the use stage is different due to the energy mixes.

The impacts of the use stage with HU-2019 energy mix was compared to that with Nation-2019 energy mix, using the corresponding contextualised database, as shown in Figure 5.25. If national average is used in LCA (construction materials in the construction and renovation stage and electricity used in the use stage), it overestimates 9 indicators by less than 1.5 %, except CED (5.4 %), ADP (7.4 %) and Rad.W (236.9 %).
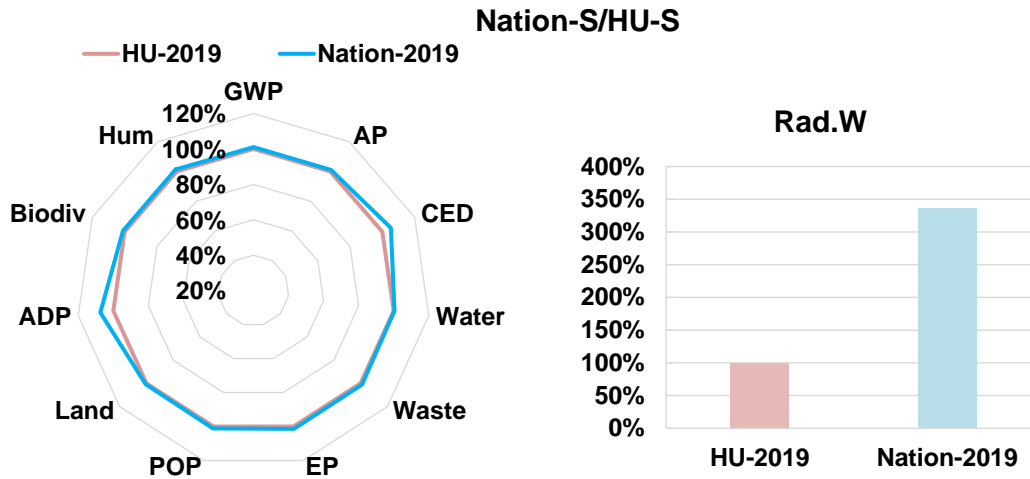
Figure 5.25: Impacts comparison of HU-2019 and Nation-2019 for the use stage in Wuhan, Hubei

The comparison for Beijing is shown in Figure 5.26. If Nation-2019 is used for the use stage, the environmental impacts are underestimated for 10 indicators except for ADP and Rad.W. GWP and CED are underestimated by 28.4 % and 14.6 %. Rad.W is overestimated by 240 %, due to more share of nuclear energy in Nation-2019 and no nuclear energy in BJ-2019.
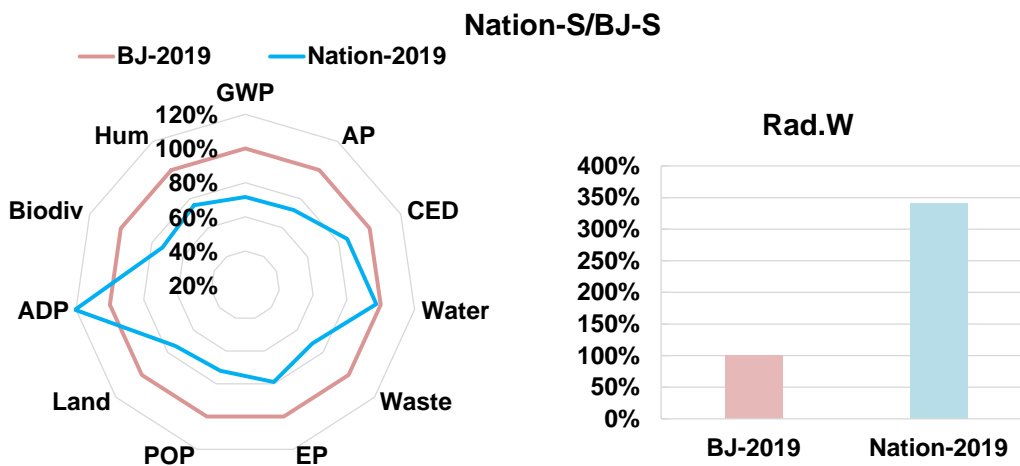
Figure 5.26: Impacts comparison of BJ-2019 and Nation-2019 for the use stage in Beijing

For Guangdong, the environmental impacts of the use stage with energy mix Nation-2019 are close to GD-2019 except for Rad.W and CED (70 % and 13.5 % smaller respectively), as illustrated in Figure 5.27. The differences of the other impacts are smaller than 2 %.
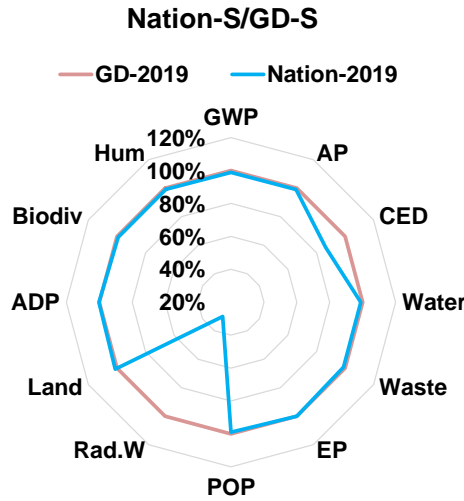
Figure 5.27: Impacts comparison of GD-2019 and Nation-2019 for the use stage in Guangzhou, Guangdong

As a province that relies on thermal power and wind power in 2019, the national average mix overestimates Rad.W by 253 % in Inner Mongolia. The other 11 indicators are all underestimated by from 1.4 % (Water) to 17.3 % (GWP), shown in Figure 5.28. This indicates that the energy structure of Inner Mongolia is less environmentally friendly than the national average.
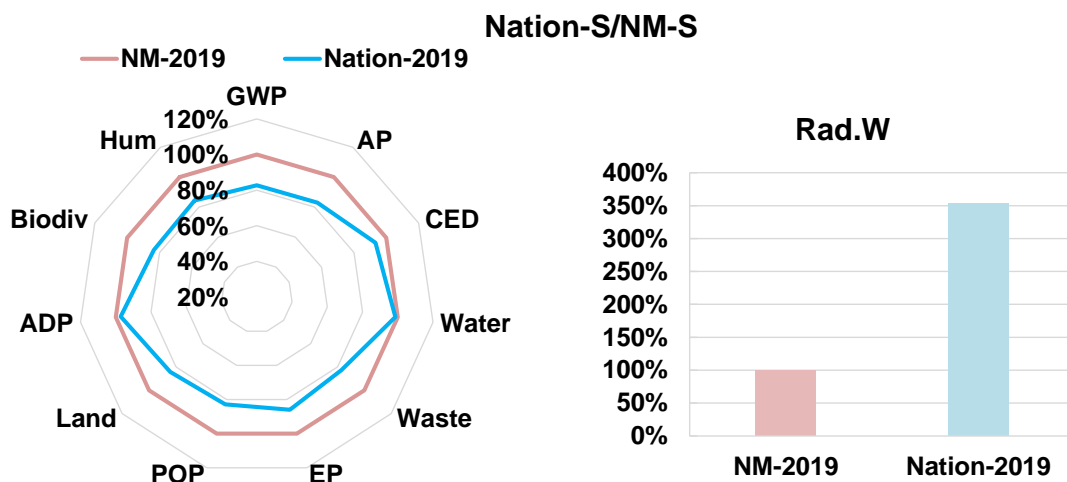
Figure 5.28: Impacts comparison of NM-2019 and Nation-2019 for the use stage in Hohhot, Inner Mongolia

The share of hydro power in Yunnan province reaches 82 %, resulting significantly smaller impacts in the use stage compared to that with Nation-2019, as shown in Figure 5.29. All indicators are overestimated by using Nation-2019, of which Water (6.8 % higher) and ADP (15.3 % higher) are the two most close to YN-2019. GWP is the most overestimated indicator by 492 %. This indicates that enormous differences will be obtained if LCA in Yunnan use the national average mix instead of the local mix.
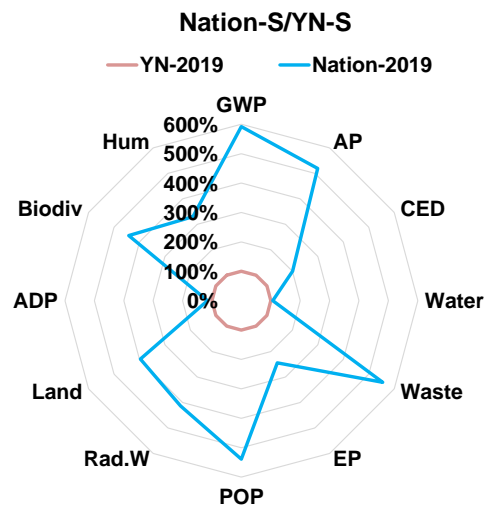
Figure 5.29: Impacts comparison of YN-2019 and Nation-2019 for the use stage in Kunming, Yunnan

This section discussed the effects of the electricity production mix on a spatial scale in China based on the static mix approach. The impacts evaluation results were compared between the static local energy mix in 2019 and the static national average energy mix in 2019 (which is adopted in most studies). The electricity production mix is different according to the region. Using a national average mix can relatively accurately estimate some environmental indicators in some provinces, e.g. GWP, EP and POP in Guangdong. However for most provinces, it brought non-negligible differences. For Yunnan, the overestimation of GWP can reach to around 5 times. The results indicated that choosing an appropriate energy mix is essential for building LCA in China.

5.4.4.2. Local static versus local dynamic

This section evaluates the differences of the impacts of the static local (Local-S) energy mix 2019 and the dynamic local (Local-D) energy mix for four future scenarios in the use stage. Taking into account the evolution of electricity production mixes, the dynamic approach is considered as the reference appropriately indicating the environmental impacts and the static approach is compared to the dynamic approach to show the differences that might be caused by the static approach.

As shown in Figure 5.30, for the ES scenario in Hubei, the environmental impacts evaluated using the static approach are close to the dynamic approach for all indicators except for Land

(overestimated by 118 %). ADP is the indicator with the second largest difference of -6 % and CED is the third with a difference of -4 %. The differences of other indicators are around 1 %. The differences become larger when the scenario moves towards lower carbon emissions (the LC and ELC scenarios). GWP and CED evaluated by the static approach is 17 % and 2 % higher in the LC scenario and 25 % and 6 % higher in the ELC scenario. ADP is the only underestimated indicator, by 13 % and 17 % in the LC and ELC scenarios, respectively. The HRE scenario is different from low carbon scenarios, in which higher renewable energy share is used. 9 indicators are more overestimated in this scenario compared to the ELC scenario, such as GWP (by 98 %), AP (by 62 %), CED (by 18 %) and Waste (by 103 %). Land is underestimated by 71 % in the HRE scenario, while it is overestimated in the ES, LC and ELC scenarios. Rad.W is underestimated by 10 %.
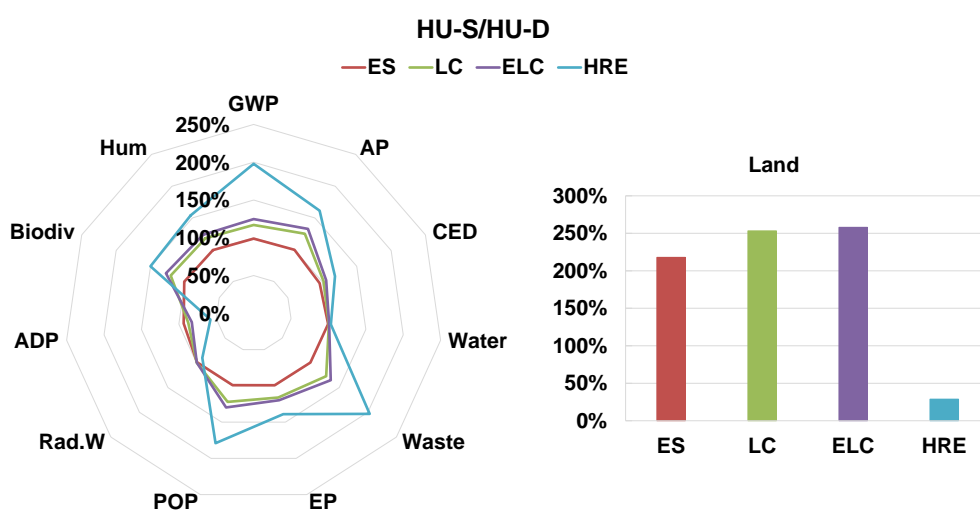
Figure 5.30: Impacts comparison of HU-static and HU-dynamic for the use stage in Wuhan, Hubei

The comparison for Beijing is illustrated in Figure 5.31. In the ES scenario, the differences are small (< 5 %) for most indicators except for Land, which is overestimated in the ES, LC and ELC scenarios. The differences become larger for the LC and ELC scenarios, for example, GWP and AP in the ELC scenario are overestimated by 12 % and 21 %. Similar to Hubei, the differences are more significant in the HRE scenario. GWP, AP and EP evaluated by the static approach are respectively 43 %, 13 % and 50 % higher than the dynamic approach. Rad.W and Land are 13 % and 85 % lower. The variations of CED, Waste, water, ADP and Biodiv are smaller than 7 %.
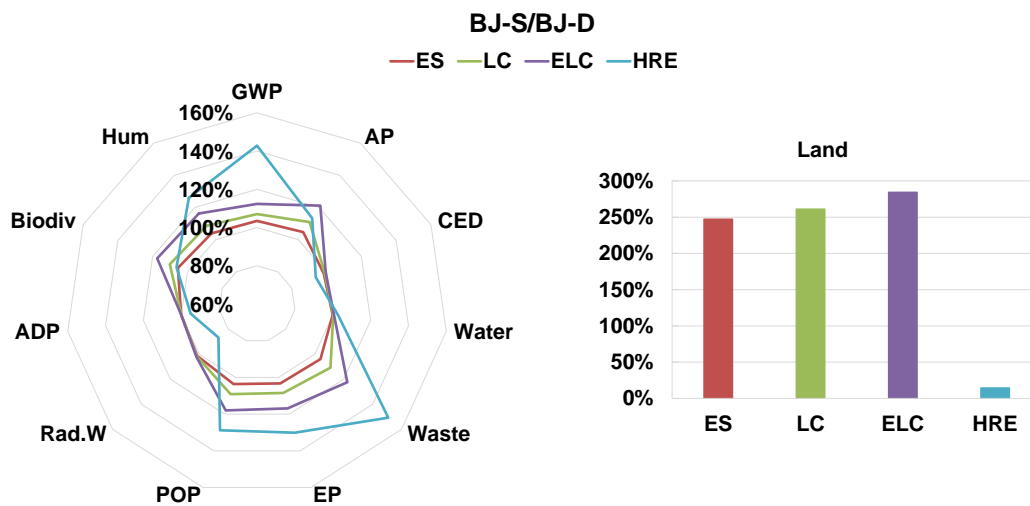
Figure 5.31: Impacts comparison of BJ-static and BJ-dynamic for the use stage in Beijing

Large differences of several indicators are observed in Guangdong for the ES, LC and ELC scenarios, as shown in Figure 5.32. The GWP is overestimated by 1.83 times, 5.68 times and 9.14 times by the static approach compared to the dynamic approach, because the share of nuclear increases sharply. Land is another indicator which is significantly overestimated, by 4 times, 7 times and 8.5 times. Other indicators related to thermal power such as AP, POP and Waste are massively overvalued as well. The difference of CED is smaller than 10 % and that of Water is 1 %. In contrast, Rad.W is 26 % of that in the ELC scenario, because the static approach does not consider the increase of nuclear production. Compared to the low carbon scenarios, in the HRE scenario the evolution is relatively less variable. 10 indicators are overestimated by from 2 % (CED, Water) to 59 % (Waste). GWP is overvalued by 52 %. Land and ADP are underestimated by 83 % and 15 %, respectively.
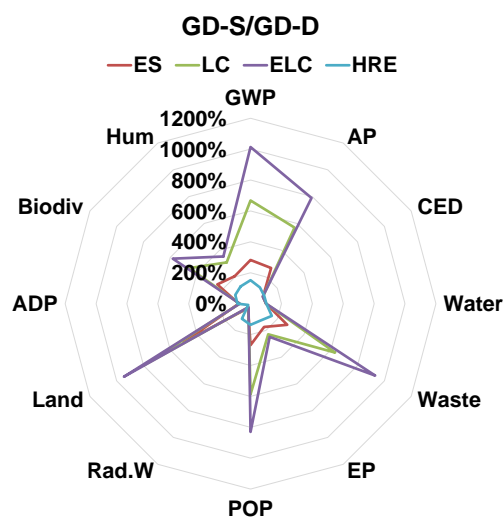
Figure 5.32: Impacts comparison of GD-static and GD-dynamic for the use stage in Guangzhou, Guangdong

For Inner Mongolia, the difference in the HRE scenario is significantly larger compared to the ES, LC and ELC scenarios in most indicators, as illustrated in Figure 5.33. The differences are less than 10 % for 11 indicators except for Land (overestimated by 1.4 times) in the ES scenario, and this value increases to 21 % in the LC scenario and 44 % in the ELC scenario. In the HRE scenario, the electricity is mainly produced by wind and solar power instead of thermal power in 2019, the static approach largely overvalued the impacts related to thermal power such as GWP by 3.2 times, AP by 2.52 times, CED by 0.79 times, Waste by 2.93 times, POP by 2.78 times, Biodiv by 2.22 times and Hum by 1.46.
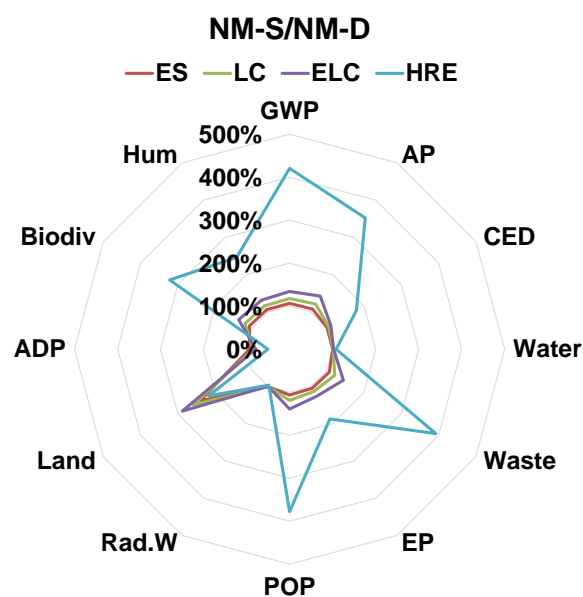
Figure 5.33: Impacts comparison of NM-static and NM-dynamic for the use stage in Hohhot, Inner Mongolia

In the static approach, the share of hydro power reaches to 82 % in Yunnan in 2019, this structure leads to different features compared to other cities. In the ES scenario, all indicators are underestimated except for Land (3 % higher) and the difference varies from 2 % (Water) to 55 % (GWP). In the LC scenario, the impacts evaluation is relatively accurate for 11 indicators, and the difference is smaller than 6 %. In the ELC scenario, the differences become larger, e.g. GWP is overestimated by 153 %, AP by 108 %, CED by 12 %, Waste by 133 %, POP by 117 %. Rad.W, ADP and are underestimated by 1 % and 14 %. The differences in the HRE scenario is similar to the ELC scenario but slightly smaller, except for Rad.W (8 %). The differences of GWP and CED are 137 % and 9 %, respectively.
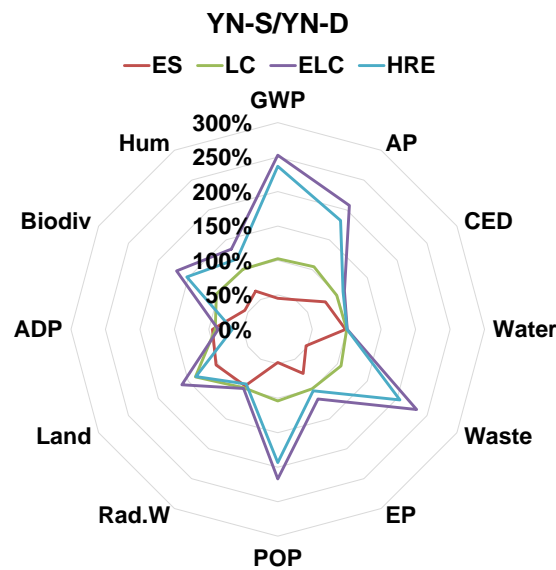
Figure 5.34: Impacts comparison of YN-static and YN-dynamic for the use stage in Kunming, Yunnan

This section discussed the effects of temporal variation of energy mixes in China, by comparing the static approach with the dynamic approach considering four future scenarios. The results showed that the static approach might cause huge differences compared to the dynamic approach for most environmental impact indicators. The differences highly depend on the predicted future scenarios. The differences also show regional features. For example, in Guangdong, the difference of GWP can reach to around 900 % in the ELC scenario, however it is relatively accurately evaluated in Yunnan in the LC scenario. Although the predicted scenarios might not reflect the real evolution in the future, they provide a picture of different levels of renewable energy shares, in which the importance of the dynamic approach is analysed. It can be inferred that the static approach which is usually adopted in the existing researches are not appropriate for building LCA considering the long lifespan of buildings.

5.4.5. *Sensitivity analysis*

5.4.5.1. **Lifespan**

Lifespan is an important parameter that affects the total environmental impacts of a building. A sensitivity analysis was performed to investigate the effects of this parameter. The impacts of the use stage during the years after 2068 are assumed to be identical as year 2068. The CO_{2eq} emissions and primary energy consumption per m^2 per year of the case study are represented in Figure 5.35 and Figure 5.36.

It can be inferred that as the lifespan increases, CO_{2eq} emissions per m^2 per year decrease for all scenarios and all provinces. For HU, BJ, NM and YN, CO_{2eq} emissions are the most sensitive to the

lifespan in HRE scenario, with a drop from $50 \, \text{kg/m}^2$.year for 50 years to $33.7 \, \text{kg/m}^2$.year for 200 years (drop by 33 %) in HU, from $96.3 \, \text{kg/m}^2$.year to $75.3 \, \text{kg/m}^2$.year (drop by 22 %) in BJ, from $40.6 \, \text{kg/m}^2$.year to $19.6 \, \text{kg/m}^2$.year (drop by 52 %) in NM, and from $18.4 \, \text{kg/m}^2$.year to $12.7 \, \text{kg/m}^2$.year (drop by 33 %) in YN. For GD, it is more sensitive in the ES/LC/ELC scenarios with a drop of 50 %/45 %/40 % from 50 years to 200 years. It is the least sensitive in the static approach for HU, BJ, GD and NM, and in the ES scenario for YN. The corresponding drops are 6 % (HU), 4 % (BJ), 7 % (GD), 4 % (NM) and 4 % (YN). The ranking of CO_{2eq} emissions per m^2 per year among five regions are BJ > GD > HU > NM > YN in the HRE scenario for all lifespans. This ranking changes to BJ > NM > HU > GD > YN in the static approach. The ranking is BJ > NM > HU > YN > GD in the ES/LC and ELC scenarios with a lifespan of 100, 150 and 200 years. It changes to BJ > NM > HU > GD > YN in the ELC scenario with a lifespan of 50 and 70 years.

Compared to CO_{2eq} emissions, the primary energy consumption is less sensitive to the lifespan. From 50 years to 200 years, the reduction is between 2 % and 20 % for all scenarios and all provinces. For HU, lifespan is the most sensitive in the HRE scenario, with a drop of 11 % compared to 6 % in the static approach. The lifespan is the least sensitive in BJ, with a variation of 5 % for all scenarios except for the HRE scenario (2 %). In GD, the difference is also not large (6 %). It is more sensitive using the HRE scenario in NM and YN by a drop of 20 % and 11 % respectively. The ranking of primary energy consumption per m^2 per year among five provinces are BJ > GD > HU > NM > YN in the HRE scenario for all lifespans. This ranking changes to NM > BJ > GD > HU > YN using the static approach. In the ES/LC/ELC scenarios, the ranking is BJ > NM > GD > HU > YN. The highest primary consumption is $361 \, \text{kWh/m}^2$.year in BJ for a lifespan of 50 years by the static approach and the smallest is $133 \, \text{kWh/m}^2$.year in YN for a lifespan of 200 years for the HRE scenario.
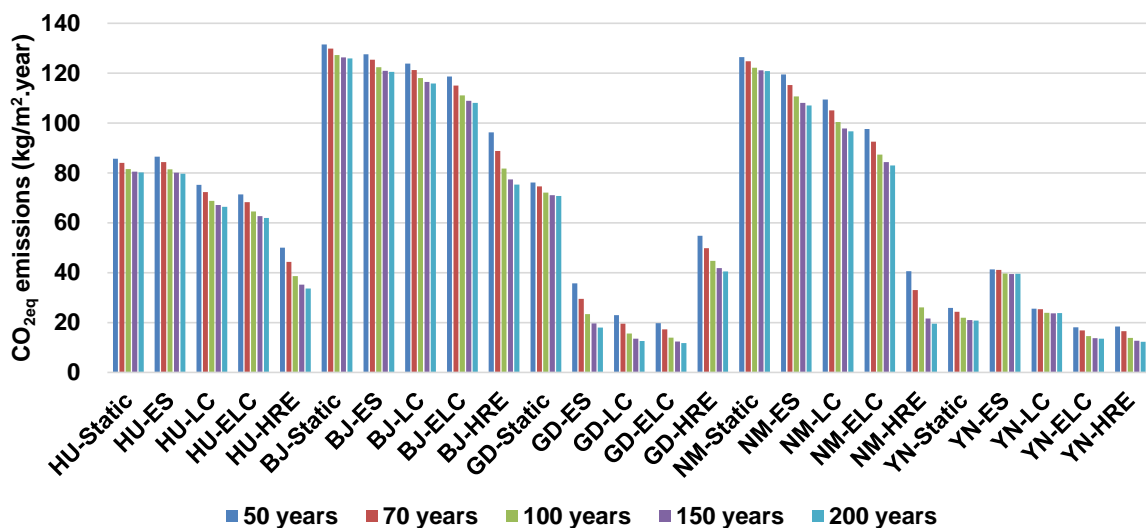
Figure 5.35: CO_{2eq} emissions for different lifespans and different scenarios
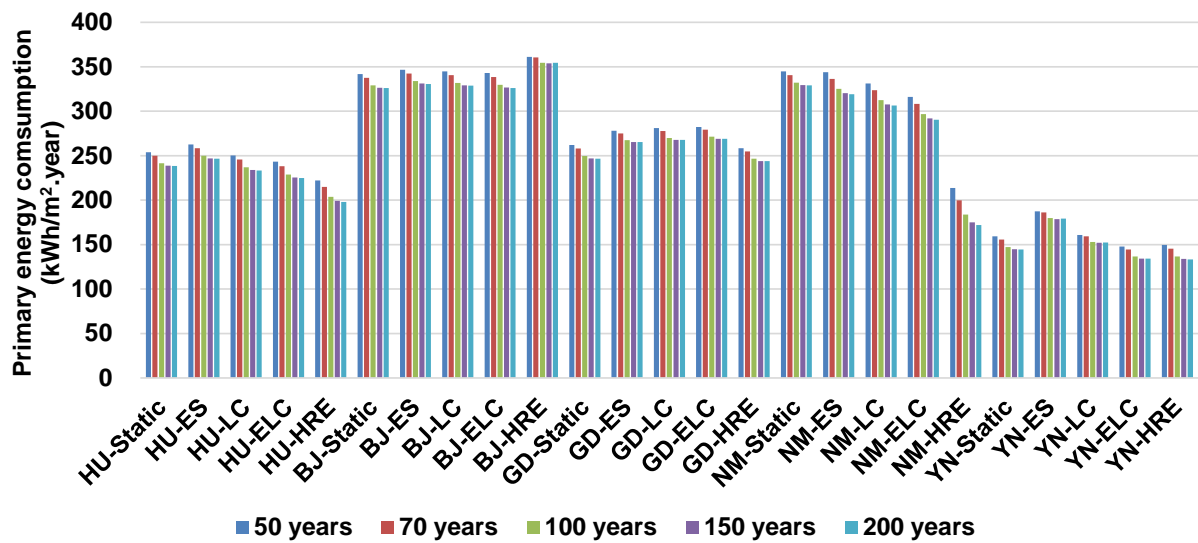
Figure 5.36: Primary energy consumption for different lifespans and different scenarios

The CO_{2eq} emissions share of each stage for a lifespan of 50 years and 200 years is shown in Figure 5.37, evaluated by the static approach with the national average energy mix 2019 and the dynamic approach for five cities. In general, the share of the construction stage decreases and the renovation stage contributes more when the lifespan increases. It can be inferred that the static approach with the national average energy mix 2019 might cause non-negligible differences in the HRE scenario for these provinces except for Beijing. It might also lead to a different order of the importance of each stage for some provinces in some scenarios. For example, for a lifespan of 50 years in Guangdong, this approach could evaluate the shares in the HRE scenario with small differences (< 7 %). However for the ELC scenario, it predicts the ranking is use > construction > renovation > deconstruction, which is contradictory to the order given by the dynamic approach: construction > use > renovation > deconstruction. This misevaluation is also observed for Yunnan. The static approach considering a national average mix overestimates the share of the use stage, because it does not consider the emissions reduction due to more renewable energy share in the future. This effect could be magnified in some provinces with higher renewable share (e.g. Yunnan with high hydro and Guangdong in the ELC scenario with high nuclear production) and also by a longer lifespan (e.g. 200 years). This is another element suggesting that the commonly used static approach using a national average electricity production mix is not appropriate for building LCA.
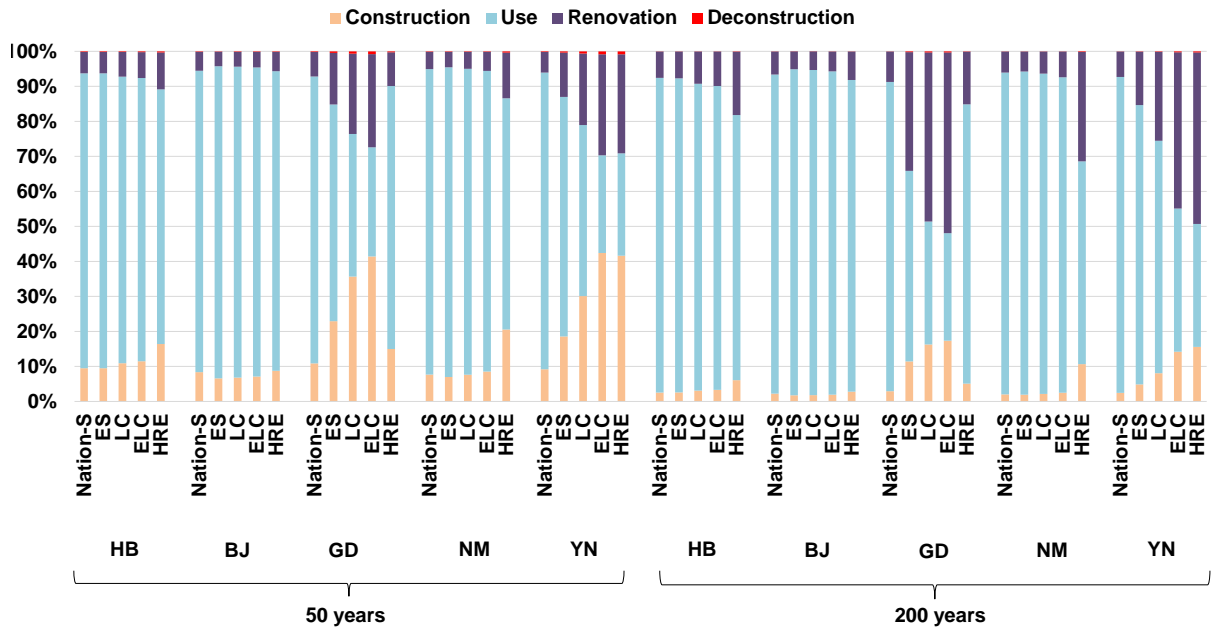
Figure 5.37: CO$_{2eq}$ emissions share of each stage for a lifespan of 50 years and 200 years

5.4.5.2. GCHP

In the discussion above, the LCA was based on a 'traditional' approach: the two refined boundary conditions presented in chapter 2 to 4 were not considered. The COPs of the GCHP system were based on reference values from a Chinese standard instead of the values given by the GCHP model. The weather file in the energy performance evaluation was the one collected by the weather station, without considering the microclimate. Thus, this section links these boundary conditions with LCA, aiming at providing a more precise evaluation.

According to chapter 3, the annual average COP for heating, COP$_{heating}$, is 4.6, instead of 3.1 used in the previous evaluations. The annual average COP for DHW, COP$_{DWH}$, can be estimated by:

$$\text{COP}_{\text{DHW}} = \text{COP}_{\text{heating}} \times \frac{\text{COP}_{\text{DHW}}^{\text{Carnot}}}{\text{COP}_{\text{heating}}^{\text{Carnot}}} \tag{5-9}$$

where $\text{COP}_{\text{DHW}}^{\text{Carnot}}$ and $\text{COP}_{\text{heating}}^{\text{Carnot}}$ are the COP at Carnot efficiency for DWH and heating, which are calculated by:

$$\text{COP}_{\text{DHW}}^{\text{Carnot}} = \frac{T_{\text{out,cd}}^{\text{DWH}}}{T_{\text{out,cd}}^{\text{DWH}} - T_{\text{out,ev}}^{\text{DWH}}} \tag{5-10}$$

$$\text{COP}_{\text{heating}}^{\text{Carnot}} = \frac{T_{\text{out,cd}}^{\text{heating}}}{T_{\text{out,cd}}^{\text{heating}} - T_{\text{out,ev}}^{\text{heating}}} \tag{5-11}$$

in which $T_{out,cd}^{DWH}$ and $T_{out,cd}^{heating}$ are the annual average outlet water temperature of the condenser for DWH and heating; $T_{out,ev}^{DWH}$ and $T_{out,ev}^{heating}$ are the annual average outlet water temperature of the evaporator for DWH and heating.

$T_{out,cd}^{DWH}$ equals to 60 °C, according to the report of GCHP manufacturer[33]. $T_{out,cd}^{heating}$ equals to 44.7 °C and $T_{out,ev}^{heating} = T_{out,ev}^{DWH} = 10$ °C, based on the simulation results in chapter 3. With these figures, $COP_{DWH} = 3.3$.

Because the GCHP model is only applied for the heating mode, the annual average energy efficiency ratio (EER) $EER_{cooling}$ for "normal" cooling (cooling in summer) needs to be estimated from the heating mode, instead of directly given by the model. It is determined by:

$$EER_{cooling} = EER_{heating} \times \frac{EER_{cooling}^{Carnot}}{EER_{heating}^{Carnot}} \qquad (5\text{-}12)$$

where $EER_{heating}$ is the "virtual" EER for cooling, in the "virtual" reverse cycle under the same condition as the heating mode. It equals to the ratio of the annual total heat flux in the evaporator Q_{ev}^{annual} and the annual total energy consumption by the compressor W^{annual} in the heating mode, which is given by the GCHP model:

$$EER_{heating} = \frac{Q_{ev}^{annual}}{W^{annual}} = 3.5 \qquad (5\text{-}13)$$

$EER_{heating}^{Carnot}$ and $EER_{cooling}^{Carnot}$ are the annual average EER at Carnot efficiency for "virtual" cooling under the heating mode condition, and "normal" cooling respectively:

$$EER_{heating}^{Carnot} = \frac{T_{out,ev}^{heating}}{T_{out,cd}^{heating} - T_{out,ev}^{heating}} = 8.2 \qquad (5\text{-}14)$$

$$EER_{cooling}^{Carnot} = \frac{T_{out,ev}^{cooling}}{T_{out,cd}^{cooling} - T_{out,ev}^{cooling}} \qquad (5\text{-}15)$$

where $T_{out,ev}^{cooling}$ and $T_{out,cd}^{cooling}$ are 7 °C and 30 °C, respectively, given by the report of GCHP manufacturer[15] under nominal conditions.

By applying equation (5-12) to (5-15), $EER_{cooling} = 5.2$. The comparison of the COP before and after applying the GCHP model in chapter 3 is shown in Table 5-8. It should be noted that, according to chapter 3, around 2.5 % of the heating load is satisfied by the thermal resistance, which is assumed to be identical in both cases. This results in a decrease in $COP_{heating}$ for the whole system.

---

[33] https://wenku.baidu.com/view/5b714388aeaad1f347933f0d.html

Table 5-8   *Energy efficiency of the GCHP system obtained with and without the GCHP model*

	Without GCHP model (thermal resistance not included)	**With GCHP model (thermal resistance not included)**	**Without GCHP model (thermal resistance included)**	**With GCHP model (thermal resistance included)**
$COP_{heating}$	3.1	4.6	2.9	4.2
COP_{DHW}	3	3.3	3	3.3
$EER_{cooling}$	3.9	5.2	3.9	5.2
Comments	*Obtained from reference*	*Directly or derived from simulation results*	*Obtained from Reference and derived from simulation results*	*Directly or derived from simulation results*

The environmental impacts of the use stage were evaluated for Wuhan considering the COPs obtained with and without the GCHP model, for a lifespan of 50 years, as shown in Figure 5.38. It can be inferred that, if the GCHP model is not used, all indicators were overestimated. 9 indicators (e.g. GWP, AP, CED, Biodiv) out of 12 were evaluated to be approximately 13 % higher, whereas it had a small influence on Water. The overestimation was not sensitive to the future energy mix scenario: for the HRE scenario with the highest renewable energy potential, the difference was still close to 12 %. Considering the COPs calculated by the GCHP model presented in this thesis, a more accurate evaluation could be obtained.
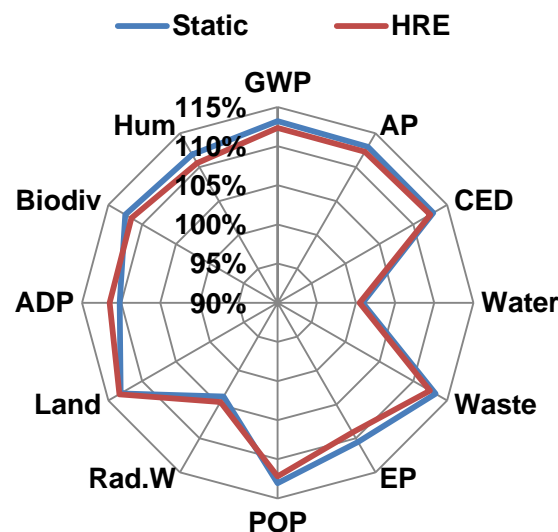
Figure 5.38: Environmental impacts comparison: COP obtained without the GCHP model in the static approach and in HRE scenario for Wuhan compared to with GCHP model (use stage, lifespan of 50 years)

5.4.5.3. Microclimate

The more precise simulation results regarding the heating and cooling loads of the case study were estimated to be 47.1 kWh/m^2 and 46.7 kWh/m^2 considering the microclimate conditions (detailed information seen chapter 4), instead of 48.7 kWh/m^2 and 44.9 kWh/m^2 estimated using the original EPW weather data. The simulation using the original EPW showed a larger heating load (3.5 % difference), a smaller cooling load (3.9 % difference) and a smaller total energy load (0.2 % difference), compared to the more precise simulation. The effects of the microclimate conditions on the environmental impacts during the lifespan of the case study are presented in this section.

Using the COPs presented in section 5.4.5.2, the electricity consumption was evaluated and shown in Figure 5.39. It can be inferred that under the microclimate conditions, although the electricity consumptions for heating and cooling were different, the total electricity consumption was nearly the same. This resulted in similar environmental impacts during the whole lifespan (same impacts in other stages as well). However, the heating/cooling load varies with the region. In Wuhan, they are evaluated to be close, leading to a similar total electricity consumption. In the regions where the heating and cooling loads are not balanced (shown in Figure 5.12), such as where the heating load is larger than the cooling load (Hohhot and Beijing) and the heating load is small (Guangzhou and Kunming), the microclimate might have a non-negligible influence on the environmental impacts. It should be noted that this small difference is based on LCA using annual average energy mix. In fact, the environmental impacts of one kWh electricity vary hourly and also seasonally, due to the fact that different technologies are used in different time in one day (peak technologies (e.g. natural gas) and dispatchable technologies (e.g. hydro) are used to meet the electricity consumption, leading to much higher environmental impacts in peak hours in one day) and in different seasons (e.g. a higher share of hydro power in summer in Hubei). This difference might be larger if LCA is performed using an hourly timestep.
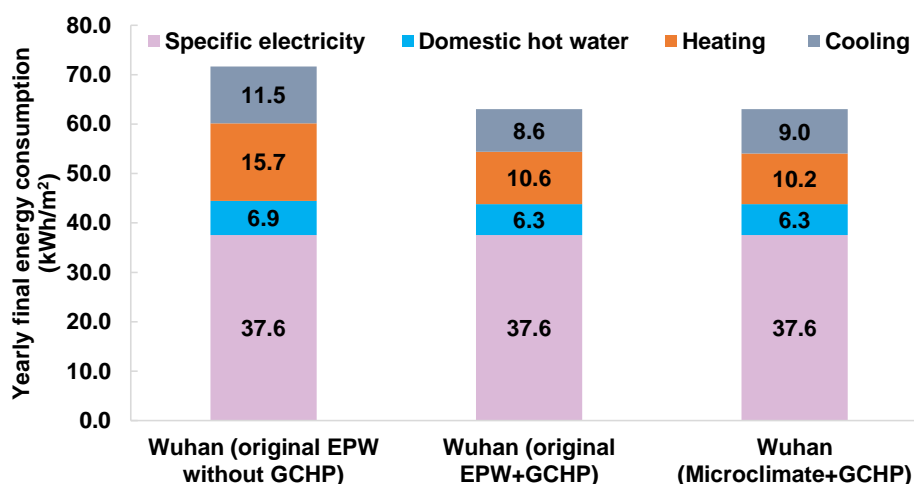
Figure 5.39 : Total yearly final energy consumption per square meter considering different boundary conditions

5.5.   Conclusions and perspectives

5.5.1.   *Conclusions*

As a large country, different regions in China show different climate conditions and energy mix features. The environmental impacts of a building related to electricity therefore vary on a regional scale. During the energy transition process, the energy mix will evolve to a higher share of renewable energy on a temporal scale. The LCA method is widely used to assess the environmental impacts of a building, which is highly connected to its background systems, particularly the electricity production and grid system. Many studies use a static national average electricity production mix and the evolution of this mix is not considered in most building LCA studies in China. This assumption might affect the precision and credibility of the evaluation results.

This chapter is dedicated to study this question by considering local electricity production mix features and their future evolution. Dynamic building energy simulation was performed for a case study in five cities in different climate zones in China. Four types of regional future energy mix scenarios were derived from the national scenario. The impacts of the production of building materials used in construction/renovation stages and of the use stage are influenced by the electricity system, thus the contextualisation of materials and electricity in the LCI database ecoinvent v3.4 was performed under national and regional electricity production mixes. LCA was applied to the case study afterwards. The environmental impacts were compared between using each local energy mix and using the national average energy mix, in the static approach which does not consider the future scenario and the dynamic approach accounting for the future evolution.

The results indicated that differences were small (below 8 %) regarding the environmental impacts of the material fabrication in the construction stage using the local database compared to that using the database contextualised with the national average electricity mix. The choice of a contextualised database was not a key factor affecting the total environmental impact. However this importance, particularly for CO_2 emissions, might increase in the future with a longer lifespan because the construction and renovation stages will occupy larger shares in total impacts (e.g. less CO_2 emissions in the use stage in the future due to cleaner electricity). The use stage was the main contributor in most environmental impacts and the choice of an electricity production mix highly influenced the LCA results. On a regional scale, using the national average mix in the static approach can relatively accurately estimate some environmental indicators in some provinces, e.g. GWP, EP and POP in Guangdong. However, for most provinces, it brought non-negligible differences. For Yunnan, the overestimation of GWP can reach around 5 times in the use stage of a 50 years lifespan. On a temporal scale, the static approach might cause huge differences compared to the dynamic approach for most environmental impact indicators. The differences highly depend on the predicted future scenarios and also show regional features. For example, in Guangdong, the difference of GWP can reach around 900 % in the ELC scenario, nevertheless it is relatively small in Yunnan in the LC scenario. In the static approach in Hubei, the studied case emits nearly 53.4 kilotons CO_{2eq} and consumes approximately 570 000 GJ of primary energy over 50 years, corresponding to 76 kg

CO_{2eq}/m^2.year and 254 kWh/m^2.year. These values were estimated to be 86, 75, 71, 50 kg CO_{2eq}/m^2.year and 263, 250, 243, 222 kWh/m^2.year for the ES, LC, ELC and HRE scenarios using the dynamic approach.

A sensitivity analysis concerning the lifespan was performed. It indicated that the environmental impacts were sensitive to the lifespan. The static approach using a national average mix overestimates the share of the use stage and this effect could be magnified in some provinces with higher renewable share and also by a longer lifespan (e.g. 200 years).

The effects of the boundary conditions regarding the ground and the microclimate presented in the previous chapters were investigated as well. The use of the GCHP system obviously increased the environmental impacts in the construction stage, but it reduced the environmental impacts during the use stage compared to traditional equipments with lower efficiency. The COPs were more precisely evaluated using the proposed GCHP model. In the case study in Wuhan, most environmental indicators were overestimated by 13 % in the use stage without applying the GCHP model. The microclimate had a negligible effect, because the heating and cooling loads variations were opposite in Wuhan. However, its effect might be larger in the regions where heating and cooling loads are not balanced, or if the hourly variation of the electricity mix is taken into consideration.

This chapter reveals the importance of appropriate choice of energy mix in building LCA in China. If the electricity exchange between regions is limited, according to the grid infrastructure, the local electricity mix accounting for future evolution may be recommended for the future building LCA work instead of a static national average energy mix. The contextualised database presented in this chapter can be a reference for future work concerning building LCA in China.

5.5.2. *Perspectives*

One limitation of the database contextualisation is that it only considered the replacement of electricity. In fact, the technologies used in the material fabrication or electricity generation could vary for different countries, which is also indicated by (European Commission-Joint Research Centre-Institute for Environment and Sustainability, 2010). A more detailed contextualisation process would be beneficial in the future work.

Due to the limited data availability, the power grid interactions between different provinces were not considered in this chapter. The evaluation could be more precise if they were taken into account. The impacts of power technologies were assumed to be identical in all the five provinces of China. This assumption is beneficial for us to focus on the influence of the electricity production mix, however, it does not reflect the reality that their impacts could vary in different locations. Thus, the combination of local technologies and local electricity mix can be studied in future works to provide more accurate evaluation.

The studied case was kept identical for all cities in different climate zones, which is not realistic because it does not meet the energy regulations in some regions, regarding e.g. the insulation layer. A sensitivity analysis of the insulation technologies can be a research perspective. The heating/cooling

was assumed to be supplied by GCHP in this study, but in reality, various heating/cooling technologies are used in China, especially in different regions. Therefore, this study can be extended to more regional technologies in the future. Estimating the effects of different energy mixes in China on environmental impacts combined with COPs evaluated by the GCHP model based on hourly timestep could be another perspective, which may show the difference of environmental impacts of the electricity for heating and cooling in different seasons.

The choice of an electricity mix depends on the goal of each LCA study. Evaluating the benefit of a higher energy performance, e.g. higher insulation, more efficient systems or local renewable electricity production, may require another type of LCA called "consequential LCA" (Ekvall and Weidema, 2004 ; Mathiesen et al., 2009 ; Lund et al., 2010 ; Earles and Halog, 2011 ; Dandres et al., 2017b). For instance if electricity is saved in Yunnan, it allows more electricity to be exported from Yunnan to another region where the most expensive production, e.g. using coal power plants, can be avoided. The benefit of energy saving or local production is then much higher that considering the regional electricity mix in Yunnan.

Interaction of the building sector with the electric system may have other consequences. Considering energy transition scenarios like the LC or ELC scenario may induce replacing gas and fuel boilers by heat pumps, leading to a huge peak demand in cold winter days and making these low carbon scenarios very difficult to achieve because renewable production cannot satisfy this peak demand. Accounting for future scenarios should therefore be complemented by uncertainty calculations (Pannier, 2017).

Electricity uses like heating and cooling, and to some extent lighting, are highly variable according to the season and the hour of the day. The electricity production mix may vary accordingly because some techniques (e.g. hydroelectricity) may be used as a base production whereas more expensive production processes (e.g. thermal plants) may be needed to satisfy the peak demand. Environmental impacts are therefore varying not only on the long term, but also hourly within one year. Specific models have been developed to account for such temporal variation (Beloin-Saint-Pierre et al., 2017 ; Roux et al., 2017). Calibrating such a model in the Chinese context would be very useful to evaluate more precisely impacts related to electricity consumption.

Chapter 6. Conclusions and perspectives

This chapter summarises the main achievements and future work on the topics of this thesis.

6.1.   Conclusions

Urbanisation process in China is still undergoing and it makes the Chinese building construction sector very active. This leads to a high pressure on resources, as well as environmental impacts such as primary energy consumption and GHG emissions during the long lifespan of buildings. The highest reduction potential of these impacts corresponds to decisions made during the building's design phase. This process can be accomplished with the aid of computer simulation/evaluation tools (e.g. DBES model COMFIE and building LCA model EQUER). The accurate evaluation by these tools relies on boundary conditions. This thesis aims at improving the quantitative evaluation methodology of a building's environmental impacts based upon DBES model and LCA, by refining three boundary conditions regarding: the ground, the microclimate, and the background systems in LCA.

A DBES tool integrated with a vertical GCHP model can be beneficial to building designers' decisions making, and interesting for researchers to study the overall performance of a GCHP system, especially if it can provide the simulation results for a large-scale boreholes GHE in a reasonable computation time. To solve this problem, chapter 2 presented a fast calculation model of a large-scale boreholes GHE based on the FLS model. The main goal of this model is to calculate the outlet fluid temperature, in relation with a heat pump model in the DBES model COMFIE. This temperature is calculated from the wall temperature of each borehole, which is determined by the thermal response factor G. The three-points method in the proposed model uses the average temperature of three points located at the top, middle and bottom of the borehole wall to represent its temperature, avoiding non-negligible errors of using the borehole middle point temperature for a long operation time. This three-points method shows a good accuracy (difference < 3 % compared to the double integration method), meanwhile it remains in the form of a single integration to keep a reasonable computation time. In the global model, the first step is to sort the large number of boreholes in increasing distance categories. In the second step, the 2D heat conduction equation determines when interactions between boreholes are negligible and when detailed calculations are needed. In the third step, the 2D heat conduction equation evaluates how often the interactions have to be recalculated. In the last step, the thermal response factors are computed by the three-points method. An example of a 26×26 square borehole matrix was studied. The results showed that the proposed model provides accurate results for the thermal response factors, meanwhile the calculation time for one simulated year takes only 4 seconds which represents a reduction by a factor 1 000 000 compared to the double integration method without any simplification. In this case, simulating 20 years of operation with a timestep of one hour only required 1 minute. This model is suitable not only for a square borehole configuration, but also for other configurations such as L-shaped, box-shaped, U-shaped and even irregular. Its universality and calculation speed facilitate its integration into building energy simulation tools.

Afterwards, the proposed large-scale boreholes GHE model was integrated in a water-water heat pump model in COMFIE in chapter 3. The integration process was described in detail. A case study containing a large 26×26 boreholes field in Wuhan (China) allowed to test its usability and simulation speed. The GHE model did not bring noticeable extra calculation time for this case study. The heat pump system performance was analysed under different borehole spacing B and borehole

depth H. The results showed that the average COP increased with both B and H. The total electricity consumption with $B = 8$ m, $H = 133$ m was reduced by 6 % compared to $B = 3$ m, $H = 133$ m. This model was also extended for a multi-year simulation. The results showed that the performance of the GCHP system decreased with time when only heating is considered. The DBES model integrated with the vertical GCHP model, on top of benefit for the designers of a GHE can also be used to optimise the system performance, based on COP evaluated by hourly simulation accounting for the dynamic loads of the building.

The second boundary condition is the microclimate. Certain microclimate effects are observed in urban areas such as UHI effect, which are not reflected in the normal weather files used in the DBES tools. As an essential boundary condition of a building, the microclimate can influence the building energy and comfort simulation results. Chapter 4 quantitatively analysed the UHI effect on the energy performance of the case study in Wuhan (China). A site-specific weather file generation method was proposed, accounting for the UHI effect, which can provide local hourly air temperature. The method of coupling the 3D numerical microclimate simulation tool ENVI-met with the DBES tool COMFIE was introduced, allowing to provide relatively more accurate simulation results with local weather conditions. Four representative days were chosen and simulated in ENVI-met. For the average urban heat island intensity, UHII, during one representative day for each season, the following ranking was observed: summer > spring > winter > autumn. The site-specific weather files were generated considering the UHI effect for four orientations and six heights based on the microclimate simulation results. The yearly average UHII at the height of 3 m was estimated to be 0.45 °C. More precise energy simulation (which considers the temperature variation along the height and in the orientation) results were obtained: the total heating and cooling loads were 586 000 kWh (47.1 kWh/m^2) and 582 000 kWh (46.7 kWh/m^2), respectively. The simulation using the original weather file had a heating load 3.5 % larger, a cooling load 3.9 % smaller, and a total energy load 0.2 % smaller. If only the weather file at the height of 3 m in the south was used, without considering the temperature variation along the height (which is used in many UHI studies), the heating load decreased by 5.4 % and the cooling load increased by 6.9 % compared to the original weather file, leading to a larger difference than the more precise simulation. Therefore, the microclimate is expected to have a larger influence on low-rise buildings. At the height of 3 m, the orientation slightly affected the heating load, but had a larger influence on the cooling load. In our case study, the heating and cooling loads are almost balanced, resulting in a minor difference in the total energy load due to the microclimate. However, its effect could be stronger in other climate zones where the difference of the heating and cooling loads is large.

LCA is widely used to assess the environmental impacts of a building, which is highly connected to its background systems, particularly the local electricity production mix and grid system. Many building LCA studies in China have used a static national average electricity production mix without taking into account its evolution. This assumption might affect the precision and credibility of the evaluation results. Chapter 5 is dedicated to study this question by considering local electricity production mix features and their future evolution. Dynamic building energy simulation was performed for five cities in different climate zones in China. Four types of regional future energy mix

were derived from the national scenario for each related region. The building materials in the construction/renovation stage and the use stage are related to the electricity mix, thus the contextualisation of materials fabrication and electricity production processes in the LCI database ecoinvent v3.4 was undertaken considering the national and regional energy mixes. The environmental impacts were compared between the local energy mixes and the national average energy mix, in the static approach which does not consider the future scenario, and in the dynamic approach accounting for future evolution.

The results indicated that differences were small (below 8 %) regarding the environmental impacts of materials fabrication in the construction stage using the local database compared to that using the database contextualised with the national average electricity mix. The choice of a contextualised database was not a key factor affecting the total environmental impact. However this importance, particularly for CO_2 emissions, might increase in the future because the construction and renovation stages will occupy larger shares in total impacts (e.g. less CO_2 emissions in the use stage in the future due to cleaner electricity). The use stage was the main contributor in most environmental impacts and the choice of an electricity production mix highly influenced the LCA results. On a regional scale, using the national average mix in the static approach can relatively accurately estimate some environmental indicators in some provinces, e.g. GWP, EP and POP in Guangdong. However, for most provinces, it brought non-negligible differences. For Yunnan, the overestimation of GWP can reach around 5 times in the use stage with a 50 years lifespan. On a temporal scale, the static approach might cause large differences compared to the dynamic approach for most environmental impact indicators. The differences highly depend on the predicted future scenarios and also show regional features. For example, in Guangdong, the difference of GWP can reach around 900 % in the ELC scenario, nevertheless it is relatively small in Yunnan in the LC scenario. According to the static approach in Hubei, the studied case emits nearly 53.4 kiloton CO_{2eq} and consumes approximately 570 000 GJ of primary energy over 50 years, corresponding to 76 kg CO_{2eq}/m^2.year and 254 kWh/m^2.year. These values were estimated to be 86, 75, 71, 50 kg CO_{2eq}/m^2.year and 263, 250, 243, 222 kWh/m^2.year for the ES, LC, ELC and HRE scenarios using the dynamic approach. A sensitivity analysis indicated that the environmental impacts were sensitive to the lifespan. The static approach using a national average mix overestimated the share of the use stage and this effect could be magnified in some provinces with higher renewable share, and also with a longer building lifespan (e.g. 200 years). The local electricity mix accounting for future evolution is suggested for future building LCA work instead of a static national average energy mix. The contextualised database presented in this chapter can be a reference to the future work concerning building LCA in China.

Finally, the effects of the boundary conditions regarding the ground and the microclimate were investigated as well. The use of the GCHP system obviously increased the environmental impacts in the construction stage, but it reduced the environmental impacts during the use stage compared to traditional equipments with lower efficiency. The COPs were more precisely evaluated using the proposed GCHP model. In the case study in Wuhan, most environmental indicators were overestimated by 13 % in the use stage without applying the GCHP model. The microclimate had a negligible effect, because the heating and cooling loads variations were opposite in Wuhan. However,

its effect might be larger in the regions where heating and cooling loads are not balanced, or if the hourly variation of the electricity mix is taken into consideration.

In summary, this thesis made efforts to refine the boundary conditions in the environmental impacts evaluation of Chinese buildings. The methods proposed in the thesis were integrated in the computer tools which are beneficial to building designers to improve a building's environmental performance.

6.2. Perspectives

Although a great effort has been made to provide a more accurate evaluation of the environmental impacts of Chinese buildings by refining three key aspects, there are still many perspectives.

The large-borehole GHE model focuses on a square field, which can be extended to other shapes. In the assumptions, the heating load is uniformly distributed to each borehole. The model could be improved by considering a non-uniform distribution of the heating load. Besides, the assumption that the line heat source does not vary along with depth should be improved. The comparison of the proposed model and some experimental results can be a complementary validation providing more information about the accuracy of the model. In the whole GCHP model, the power consumption of the pumps are not considered, thus in the future work it can be refined and a COP for the whole GCHP system could be obtained to have a more accurate evaluation of the performance. The distribution model is a simplified model, which can be improved if more data is available. The parameter identification of a large-scale heat pump is based on the scaling rules, which can be more accurately obtained if the datasheets are available from the manufacturer. More representative technologies regarding the compressor should be modelled, especially for the large-scale heat pump. This GCHP model could be extended to the cooling and DHW modes as well. The accuracy of the whole model should be experimentally validated.

The study regarding the microclimate investigated the influence of air temperature. However, other site-specific climate parameters such as relative humidity, solar radiation, longwave radiation, and wind affecting the building energy loads should be considered. The method of generating the hourly UHII is based on the linear interpolation between four representative days in each season, which might not precisely evaluate the UHII for every hour. Although this is a good attempt to account for the local UHI effect on the building energy performance, a more accurate method generating the hourly UHII would be beneficial. Besides, measurements of the local climate parameters could be helpful to validate the simulation results. The energy performance of other uses of buildings can also be investigated, such as office buildings only operating in the daytime.

One limitation of the LCA database contextualisation is that it only considered the replacement of electricity. In fact, the technologies used in the material fabrication or electricity generation could vary in different countries. A more detailed contextualisation process should be developed. Due to a lack of data, power grid interactions between different provinces were not considered in this thesis. The evaluation could be more precise if they were taken into account. The impacts of each power

technology were assumed to be identical in all five provinces. This assumption helped us focus on the influence of the energy mix; however, it does not reflect the reality that their impacts could vary in different locations. Thus, the combination of local technologies and local electricity mix could be studied to provide a more reasonable evaluation. Another assumption is the case study was kept identical for all cities in different climate zones, meaning it could not meet the energy regulations in some regions. A sensitivity analysis of the insulation technologies can be a research perspective. The heating/cooling was assumed to be supplied by a GCHP system in this study, but in reality various heating/cooling technologies are used in China, especially in different regions. Therefore, this study should be extended to more regional technologies in the future.

Some energy transition scenarios like the LC or ELC scenario may induce replacing gas and fuel boilers by heat pumps, leading to a huge peak demand in cold winter days in which renewable production cannot satisfy this peak demand. Accounting for future scenarios using a long term dynamic model should therefore be complemented by uncertainty calculations. Besides, the environmental impacts of one kWh electricity vary hourly and also seasonally, due to the fact that different technologies are used in different time in one day (peak technologies (e.g. natural gas) and dispatchable technologies (e.g. hydro) are used to meet the electricity consumption, leading to much higher environmental impacts in peak hours in one day) and in different seasons (e.g. a higher share of hydro power in summer in Hubei). Calibrating such a short term dynamic model in the Chinese context would be very useful to evaluate more precisely impacts related to electricity consumption.

The combination of these three boundary conditions was based on a timestep of one year. In fact, the energy mix changes in different seasons and even depends on time within each day. Estimating the effects of different energy mixes in China on environmental impacts combined with COPs evaluated by the GCHP model under local microclimate based on hourly timestep is another perspective.

REFERENCE

Abd Rashid, A.F., and Yusoff, S. (2015). *A review of life cycle assessment method for building industry*. Renew. Sustain. Energy Rev. *45*, DOI : 10.1016/j.rser.2015.01.043, 244–248 p.

Acero, J.A., and Arrizabalaga, J. (2018). *Evaluating the performance of ENVI-met model in diurnal cycles for different meteorological conditions*. Theor. Appl. Climatol. *131*, DOI : 10.1007/s00704-016-1971-y, 455–469 p.

Adalberth, K. (1997). *Energy use during the life cycle of single-unit dwellings: Examples*. Build. Environ. *32*, DOI : 10.1016/S0360-1323(96)00069-8, 321–329 p.

Aktas, C.B., and Bilec, M.M. (2012). *Impact of lifetime on US residential building LCA results*. Int. J. Life Cycle Assess. *17*, DOI : 10.1007/s11367-011-0363-x, 337–349 p.

Ayyad, Y., and Sharples, S. (2019). *Envi-MET validation and sensitivity analysis using field measurements in a hot arid climate*. IOP Conf. Ser. Earth Environ. Sci. *329*, DOI : 10.1088/1755-1315/329/1/012040, 012040 p.

Azam, M.-H., Bernard, J., Morille, B., Musy, M., and Andrieu, H. (2018). *A pavement-watering thermal model for SOLENE-microclimat: Development and evaluation*. Urban Clim. *25*, DOI : 10.1016/j.uclim.2018.04.005, 22–36 p.

Ball, D.A., Fischer, R.D., and Hodgett, D.L. (1983). *Design methods for ground-source heat pumps*. (Washington, D.C, USA), 416–440 p.

Bare, J.C., and Gloria, T.P. (2008). *Environmental impact assessment taxonomy providing comprehensive coverage of midpoints, endpoints, damages, and areas of protection*. J. Clean. Prod. *16*, DOI : 10.1016/j.jclepro.2007.06.001, 1021–1035 p.

Bare, J.C., Hofstetter, P., Pennington, D.W., and Udo, de H. (2000). *Midpoints versus endpoints: The sacrifices and benefits*. Int. J. Life Cycle Assess. *5*, DOI : 10.1053/jhep.2001.21045, 319–326 p.

Beccali, M., Cellura, M., Fontana, M., Longo, S., and Mistretta, M. (2013). *Energy retrofit of a single-family house: Life cycle net energy saving and environmental benefits*. Renew. Sustain. Energy Rev. *27*, DOI : 10.1016/j.rser.2013.05.040, 283–293 p.

Beck, M., Bayer, P., de Paly, M., Hecht-Méndez, J., and Zell, A. (2013). *Geometric arrangement and operation mode adjustment in low-enthalpy geothermal borehole fields for heating*. Energy *49*, DOI : 10.1016/j.energy.2012.10.060, 434–443 p.

Beckman, W.A., Broman, L., Fiksel, A., Klein, S.A., Lindberg, E., Schuler, M., and Thornton, J. (1994). *TRNSYS The most complete solar energy system modeling and simulation software*. Renew. Energy *5*, DOI : 10.1016/0960-1481(94)90420-0, 486–488 p.

Beier, R.A., Smith, M.D., and Spitler, J.D. (2011). *Reference data sets for vertical borehole ground heat exchanger models and thermal response test analysis*. Geothermics *40*, DOI : 10.1016/j.geothermics.2010.12.007, 79–85 p.

Belcher, S.E., Hacker, J.N., and Powell, D.S. (2005). *Constructing design weather data for future climates*. Build. Serv. Eng. Res. Technol. *26*, DOI : 10.1191/0143624405bt112oa, 49–61 p.

Beloin-Saint-Pierre, D., Levasseur, A., Margni, M., and Blanc, I. (2017). *Implementing a Dynamic Life Cycle Assessment Methodology with a Case Study on Domestic Hot Water Production*. J. Ind. Ecol. *21*, DOI : 10.1111/jiec.12499, 1128–1138 p.

Bernier, M.A. (2001). *Ground-coupled heat pump system simulation*. ASHRAE Trans. *107*, 605–616 p.

Bernier, M., Pinel, P., Labib, R., and Paillot, R. (2004). *A multiple load aggregation algorithm for annual hourly simulations of GCHP systems*. HVACR Res. *10*, DOI : 10.1080/10789669.2004.10391115, 471–487 p.

Biglarian, H., Abbaspour, M., and Saidi, M.H. (2017). *A numerical model for transient simulation of borehole heat exchangers*. Renew. Energy *104*, DOI : 10.1016/j.renene.2016.12.010, 224–237 p.

Blengini, G.A. (2009). *Life cycle of buildings, demolition and recycling potential: A case study in Turin, Italy*. Build. Environ. *44*, DOI : 10.1016/j.buildenv.2008.03.007, 319–330 p.

Blengini, G.A., and Di Carlo, T. (2010). *The changing role of life cycle phases, subsystems and materials in the LCA of low energy buildings*. Energy Build. *42*, DOI : 10.1016/j.enbuild.2009.12.009, 869–880 p.

Blom, I., Itard, L., and Meijer, A. (2011). *Environmental impact of building-related and user-related energy consumption in dwellings*. Build. Environ. *46*, DOI : 10.1016/j.buildenv.2011.02.002, 1657–1669 p.

Bonamente, E., and Cotana, F. (2015). *Carbon and energy footprints of prefabricated industrial buildings: A systematic life cycle assessment analysis*. Energies *8*, DOI : 10.3390/en81112335, 12685–12701 p.

Bouyer, J., Inard, C., and Musy, M. (2011). *Microclimatic coupling as a solution to improve building energy simulation in an urban context*. Energy Build. *43*, DOI : 10.1016/j.enbuild.2011.02.010, 1549–1559 p.

Brás, A., and Gomes, V. (2015). *LCA implementation in the selection of thermal enhanced mortars for energetic rehabilitation of school buildings*. Energy Build. *92*, DOI : 10.1016/j.enbuild.2015.01.007, 1–9 p.

Brasselet, J.-P., Domblides, J.-P., and Marchio, D. (1993). *Banc d'essais comparatif de progiciels de calculs de charges hygrothermiques*. Rapport d'étude pour l'AFME et EDF, AICVF-AITF-ARMINES.

Broadbent, A.M., Coutts, A.M., Tapper, N.J., and Demuzere, M. (2018). *The cooling effect of irrigation on urban microclimate during heatwave conditions*. Urban Clim. *23*, DOI : 10.1016/j.uclim.2017.05.002, 309–329 p.

Brun, A., Spitz, C., Wurtz, E., and Mora, L. (2009). *Behavioural Comparison of Some Predictive Tools Used in a Low-Energy Building*. Eleventh International IBPSA Conference (Glasgow, Scotland).

Bruse, M., and Fleer, H. (1998). *Simulating surface–plant–air interactions inside urban environments with a three dimensional numerical model*. Environ. Model. Softw. *13*, DOI : 10.1016/S1364-8152(98)00042-5, 373–384 p.

Bueno, B., Norford, L., Hidalgo, J., and Pigeon, G. (2013). *The urban weather generator*. J. Build. Perform. Simul. *6*, DOI : 10.1080/19401493.2012.718797, 269–281 p.

Cardinali, M., Pisello, A.L., Piselli, C., Pigliautile, I., and Cotana, F. (2020). *Microclimate mitigation for enhancing energy and environmental performance of Near Zero Energy Settlements in Italy*. Sustain. Cities Soc. *53*, DOI : 10.1016/j.scs.2019.101964, 101964 p.

Carslaw, H.S., and Jaeger, J.C. (1946). *Conduction of heat in solids*, Ed. Oxford University Press.

Castaldo, V.L., Pisello, A.L., Piselli, C., Fabiani, C., Cotana, F., and Santamouris, M. (2018). *How outdoor microclimate mitigation affects building thermal-energy performance: A new design-stage method for energy saving in residential near-zero energy settlements in Italy*. Renew. Energy *127*, DOI : 10.1016/j.renene.2018.04.090, 920–935 p.

Chan, A.L.S. (2011). *Developing a modified typical meteorological year weather file for Hong Kong taking into account the urban heat island effect*. Build. Environ. *46*, DOI : 10.1016/j.buildenv.2011.04.038, 2434–2441 p.

Chen, S., Witte, F., Kolditz, O., and Shao, H. (2020). *Shifted thermal extraction rates in large Borehole Heat Exchanger array – A numerical experiment*. Appl. Therm. Eng. *167*, DOI : 10.1016/j.applthermaleng.2019.114750, 114750 p.

Chen, Y., Pan, B., Zhang, X., and Du, C. (2019). *Thermal response factors for fast parameterized design and long-term performance simulation of vertical GCHP systems*. Renew. Energy *136*, DOI : 10.1016/j.renene.2018.12.114, 793–804 p.

Chua, K.J., Chou, S.K., Yang, W.M., and Yan, J. (2013). *Achieving better energy-efficient air conditioning – A review of technologies and strategies*. Appl. Energy *104*, DOI : 10.1016/j.apenergy.2012.10.037, 87–104 p.

Cimmino, M. (2018). *Fast calculation of the g-functions of geothermal borehole fields using similarities in the evaluation of the finite line source solution*. J. Build. Perform. Simul. *Taylor & Francis*, *11*, DOI : 10.1080/19401493.2017.1423390, 655–668 p.

Cimmino, M., and Bernier, M. (2014). *A semi-analytical method to generate g-functions for geothermal bore fields*. Int. J. Heat Mass Transf. *70*, DOI : 10.1016/j.ijheatmasstransfer.2013.11.037, 641–650 p.

Claesson, J., and Javed, S. (2011). *An analytical method to calculate borehole fluid temperatures for time-scales from minutes to decades*. ASHRAE Trans. *117*, 279–288 p.

Claesson, J., and Javed, S. (2012). *A load-aggregation method to calculate extraction temperatures of borehole heat exchangers*. ASHRAE Trans. *118*, 530–539 p.

Cole, R.J., and Kernan, P.C. (1996). *Life-cycle energy use in office buildings*. Build. Environ. *31*, DOI : 10.1016/0360-1323(96)00017-0, 307–317 p.

Collinge, W.O., Rickenbacker, H.J., Landis, A.E., Thiel, C.L., and Bilec, M.M. (2018). *Dynamic Life Cycle Assessments of a Conventional Green Building and a Net Zero Energy Building: Exploration of Static, Dynamic, Attributional, and Consequential Electricity Grid Models*. Environ. Sci. Technol. *American Chemical Society*, *52*, DOI : 10.1021/acs.est.7b06535, 11429–11438 p.

Conti, P., Testi, D., and Grassi, W. (2016). *Revised heat transfer modeling of double-U vertical ground-coupled heat exchangers*. Appl. Therm. Eng. *106*, DOI : 10.1016/j.applthermaleng.2016.06.097, 1257–1267 p.

Crawley, D.B., Lawrie, L.K., Winkelmann, F.C., Buhl, W.F., Huang, Y.J., Pedersen, C.O., Strand, R.K., Liesen, R.J., Fisher, D.E., Witte, M.J., et al. (2001). *EnergyPlus: creating a new-generation building energy simulation program*. Energy Build. *33*, DOI : 10.1016/S0378-7788(00)00114-6, 319–331 p.

Cui, P., Lin, Y., Fang, Z., and Sun, L. (2016). *Study on the representative borehole in ground heat exchanger design*. Procedia Eng. *146*, DOI : 10.1016/j.proeng.2016.06.405, 579–585 p.

Cui, Y., Yan, D., Hong, T., and Ma, J. (2017). *Temporal and spatial characteristics of the urban heat island in Beijing and the impact on building design and energy performance*. Energy *130*, DOI : 10.1016/j.energy.2017.04.053, 286–297 p.

Cullin, J.R., and Spitler, J.D. (2011). *A computationally efficient hybrid time step methodology for simulation of ground heat exchangers*. Geothermics *40*, DOI : 10.1016/j.geothermics.2011.01.001, 144–156 p.

Dandres, T., Farrahi Moghaddam, R., Nguyen, K.K., Lemieux, Y., Samson, R., and Cheriet, M. (2017a). *Consideration of marginal electricity in real-time minimization of distributed data centre emissions*. J. Clean. Prod. *143*, DOI : 10.1016/j.jclepro.2016.12.143, 116–124 p.

Dandres, T., Vandromme, N., Obrekht, G., Wong, A., Nguyen, K.K., Lemieux, Y., Cheriet, M., and Samson, R. (2017b). *Consequences of Future Data Center Deployment in Canada on Electricity Generation and Environmental Impacts: A 2015–2030 Prospective Study*. J. Ind. Ecol. *21*, DOI : 10.1111/jiec.12515, 1312–1322 p.

De la Flor, F.S., and Domínguez, S.A. (2004). *Modelling microclimate in urban environments and assessing its influence on the performance of surrounding buildings*. Energy Build. *36*, DOI : 10.1016/j.enbuild.2004.01.050, 403–413 p.

Deerman, J.D., and Kavanaugh, S.P. (1991). *Simulation of vertical U-tube ground-coupled heat pump systems using the cylindrical heat source solution*. ASHRAE Trans. *97*, 287–295 p.

Deng, Y., and Jiang, H. (2018). *The development overview of artificial mind*. ACM International Conference Proceeding Series. DOI : 10.1145/3241748.3241755, 111–116 p.

Deng, J.-Y., Wong, N.H., and Zheng, X. (2016). *The study of the effects of building arrangement on microclimate and energy demand of cbd in nanjing, china*. Procedia Eng. *169*, DOI : 10.1016/j.proeng.2016.10.006, 44–54 p.

Diao, N.R., Zeng, H.Y., and Fang, Z.H. (2004). *Improvement in Modeling of Heat Transfer in Vertical Ground Heat Exchangers*. HVACR Res. *10*, DOI : 10.1080/10789669.2004.10391114, 459–470 p.

Earles, J.M., and Halog, A. (2011). *Consequential life cycle assessment: a review*. Int. J. Life Cycle Assess. *16*, DOI : 10.1007/s11367-011-0275-9, 445–453 p.

Ekvall, T., and Weidema, B.P. (2004). *System boundaries and input data in consequential life cycle inventory analysis*. Int. J. Life Cycle Assess. *9*, DOI : 10.1007/BF02994190, 161–171 p.

Elbakheit, A.R. (2018). *Effect of turbine resistance and positioning on performance of Aerofoil wing building augmented wind energy generation*. Energy Build. *174*, DOI : 10.1016/j.enbuild.2018.06.025, 365–371 p.

Elnabawi, M., Hamza, N., and Dudek, S. (2013). *Use and evaluation of the Envi-met model for two different urban forms in cairo, egypt: measurements and model simulations*. 13th Int. Conf. Int. Build. Perform. Simul. Assoc.

Elwy, I., Ibrahim, Y., Fahmy, M., and Mahdy, M. (2018). *Outdoor microclimatic validation for hybrid simulation workflow in hot arid climates against ENVI-met and field measurements*. Energy Procedia *153*, DOI : 10.1016/j.egypro.2018.10.009, 29–34 p.

Erell, E., and Williamson, T. (2006). *Simulating air temperature in an urban street canyon in all weather conditions using measured data at a reference meteorological station*. Int. J. Climatol. *26*, DOI : 10.1002/joc.1328, 1671–1694 p.

ERINDRC (2009). *China's Low Carbon Development Pathways by 2050-Scenario Analysis of Energy Demand and Carbon Emissions*, Ed. Science Press.

ERINDRC (2015). *China 2050 high renewable energy penetration scenario and roadmap study*, https://www.efchina.org/Reports-en/china-2050-high-renewable-energy-penetration-scenario-and-roadmap-study-en?set_language=en.

Eskilson, P. (1987). *Thermal analysis of heat extraction boreholes*, Lund University.

European Commission-Joint Research Centre-Institute for Environment and Sustainability (2010). *International Reference Life Cycle Data System (ILCD) Handbook - General guide for Life Cycle Assessment - Detailed guidance*, Ed. Publications Office of the European Union, 394 p.

Fan, J.-L., Zhang, Y.-J., and Wang, B. (2017). *The impact of urbanization on residential energy consumption in China: An aggregated and disaggregated analysis*. Renew. Sustain. Energy Rev. *75*, DOI : 10.1016/j.rser.2016.10.066, 220–233 p.

Favi, C., Meo, I., Di Giuseppe, E., Iannaccone, M., D'Orazio, M., and Germani, M. (2017). *Towards a probabilistic approach in LCA of building retrofit measures*. Energy Procedia *134*, DOI : 10.1016/j.egypro.2017.09.584, 394–403 p.

Filliard, B. (2009). *Étude de la possibilité de récupération de chaleur par voie thermodynamique pour la réhabilitation des maisons individuelles*, PhD thesis, École Nationale Supérieure des Mines de Paris.

Filliard, B., Guiavarch, A., and Peuportier, B. (2009). *Performance evaluation of an air-to-air heat pump coupled with temperate air-sources integrated into a dwelling*. In Proceedings of Building Simulation, (Glasgow), 8 p.

Fisher, D., Rees, S., Padhmanabhan, S., and Murugappan, A. (2006). *Implementation and validation of ground-source heat pump system models in an integrated building and system simulation environment*. Hvacr Res. *12*, DOI : 10.1080/10789669.2006.10391201, 693–710 p.

Fossa, M., Priarone, A., and Silenzi, F. (2020). *Superposition of the single point source solution to generate temperature response factors for geothermal piles*. Renew. Energy *145*, DOI : 10.1016/j.renene.2019.05.011, 805–813 p.

Frischknecht, R., Birgisdottir, H., Chae, C.-U., Lützkendorf, T., Passer, A., Alsema, E., Balouktsi, M., Berg, B., Dowdell, D., Martínez, A.G., et al. (2019). *Comparison of the environmental assessment of an identical office building with national methods*. IOP Conf. Ser. Earth Environ. Sci. *IOP Publishing*, *323*, DOI : 10.1088/1755-1315/323/1/012037, 012037 p.

Gasche, J.L., Andreotti, T., and Maia, C.R.M. (2012). *A model to predict R134a refrigerant leakage through the radial clearance of rolling piston compressors*. Int. J. Refrig. *35*, DOI : 10.1016/j.ijrefrig.2012.07.015, 2223–2232 p.

Gens, A., Hurley, J.F., Tuomisto, J.T., and Friedrich, R. (2014). *Health impacts due to personal exposure to fine particles caused by insulation of residential buildings in Europe*. Atmos. Environ. *84*, DOI : 10.1016/j.atmosenv.2013.11.054, 213–221 p.

Goedkoop, M., Heijungs, R., Huijbregts, M., De Schryver, A., Struijs, J., and Van Zelm, R. (2008). *ReCiPE 2008: A life cycle impact assessment method which comprises harmonised category indicators at the midpoint and the endpoint level*.

Gong, X., Xia, L., Ma, Z., Chen, G., and Wei, L. (2018). *Investigation on the optimal cooling tower input capacity of a cooling tower assisted ground source heat pump system*. Energy Build. *174*, DOI : 10.1016/j.enbuild.2018.06.024, 239–253 p.

Gu, Y., and O'Neal, D. (1998). *Development of an equivalent diameter expression for vertical U-Tubes used in ground-coupled heat pumps*. ASHRAE Trans. *104*, 347–355 p.

Guattari, C., Evangelisti, L., and Balaras, C.A. (2018). *On the assessment of urban heat island phenomenon and its effects on building energy performance: A case study of Rome (Italy)*. Energy Build. *158*, DOI : 10.1016/j.enbuild.2017.10.050, 605–615 p.

Gultekin, A., Aydin, M., and Sisman, A. (2019). *Effects of arrangement geometry and number of boreholes on thermal interaction coefficient of multi-borehole heat exchangers*. Appl. Energy *237*, DOI : 10.1016/j.apenergy.2019.01.027, 163–170 p.

Hall, I.J., Prairie, R.R., Anderson, H.E., and Boes, E.C. (1978). *Generation of a typical meteorological year*, Sandia Labs., Albuquerque, NM (USA), SAND-78-1096C; CONF-780639-1, https://www.osti.gov/biblio/7013202.

Hart, D.P., and Couvillion, R. (1986). *Earth-coupled Heat Transfer*, Ed. National Water Well Association, 208 p.

Hassid, S., Santamouris, M., Papanikolaou, N., Linardi, A., Klitsikas, N., Georgakis, C., and Assimakopoulos, D.N. (2000). *The effect of the Athens heat island on air conditioning load*. Energy Build. *32*, DOI : 10.1016/S0378-7788(99)00045-6, 131–141 p.

Healy, P., and Ugursal, V. (1997). *Performance and economic feasibility of ground source heat pumps in cold inmate*. Int. J. Energy Res. *21*, DOI : 10.1002/(SICI)1099-114X(199708)21:10<857::AID-ER279>3.0.CO;2-1, 857–870 p.

Hellström, G. (1991). *Ground heat storage : thermal analyses of duct storage systems*, PhD thesis, Lund University.

Herfray, G. (2011). *Contribution à l'évaluation des impacts environnementaux des quartiers*, PhD thesis, École Nationale Supérieure des Mines de Paris.

Hong, J., Zhang, F., Xu, C., Xu, X., and Li, X. (2015). *Evaluation of life cycle inventory at macro level: a case study of mechanical coke production in China*. Int. J. Life Cycle Assess. *20*, DOI : 10.1007/s11367-015-0876-9, 751–764 p.

Hong, J., Chen, W., Qi, C., Ye, L., and Xu, C. (2016). *Life cycle assessment of multicrystalline silicon photovoltaic cell production in China*. Sol. Energy *133*, DOI : 10.1016/j.solener.2016.04.013, 283–293 p.

Hong, J., Chen, Y., Liu, J., Ma, X., Qi, C., and Ye, L. (2017). *Life cycle assessment of copper production: a case study in China*. Int. J. Life Cycle Assess. *23*, DOI : 10.1007/s11367-017-1405-9.

Hong, J., Yu, Z., Fu, X., and Hong, J. (2019). *Life cycle environmental and economic assessment of coal seam gas-based electricity generation*. Int. J. Life Cycle Assess. *24*, DOI : 10.1007/s11367-019-01599-6, 1828–1839 p.

Hou, G., Taherian, H., and Li, L. (2020). *A predictive TRNSYS model for long-term operation of a hybrid ground source heat pump system with innovative horizontal buried pipe type*. Renew. Energy *151*, DOI : 10.1016/j.renene.2019.11.113, 1046–1054 p.

Huang, Q., Huang, J., Yang, X., Fang, C., and Liang, Y. (2019). *Quantifying the seasonal contribution of coupling urban land use types on Urban Heat Island using Land Contribution Index: A case study in Wuhan, China*. Sustain. Cities Soc. *44*, DOI : 10.1016/j.scs.2018.10.016, 666–675 p.

Huttner, S. (2012). *Further development and application ofthe 3D microclimate simulation ENVI-met*, PhD thesis, Johannes Gutenberg University Mainz.

Ignatius, M., Wong, N.H., and Jusuf, S.K. (2016). *The significance of using local predicted temperature for cooling load simulation in the tropics*. Energy Build. *118*, DOI : 10.1016/j.enbuild.2016.02.043, 57–69 p.

Ikeda, S., Choi, W., and Ooka, R. (2017). *Optimization method for multiple heat source operation including ground source heat pump considering dynamic variation in ground temperature*. Appl. Energy *193*, DOI : 10.1016/j.apenergy.2017.02.047, 466–478 p.

Imhoff, M.L., Zhang, P., Wolfe, R.E., and Bounoua, L. (2010). *Remote sensing of the urban heat island effect across biomes in the continental USA*. Remote Sens. Environ. *114*, DOI : 10.1016/j.rse.2009.10.008, 504–513 p.

Ingersoll, L.R. (1954). *Heat conduction: with engineering, geological, and other applications*, Ed. University of Wisconsin Press, 350 p.

Ingersoll, L.R., and Plass, H.J. (1948). *Theory of the ground pipe heat source for the heat pump*. ASHRAE Trans. *54*, 339–348 p.

International Energy Agency (2010). *World energy outlook 2010*. https://webstore.iea.org/world-energy-outlook-2010.

ISO 14040:2006 (2006). *Environmental management — Life cycle assessment — Principles and framework*, https://www.iso.org/obp/ui/#iso:std:iso:14040:ed-2:v1:en.

ISO 14044:2006 (2006). *Environmental management — Life cycle assessment — Requirements and guidelines*, https://www.iso.org/standard/38498.html.

Itten, R., Frischknecht, R., and Stucki, M. (2012). *Life Cycle Inventories of Electricity Mixes and Grid*, treeze Ltd., Version 1.3.

Iyer-Raniga, U., and Wong, J.P.C. (2012). *Evaluation of whole life cycle assessment for heritage buildings in Australia*. Build. Environ. *47*, DOI : 10.1016/j.buildenv.2011.08.001, 138–149 p.

Javed, S., and Claesson, J. (2011). *New analytical and numerical solutions for the short-term analysis of vertical ground heat exchangers*. ASHRAE Transactions, *117*, 3–12 p.

Ji, C., Ma, X., Zhai, Y., Zhang, R., Shen, X., Zhang, T., and Hong, J. (2020). *Environmental impact assessment of galvanized sheet production: a case study in Shandong Province, China*. Int. J. Life Cycle Assess. *25*, DOI : 10.1007/s11367-020-01735-7, 760–770 p.

Jiang, Y., Yan, D., Guo, S., and Hu, S. (2018). *China Building Energy Use 2018*, Building energy research centre. https://berc.bestchina.org/?ky/Article250/92.html.

Jin, H., and Spitler, J. (2003). *Parameter estimation based model of water-to-water heat pumps with scroll compressors and water/glycol solutions*. Build. Serv. Eng. Res. Technol. *24*, DOI : 10.1191/0143624403bt072oa, 203–219 p.

Jin, H., Liu, Z., Jin, Y., Kang, J., and Liu, J. (2017a). *The effects of residential area building layout on outdoor wind environment at the pedestrian level in severe cold regions of China*. Sustainability *9*, DOI : 10.3390/su9122310, 2310 p.

Jin, H., Shao, T., and Zhang, R. (2017b). *Effect of water body forms on microclimate of residential district*. Energy Procedia *134*, DOI : 10.1016/j.egypro.2017.09.615, 256–265 p.

Jönsson, Å. (2000). *Tools and methods for environmental assessment of building products—methodological analysis of six selected approaches*. Build. Environ. *35*, DOI : 10.1016/S0360-1323(99)00016-5, 223–238 p.

Katsura, T., Nagano, K., and Takeda, S. (2008). *Method of calculation of the ground temperature for multiple ground heat exchangers*. Appl. Therm. Eng. *28*, DOI : 10.1016/j.applthermaleng.2007.12.013, 1995–2004 p.

Kavousian, A., Rajagopal, R., and Fischer, M. (2013). *Determinants of residential electricity consumption: Using smart meter data to examine the effect of climate, building characteristics, appliance stock, and occupants' behavior*. Energy *55*, DOI : 10.1016/j.energy.2013.03.086, 184–194 p.

Kerme, E.D., and Fung, A.S. (2020). *Heat transfer simulation, analysis and performance study of single U-tube borehole heat exchanger*. Renew. Energy *145*, DOI : 10.1016/j.renene.2019.06.004, 1430–1448 p.

Khan, M.H., Varanasi, A., Spitler, J.D., Fisher, D.E., and Delahoussaye, R.D. (2003). *Hybrid ground source heat pump system simulation using visual modeling tool for HVACSIM+*. In Proceedings of Building Simulation 2003, 641–648 p.

Kofoworola, O.F., and Gheewala, S.H. (2009). *Life cycle energy assessment of a typical office building in Thailand*. Energy Build. *41*, DOI : 10.1016/j.enbuild.2009.06.002, 1076–1083 p.

Kohler, N.A. (1986). *Analyse énergétique de la construction de l''utilisation et de la démolition de bâtiments*, PhD thesis, École polytechnique fédérale de Lausanne.

Kolokotroni, M., Giannitsaris, I., and Watkins, R. (2006). *The effect of the London urban heat island on building summer cooling demand and night ventilation strategies*. Sol. Energy *80*, DOI : 10.1016/j.solener.2005.03.010, 383–392 p.

Kolokotroni, M., Ren, X., Davies, M., and Mavrogianni, A. (2012). *London's urban heat island: Impact on current and future energy consumption in office buildings*. Energy Build. *47*, DOI : 10.1016/j.enbuild.2011.12.019, 302–311 p.

Koohi-Fayegh, S., and Rosen, M.A. (2014). *An analytical approach to evaluating the effect of thermal interaction of geothermal heat exchangers on ground heat pump efficiency*. Energy Convers. Manag. *78*, DOI : 10.1016/j.enconman.2013.09.064, 184–192 p.

Kosorić, V., Lau, S.-K., Tablada, A., and Lau, S.S.-Y. (2018). *General model of Photovoltaic (PV) integration into existing public high-rise residential buildings in Singapore – Challenges and benefits*. Renew. Sustain. Energy Rev. *91*, DOI : 10.1016/j.rser.2018.03.087, 70–89 p.

Kurevija, T., Vulin, D., and Krapec, V. (2012). *Effect of borehole array geometry and thermal interferences on geothermal heat pump system*. Energy Convers. Manag. *60*, DOI : 10.1016/j.enconman.2012.02.012, 134–142 p.

Lac, C., Chaboureau, P., Masson, V., Pinty, P., Tulet, P., Escobar, J., Leriche, M., Barthe, C., Aouizerats, B., Augros, C., et al. (2018). *Overview of the Meso-NH model version 5.4 and its applications*. Geosci. Model Dev. *11*, DOI : 10.5194/gmd-11-1929-2018, 1929–1969 p.

Lai, D., Qi, Y., Liu, J., Dai, X., Zhao, L., and Wei, S. (2018). *Ventilation behavior in residential buildings with mechanical ventilation systems across different climate zones in China*. Build. Environ. *143*, DOI : 10.1016/j.buildenv.2018.08.006, 679–690 p.

Lamarche, L. (2009). *A fast algorithm for the hourly simulations of ground-source heat pumps using arbitrary response factors*. Renew. Energy *34*, DOI : 10.1016/j.renene.2009.02.010, 2252–2258 p.

Lamarche, L., and Beauchamp, B. (2007). *A fast algorithm for the simulation of GCHP systems*. ASHRAE Trans. *113 PART 1*, 470–476 p.

Lamarche, L., Kajl, S., and Beauchamp, B. (2010). *A review of methods to evaluate borehole thermal resistances in geothermal heat-pump systems*. Geothermics *39*, DOI : 10.1016/j.geothermics.2010.03.003, 187–200 p.

Lauzet, N., Rodler, A., Musy, M., Azam, M.-H., Guernouti, S., Mauree, D., and Colinart, T. (2019). *How building energy models take the local climate into account in an urban context – A review*. Renew. Sustain. Energy Rev. *116*, DOI : 10.1016/j.rser.2019.109390, 109390 p.

Lebert, A., ARMINES-CES, BYCN, CSTB, Fédération maisons de qualité, and IZUBA Energies (2014). *Projet ANR BENEFIS : Bilan ENergétique et Environnemental FIable Simple et reproductible des bâtiments, Tâche 5 : diffusion et communication, Rapport final, ANR 2011 VILD 001 01, DEE/EICV - 14.100*, extranet.cstb.fr/sites/anr/benefis/.../Rapports%20du%20projet/BENEFIS_5_Com.pdf, 237 p.

Li, Y.Z. (2017). *Urbanization and economic growth in China—an empirical research based on VAR model*. Int. J. Econ. Finance *9*, 210–219 p.

Li, J., and Shui, B. (2015). *A comprehensive analysis of building energy efficiency policies in China: status quo and development perspective*. J. Clean. Prod. *90*, DOI : 10.1016/j.jclepro.2014.11.061, 326–344 p.

Li, M., and Lai, A.C.K. (2012). *New temperature response functions (G functions) for pile and borehole ground heat exchangers based on composite-medium line-source theory*. Energy *38*, DOI : 10.1016/j.energy.2011.12.004, 255–263 p.

Li, M., and Lai, A.C.K. (2015). *Review of analytical models for heat transfer by vertical ground heat exchangers (GHEs): A perspective of time and space scales*. Appl. Energy *151*, DOI : 10.1016/j.apenergy.2015.04.070, 178–191 p.

Li, C., Zhou, J., Cao, Y., Zhong, J., Liu, Y., Kang, C., and Tan, Y. (2014a). *Interaction between urban microclimate and electric air-conditioning energy consumption during high temperature season*. Appl. Energy *117*, DOI : 10.1016/j.apenergy.2013.11.057, 149–156 p.

Li, H., Zhou, Y., Li, X., Meng, L., Wang, X., Wu, S., and Sodoudi, S. (2018a). *A new method to quantify surface urban heat island intensity*. Sci. Total Environ. *624*, DOI : 10.1016/j.scitotenv.2017.11.360, 262–272 p.

Li, M., Li, P., Chan, V., and Lai, A.C.K. (2014b). *Full-scale temperature response function (G-function) for heat transfer by borehole ground heat exchangers (GHEs) from sub-hour to decades*. Appl. Energy *136*, DOI : 10.1016/j.apenergy.2014.09.013, 197–205 p.

Li, W., Li, X., Wang, Y., and Tu, J. (2018b). *An integrated predictive model of the long-term performance of ground source heat pump (GSHP) systems*. Energy Build. *159*, DOI : 10.1016/j.enbuild.2017.11.012, 309–318 p.

Li, X., Yang, F., Zhu, Y., and Gao, Y. (2014c). *An assessment framework for analyzing the embodied carbon impacts of residential buildings in China*. Energy Build. *85*, DOI : 10.1016/j.enbuild.2014.09.051, 400–409 p.

Li, X., Zhou, Y., Asrar, G.R., Imhoff, M., and Li, X. (2017). *The surface urban heat island response to urban expansion: A panel analysis for the conterminous United States*. Sci. Total Environ. *605–606*, DOI : 10.1016/j.scitotenv.2017.06.229, 426–435 p.

Li, X., Zhou, Y., Yu, S., Jia, G., Li, H., and Li, W. (2019). *Urban heat island impacts on building energy consumption: A review of approaches and findings*. Energy *174*, DOI : 10.1016/j.energy.2019.02.183, 407–419 p.

Liang, W., and Yang, M. (2019). *Urbanization, economic growth and environmental pollution: Evidence from China*. Sustain. Comput. Inform. Syst. *21*, DOI : 10.1016/j.suscom.2018.11.007, 1–9 p.

Liang, W., Huang, J., Jones, P., Wang, Q., and Hang, J. (2018). *A zonal model for assessing street canyon air temperature of high-density cities*. Build. Environ. *132*, DOI : 10.1016/j.buildenv.2018.01.035, 160–169 p.

Lin, B., and Liu, H. (2015). *China's building energy efficiency and urbanization*. Energy Build. *86*, DOI : 10.1016/j.enbuild.2014.09.069, 356–365 p.

Liu, X., and Hellstrom, G. (2014). *Enhancements of an integrated simulation tool for groundsource heat pump system design and energy analysis*. https://www.semanticscholar.org/paper/

ENHANCEMENTS-OF-AN-INTEGRATED-SIMULATION-TOOL-FOR-Liu-Hellstrom/cf2f3f9df57b8d75d78b9e60337681315df7a940

Liu, X., and Shi, Z. (2001). *Improved method makes a soft landing of well path*. Oil Gas J. *99*, 47–51 p.

Liu, Q., Lei, Q., Xu, H., and Yuan, J. (2018). *China's energy revolution strategy into 2030*. Resour. Conserv. Recycl. *128*, DOI : 10.1016/j.resconrec.2017.09.028, 78–89 p.

Liu, X., Wang, H., Chen, J., He, Q., Zhang, H., Jiang, R., Chen, X., and Hou, P. (2010). *Method and basic model for development of Chinese reference life cycle database*. Acta Sci. Circumstantiae *30*, 2136–2144 p.

Liu, Y., Fang, F., and Li, Y. (2014). *Key issues of land use in China and implications for policy making*. Land Use Policy *40*, DOI : 10.1016/j.landusepol.2013.03.013, 6–12 p.

Liu, Y., Stouffs, R., Tablada, A., Wong, N.H., and Zhang, J. (2017). *Comparing micro-scale weather data to building energy consumption in Singapore*. Energy Build. *152*, DOI : 10.1016/j.enbuild.2016.11.019, 776–791 p.

Liu, Z., Li, Y., Xu, W., Yin, H., Gao, J., Jin, G., Lun, L., and Jin, G. (2019). *Performance and feasibility study of hybrid ground source heat pump system assisted with cooling tower for one office building based on one Shanghai case*. Energy *173*, DOI : 10.1016/j.energy.2019.02.061, 28–37 p.

Lobaccaro, G., Croce, S., Vettorato, D., and Carlucci, S. (2018). *A holistic approach to assess the exploitation of renewable energy sources for design interventions in the early design phases*. Energy Build. *175*, DOI : 10.1016/j.enbuild.2018.06.066, 235–256 p.

López-Cabeza, V.P., Galán-Marín, C., Rivera-Gómez, C., and Roa-Fernández, J. (2018). *Courtyard microclimate ENVI-met outputs deviation from the experimental data*. Build. Environ. *144*, DOI : 10.1016/j.buildenv.2018.08.013, 129–141 p.

Lotteau, M., Loubet, P., Pousse, M., Dufrasnes, E., and Sonnemann, G. (2015). *Critical review of life cycle assessment (LCA) for the built environment at the neighborhood scale*. Build. Environ. *93*, DOI : 10.1016/j.buildenv.2015.06.029, 165–178 p.

Lowe, S.A. (2016). *An energy and mortality impact assessment of the urban heat island in the US*. Environ. Impact Assess. Rev. *56*, DOI : 10.1016/j.eiar.2015.10.004, 139–144 p.

Lucia, U., Simonetti, M., Chiesa, G., and Grisolia, G. (2017). *Ground-source pump system for heating and cooling: Review and thermodynamic approach*. Renew. Sustain. Energy Rev. *70*, DOI : 10.1016/j.rser.2016.11.268, 867–874 p.

Lund, H., Mathiesen, B.V., Christensen, P., and Schmidt, J.H. (2010). *Energy system analysis of marginal electricity supply in consequential LCA*. Int. J. Life Cycle Assess. *15*, DOI : 10.1007/s11367-010-0164-7, 260–271 p.

Ma, M., Cai, W., and Cai, W. (2018). *Carbon abatement in China's commercial building sector: A bottom-up measurement model based on Kaya-LMDI methods*. Energy *165*, DOI : 10.1016/j.energy.2018.09.070, 350–368 p.

Ma, W., Li, M., Li, P., and Lai, A.C.K. (2015). *New quasi-3D model for heat transfer in U-shaped GHEs (ground heat exchangers): Effective overall thermal resistance*. Energy *90*, DOI : 10.1016/j.energy.2015.07.098, 578–587 p.

Magli, S., Lodi, C., Lombroso, L., Muscio, A., and Teggi, S. (2015). *Analysis of the urban heat island effects on building energy consumption*. Int. J. Energy Environ. Eng. *6*, DOI : 10.1007/s40095-014-0154-9, 91–99 p.

Magnier, L., and Haghighat, F. (2010). *Multiobjective optimization of building design using TRNSYS simulations, genetic algorithm, and Artificial Neural Network*. Build. Environ. *45*, DOI : 10.1016/j.buildenv.2009.08.016, 739–746 p.

Maheshwari, B., Pinto, U., Akbar, S., and Fahey, P. (2020). *Is urbanisation also the culprit of climate change? – Evidence from Australian cities*. Urban Clim. *31*, DOI : 10.1016/j.uclim.2020.100581, 100581 p.

Man, Y., Yang, H., and Wang, J. (2010a). *Study on hybrid ground-coupled heat pump system for air-conditioning in hot-weather areas like Hong Kong*. Appl. Energy *87*, DOI : 10.1016/j.apenergy.2009.04.044, 2826–2833 p.

Man, Y., Yang, H., Diao, N., Liu, J., and Fang, Z. (2010b). *A new model and analytical solutions for borehole and pile ground heat exchangers*. Int. J. Heat Mass Transf. *53*, DOI : 10.1016/j.ijheatmasstransfer.2010.03.001, 2593–2601 p.

Marcotte, D., and Pasquier, P. (2008a). *On the estimation of thermal resistance in borehole thermal conductivity test*. Renew. Energy *33*, DOI : 10.1016/j.renene.2008.01.021, 2407–2415 p.

Marcotte, D., and Pasquier, P. (2008b). *Fast fluid and ground temperature computation for geothermal ground-loop heat exchanger systems*. Geothermics *37*, DOI : 10.1016/j.geothermics.2008.08.003, 651–665 p.

Martínez-Rocamora, A., Solís-Guzmán, J., and Marrero, M. (2016). *LCA databases focused on construction materials: A review*. Renew. Sustain. Energy Rev. *58*, DOI : 10.1016/j.rser.2015.12.243, 565–573 p.

Maslesa, E., Jensen, P.A., and Birkved, M. (2018). *Indicators for quantifying environmental building performance: A systematic literature review*. J. Build. Eng. *19*, DOI : 10.1016/j.jobe.2018.06.006, 552–560 p.

Masson, V. (2000). *A physically-based scheme for the urban energy budget in atmospheric models*. Bound.-Layer Meteorol. *94*, DOI : 10.1023/A:1002463829265, 357–397 p.

Mathiesen, B.V., Münster, M., and Fruergaard, T. (2009). *Uncertainties related to the identification of the marginal energy technology in consequential life cycle assessments*. J. Clean. Prod. *17*, DOI : 10.1016/j.jclepro.2009.04.009, 1331–1338 p.

Mauree, D., Blond, N., Kohler, M., and Clappier, A. (2017). *On the coherence in the boundary layer: development of a canopy interface model*. Front. Earth Sci. *Frontiers*, *4*, DOI : 10.3389/feart.2016.00109.

McLeod, R.S., Hopfe, C.J., and Rezgui, Y. (2012). *A proposed method for generating high resolution current and future climate data for Passivhaus design*. Energy Build. *55*, DOI : 10.1016/j.enbuild.2012.08.045, 481–493 p.

Miguet, F., and Groleau, D. (2002). *A daylight simulation tool for urban and architectural spaces—application to transmitted direct and diffuse light through glazing*. Build. Environ. *37*, DOI : 10.1016/S0360-1323(02)00049-5, 833–843 p.

Mitchell, M.S., and Spitler, J.D. (2019). *Characterization, testing, and optimization of load aggregation methods for ground heat exchanger response-factor models*. Sci. Technol. Built Environ. *25*, DOI : 10.1080/23744731.2019.1648936, 1036–1051 p.

MOHURD (2010). *Design standard for energy efficiency of residential buildings in hot summer and cold winter zone*, Ed. China Architecture & Building Press.

MOHURD (2016). *Code for thermal design of civil building*, Ed. China Architecture Press.

MOHURD (2019). *Uniform standard for design of civil buildings*, Ed. China Architecture & Building Press.

MOHURD-Hubei (2017). *Technical regulations for ground-source heat pump systems*, Ed. China Architecture & Building Press.

Mustafa Omer, A. (2008). *Ground-source heat pumps systems and applications*. Renew. Sustain. Energy Rev. *12*, DOI : 10.1016/j.rser.2006.10.003, 344–371 p.

Musy, M., Malys, L., Morille, B., and Inard, C. (2015). *The use of SOLENE-microclimat model to assess adaptation strategies at the district scale*. Urban Clim. *14*, DOI : 10.1016/j.uclim.2015.07.004, 213–223 p.

Naldi, C., and Zanchini, E. (2019). *A new numerical method to determine isothermal g-functions of borehole heat exchanger fields*. Geothermics *77*, DOI : 10.1016/j.geothermics.2018.10.007, 278–287 p.

Negishi, K., Lebert, A., Almeida, D., Chevalier, J., and Tiruta-Barna, L. (2019). *Evaluating climate change pathways through a building's lifecycle based on Dynamic Life Cycle Assessment*. Build. Environ. *164*, DOI : 10.1016/j.buildenv.2019.106377, 106377 p.

Ochsendorf, J., Keith Norford, L., Brown, D., Durschlag, H., Hsu, S.L., Love, A., Santero, N., Swei, O., Webb, A., and Wildnauer, M. (2011). *Methods, Impacts, and Opportunities in the Concrete Building Life Cycle*, Technical Report, MIT Concrete Sustainability Hub, http://dspace.mit.edu/handle/1721.1/105108.

Oke, T.R. (1982). *The energetic basis of the urban heat island (Symons Memorial Lecture, 20 May 1980)*. Q. J. R. Meteorol. Soc. *108*, 1–24 p.

Oke, T.R. (2002). *Boundary Layer Climates*, Ed. Routledge, ISBN : 978-1-134-95133-8, 460 p.

Olkkonen, V., and Syri, S. (2016). *Spatial and temporal variations of marginal electricity generation: the case of the Finnish, Nordic, and European energy systems up to 2030*. J. Clean. Prod. *126*, DOI : 10.1016/j.jclepro.2016.03.112, 515–525 p.

Ortiz-Rodríguez, O., Castells, F., and Sonnemann, G. (2009). *Sustainability in the construction industry: A review of recent developments based on LCA*. Constr. Build. Mater. *23*, DOI : 10.1016/j.conbuildmat.2007.11.012, 28–39 p.

Ortiz-Rodríguez, O., Castells, F., and Sonnemann, G. (2010). *Life cycle assessment of two dwellings: One in Spain, a developed country, and one in Colombia, a country under development*. Sci. Total Environ. *408*, DOI : 10.1016/j.scitotenv.2010.02.021, 2435–2443 p.

Oyarzo, J., and Peuportier, B. (2014). *Life cycle assessment model applied to housing in Chile*. J. Clean. Prod. *69*, DOI : 10.1016/j.jclepro.2014.01.090, 109–116 p.

Ozudogru, T.Y., Olgun, C.G., and Senol, A. (2014). *3D numerical modeling of vertical geothermal heat exchangers*. Geothermics *51*, DOI : 10.1016/j.geothermics.2014.02.005, 312–324 p.

Padhmanabhan, S. (2005). *Modeling, verification and optimization of hybrid ground source heat pump systems in Energyplus*, Master thesis, Oklahoma State University, 116 p.

Pahud, D., and Hellström, G. (1996). *The new duct ground heat model for TRNSYS*. In Eurotherm, Physical Models for Thermal Energy Stores, (Eindhoven, Netherlands: Université de Genève), 127–136 p.

Palacios-Munoz, B., Peuportier, B., Gracia-Villa, L., and López-Mesa, B. (2019). *Sustainability assessment of refurbishment vs. new constructions by means of LCA and durability-based estimations of buildings lifespans: A new approach*. Build. Environ. *160*, DOI : 10.1016/j.buildenv.2019.106203, 106203 p.

Palme, M., Inostroza, L., Villacreses, G., Lobato-Cordero, A., and Carrasco, C. (2017). *From urban climate to energy consumption. Enhancing building performance simulation by including the urban heat island effect*. Energy Build. *145*, DOI : 10.1016/j.enbuild.2017.03.069, 107–120 p.

Pannier, M.-L. (2017). *Etude de la quantification des incertitudes en analyse de cycle de vie des bâtiments*, PhD thesis, MINES ParisTech PSL, 484 p.

Pei, L. (2015). *The Study on Eco-design of High-rise Residential Buildings in Wuhan Based on Energy Simulation and Life Cycle Assessment*, Master thesis, Huazhong University of Science & Technology.

Peuportier, B. (1993). *COMFIE, logiciel pour l'architecture bioclimatique, quelques applications pour les vérandas*, In Journée technique GENEC (CEA), https://docplayer.fr/12225666-Comfie-logiciel-pour-la-conception-bioclimatique.html.

Peuportier, B. (2005). *Bancs d'essais de logiciels de simulation thermique*. In Journée Thématique IBPSA France - SFT 2005, Outil de Simulation Thermo-Aéraulique Du Bâtiment, (La Rochelle, France),.

Peuportier, B., and Blanc-Sommereux, I. (1990). *Simulation Tool with Its Expert Interface for the Thermal Design of Multizone Buildings*. Int. J. Sol. Energy *8*, DOI : 10.1080/01425919008909714, 109–120 p.

Peuportier, B., Kellenberger, D., Anink, D., Mötzl, H., Anderson, J., Vares, S., Chevalier, J., and König, H. (2004). *Inter-comparison and benchmarking of LCA-based environmental assessment and design tools*. SB04 Warsaw: Regional Central and Eastern European Conference on Sustainable Building, (Warsaw, Poland).

Peuportier, B., Thiers, S., and Guiavarch, A. (2013). *Eco-design of buildings using thermal simulation and life cycle assessment*. J. Clean. Prod. *39*, DOI : 10.1016/j.jclepro.2012.08.041, 73–78 p.

Pigeon, G., Zibouche, K., Bueno, B., Le Bras, J., and Masson, V. (2014). *Improving the capabilities of the Town Energy Balance model with up-to-date building energy simulation algorithms: an application to a set of representative buildings in Paris*. Energy Build. *76*, DOI : 10.1016/j.enbuild.2013.10.038, 1–14 p.

Polster, B. (1995). *Contribution à l'étude de l'impact environnemental des bâtiments par analyse du cycle de vie*, PhD thesis, École Nationale Supérieure des Mines de Paris, 268 p.

Popovici, E. (2005). *Contribution to the life cycle assessment of settlements*, PhD thesis, École Nationale Supérieure des Mines de Paris, 244 p.

Priarone, A., and Fossa, M. (2016). *Temperature response factors at different boundary conditions for modelling the single borehole heat exchanger*. Appl. Therm. Eng. *103*, DOI : 10.1016/j.applthermaleng.2016.04.038, 934–944 p.

Radhi, H., and Sharples, S. (2013). *Quantifying the domestic electricity consumption for air-conditioning due to urban heat islands in hot arid regions*. Appl. Energy *112*, DOI : 10.1016/j.apenergy.2013.06.013, 371–380 p.

Recht, T., Munaretto, F., Schalbart, P., and Peuportier, B. (2014). *Analyse de la fiabilité de COMFIE par comparaison à des mesures. Application à un bâtiment passif*. IBPSA France, (Arras), 8 p.

Redon, E.C., Lemonsu, A., Masson, V., Morille, B., and Musy, M. (2017). *Implementation of street trees within the solar radiative exchange parameterization of TEB in SURFEX v8.0*. Geosci. Model Dev. *Copernicus GmbH*, *10*, DOI : https://doi.org/10.5194/gmd-10-385-2017, 385–411 p.

Ren, Z., Wang, X., Chen, D., Wang, C., and Thatcher, M. (2014). *Constructing weather data for building simulation considering urban heat island*. Build. Serv. Eng. Res. Technol. *SAGE Publications Ltd STM*, *35*, DOI : 10.1177/0143624412467194, 69–82 p.

Rosenbaum, R.K., Meijer, A., Demou, E., Hellweg, S., Jolliet, O., Lam, N.L., Margni, M., and McKone, T.E. (2015). *Indoor Air Pollutant Exposure for Life Cycle Assessment: Regional Health Impact Factors for Households*. Environ. Sci. Technol. *49*, DOI : 10.1021/acs.est.5b00890, 12823–12831 p.

Rossi, B., Marique, A.-F., Glaumann, M., and Reiter, S. (2012). *Life-cycle assessment of residential buildings in three different European locations, basic tool*. Build. Environ. *51*, DOI : 10.1016/j.buildenv.2011.11.017, 395–401 p.

Roux, C., Schalbart, P., Assoumou, E., and Peuportier, B. (2016a). *Integrating climate change and energy mix scenarios in LCA of buildings and districts*. Appl. Energy *184*, DOI : 10.1016/j.apenergy.2016.10.043, 619–629 p.

Roux, C., Schalbart, P., and Peuportier, B. (2016b). *Accounting for temporal variation of electricity production and consumption in the LCA of an energy-efficient house*. J. Clean. Prod. *113*, DOI : 10.1016/j.jclepro.2015.11.052, 532–540 p.

Roux, C., Schalbart, P., and Peuportier, B. (2017). *Development of an electricity system model allowing dynamic and marginal approaches in LCA—tested in the French context of space heating in buildings*. Int. J. Life Cycle Assess. *22*, DOI : 10.1007/s11367-016-1229-z, 1177–1190 p.

Salata, F., Golasi, I., de Lieto Vollaro, R., and de Lieto Vollaro, A. (2016). *Urban microclimate and outdoor thermal comfort. A proper procedure to fit ENVI-met simulation outputs to experimental data.* Sustain. Cities Soc. *26*, DOI : 10.1016/j.scs.2016.07.005, 318–343 p.

Salmon, N., Duclos, L., Filit, F., Peuportier, B., Herfray, G., Chevalier, J., Schiopu, N., Lasvaux, S., Lebert, A., Sénégas, J.-L., et al. (2011). *Connaissance de l'impact environnemental des bâtiments // COIMBA 2011, Développement des outils d'évaluation de la qualité environnementale des bâtiments par analyse de cycle de vie*, Nobatek, ARMINES, CSTB, IZUBA Energies, ENERTECH, http://www.nobatek.com/downloads/Etudes%20publiques/Coimba_Synthese_NOBATEK.pdf, 9 p.

Salvati, A., Coch Roura, H., and Cecere, C. (2015). *Urban morphology and energy performance: the direct and indirect contribution in mediterranean climate*. PLEA 2015 Architecture in (R)Evolution – 31st International PLEA Conference – Bologna 9-11 September, (Building Green Futures), 1–8 p.

Salvati, A., Coch Roura, H., and Cecere, C. (2017). *Assessing the urban heat island and its energy impact on residential buildings in Mediterranean climate: Barcelona case study*. Energy Build. *146*, DOI : 10.1016/j.enbuild.2017.04.025, 38–54 p.

Santamouris, M. (2015). *Analyzing the heat island magnitude and characteristics in one hundred Asian and Australian cities and regions*. Sci. Total Environ. *512–513*, DOI : 10.1016/j.scitotenv.2015.01.060, 582–598 p.

Santamouris, M., Papanikolaou, N., Livada, I., Koronakis, I., Georgakis, C., Argiriou, A., and Assimakopoulos, D.N. (2001). *On the impact of urban climate on the energy consumption of buildings*. Sol. Energy *70*, DOI : 10.1016/S0038-092X(00)00095-5, 201–216 p.

Sarbu, I., and Sebarchievici, C. (2014). *General review of ground-source heat pump systems for heating and cooling of buildings*. Energy Build. *70*, DOI : 10.1016/j.enbuild.2013.11.068, 441–454 p.

Shah, V.P., and Ries, R.J. (2009). *A characterization model with spatial and temporal resolution for life cycle impact assessment of photochemical precursors in the united States*. Int. J. Life Cycle Assess. *14*, DOI : 10.1007/s11367-009-0084-6, 313–327 p.

Sharma, A., Saxena, A., Sethi, M., Shree, V., and Varun (2011). *Life cycle assessment of buildings: A review*. Renew. Sustain. Energy Rev. *15*, DOI : 10.1016/j.rser.2010.09.008, 871–875 p.

Sharmin, T., and Steemers, K. (2017). *Understanding ENVI-met (V4) model behaviour in relation to environmental variables*. In PLEA 2017 Edinburgh: Design to Thrive, (Edinburgh: PLEA 2017), 2156–2164 p.

Shonder, J.A., and Hughes, P.J. (1998). *Increasing confidence in geothermal heat pump design methods*. (Richard Stockton College, NJ, USA), 9 p.

Shonder, J., Martin, M., Hughes, P., and Thornton, J. (2000). *Geothermal Heat Pumps in K–12 Schools: A Case Study of the Lincoln, Nebraska Schools*. US Dep. Energy Publ.

Skelhorn, C.P., Levermore, G., and Lindley, S.J. (2016). *Impacts on cooling energy consumption due to the UHI and vegetation changes in Manchester, UK*. Energy Build. *122*, DOI : 10.1016/j.enbuild.2016.01.035, 150–159 p.

Spitz, C. (2012). *Analyse de la fiabilité des outils de simulation et des incertitudes de métrologie appliquée à l'efficacité énergétique des bâtiments*, PhD thesis, Université de Grenoble.

Stazi, F., Vegliò, A., Di Perna, C., and Munafò, P. (2012). *Retrofitting using a dynamic envelope to ensure thermal comfort, energy savings and low environmental impact in Mediterranean climates*. Energy Build. *54*, DOI : 10.1016/j.enbuild.2012.07.020, 350–362 p.

Su, S., Li, X., Wang, T., and Zhu, Y. (2016). *A comparative study of environmental performance between CFST and RC columns under combinations of compression and bending*. J. Clean. Prod. *137*, DOI : 10.1016/j.jclepro.2016.07.043, 10–20 p.

Su, S., Li, X., Zhu, Y., and Lin, B. (2017). *Dynamic LCA framework for environmental impact assessment of buildings*. Energy Build. *149*, DOI : 10.1016/j.enbuild.2017.05.042, 310–320 p.

Su, S., Li, X., and Zhu, Y. (2019). *Dynamic assessment elements and their prospective solutions in dynamic life cycle assessment of buildings*. Build. Environ. *158*, DOI : 10.1016/j.buildenv.2019.05.008, 248–259 p.

Su, X., Tian, S., Shao, X., and Zhao, X. (2020). *Embodied and operational energy and carbon emissions of passive building in HSCW zone in China: A case study*. Energy Build. *222*, DOI : 10.1016/j.enbuild.2020.110090, 110090 p.

Sun, Y., and Augenbroe, G. (2014). *Urban heat island effect on energy application studies of office buildings*. Energy Build. *77*, DOI : 10.1016/j.enbuild.2014.03.055, 171–179 p.

Takano, A., Pal, S.K., Kuittinen, M., Alanne, K., Hughes, M., and Winter, S. (2015). *The effect of material selection on life cycle energy balance: A case study on a hypothetical building model in Finland*. Build. Environ. *89*, DOI : 10.1016/j.buildenv.2015.03.001, 192–202 p.

Teza, G., Galgaro, A., and De Carli, M. (2012). *Long-term performance of an irregular shaped borehole heat exchanger system: Analysis of real pattern and regular grid approximation*. Geothermics *43*, DOI : 10.1016/j.geothermics.2012.02.004, 45–56 p.

Thiers, S. (2008). *Bilans énergétiques et environnementaux de bâtiments à énergie positive*, PhD thesis, École Nationale Supérieure des Mines de Paris.

Toparlar, Y., Blocken, B., Maiheu, B., and van Heijst, G.J.F. (2017). *A review on the CFD analysis of urban microclimate*. Renew. Sustain. Energy Rev. *80*, DOI : 10.1016/j.rser.2017.05.248, 1613–1640 p.

Toparlar, Y., Blocken, B., Maiheu, B., and van Heijst, G.J.F. (2018). *Impact of urban microclimate on summertime building cooling demand: A parametric analysis for Antwerp, Belgium*. Appl. Energy *228*, DOI : 10.1016/j.apenergy.2018.06.110, 852–872 p.

Treyer, K., and Bauer, C. (2016). *Life cycle inventories of electricity generation and power supply in version 3 of the ecoinvent database—part II: electricity markets*. Int. J. Life Cycle Assess. *21*, DOI : 10.1007/s11367-013-0694-x, 1255–1268 p.

Tsoka, S., Tsikaloudaki, K., and Theodosiou, T. (2017). *Urban space's morphology and microclimatic analysis: A study for a typical urban district in the Mediterranean city of Thessaloniki, Greece*. Energy Build. *156*, DOI : 10.1016/j.enbuild.2017.09.066, 96–108 p.

Tsoka, S., Tolika, K., Theodosiou, T., Tsikaloudaki, K., and Bikas, D. (2018). *A method to account for the urban microclimate on the creation of 'typical weather year' datasets for building energy simulation, using stochastically generated data*. Energy Build. *165*, DOI : 10.1016/j.enbuild.2018.01.016, 270–283 p.

Utama, A., and Gheewala, S.H. (2008). *Life cycle energy of single landed houses in Indonesia*. Energy Build. *40*, DOI : 10.1016/j.enbuild.2008.04.017, 1911–1916 p.

Van Ooteghem, K., and Xu, L. (2012). *The life-cycle assessment of a single-storey retail building in Canada*. Build. Environ. *49*, DOI : 10.1016/j.buildenv.2011.09.028, 212–226 p.

Venkatarama Reddy, B.V., and Jagadish, K.S. (2003). *Embodied energy of common and alternative building materials and technologies*. Energy Build. *35*, DOI : 10.1016/S0378-7788(01)00141-4, 129–137 p.

Verbeeck, G., and Hens, H. (2010). *Life cycle inventory of buildings: A calculation method*. Build. Environ. *45*, DOI : 10.1016/j.buildenv.2009.10.012, 1037–1041 p.

Villoria Sáez, P., del Río Merino, M., Porras-Amores, C., and San-Antonio González, A. (2014). *Assessing the accumulation of construction waste generation during residential building construction works*. Resour. Conserv. Recycl. *93*, DOI : 10.1016/j.resconrec.2014.10.004, 67–74 p.

Walzberg, J., Dandres, T., Merveille, N., Cheriet, M., and Samson, R. (2019). *Accounting for fluctuating demand in the life cycle assessments of residential electricity consumption and demand-side management strategies*. J. Clean. Prod. *240*, DOI : 10.1016/j.jclepro.2019.118251, 118251 p.

Wang, G., Wang, W., Luo, J., and Zhang, Y. (2019a). *Assessment of three types of shallow geothermal resources and ground-source heat-pump applications in provincial capitals in the Yangtze River Basin, China*. Renew. Sustain. Energy Rev. *111*, DOI : 10.1016/j.rser.2019.05.029, 392–421 p.

Wang, J., Zhang, Y., and Wang, Y. (2018). *Environmental impacts of short building lifespans in China considering time value*. J. Clean. Prod. *203*, DOI : 10.1016/j.jclepro.2018.08.314, 696–707 p.

Wang, L., Zhou, X., and Wei, X. (2007). *Heat Conduction: Mathematical Models and Analytical Solutions*, Ed. Springer Science & Business Media, ISBN : 978-3-540-74303-3, 524 p.

Wang, Q., Tang, H., Ma, Q., Mu, R., Yuan, X., Hong, J., Zhang, J., Zuo, J., Mu, Z., Cao, S., et al. (2019b). *Life cycle assessment and the willingness to pay of waste polyester recycling*. J. Clean. Prod. *234*, DOI : 10.1016/j.jclepro.2019.06.123, 275–284 p.

Wang, Y., Wang, F., Hong, J., and Sun, M. (2016). *The development of life cycle assessment theory research in China and analysis of countermeasures*. Acta Ecol. Sin. *36*, 7179–7184 p.

Watkins, R., Palmer, J., Kolokotroni, M., and Littlefair, P. (2002). *The balance of the annual heating and cooling demand within the London urban heat island*. Build. Serv. Eng. Res. Technol. *23*, DOI : 10.1191/0143624402bt043oa, 207–213 p.

Wei, Y., Huang, C., Li, J., and Xie, L. (2016). *An evaluation model for urban carrying capacity: A case study of China's mega-cities*. Habitat Int. *53*, DOI : 10.1016/j.habitatint.2015.10.025, 87–96 p.

Wu, H.J., Yuan, Z.W., Zhang, L., and Bi, J. (2012). *Life cycle energy consumption and CO2 emission of an office building in China*. Int. J. Life Cycle Assess. *17*, DOI : 10.1007/s11367-011-0342-2, 105–118 p.

Wu, N., Shi, P., Zhu, G., and Pan, X. (2017). *Changes of soil relative moisture content and influencing factor in the yangtze basin during 1992-2012*. Resour. Environ. Yangtze Basin *26*, DOI : 10.11870/cjlyzyyhj201707006, 1001–1010 p.

Xie, B.-C., Zhai, J.-X., Sun, P.-C., and Ma, J.-J. (2020a). *Assessment of energy and emission performance of a green scientific research building in Beijing, China*. Energy Build. DOI : 10.1016/j.enbuild.2020.110248, 110248 p.

Xie, X., Jiang, X., Zhang, T., and Huang, Z. (2020b). *Study on impact of electricity production on regional water resource in China by water footprint*. Renew. Energy *152*, DOI : 10.1016/j.renene.2020.01.025, 165–178 p.

Xu, J. (2010). *Research on variable-period model of heat exchanger of ground source heat pump*, PhD thesis, Zhejiang University.

Yan, D., Xie, X., Song, F., and Jiang, Y. (2004). *Building environment design simulation software DeST (1): An overview of developments and information of building simulation and DeST*. HV&AC *34*, 48–56 p.

Yang, X. (2012). *A simulation method for the effects of urban microclimate on building cooling energy use*, PhD Thesis, South China University of Technology.

Yang, J., and Chen, B. (2014). *Global warming impact assessment of a crop residue gasification project—A dynamic LCA perspective*. Appl. Energy *122*, DOI : 10.1016/j.apenergy.2014.02.034, 269–279 p.

Yang, Y., and Li, M. (2014). *Short-time performance of composite-medium line-source model for predicting responses of ground heat exchangers with single U-shaped tube*. Int. J. Therm. Sci. *82*, DOI : 10.1016/j.ijthermalsci.2014.04.002, 130–137 p.

Yang, H., Cui, P., and Fang, Z. (2010a). *Vertical-borehole ground-coupled heat pumps: A review of models and systems*. Appl. Energy *87*, DOI : 10.1016/j.apenergy.2009.04.038, 16–27 p.

Yang, W., Zhou, J., Xu, W., and Zhang, G. (2010b). *Current status of ground-source heat pumps in China*. Energy Policy *38*, DOI : 10.1016/j.enpol.2009.09.021, 323–332 p.

Yang, X., Zhao, L., Bruse, M., and Meng, Q. (2012). *An integrated simulation method for building energy performance assessment in urban environments*. Energy Build. *54*, DOI : 10.1016/j.enbuild.2012.07.042, 243–251 p.

Yang, X., Zhao, L., Bruse, M., and Meng, Q. (2013). *Evaluation of a microclimate model for predicting the thermal behavior of different ground surfaces*. Build. Environ. *60*, DOI : 10.1016/j.buildenv.2012.11.008, 93–104 p.

Yang, X., Yao, L., Jin, T., Peng, L.L.H., Jiang, Z., Hu, Z., and Ye, Y. (2018a). *Assessing the thermal behavior of different local climate zones in the Nanjing metropolis, China*. Build. Environ. *137*, DOI : 10.1016/j.buildenv.2018.04.009, 171–184 p.

Yang, X., Hu, M., Wu, J., and Zhao, B. (2018b). *Building-information-modeling enabled life cycle assessment, a case study on carbon footprint accounting for a residential building in China*. J. Clean. Prod. *183*, DOI : 10.1016/j.jclepro.2018.02.070, 729–743 p.

Yang, X., Yao, L., Peng, L.L.H., Jiang, Z., Jin, T., and Zhao, L. (2019). *Evaluation of a diagnostic equation for the daily maximum urban heat island intensity and its application to building energy simulations*. Energy Build. *193*, DOI : 10.1016/j.enbuild.2019.04.001, 160–173 p.

Yang, X., Peng, L.L.H., Jiang, Z., Chen, Y., Yao, L., He, Y., and Xu, T. (2020). *Impact of urban heat island on energy demand in buildings: Local climate zones in Nanjing*. Appl. Energy *260*, DOI : 10.1016/j.apenergy.2019.114279, 114279 p.

Yang, Z., Ghahramani, A., and Becerik-Gerber, B. (2016). *Building occupancy diversity and HVAC (heating, ventilation, and air conditioning) system energy efficiency*. Energy *109*, DOI : 10.1016/j.energy.2016.04.099, 641–649 p.

Yavuzturk, C., and Spitler, J. (1999). *A short time step response factor model for vertical ground loop heat exchangers*. ASHRAE Trans. *105*.

Yavuzturk, C., and Spitler, J.D. (2000). *Comparative Study of Operating and Control Strategies for Hybrid Ground-Source Heat Pump Systems Using a Short Time Step Simulation Model*. ASHRAE Trans. 19 p.

Yu, M., Ma, T., Zhang, K., Cui, P., Hu, A., and Fang, Z. (2016). *Simplified heat transfer analysis method for large-scale boreholes ground heat exchangers*. Energy Build. *116*, DOI : 10.1016/j.enbuild.2016.02.001, 593–601 p.

Yu, X., Li, H., Yao, S., Nielsen, V., and Heller, A. (2020). *Development of an efficient numerical model and analysis of heat transfer performance for borehole heat exchanger*. Renew. Energy DOI : 10.1016/j.renene.2020.01.044.

Zanchini, E., and Jahanbin, A. (2018). *Simple equations to evaluate the mean fluid temperature of double-U-tube borehole heat exchangers*. Appl. Energy *231*, DOI : 10.1016/j.apenergy.2018.09.094, 320–330 p.

Zarrella, A., Scarpa, M., and De Carli, M. (2011). *Short time step analysis of vertical ground-coupled heat exchangers: The approach of CaRM*. Renew. Energy *36*, DOI : 10.1016/j.renene.2011.01.032, 2357–2367 p.

Zeng, H., and Fang, Z. (2002). *A fluid temperature model for vertical U-tube geothermal heat exchangers*. J. Shandong Inst. Archit. 7–11 p.

Zeng, H., Diao, N., and Fang, Z. (2003). *Heat transfer analysis of boreholes in vertical ground heat exchangers*. Int. J. Heat Mass Transf. *46*, DOI : 10.1016/S0017-9310(03)00270-9, 4467–4481 p.

Zeng, H.Y., Diao, N.R., and Fang, Z.H. (2002). *A finite line-source model for boreholes in geothermal heat exchangers*. Heat Transfer—Asian Res. *31*, DOI : 10.1002/htj.10057, 558–567 p.

Zhang, D. (2010). *Research into heat exchange between wells of the U-tube ground heat exchanger*, PhD thesis, Southwest Jiaotong University.

Zhang, Y., and Wang, Y. (2013). *Barriers' and policies' analysis of China's building energy efficiency*. Energy Policy *62*, DOI : 10.1016/j.enpol.2013.06.128, 768–773 p.

Zhang, C., Wang, Y., Liu, Y., Kong, X., and Wang, Q. (2018a). *Computational methods for ground thermal response of multiple borehole heat exchangers: A review*. Renew. Energy *127*, DOI : 10.1016/j.renene.2018.04.083, 461–473 p.

Zhang, L., Zhang, Q., and Huang, G. (2016). *A transient quasi-3D entire time scale line source model for the fluid and ground temperature prediction of vertical ground heat exchangers (GHEs)*. Appl. Energy *170*, DOI : 10.1016/j.apenergy.2016.02.099, 65–75 p.

Zhang, L., Zhan, Q., and Lan, Y. (2018b). *Effects of the tree distribution and species on outdoor environment conditions in a hot summer and cold winter zone: A case study in Wuhan residential quarters*. Build. Environ. *130*, DOI : 10.1016/j.buildenv.2017.12.014, 27–39 p.

Zhang, L., Huang, G., Zhang, Q., and Wang, J. (2018c). *An hourly simulation method for the energy performance of an office building served by a ground-coupled heat pump system*. Renew. Energy *126*, DOI : 10.1016/j.renene.2018.03.082, 495–508 p.

Zhang, Q., Lv, N., Chen, S., Shi, H., and Chen, Z. (2015). *Study on Operating and Control Strategies for Hybrid Ground Source Heat Pump System*. Procedia Eng. *121*, DOI : 10.1016/j.proeng.2015.09.172, 1894–1901 p.

Zhao, H., and Magoulès, F. (2012). *A review on the prediction of building energy consumption*. Renew. Sustain. Energy Rev. *16*, DOI : 10.1016/j.rser.2012.02.049, 3586–3592 p.

Zhou, J., Zhang, X., and Shen, L. (2015). *Urbanization bubble: Four quadrants measurement model*. Cities *46*, DOI : 10.1016/j.cities.2015.04.007, 8–15 p.

Zhou, W., Wang, J., and Cadenasso, M.L. (2017). *Effects of the spatial configuration of trees on urban heat mitigation: A comparative study*. Remote Sens. Environ. *195*, DOI : 10.1016/j.rse.2017.03.043, 1–12 p.

Zinzi, M., and Carnielo, E. (2017). *Impact of urban temperatures on energy performance and thermal comfort in residential buildings. The case of Rome, Italy*. Energy Build. *157*, DOI : 10.1016/j.enbuild.2017.05.021, 20–29 p.

Zogou, O., and Stamatelos, A. (2007). *Optimization of thermal performance of a building with ground source heat pump system*. Energy Convers. Manag. *48*, DOI : 10.1016/j.enconman.2007.07.012, 2853–2863 p.

Zoras, S., Veranoudis, S., and Dimoudi, A. (2017). *Micro-climate adaptation of whole building energy simulation in large complexes*. Energy Build. *150*, DOI : 10.1016/j.enbuild.2017.05.060, 81–89 p.

Zurmuhl, D.P., Lukawski, M.Z., Aguirre, G.A., Law, W.R., Schnaars, G.P., Beckers, K.F., Anderson, C.L., and Tester, J.W. (2019). *Hybrid geothermal heat pumps for cooling telecommunications data centers*. Energy Build. *188–189*, DOI : 10.1016/j.enbuild.2019.01.042, 120–128 p.

Annex A. National and regional electricity production mix in China

Table Annex-1 Power generation in the ES, LC and ELC scenarios, unit: 10^9 kWh (ERINDRC, 2009)

Year	Coal	Natural gas	Oil	Hydro	Nuclear	Wind	Solar	Total
2020-ES	4040	315	4	1088	525	200	39	6211
2020-LC	2998	315	3	1190	700	353	94	5653
2020-ELC	2662	315	3	1207	770	423	99	5479
2035-ES	5091	630	0	1326	1050	376	262	8735
2035-LC	3493	630	0	1394	1470	470	351	7808
2035-ELC	2763	630	0	1394	1750	705	462	7704
2050-ES	4700	945	0	1320	2100	805	795	10665
2050-LC	3075	945	0	1485	2450	874	1028	9857
2050-ELC	1625	945	0	1551	2940	1035	1174	9270

Table Annex-2 Power generation in Hubei, unit: 10^8 kWh

Scenario	Year	Coal	Natural gas	Oil	Biomass	Biogas	Else	Thermal	Hydro	Nuclear	Wind	Solar	Total
2019	2019	1342.5	69.0	0.5	30.2	2.7	40.4	1485.3	563.2	0	73.8	56.8	2179.1
ES-2020	2020	1233.3	96.2	1.2	0	0	0	1330.7	470.6	0	36.4	9.9	1847.6
ES-2025	2025	1383.9	132.4	0.8	0	0	0	1517.1	505.0	0	47.1	28.7	2097.9
ES-2030	2030	1533.3	169.8	0.4	0	0	0	1703.5	539.3	0	57.7	47.6	2348.1
ES-2035	2035	1681.8	208.1	0	0	0	0	1889.9	573.6	0	68.4	66.4	2598.4
ES-2040	2040	1751.6	259.5	0	0	0	0	2011.1	572.7	0	94.4	111.5	2789.8
ES-2045	2045	1816.4	315.9	0	0	0	0	2132.3	571.9	0	120.5	156.6	2981.1
ES-2050	2050	1876.2	377.2	0	0	0	0	2253.4	571.0	0	146.5	201.6	3172.5
LC-2020	2020	963.6	114.0	1.1	0	0	0	1078.8	514.8	0	64.2	23.8	1681.6
LC-2025	2025	1067.1	166.3	0.8	0	0	0	1234.2	544.2	0	71.3	45.6	1895.3
LC-2030	2030	1165.1	224.1	0.4	0	0	0	1389.7	573.6	0	78.4	67.3	2109.0
LC-2035	2035	1258.2	286.9	0	0	0	0	1545.1	603.0	0	85.5	89.0	2322.6
LC-2040	2040	1263.7	389.7	0	0	0	0	1653.4	616.1	0	110	146.3	2525.8
LC-2045	2045	1241.4	520.3	0	0	0	0	1761.7	629.2	0	134.5	203.5	2729.0
LC-2050	2050	1182.4	687.6	0	0	0	0	1870	642.4	0	159.1	260.7	2932.2
ELC-2020	2020	898.3	106.3	1.0	0	0	0	1005.6	522.1	0	77.0	25.1	1629.8
ELC-2025	2025	995.6	155.1	0.7	0	0	0	1151.5	549.1	0	94.1	55.8	1850.5
ELC-2030	2030	1087.7	209.2	0.4	0	0	0	1297.4	576.0	0	111.2	86.5	2071.1
ELC-2035	2035	1175.3	268.0	0	0	0	0	1443.2	603.0	0	128.3	117.2	2291.7
ELC-2040	2040	1143.2	352.5	0	0	0	0	1495.7	625.6	0	148.3	177.4	2447.0
ELC-2045	2045	1090.9	457.2	0	0	0	0	1548.1	648.3	0	168.3	237.6	2602.3
ELC-2050	2050	1012.0	588.5	0	0	0	0	1600.5	670.9	0	188.4	297.7	2757.6
HRE-2020	2020	1517.9	158.7	0.6	36.8	35.9	0	1749.8	528.2	0	137.0	57.8	2472.9
HRE-2025	2025	1550.9	178.1	0.6	57.3	37.6	0	1824.5	700.8	0	275.3	182.1	2982.7
HRE-2030	2030	1573.9	194.1	0.7	92.7	40.7	0	1902.1	776.0	0	472.2	379.4	3529.8
HRE-2035	2035	1322.2	224.1	0.8	174.2	47.8	0	1769.1	774.3	0	710.5	620.1	3874.0
HRE-2040	2040	990.1	257.1	1.0	313.5	54.5	0	1616.2	800.7	0	862.8	862.3	4142.0
HRE-2045	2045	753.5	253.7	1.1	475.9	68.4	0	1552.6	871.2	0	933.6	1068.8	4426.1
HRE-2050	2050	600.5	269.6	1.2	556.0	80.4	0	1507.6	946.0	0	973.6	1093.1	4520.4

Table Annex-3 Power generation in Beijing, unit: 10^8 kWh

Scenario	Year	Coal	Natural gas	Oil	Biomass	Biogas	Else	Thermal	Hydro	Nuclear	Wind	Solar	Total
2019	2019	380.1	19.5	0.1	8.5	0.8	11.4	420.5	10.1	0	0	0.5	431.1
ES-2020	2020	330.9	25.8	0.3	0	0	0	357.0	8.4	0	0	0.1	365.6
ES-2025	2025	370.1	35.4	0.2	0	0	0	405.7	9.1	0	0	0.3	415.1
ES-2030	2030	409.1	45.3	0.1	0	0	0	454.5	9.7	0	0	0.5	464.6
ES-2035	2035	447.8	55.4	0	0	0	0	503.2	10.3	0	0	0.6	514.1
ES-2040	2040	470.9	69.8	0	0	0	0	540.6	10.3	0	0	1.1	552.0
ES-2045	2045	492.4	85.6	0	0	0	0	578.1	10.3	0	0	1.5	589.8
ES-2050	2050	512.5	103.0	0	0	0	0	615.5	10.2	0	0	1.9	627.7
LC-2020	2020	292.3	30.7	0.3	0	0	0	323.3	9.2	0	0	0.2	332.7
LC-2025	2025	321.9	42.7	0.2	0	0	0	364.8	9.8	0	0	0.4	375.0
LC-2030	2030	350.9	55.4	0.1	0	0	0	406.3	10.3	0	0	0.6	417.3
LC-2035	2035	379.4	68.4	0	0	0	0	447.9	10.8	0	0	0.9	459.6
LC-2040	2040	399.7	87.6	0	0	0	0	487.3	11.0	0	0	1.4	499.8
LC-2045	2045	417.6	109.1	0	0	0	0	526.7	11.3	0	0	2.0	540
LC-2050	2050	433.0	133.1	0	0	0	0	566.1	11.5	0	0	2.5	580.2
ELC-2020	2020	279.5	33.1	0.3	0	0	0	312.9	9.4	0	0	0.2	322.5
ELC-2025	2025	307.6	47.9	0.2	0	0	0	355.7	9.8	0	0	0.5	366.1
ELC-2030	2030	334.2	64.3	0.1	0	0	0	398.6	10.3	0	0	0.8	409.8
ELC-2035	2035	359.5	82.0	0	0	0	0	441.5	10.8	0	0	1.1	453.4
ELC-2040	2040	360.2	111.1	0	0	0	0	471.2	11.2	0	0	1.7	484.2
ELC-2045	2045	353.0	147.9	0	0	0	0	501.0	11.6	0	0	2.3	514.9
ELC-2050	2050	335.6	195.1	0	0	0	0	530.7	12.0	0	0	2.9	545.6
HRE-2020	2020	415.7	43.5	0.2	10.1	9.8	0	479.3	9.5	0	0	0.6	489.3
HRE-2025	2025	489.5	56.2	0.2	18.1	11.9	0	575.8	12.6	0	0	1.8	590.2
HRE-2030	2030	563.4	69.5	0.2	33.2	14.6	0	680.8	13.9	0	0	3.7	698.4
HRE-2035	2035	558.0	94.6	0.3	73.5	20.2	0	746.6	13.9	0	0	6.0	766.5
HRE-2040	2040	488.2	126.8	0.5	154.6	26.9	0	796.8	14.4	0	0	8.3	819.5
HRE-2045	2045	412.4	138.9	0.6	260.5	37.5	0	849.8	15.6	0	0	10.3	875.7
HRE-2050	2050	345.3	155.0	0.7	319.7	46.2	0	866.9	17.0	0	0	10.6	894.4

Table Annex-4 Power generation in Guangdong, unit: 10^8 kWh

Scenario	Year	Coal	Natural gas	Oil	Biomass	Biogas	Else	Thermal	Hydro	Nuclear	Wind	Solar	Total
2019	2019	2912.4	149.7	1.0	65.5	5.8	87.7	3222.2	307.8	977.7	72.0	31.0	4610.7
ES-2020	2020	1982.6	154.6	2.0	0	0	0	2139.2	257.2	1472.0	35.5	5.4	3909.3
ES-2025	2025	1950.8	186.6	1.2	0	0	0	2138.6	276.0	1962.7	45.9	15.7	4438.9
ES-2030	2030	1924.4	213.1	0.5	0	0	0	2138.0	294.7	2453.4	56.3	26.0	4968.4
ES-2035	2035	1902.1	235.4	0	0	0	0	2137.4	313.5	2944.0	66.7	36.3	5498.0
ES-2040	2040	1316.5	195.1	0	0	0	0	1511.5	313.0	3925.4	92.1	60.9	5902.9
ES-2045	2045	754.4	131.2	0	0	0	0	885.6	312.6	4906.7	117.5	85.5	6307.9
ES-2050	2050	216.2	43.5	0	0	0	0	259.6	312.1	5888.1	142.9	110.1	6712.8
LC-2020	2020	1119.7	117.6	1.1	0	0	0	1238.4	281.3	1962.7	62.6	13.0	3558.1
LC-2025	2025	825.9	109.7	0.5	0	0	0	936.0	297.4	2682.3	69.6	24.9	4010.3
LC-2030	2030	547.2	86.3	0.2	0	0	0	633.7	313.5	3402.0	76.5	36.8	4462.4
LC-2035	2035	280.6	50.6	0	0	0	0	331.3	329.6	4121.6	83.4	48.6	4914.5
LC-2040	2040	0	0	0	0	0	0	0	321.1	4842.3	103.4	77.6	5344.4
LC-2045	2045	0	0	0	0	0	0	0	297.9	5260	116.4	100	5774.3
LC-2050	2050	0	0	0	0	0	0	0	283.3	5672.6	128.6	119.6	6204.2
ELC-2020	2020	817.8	96.8	0.9	0	0	0	915.5	285.4	2159.0	75.1	13.7	3448.6
ELC-2025	2025	361.6	56.3	0.3	0	0	0	418.2	300.1	3074.9	91.8	30.5	3915.4
ELC-2030	2030	0	0	0	0	0	0	0	308.1	3921.3	106.4	46.5	4382.2
ELC-2035	2035	0	0	0	0	0	0	0	289.1	4391.0	111.1	57.9	4849.1
ELC-2040	2040	0	0	0	0	0	0	0	257.0	4728.8	112.0	79.9	5177.6
ELC-2045	2045	0	0	0	0	0	0	0	241.5	5055.0	115.0	94.7	5506.2
ELC-2050	2050	0	0	0	0	0	0	0	229.8	5377.5	118.5	108.9	5834.7
HRE-2020	2020	3284.2	343.3	1.3	79.6	77.6	0	3785.9	288.7	992.6	133.6	31.6	5232.4
HRE-2025	2025	3656.1	419.8	1.5	135.2	88.6	0	4301.3	383.0	1258.9	268.5	99.5	6311.2
HRE-2030	2030	4202.4	518.2	1.8	247.6	108.6	0	5078.6	424.1	1298.2	460.5	207.2	7468.7
HRE-2035	2035	4024.7	682.1	2.5	530.4	145.5	0	5385.2	423.2	1357.1	692.8	338.7	8197.0
HRE-2040	2040	3362.6	873.1	3.3	1064.8	185.0	0	5488.8	437.6	1525.3	841.4	471.0	8764.1
HRE-2045	2045	2814.5	947.6	4.1	1777.6	255.7	0	5799.5	476.2	1595.4	910.4	583.7	9365.2
HRE-2050	2050	2263.0	1015.9	4.4	2095.1	303.0	0	5681.5	517.1	1819.7	949.5	597.0	9564.7

Table Annex-5 Power generation in Inner Mongolia, unit: 10^8 kWh

Scenario	Year	Coal	Natural gas	Oil	Biomass	Biogas	Else	Thermal	Hydro	Nuclear	Wind	Solar	Total
2019	2019	4124.3	212.0	1.4	92.8	8.3	124.2	4563	58	0	666	160	5447
ES-2020	2020	3905.4	304.5	3.9	0	0	0	4213.7	48.5	0	328.3	27.9	4618.4
ES-2025	2025	4274.8	408.9	2.6	0	0	0	4686.4	52.0	0	424.6	81.0	5244.0
ES-2030	2030	4643.4	514.2	1.3	0	0	0	5159.0	55.5	0	520.9	134.2	5869.6
ES-2035	2035	5011.5	620.2	0	0	0	0	5631.6	59.1	0	617.2	187.3	6495.2
ES-2040	2040	5006.5	741.8	0	0	0	0	5748.3	59.0	0	852.0	314.3	6973.6
ES-2045	2045	4996.2	868.8	0	0	0	0	5865.0	58.9	0	1086.7	441.3	7452.0
ES-2050	2050	4980.3	1001.4	0	0	0	0	5981.7	58.8	0	1321.5	568.4	7930.4
LC-2020	2020	3167.8	332.8	3.2	0	0	0	3503.8	53.0	0	579.5	67.2	4203.5
LC-2025	2025	3449.4	458.0	2.2	0	0	0	3909.6	56.0	0	643.5	128.4	4737.6
LC-2030	2030	3726.5	587.9	1.1	0	0	0	4315.5	59.1	0	707.5	189.7	5271.8
LC-2035	2035	3999.9	721.4	0	0	0	0	4721.3	62.1	0	771.6	250.9	5805.9
LC-2040	2040	3974.4	871.0	0	0	0	0	4845.4	63.5	0	992.6	412.3	6313.8
LC-2045	2045	3939.9	1029.6	0	0	0	0	4969.6	64.8	0	1213.7	573.6	6821.7
LC-2050	2050	3896.3	1197.4	0	0	0	0	5093.7	66.2	0	1434.8	734.9	7329.5
ELC-2020	2020	2907.8	344.1	3.3	0	0	0	3255.2	53.8	0	694.4	70.8	4074.1
ELC-2025	2025	3080.8	480	2.3	0	0	0	3563.1	56.5	0	848.7	157.3	4625.6
ELC-2030	2030	3245.5	624.3	1.2	0	0	0	3871.0	59.3	0	1003.0	243.8	5177.1
ELC-2035	2035	3402.9	775.9	0	0	0	0	4178.9	62.1	0	1157.3	330.3	5728.6
ELC-2040	2040	3221.2	993.2	0	0	0	0	4214.4	64.4	0	1337.9	500	6116.7
ELC-2045	2045	2994.9	1255.1	0	0	0	0	4250	66.8	0	1518.5	669.6	6504.9
ELC-2050	2050	2709.7	1575.8	0	0	0	0	4285.6	69.1	0	1699.1	839.3	6893.1
HRE-2020	2020	4101.3	428.7	1.6	99.4	96.9	0	4727.9	54.4	0	1236.1	163.0	6181.4
HRE-2025	2025	3728.7	428.2	1.5	137.9	90.4	0	4386.7	72.2	0	2483.8	513.3	7455.9
HRE-2030	2030	2825.0	348.3	1.2	166.4	73.0	0	3414.0	79.9	0	4260	1069.5	8823.4
HRE-2035	2035	1081.6	183.3	0.7	142.5	39.1	0	1447.2	79.7	0	6408.8	1748.0	9683.7
HRE-2040	2040	35.3	9.2	0	11.2	1.9	0	57.6	82.5	0	7782.9	2430.7	10353.7
HRE-2045	2045	0	0	0	0	0	0	0	86.0	0	8073.7	2904.1	11063.8
HRE-2050	2050	0	0	0	0	0	0	0	92.3	0	8299.7	2907.6	11299.6

Table Annex-6 Power generation in Yunnan, unit: 10^8 kWh

Year	Scenario	Coal	Natural gas	Oil	Biomass	Biogas	Else	Thermal	Hydro	Nuclear	Wind	Solar	Total
2019	2019	287.4	14.8	0.1	6.5	0.6	8.7	318.01	2853.31	0	243.49	47.34	3462.15
2020	ES-2020	391.8	30.5	0.4	0	0	0	422.7	2384.5	0	120	8.2	2935.5
2025	ES-2025	543.2	52.0	0.3	0	0	0	595.5	2558.4	0	155.2	24.0	3333.1
2030	ES-2030	691.6	76.6	0.2	0	0	0	768.4	2732.3	0	190.5	39.7	3730.8
2035	ES-2035	837.6	103.6	0	0	0	0	941.2	2906.1	0	225.7	55.4	4128.4
2040	ES-2040	980.9	145.3	0	0	0	0	1126.2	2901.7	0	311.5	93.0	4432.5
2045	ES-2045	1117.0	194.3	0	0	0	0	1311.3	2897.4	0	397.3	130.6	4736.5
2050	ES-2050	1245.8	250.5	0	0	0	0	1496.3	2893.0	0	483.1	168.2	5040.6
2020	LC-2020	0	0	0	0	0	0	0	2455.6	0	198.8	17.4	2671.8
2025	LC-2025	0	0	0	0	0	0	0	2739.6	0	233.8	37.9	3011.3
2030	LC-2030	112.1	17.7	0	0	0	0	129.9	2906.1	0	258.7	56.1	3350.8
2035	LC-2035	236.2	42.6	0	0	0	0	278.8	3055.2	0	282.1	74.2	3690.3
2040	LC-2040	333.5	73.1	0	0	0	0	406.6	3121.6	0	362.9	122.0	4013.1
2045	LC-2045	423.6	110.7	0	0	0	0	534.3	3188.1	0	443.7	169.7	4335.9
2050	LC-2050	506.5	155.6	0	0	0	0	662.1	3254.6	0	524.6	217.5	4658.7
2020	ELC-2020	0	0	0	0	0	0	0	2345.3	0	228.3	16.0	2589.5
2025	ELC-2025	0	0	0	0	0	0	0	2602.0	0	292.8	45.3	2940.1
2030	ELC-2030	0	0	0	0	0	0	0	2859.4	0	360.1	71.1	3290.6
2035	ELC-2035	53.0	12.1	0	0	0	0	65.1	3055.2	0	423.1	97.7	3641.1
2040	ELC-2040	61.8	19.1	0	0	0	0	80.9	3169.9	0	489.1	147.9	3887.8
2045	ELC-2045	68.2	28.6	0	0	0	0	96.7	3284.6	0	555.2	198.1	4134.6
2050	ELC-2050	71.1	41.4	0	0	0	0	112.5	3399.3	0	621.2	248.3	4381.3
2020	HRE-2020	653.0	68.3	0.3	15.8	15.4	0	752.8	2676.0	0	451.9	48.2	3929.0
2025	HRE-2025	109.3	12.6	0	4.0	2.7	0	128.6	3550.5	0	908.1	151.9	4739.1
2030	HRE-2030	0	0	0	0	0	0	0	3779.7	0	1518.5	309.9	5608.2
2035	HRE-2035	0	0	0	0	0	0	0	3499.6	0	2173.0	482.5	6155.0
2040	HRE-2040	0	0	0	0	0	0	0	3465.2	0	2478.1	637.6	6580.9
2045	HRE-2045	0	0	0	0	0	0	0	3702.1	0	2569.8	760.4	7032.2
2050	HRE-2050	0	0	0	0	0	0	0	3880.5	0	2577.4	724.2	7182.1

Annex B. Environmental impacts of 1 kWh electricity

Table Annex-7 Environmental impacts of 1 kWh electricity with national average mix

Scenario	GWP	AP	CED	Water	Waste	EP	POP	Rad.W	Land	ADP	Biodiv	Hum
	kg CO2 eq.	kg SO2 eq.	MJ	L	kg	kg PO4 eq.	kg ethylene eq.	m³	m².year	kg antimony eq.	PDF.m². year	DALYs
2019	0.990	7.086E-03	10.423	3.007	1.057	4.687E-04	2.581E-03	3.467E-09	0.036	6.398E-06	0.349	2.329E-06
ES-2020	1.002	7.269E-03	11.033	3.235	1.100	4.784E-04	2.658E-03	5.826E-09	0.015	5.726E-06	0.349	2.364E-06
ES-2025	0.968	6.981E-03	11.020	3.193	1.055	4.635E-04	2.556E-03	6.763E-09	0.015	6.123E-06	0.337	2.286E-06
ES-2030	0.941	6.754E-03	11.010	3.159	1.020	4.517E-04	2.476E-03	7.501E-09	0.015	6.436E-06	0.327	2.225E-06
ES-2035	0.919	6.571E-03	11.002	3.132	0.991	4.422E-04	2.412E-03	8.096E-09	0.014	6.688E-06	0.319	2.175E-06
ES-2040	0.846	6.013E-03	10.905	3.027	0.904	4.132E-04	2.210E-03	9.964E-09	0.014	7.419E-06	0.294	2.019E-06
ES-2045	0.782	5.526E-03	10.820	2.935	0.828	3.880E-04	2.035E-03	1.159E-08	0.013	8.057E-06	0.272	1.882E-06
ES-2050	0.726	5.099E-03	10.746	2.854	0.762	3.658E-04	1.881E-03	1.303E-08	0.012	8.617E-06	0.253	1.763E-06
LC-2020	0.831	5.997E-03	10.458	2.883	0.905	4.086E-04	2.195E-03	8.323E-09	0.013	6.392E-06	0.290	1.996E-06
LC-2025	0.789	5.647E-03	10.523	2.856	0.850	3.899E-04	2.071E-03	1.001E-08	0.013	6.873E-06	0.275	1.900E-06
LC-2030	0.756	5.367E-03	10.574	2.835	0.806	3.749E-04	1.973E-03	1.135E-08	0.012	7.255E-06	0.263	1.823E-06
LC-2035	0.728	5.139E-03	10.616	2.818	0.771	3.628E-04	1.892E-03	1.244E-08	0.012	7.568E-06	0.253	1.760E-06
LC-2040	0.658	4.601E-03	10.477	2.702	0.687	3.356E-04	1.698E-03	1.395E-08	0.011	8.442E-06	0.229	1.610E-06
LC-2045	0.598	4.142E-03	10.358	2.603	0.615	3.125E-04	1.533E-03	1.523E-08	0.011	9.187E-06	0.209	1.482E-06
LC-2050	0.546	3.748E-03	10.256	2.518	0.553	2.926E-04	1.390E-03	1.633E-08	0.010	9.828E-06	0.191	1.372E-06
ELC-2020	0.768	5.526E-03	10.266	2.759	0.833	3.827E-04	2.024E-03	9.387E-09	0.012	6.602E-06	0.269	1.860E-06
ELC-2025	0.699	4.981E-03	10.273	2.688	0.748	3.542E-04	1.829E-03	1.168E-08	0.012	7.344E-06	0.245	1.709E-06
ELC-2030	0.645	4.553E-03	10.279	2.633	0.682	3.317E-04	1.676E-03	1.348E-08	0.011	7.928E-06	0.226	1.590E-06
ELC-2035	0.601	4.206E-03	10.283	2.589	0.628	3.136E-04	1.552E-03	1.493E-08	0.011	8.400E-06	0.210	1.494E-06
ELC-2040	0.508	3.493E-03	10.123	2.442	0.517	2.763E-04	1.295E-03	1.710E-08	0.010	9.366E-06	0.178	1.292E-06
ELC-2045	0.426	2.865E-03	9.981	2.314	0.419	2.435E-04	1.068E-03	1.902E-08	0.009	1.022E-05	0.150	1.115E-06
ELC-2050	0.353	2.308E-03	9.856	2.199	0.332	2.143E-04	8.670E-04	2.072E-08	0.008	1.097E-05	0.125	9.573E-07

HRE-2020	0.943	7.416E-03	10.468	2.943	1.023	4.588E-04	2.507E-03	3.157E-09	0.036	6.508E-06	0.344	2.263E-06
HRE-2025	0.774	6.124E-03	9.572	2.484	0.839	4.007E-04	2.072E-03	3.312E-09	0.040	8.187E-06	0.289	1.928E-06
HRE-2030	0.626	5.026E-03	8.740	2.065	0.680	3.545E-04	1.699E-03	2.974E-09	0.047	1.019E-05	0.242	1.647E-06
HRE-2035	0.434	3.636E-03	7.786	1.533	0.468	2.910E-04	1.210E-03	2.896E-09	0.061	1.252E-05	0.183	1.277E-06
HRE-2040	0.282	2.539E-03	7.139	1.125	0.300	2.408E-04	8.332E-04	3.059E-09	0.079	1.446E-05	0.139	9.871E-07
HRE-2045	0.206	2.064E-03	6.858	0.913	0.218	2.172E-04	6.584E-04	3.036E-09	0.098	1.566E-05	0.121	8.511E-07
HRE-2050	0.169	1.839E-03	6.744	0.823	0.177	2.030E-04	5.683E-04	3.322E-09	0.104	1.573E-05	0.111	7.789E-07

Table Annex-8 Environmental impacts of 1 kWh electricity with Hubei mix

Scenario	GWP	AP	CED	Water	Waste	EP	POP	Rad.W	Land	ADP	Biodiv	Hum
	kg CO2 eq.	kg SO2 eq.	MJ	L	kg	kg PO4 eq.	kg ethylene eq.	m³	m².year	kg antimony eq.	PDF.m². year	DALYs
2019	0.980	7.007E-03	9.871	2.819	1.046	4.608E-04	2.552E-03	3.943E-10	0.036	5.838E-06	0.345	2.293E-06
ES-2020	1.027	7.449E-03	10.331	3.033	1.128	4.862E-04	2.724E-03	3.996E-10	0.016	5.135E-06	0.357	2.408E-06
ES-2025	1.024	7.377E-03	10.357	3.031	1.115	4.832E-04	2.702E-03	3.966E-10	0.016	5.405E-06	0.355	2.393E-06
ES-2030	1.021	7.315E-03	10.377	3.028	1.105	4.805E-04	2.683E-03	3.936E-10	0.016	5.617E-06	0.354	2.381E-06
ES-2035	1.018	7.261E-03	10.393	3.026	1.095	4.781E-04	2.666E-03	3.908E-10	0.016	5.788E-06	0.352	2.370E-06
ES-2040	0.999	7.075E-03	10.346	2.984	1.065	4.695E-04	2.603E-03	4.022E-10	0.016	6.267E-06	0.345	2.324E-06
ES-2045	0.982	6.897E-03	10.304	2.945	1.035	4.609E-04	2.543E-03	4.121E-10	0.016	6.684E-06	0.338	2.280E-06
ES-2050	0.966	6.725E-03	10.266	2.908	1.007	4.524E-04	2.485E-03	4.207E-10	0.015	7.050E-06	0.332	2.237E-06
LC-2020	0.901	6.459E-03	9.659	2.683	0.974	4.305E-04	2.368E-03	3.835E-10	0.014	5.469E-06	0.313	2.121E-06
LC-2025	0.901	6.371E-03	9.737	2.694	0.958	4.261E-04	2.344E-03	3.840E-10	0.014	5.765E-06	0.311	2.105E-06
LC-2030	0.898	6.275E-03	9.797	2.697	0.941	4.211E-04	2.316E-03	3.828E-10	0.014	6.000E-06	0.309	2.085E-06
LC-2035	0.894	6.175E-03	9.844	2.696	0.924	4.156E-04	2.286E-03	3.806E-10	0.014	6.191E-06	0.306	2.064E-06
LC-2040	0.856	5.771E-03	9.754	2.608	0.857	3.942E-04	2.151E-03	3.937E-10	0.014	6.814E-06	0.291	1.960E-06
LC-2045	0.816	5.327E-03	9.669	2.515	0.783	3.696E-04	2.002E-03	4.043E-10	0.013	7.341E-06	0.274	1.845E-06
LC-2050	0.771	4.819E-03	9.586	2.412	0.699	3.408E-04	1.834E-03	4.127E-10	0.012	7.791E-06	0.255	1.713E-06
ELC-2020	0.868	6.225E-03	9.456	2.588	0.939	4.178E-04	2.281E-03	3.776E-10	0.014	5.550E-06	0.302	2.052E-06
ELC-2025	0.862	6.107E-03	9.504	2.585	0.918	4.128E-04	2.246E-03	3.823E-10	0.014	6.020E-06	0.298	2.029E-06
ELC-2030	0.856	5.989E-03	9.539	2.579	0.898	4.073E-04	2.209E-03	3.844E-10	0.014	6.388E-06	0.295	2.004E-06

ELC-2035	0.849	5.874E-03	9.566	2.570	0.878	4.017E-04	2.174E-03	3.850E-10	0.014	6.685E-06	0.291	1.978E-06
ELC-2040	0.802	5.422E-03	9.412	2.456	0.804	3.776E-04	2.019E-03	3.966E-10	0.013	7.345E-06	0.273	1.858E-06
ELC-2045	0.755	4.947E-03	9.273	2.342	0.727	3.517E-04	1.858E-03	4.064E-10	0.013	7.923E-06	0.255	1.733E-06
ELC-2050	0.706	4.430E-03	9.136	2.222	0.642	3.226E-04	1.683E-03	4.144E-10	0.012	8.432E-06	0.235	1.595E-06
HRE-2020	0.962	7.535E-03	10.137	2.854	1.042	4.619E-04	2.555E-03	4.135E-10	0.036	5.914E-06	0.350	2.288E-06
HRE-2025	0.825	6.492E-03	9.415	2.477	0.892	4.138E-04	2.203E-03	4.253E-10	0.042	7.244E-06	0.305	2.014E-06
HRE-2030	0.718	5.710E-03	8.905	2.187	0.776	3.806E-04	1.936E-03	4.566E-10	0.051	8.887E-06	0.273	1.814E-06
HRE-2035	0.573	4.722E-03	8.349	1.794	0.610	3.316E-04	1.576E-03	5.026E-10	0.077	1.077E-05	0.234	1.540E-06
HRE-2040	0.432	3.782E-03	7.968	1.408	0.446	2.820E-04	1.242E-03	5.537E-10	0.120	1.237E-05	0.201	1.279E-06
HRE-2045	0.333	3.242E-03	7.788	1.129	0.336	2.486E-04	1.029E-03	5.958E-10	0.166	1.339E-05	0.184	1.109E-06
HRE-2050	0.281	2.980E-03	7.683	0.981	0.275	2.274E-04	9.101E-04	6.042E-10	0.187	1.343E-05	0.175	1.012E-06

Table Annex-9 Environmental impacts of 1 kWh electricity with Beijing mix

Scenario	GWP	AP	CED	Water	Waste	EP	POP	Rad.W	Land	ADP	Biodiv	Hum
	kg CO2 eq.	kg SO2 eq.	MJ	L	kg	kg PO4 eq.	kg ethylene eq.	m³	m².year	kg antimony eq.	PDF.m². year	DALYs
2019	1.391	9.892E-03	12.268	3.959	1.477	6.209E-04	3.609E-03	4.706E-10	0.049	5.052E-06	0.485	3.163E-06
ES-2020	1.386	1.001E-02	12.506	4.066	1.515	6.330E-04	3.666E-03	4.875E-10	0.020	5.011E-06	0.479	3.182E-06
ES-2025	1.376	9.872E-03	12.502	4.044	1.493	6.247E-04	3.621E-03	4.718E-10	0.020	5.018E-06	0.474	3.147E-06
ES-2030	1.368	9.757E-03	12.497	4.026	1.474	6.179E-04	3.584E-03	4.588E-10	0.019	5.024E-06	0.470	3.118E-06
ES-2035	1.361	9.661E-03	12.494	4.010	1.458	6.120E-04	3.553E-03	4.478E-10	0.019	5.029E-06	0.467	3.093E-06
ES-2040	1.347	9.484E-03	12.486	3.980	1.429	6.011E-04	3.496E-03	4.475E-10	0.019	5.045E-06	0.461	3.047E-06
ES-2045	1.333	9.305E-03	12.478	3.950	1.399	5.900E-04	3.437E-03	4.471E-10	0.018	5.058E-06	0.454	3.000E-06
ES-2050	1.319	9.122E-03	12.469	3.918	1.369	5.787E-04	3.378E-03	4.466E-10	0.018	5.069E-06	0.447	2.952E-06
LC-2020	1.362	9.740E-03	12.446	4.006	1.471	6.165E-04	3.576E-03	4.841E-10	0.019	5.013E-06	0.469	3.109E-06
LC-2025	1.347	9.537E-03	12.440	3.973	1.438	6.042E-04	3.510E-03	4.690E-10	0.019	5.022E-06	0.462	3.057E-06
LC-2030	1.334	9.362E-03	12.434	3.945	1.409	5.935E-04	3.453E-03	4.559E-10	0.019	5.028E-06	0.455	3.012E-06
LC-2035	1.322	9.208E-03	12.428	3.920	1.384	5.841E-04	3.404E-03	4.444E-10	0.018	5.032E-06	0.450	2.972E-06
LC-2040	1.303	8.953E-03	12.413	3.875	1.341	5.683E-04	3.320E-03	4.438E-10	0.018	5.053E-06	0.441	2.905E-06
LC-2045	1.282	8.691E-03	12.397	3.829	1.298	5.521E-04	3.235E-03	4.430E-10	0.017	5.070E-06	0.431	2.837E-06

LC-2050	1.261	8.425E-03	12.380	3.782	1.254	5.356E-04	3.148E-03	4.421E-10	0.017	5.083E-06	0.421	2.767E-06
ELC-2020	1.352	9.624E-03	12.427	3.981	1.451	6.093E-04	3.537E-03	4.873E-10	0.019	5.011E-06	0.464	3.077E-06
ELC-2025	1.332	9.357E-03	12.418	3.938	1.408	5.930E-04	3.451E-03	4.713E-10	0.019	5.025E-06	0.455	3.009E-06
ELC-2030	1.313	9.111E-03	12.407	3.897	1.367	5.779E-04	3.371E-03	4.564E-10	0.018	5.034E-06	0.446	2.945E-06
ELC-2035	1.296	8.883E-03	12.396	3.859	1.330	5.640E-04	3.297E-03	4.427E-10	0.018	5.041E-06	0.438	2.886E-06
ELC-2040	1.258	8.397E-03	12.357	3.771	1.249	5.339E-04	3.138E-03	4.405E-10	0.017	5.057E-06	0.420	2.758E-06
ELC-2045	1.212	7.819E-03	12.311	3.667	1.154	4.980E-04	2.949E-03	4.376E-10	0.015	5.066E-06	0.399	2.606E-06
ELC-2050	1.156	7.119E-03	12.257	3.540	1.037	4.546E-04	2.720E-03	4.340E-10	0.014	5.068E-06	0.373	2.421E-06
HRE-2020	1.321	1.034E-02	12.381	3.879	1.424	6.019E-04	3.498E-03	4.816E-10	0.050	5.046E-06	0.477	3.052E-06
HRE-2025	1.297	1.015E-02	12.398	3.812	1.391	5.906E-04	3.439E-03	4.902E-10	0.064	5.104E-06	0.473	3.004E-06
HRE-2030	1.267	9.993E-03	12.469	3.729	1.354	5.788E-04	3.382E-03	5.066E-10	0.089	5.182E-06	0.471	2.956E-06
HRE-2035	1.172	9.538E-03	12.636	3.464	1.226	5.358E-04	3.172E-03	5.527E-10	0.160	5.284E-06	0.463	2.783E-06
HRE-2040	1.005	8.674E-03	13.010	2.996	1.009	4.642E-04	2.831E-03	6.381E-10	0.295	5.404E-06	0.451	2.497E-06
HRE-2045	0.832	8.064E-03	13.444	2.495	0.806	3.990E-04	2.527E-03	7.358E-10	0.455	5.522E-06	0.449	2.242E-06
HRE-2050	0.722	7.711E-03	13.631	2.182	0.667	3.531E-04	2.306E-03	7.889E-10	0.543	5.556E-06	0.444	2.058E-06

Table Annex-10 *Environmental impacts of 1 kWh electricity with Guangdong mix*

Scenario	GWP	AP	CED	Water	Waste	EP	POP	Rad.W	Land	ADP	Biodiv	Hum
	kg CO2 eq.	kg SO2 eq.	MJ	L	kg	kg PO4 eq.	kg ethylene eq.	m³	m².year	kg antimony eq.	PDF.m². year	DALYs
2019	1.002	7.161E-03	12.128	3.562	1.069	4.691E-04	2.609E-03	1.401E-08	0.036	6.380E-06	0.353	2.351E-06
ES-2020	0.784	5.712E-03	12.647	3.549	0.864	3.901E-04	2.086E-03	2.451E-08	0.012	7.029E-06	0.275	1.911E-06
ES-2025	0.687	4.987E-03	12.748	3.486	0.753	3.493E-04	1.823E-03	2.870E-08	0.010	7.442E-06	0.242	1.700E-06
ES-2030	0.611	4.427E-03	12.828	3.438	0.668	3.178E-04	1.619E-03	3.199E-08	0.009	7.767E-06	0.216	1.537E-06
ES-2035	0.551	3.983E-03	12.894	3.401	0.600	2.928E-04	1.457E-03	3.465E-08	0.009	8.030E-06	0.195	1.408E-06
ES-2040	0.365	2.660E-03	13.075	3.286	0.400	2.187E-04	9.705E-04	4.293E-08	0.006	8.838E-06	0.132	1.018E-06
ES-2045	0.206	1.543E-03	13.235	3.192	0.231	1.565E-04	5.586E-04	5.014E-08	0.004	9.543E-06	0.079	6.884E-07
ES-2050	0.065	5.916E-04	13.310	3.102	0.088	1.038E-04	2.037E-04	5.649E-08	0.002	1.016E-05	0.032	4.038E-07
LC-2020	0.499	3.643E-03	12.715	3.299	0.549	2.734E-04	1.329E-03	3.569E-08	0.008	8.048E-06	0.178	1.303E-06
LC-2025	0.336	2.471E-03	12.921	3.212	0.372	2.074E-04	8.993E-04	4.317E-08	0.006	8.734E-06	0.123	9.585E-07

LC-2030	0.209	1.571E-03	13.088	3.148	0.235	1.569E-04	5.680E-04	4.915E-08	0.004	9.282E-06	0.080	6.930E-07
LC-2035	0.107	8.613E-04	13.226	3.101	0.128	1.173E-04	3.058E-04	5.402E-08	0.003	9.731E-06	0.046	4.828E-07
LC-2040	0.017	2.443E-04	13.341	3.059	0.035	8.353E-05	7.676E-05	5.833E-08	0.002	1.024E-05	0.016	3.005E-07
LC-2045	0.018	2.465E-04	13.394	3.076	0.035	8.422E-05	7.761E-05	5.865E-08	0.002	1.036E-05	0.016	3.026E-07
LC-2050	0.018	2.480E-04	13.430	3.088	0.035	8.469E-05	7.820E-05	5.887E-08	0.002	1.044E-05	0.016	3.040E-07
ELC-2020	0.382	2.808E-03	12.763	3.205	0.423	2.264E-04	1.022E-03	4.044E-08	0.006	8.466E-06	0.138	1.057E-06
ELC-2025	0.162	1.244E-03	13.023	3.085	0.186	1.388E-04	4.467E-04	5.061E-08	0.003	9.423E-06	0.064	5.959E-07
ELC-2030	0.017	2.427E-04	13.225	3.021	0.035	8.313E-05	7.608E-05	5.761E-08	0.002	1.009E-05	0.016	2.993E-07
ELC-2035	0.017	2.433E-04	13.335	3.056	0.035	8.342E-05	7.638E-05	5.830E-08	0.002	1.018E-05	0.016	3.005E-07
ELC-2040	0.017	2.455E-04	13.416	3.083	0.035	8.406E-05	7.724E-05	5.880E-08	0.002	1.032E-05	0.016	3.024E-07
ELC-2045	0.018	2.466E-04	13.466	3.099	0.035	8.440E-05	7.768E-05	5.911E-08	0.002	1.040E-05	0.016	3.034E-07
ELC-2050	0.018	2.475E-04	13.503	3.111	0.035	8.467E-05	7.804E-05	5.934E-08	0.002	1.046E-05	0.016	3.043E-07
HRE-2020	0.981	7.706E-03	12.166	3.517	1.062	4.679E-04	2.606E-03	1.258E-08	0.037	6.306E-06	0.357	2.336E-06
HRE-2025	0.912	7.182E-03	11.962	3.357	0.985	4.419E-04	2.431E-03	1.321E-08	0.046	6.747E-06	0.336	2.198E-06
HRE-2030	0.892	7.072E-03	11.764	3.222	0.959	4.365E-04	2.392E-03	1.159E-08	0.063	7.094E-06	0.335	2.171E-06
HRE-2035	0.800	6.553E-03	11.623	2.942	0.843	4.000E-04	2.179E-03	1.110E-08	0.109	7.610E-06	0.320	2.003E-06
HRE-2040	0.658	5.725E-03	11.709	2.574	0.669	3.429E-04	1.868E-03	1.170E-08	0.192	8.124E-06	0.299	1.750E-06
HRE-2045	0.543	5.291E-03	11.905	2.230	0.534	3.003E-04	1.660E-03	1.153E-08	0.293	8.411E-06	0.296	1.577E-06
HRE-2050	0.455	4.877E-03	11.987	2.042	0.429	2.643E-04	1.463E-03	1.282E-08	0.335	8.544E-06	0.282	1.415E-06

Table Annex-11   *Environmental impacts of 1 kWh electricity with Inner Mongolia mix*

Scenario	GWP	AP	CED	Water	Waste	EP	POP	Rad.W	Land	ADP	Biodiv	Hum
	kg CO2 eq.	kg SO2 eq.	MJ	L	kg	kg PO4 eq.	kg ethylene eq.	m³	m².year	kg antimony eq.	PDF.m². year	DALYs
2019	1.201	8.578E-03	11.202	3.452	1.280	5.598E-04	3.127E-03	4.778E-10	0.043	6.620E-06	0.422	2.798E-06
ES-2020	1.298	9.387E-03	11.990	3.821	1.421	6.038E-04	3.437E-03	4.873E-10	0.019	5.614E-06	0.450	3.012E-06
ES-2025	1.262	9.075E-03	11.833	3.728	1.372	5.875E-04	3.327E-03	4.760E-10	0.018	5.949E-06	0.437	2.928E-06
ES-2030	1.234	8.827E-03	11.709	3.655	1.333	5.746E-04	3.241E-03	4.669E-10	0.018	6.212E-06	0.427	2.861E-06
ES-2035	1.211	8.627E-03	11.609	3.596	1.302	5.641E-04	3.171E-03	4.595E-10	0.018	6.425E-06	0.418	2.807E-06
ES-2040	1.142	8.078E-03	11.262	3.411	1.216	5.363E-04	2.974E-03	4.654E-10	0.017	7.066E-06	0.394	2.656E-06

Scenario	GWP	AP	CED	Water	Waste	EP	POP	Rad.W	Land	ADP	Biodiv	Hum
ES-2045	1.081	7.593E-03	10.959	3.249	1.140	5.115E-04	2.801E-03	4.706E-10	0.017	7.625E-06	0.373	2.523E-06
ES-2050	1.027	7.159E-03	10.692	3.104	1.072	4.893E-04	2.646E-03	4.750E-10	0.016	8.115E-06	0.354	2.404E-06
LC-2020	1.174	8.433E-03	11.339	3.485	1.273	5.547E-04	3.093E-03	4.823E-10	0.017	6.300E-06	0.407	2.748E-06
LC-2025	1.149	8.177E-03	11.265	3.425	1.232	5.407E-04	3.006E-03	4.746E-10	0.017	6.614E-06	0.397	2.680E-06
LC-2030	1.129	7.963E-03	11.205	3.375	1.198	5.289E-04	2.934E-03	4.678E-10	0.017	6.864E-06	0.389	2.624E-06
LC-2035	1.112	7.783E-03	11.155	3.334	1.168	5.190E-04	2.873E-03	4.618E-10	0.017	7.067E-06	0.382	2.576E-06
LC-2040	1.036	7.177E-03	10.785	3.134	1.073	4.882E-04	2.657E-03	4.708E-10	0.016	7.865E-06	0.356	2.410E-06
LC-2045	0.971	6.649E-03	10.469	2.961	0.990	4.613E-04	2.470E-03	4.784E-10	0.015	8.543E-06	0.333	2.265E-06
LC-2050	0.914	6.182E-03	10.196	2.810	0.916	4.373E-04	2.304E-03	4.848E-10	0.015	9.127E-06	0.312	2.137E-06
ELC-2020	1.120	8.019E-03	11.052	3.337	1.210	5.333E-04	2.943E-03	4.822E-10	0.016	6.533E-06	0.389	2.634E-06
ELC-2025	1.065	7.533E-03	10.813	3.194	1.133	5.079E-04	2.774E-03	4.755E-10	0.016	7.099E-06	0.368	2.503E-06
ELC-2030	1.020	7.135E-03	10.623	3.079	1.070	4.869E-04	2.635E-03	4.693E-10	0.015	7.544E-06	0.352	2.395E-06
ELC-2035	0.983	6.800E-03	10.469	2.983	1.017	4.691E-04	2.519E-03	4.634E-10	0.015	7.903E-06	0.338	2.305E-06
ELC-2040	0.905	6.120E-03	10.134	2.781	0.908	4.331E-04	2.280E-03	4.731E-10	0.014	8.711E-06	0.309	2.120E-06
ELC-2045	0.831	5.453E-03	9.834	2.591	0.802	3.972E-04	2.048E-03	4.812E-10	0.013	9.419E-06	0.282	1.939E-06
ELC-2050	0.758	4.776E-03	9.560	2.407	0.693	3.600E-04	1.815E-03	4.879E-10	0.012	1.005E-05	0.254	1.755E-06
HRE-2020	1.041	8.189E-03	10.684	3.102	1.130	5.088E-04	2.769E-03	4.775E-10	0.040	6.993E-06	0.380	2.506E-06
HRE-2025	0.799	6.342E-03	9.329	2.436	0.871	4.274E-04	2.146E-03	4.894E-10	0.041	9.051E-06	0.300	2.032E-06
HRE-2030	0.530	4.305E-03	7.774	1.694	0.586	3.387E-04	1.455E-03	5.041E-10	0.039	1.150E-05	0.209	1.509E-06
HRE-2035	0.218	1.943E-03	5.912	0.834	0.256	2.358E-04	6.465E-04	5.163E-10	0.030	1.433E-05	0.103	8.978E-07
HRE-2040	0.053	6.243E-04	4.758	0.381	0.085	1.848E-04	2.081E-04	5.243E-10	0.009	1.648E-05	0.041	5.696E-07
HRE-2045	0.049	5.901E-04	4.730	0.374	0.080	1.853E-04	1.978E-04	5.393E-10	0.008	1.717E-05	0.040	5.617E-07
HRE-2050	0.048	5.877E-04	4.726	0.372	0.080	1.848E-04	1.968E-04	5.362E-10	0.008	1.705E-05	0.039	5.609E-07

Table Annex-12   *Environmental impacts of 1 kWh electricity with Yunnan mix*

Scenario	GWP	AP	CED	Water	Waste	EP	POP	Rad.W	Land	ADP	Biodiv	Hum
	kg CO2 eq.	kg SO2 eq.	MJ	L	kg	kg PO4 eq.	kg ethylene eq.	m³	m².year	kg antimony eq.	PDF.m ².year	DALYs
2019	0.148	1.163E-03	4.977	0.491	0.175	1.249E-04	4.090E-04	1.796E-10	0.008	5.328E-06	0.059	5.078E-07
ES-2020	0.219	1.680E-03	5.418	0.701	0.256	1.514E-04	6.007E-04	1.838E-10	0.006	4.837E-06	0.083	6.537E-07

Evaluation of environmental impacts of buildings in China
Évaluation des impacts environnementaux des bâtiments en Chine

ES-2025	0.266	2.005E-03	5.719	0.840	0.304	1.715E-04	7.214E-04	1.993E-10	0.007	5.028E-06	0.098	7.566E-07
ES-2030	0.303	2.252E-03	5.955	0.948	0.341	1.867E-04	8.136E-04	2.106E-10	0.007	5.178E-06	0.111	8.353E-07
ES-2035	0.332	2.446E-03	6.144	1.034	0.370	1.986E-04	8.862E-04	2.190E-10	0.008	5.299E-06	0.120	8.974E-07
ES-2040	0.365	2.659E-03	6.377	1.136	0.401	2.133E-04	9.669E-04	2.383E-10	0.008	5.646E-06	0.131	9.706E-07
ES-2045	0.392	2.830E-03	6.578	1.223	0.426	2.251E-04	1.032E-03	2.550E-10	0.008	5.948E-06	0.140	1.030E-06
ES-2050	0.415	2.965E-03	6.754	1.296	0.445	2.346E-04	1.085E-03	2.696E-10	0.009	6.213E-06	0.148	1.079E-06
LC-2020	0.018	2.482E-04	4.206	0.126	0.039	7.147E-05	7.373E-05	1.412E-10	0.004	5.079E-06	0.015	2.268E-07
LC-2025	0.019	2.533E-04	4.214	0.130	0.040	7.291E-05	7.562E-05	1.473E-10	0.004	5.285E-06	0.015	2.306E-07
LC-2030	0.072	6.197E-04	4.547	0.284	0.095	9.473E-05	2.115E-04	1.643E-10	0.005	5.433E-06	0.033	3.443E-07
LC-2035	0.121	9.546E-04	4.861	0.428	0.145	1.146E-04	3.362E-04	1.789E-10	0.005	5.552E-06	0.049	4.486E-07
LC-2040	0.154	1.176E-03	5.094	0.532	0.177	1.299E-04	4.195E-04	2.000E-10	0.006	5.971E-06	0.061	5.240E-07
LC-2045	0.181	1.347E-03	5.291	0.617	0.202	1.420E-04	4.851E-04	2.179E-10	0.006	6.327E-06	0.070	5.839E-07
LC-2050	0.203	1.480E-03	5.459	0.688	0.220	1.515E-04	5.365E-04	2.332E-10	0.007	6.633E-06	0.077	6.314E-07
ELC-2020	0.019	2.513E-04	4.211	0.128	0.040	7.281E-05	7.482E-05	1.446E-10	0.004	5.159E-06	0.015	2.312E-07
ELC-2025	0.019	2.607E-04	4.225	0.135	0.041	7.567E-05	7.825E-05	1.557E-10	0.004	5.516E-06	0.015	2.393E-07
ELC-2030	0.020	2.675E-04	4.235	0.140	0.042	7.781E-05	8.074E-05	1.637E-10	0.004	5.769E-06	0.016	2.453E-07
ELC-2035	0.044	4.318E-04	4.395	0.213	0.066	8.866E-05	1.421E-04	1.760E-10	0.005	5.983E-06	0.024	2.993E-07
ELC-2040	0.048	4.578E-04	4.435	0.229	0.069	9.255E-05	1.522E-04	1.892E-10	0.005	6.389E-06	0.026	3.129E-07
ELC-2045	0.051	4.747E-04	4.469	0.243	0.071	9.560E-05	1.591E-04	2.008E-10	0.005	6.745E-06	0.027	3.234E-07
ELC-2050	0.053	4.821E-04	4.499	0.254	0.071	9.784E-05	1.629E-04	2.110E-10	0.005	7.062E-06	0.028	3.306E-07
HRE-2020	0.275	2.240E-03	5.833	0.874	0.313	1.821E-04	7.500E-04	2.287E-10	0.013	5.643E-06	0.106	8.011E-07
HRE-2025	0.058	5.712E-04	4.506	0.263	0.083	1.028E-04	1.844E-04	2.053E-10	0.006	6.644E-06	0.031	3.556E-07
HRE-2030	0.025	3.309E-04	4.332	0.186	0.050	1.005E-04	1.035E-04	2.364E-10	0.005	7.854E-06	0.021	3.145E-07
HRE-2035	0.028	3.674E-04	4.388	0.213	0.055	1.131E-04	1.167E-04	2.786E-10	0.005	9.098E-06	0.023	3.525E-07
HRE-2040	0.030	3.863E-04	4.417	0.226	0.057	1.189E-04	1.236E-04	3.010E-10	0.005	9.815E-06	0.025	3.687E-07
HRE-2045	0.031	3.915E-04	4.425	0.230	0.057	1.198E-04	1.256E-04	3.076E-10	0.006	1.008E-05	0.025	3.701E-07
HRE-2050	0.030	3.847E-04	4.415	0.225	0.056	1.178E-04	1.231E-04	2.996E-10	0.005	9.819E-06	0.025	3.646E-07

Annex C. Environmental impacts of materials contextualised with Hubei energy mix in 2019

Material	Unit	GWP	AP	CED	Water	Waste	EP	POP	Rad.W	Land	ADP	Biodiv	Hum
		kg CO2 eq.	kg SO2 eq.	MJ	L	kg	kg PO4 eq.	kg ethylene eq.	m³	m².year	kg antimony eq.	PDF.m².year	DALYs
Cement mortar	kg	0.219227	0.001001	1.498085	1.876463	0.068442	8.86E-05	0.000471	1.79E-09	0.018116	2.27E-06	0.070195	3.47E-07
Ceramic tile	kg	0.742436	0.007385	9.466628	6.513339	0.691653	0.000699	0.002188	4.22E-09	0.068619	0.00162	0.337887	8.59E-06
Concrete	kg	0.088433	0.000295	0.456328	1.512305	0.015396	3.26E-05	0.000168	8.20E-10	0.001167	1.47E-06	0.024568	1.26E-07
Expanded perlite	kg	0.33821	0.002945	5.920563	1.167593	0.183536	0.000253	0.001443	3.86E-09	0.025052	5.00E-05	0.143537	8.72E-07
Mortar	kg	0.528037	0.003131	3.785057	1.658717	0.205168	0.000286	0.001104	3.61E-09	0.030872	6.22E-06	0.181605	9.65E-07
Double glazing window with aluminum frame	m²	220.1343	1.906079	2561.294	969.3595	156.5912	0.20201	0.606756	1.53E-06	6.093225	0.008218	90.21116	0.000903
External door wood-aluminium	m²	132.697	1.436324	2355.042	764.1609	100.4518	0.152736	0.416668	1.04E-06	111.6113	0.350395	92.9004	0.000839
Internal door wood	m²	62.99868	0.545786	2083.975	293.9956	43.63203	0.050421	0.242276	6.81E-07	119.2717	0.021407	60.67185	0.000218
Painting	m²	0.938079	0.012821	15.0155	12.70521	0.58126	0.000811	0.002767	1.04E-08	0.247187	0.000278	0.703779	3.56E-06
Extruded polystyrene	kg	9.875458	0.026544	99.19069	9.731851	1.376559	0.00128	0.015036	6.84E-09	0.056289	0.000251	2.37875	1.30E-05
Aerated concrete block	kg	0.424023	0.001445	2.748279	1.976603	0.100125	0.000132	0.000715	3.64E-09	0.012066	1.24E-05	0.117809	6.71E-07
Copper	kg	1.969494	0.098187	33.68469	47.18211	20.19603	0.069272	0.02357	3.75E-08	0.252196	0.004058	10.49445	0.000134
Steel	kg	0.643436	0.004695	8.27001	1.876109	0.663425	0.000505	0.002023	5.44E-09	0.028786	1.66E-05	0.252512	3.94E-05

Material	Unit												
Hot water tank	l	1.411072	0.010411	18.38084	9.342325	1.806246	0.002577	0.004976	1.16E-08	0.136001	0.000143	0.698153	1.85E-05
Ventilation system - decentralised - 6 x 120 m3/h - steel ducts- without earth tube heat exchanger[*]	unite	10834.9	319.8589	137991.1	76602.88	9684.684	22.83111	38.78508	9.50E-05	490.0391	82.95576	8945.359	0.112861
Polyethylene (PE) high density[*]	kg	2.047969	0.010188	77.2951	3.312348	0.029601	8.45E-05	0.008035	9.47E-11	0.000342	2.42E-06	0.548293	3.04E-06
Heat pump 30kW[*]	unit	4459.123	45.19139	24538.88	15484.21	3192.315	18.35557	9.090282	1.89E-05	66.34251	0.651644	3121.325	0.043978
Borehole heat exchanger 133 m[*]	unit	2416.551	24.39126	42514.13	13758.38	2524.407	0.606027	22.47937	6.29E-05	18.06276	0.019657	953.9527	0.005171
PVC[*]	kg	2.089435	0.009392	61.85752	10.71624	0.126997	0.000212	0.010044	3.16E-09	0.003748	9.73E-06	0.565919	4.50E-06
Marble[**]	kg	0.002192	6.97E-05	0.030423	0.025362	0.000306	5.85E-07	5.41E-05	7.22E-11	9.65E-05	5.14E-08	0.001748	7.42E-09
Cable-3 lines[*]	m	3.826685	0.288559	80.91197	56.11434	17.46715	0.128206	0.042175	3.34E-08	0.352061	0.003837	16.23494	0.000259

[*]: Materials not contextualised, because no electricity process involved in its Unit Process (UPR), use the item of GLO (Globle) or RoW (Rest of World) in ecoinvent v3.4

[**]: Materials not contextualised, because no electricity process involved in its Unit Process (UPR), use the item in the French contextualised database

Annex D. Environmental impacts of materials contextualised with China average energy mix in 2019

Material	Unit	GWP	AP	CED	Water	Waste	EP	POP	Rad.W	Land	ADP	Biodiv	Hum
		kg CO2 eq.	kg SO2 eq.	MJ	L	kg	kg PO4 eq.	kg ethylene eq.	m³	m².year	kg antimony eq.	PDF.m².year	DALYs
Cement mortar	kg	0.219643	0.001004	1.51422	1.882056	0.068889	8.88E-05	0.000472	1.87E-09	0.018124	2.28E-06	0.070348	3.48E-07
Ceramic tile	kg	0.747118	0.007418	9.648298	6.576308	0.696688	0.000702	0.002201	5.20E-09	0.068712	0.00162	0.339609	8.60E-06
Concrete	kg	0.088459	0.000296	0.457359	1.512663	0.015424	3.26E-05	0.000168	8.25E-10	0.001168	1.47E-06	0.024578	1.26E-07
Expanded perlite	kg	0.339182	0.002952	5.95829	1.18067	0.184582	0.000253	0.001446	4.06E-09	0.025071	5.01E-05	0.143894	8.75E-07
Mortar	kg	0.528453	0.003134	3.801192	1.664309	0.205615	0.000286	0.001105	3.69E-09	0.03088	6.23E-06	0.181758	9.66E-07
Double glazing window with alluminum frame	m²	220.1724	1.906359	2563.212	970.0153	156.632	0.202038	0.60686	1.54E-06	6.09406	0.00822	90.22584	0.000903
External door wood-aluminium	m²	132.7795	1.436921	2358.246	765.2714	100.5406	0.152785	0.416888	1.05E-06	111.6129	0.350398	92.93077	0.000839
Internal door wood	m²	63.22753	0.547441	2092.856	297.0737	43.87815	0.050559	0.242885	7.28E-07	119.2762	0.021414	60.75602	0.000218
Painting	m²	0.938247	0.012822	15.022	12.70747	0.58144	0.000811	0.002768	1.05E-08	0.24719	0.000278	0.70384	3.56E-06
Extruded polystyrene	kg	9.890416	0.026652	99.77111	9.933031	1.392645	0.001289	0.015076	9.95E-09	0.056584	0.000252	2.384252	1.31E-05
Aerated concrete block	kg	0.424883	0.001451	2.781653	1.988171	0.10105	0.000132	0.000717	3.82E-09	0.012083	1.24E-05	0.118126	6.74E-07
Copper	kg	1.972705	0.09821	33.80931	47.2253	20.19948	0.069274	0.023578	3.82E-08	0.252259	0.004058	10.49563	0.000134
Steel	kg	0.649772	0.00474	8.51588	1.961331	0.67024	0.000509	0.00204	6.76E-09	0.028911	1.68E-05	0.254842	3.94E-05

Hot water tank	l	1.412554	0.010422	18.44636	9.36487	1.807838	0.002578	0.00498	1.20E-08	0.136032	0.000143	0.698711	1.85E-05
Ventilation system - decentralised - 6 x 120 m3/h - steel ducts- without earth tube heat exchanger[*]	unite	10834.9	319.8589	137991.1	76602.88	9684.684	22.83111	38.78508	9.50E-05	490.0391	82.95576	8945.359	0.112861
Polyethylene (PE) high density[*]	kg	2.047969	0.010188	77.2951	3.312348	0.029601	8.45E-05	0.008035	9.47E-11	0.000342	2.42E-06	0.548293	3.04E-06
Heat pump 30kW[*]	unit	4459.123	45.19139	24538.88	15484.21	3192.315	18.35557	9.090282	1.89E-05	66.34251	0.651644	3121.325	0.043978
Borehole heat exchanger 133 m[*]	unit	2416.551	24.39126	42514.13	13758.38	2524.407	0.606027	22.47937	6.29E-05	18.06276	0.019657	953.9527	0.005171
PVC[*]	kg	2.089435	0.009392	61.85752	10.71624	0.126997	0.000212	0.010044	3.16E-09	0.003748	9.73E-06	0.565919	4.50E-06
Marble[**]	kg	0.002192	6.97E-05	0.030423	0.025362	0.000306	5.85E-07	5.41E-05	7.22E-11	9.65E-05	5.14E-08	0.001748	7.42E-09
Cable-3 lines[*]	m	3.826685	0.288559	80.91197	56.11434	17.46715	0.128206	0.042175	3.34E-08	0.352061	0.003837	16.23494	0.000259

[*]: Materials not contextualised, because no electricity process involved in its Unit Process (UPR), use the item of GLO (Globle) or RoW (Rest of World) in ecoinvent v3.4

[**]: Materials not contextualised, because no electricity process involved in its Unit Process (UPR), use the item in the French contextualised database

RÉSUMÉ

Le processus d'urbanisation en Chine exerce une forte pression sur l'environnement. Le plus fort potentiel de réduction de ces impacts correspond aux décisions prises lors de la conception du bâtiment, qui peuvent s'appuyer sur des outils de simulation numérique. Cette thèse est consacrée à l'étude de trois conditions aux limites liées à l'évaluation de la performance énergétique et environnementale des bâtiments en Chine :

− Le sol : un modèle de pompe à chaleur couplée au sol est proposé, et couplé à un modèle d'échangeur de chaleur géothermique permettant le calcul rapide de la réponse d'un champ de sondes verticales de grande taille. Ce modèle peut être utilisé pour améliorer les performances énergétiques du système en phase de conception ou de gestion.

− Le microclimat : une méthode de génération de fichier climatique spécifique au site qui fournit la température horaire locale de l'air est proposée, prenant en compte l'effet d'îlot de chaleur urbain. Les effets du microclimat sur la performance énergétique du bâtiment sont étudiés quantitativement.

− Le système d'arrière-plan pour l'analyse de cycle de vie : les effets de la variation spatiale et temporelle du mix de production d'électricité en Chine sur les impacts environnementaux sont étudiés. La base de données environnementales est adaptée au contexte national et local chinois.

Les résultats montrent que les impacts environnementaux des bâtiments peuvent être évalués plus raisonnablement en considérant ces trois conditions aux limites.

MOTS CLÉS

Bâtiment, impacts environnementaux, échangeur de chaleur géothermique vertical, pompe à chaleur géothermique, microclimat, Analyse de Cycle de Vie, mix de production d'électricité.

ABSTRACT

The urbanisation process in China brings a high pressure on the environment. The highest potential to reduce these impacts corresponds to decisions made during the building's design phase, which can be supported by numerical simulation. This thesis is dedicated to the study of three boundary conditions related to the energy and environmental performance evaluation of buildings in China:

− The ground: a ground coupled heat pump model is proposed integrating a fast calculation ground heat exchanger model for a large-scale boreholes field. This model can be used to improve the energy performance of the system in the design and operation phases.

− The microclimate: a site-specific weather file generation method which can provide local hourly air temperature is proposed, accounting for the urban heat island effect. The effects of the microclimate on the building's energy performance are quantitatively investigated.

− The background system for life cycle assessment: the effects of the spatial and temporal variation of the electricity production mix in China on the environmental impacts are investigated. The environmental database is adapted to the Chinese national and local context.

The results show that the environmental impacts of buildings could be more reasonably evaluated by considering these three boundary conditions.

KEYWORDS

Building, environmental impacts, vertical ground heat exchanger, ground coupled heat pump, microclimate, life cycle assessment, electricity production mix.